UNIVERSITY OF SOUTHAMPTON

Faculty of Engineering and Physical Science
School of Electronics and Computer Science

Optomechanical electrometer based on optical mode-localization sensing

by

Yu Feng
MSc

A thesis for the degree of
Doctor of Philosophy

September 2021

University of Southampton

Abstract

Faculty of Engineering and Physical Science
School of Electronics and Computer Science

Doctor of Philosophy

Optomechanical electrometer based on optical mode-localization sensing

by Yu Feng

This work explores the feasibility of the optomechanical electrometer based on a novel sensing mechanism named optical mode-localization that originates from the mechanical mode-localization sensing mechanism. The electrometer is constructed by integrating coupled optical ring resonators and a suspended slot modulator on a silicon chip. The slot modulator is a Nano-Opto-Electrical-Mechanical-Systems (NOEMS) actuator that can tune the effective index and phase of the waveguide, and thus the perturbation in electrical charge can be transferred to the phase perturbation in the optical ring resonators. We use the modulator to create the mode-localization in the coupled optical ring resonators to accomplish ultra-high sensitivity charge sensing.

We established an analytical approximation of the index and phase change induced by the NOEMS slot modulator using the finite element analysis (FEA), including the Casimir force, optical force, electrostatic force and pull-in effect. The modulator can be configured in different ways to make the design flexible. COMSOL Multiphysics and Lumerical are used to analyze the possible configurations. The modulating performance of the fully suspended slot configurations are thoroughly analyzed.

Based on the signal flow graph analysis (Mason's rule), analytical model of the optical mode-localization based on coupled ring resonators is established. The correctness of the theoretical model is proved by Lumerical simulation. The optical mode-localization sensing has the advantages in sensitivity, accuracy, anti-aliasing and noise immunity compared with the mechanical mode-localization one. The optomechanical electrometer designed from coupled ring resonators and NOEMS slot modulator is more sensitive among other on-chip electrometers in theory.

We carried out few test runs to investigate the capability of the device fabrication. The specific structural releasing process based on HF vapour etching is developed for suspended waveguide. The specific ring resonators designed successfully extract the parameters of the necessary components. The scanning electron microscopy (SEM) pictures and output spectrum indicated that the surface roughness caused by fabrication imperfections would significantly affect the performance of the devices.

Contents

List of Figures

List of Tables

Declaration of Authorship

I declare that this thesis and the work presented in it is my own and has been generated by me as the result of my own original research.

I confirm that:

1. This work was done wholly or mainly while in candidature for a research degree at this University;
2. Where any part of this thesis has previously been submitted for a degree or any other qualification at this University or any other institution, this has been clearly stated;
3. Where I have consulted the published work of others, this is always clearly attributed;
4. Where I have quoted from the work of others, the source is always given. With the exception of such quotations, this thesis is entirely my own work;
5. I have acknowledged all main sources of help;
6. Where the thesis is based on work done by myself jointly with others, I have made clear exactly what was done by others and what I have contributed myself;
7. Parts of this work have been published as: Yu Feng, David J Thomson, Goran Z Mashanovich, and Jize Yan. Performance analysis of a silicon noems device applied as an optical modulator based on a slot waveguide. *Optics Express*, 28(25): 38206–38222, 2020

Signed:..... Date:.....

Acknowledgements

Thanks to the guidance from Jize Yan and Goran Mashanovich.
Thanks to the vital help from the silicon photonic group.
Thanks to all individuals who are helpful to this academic work.

To my parents

Chapter 1

Introduction

Silicon photonics technology that integrates photonic components on a silicon chip becomes a promising solution in many aspects, such as data centers, high-performance computing and sensing [2]. The essential multi-functional feature is developed based on mature CMOS-based fabrication technology and industrial chain resulting in high-volume production at low cost. Currently, silicon photonics has solid demands for constructing tunable photonic devices. The further extension towards multiple functions requires a strong electro-optic effect to allow the tuning. Based on conventional carrier-based modulation method, silicon lacks a high electro-optic coefficient [3]. However, silicon optomechanical structures can offer the high electro-optic coefficient to break the limitations in silicon photonics and expand the applications to sensors.

1.1 Motivation and aim

High performance sensing can be achieved by making use of the interactions between movable mechanical structure and light wave, for instance, Laser interferometer Gravitational Wave Observatory system (LIGO system), which is the state-of-art sensor for astrophysical gravitational wave researching [3]. Following the same physical conception, the optomechanical coupling between Micro/Nano-electro-Mechanical-systems (MEMS/NEMS) structure and silicon photonics is possible to promote the performance of novel devices, which is a popular research topic referred to as nano-opto-electro-mechanical system (NOEMS). NOEMS devices are constructed with optomechanical actuators and assistant optical circuitries.

The silicon suspended slot waveguide applied as a NOEMS actuator can modulate the effective refractive index and phase of the optical waveguide. It has the great potential to be applied as an essential component that is compatible with the existed silicon photonic integrated circuit (PIC). The narrow actuation gap between slot arms allows

the suspended slot modulator to be operated more effectively and flexibly than other electrostatic NOEMS actuators.

Currently, mode-localization MEMS/NEMS sensors achieve the state-of-art sensitivity among resonant MEMS/NEMS sensors [4]. The sensing is accomplished by monitoring the mode-splitting in a weakly coupled mechanical resonant system from parametric perturbation (measurand) on one of the resonators [5]. The parametric perturbation in the system induces the different amplitude of the resonant peaks from the mode-splitting, which is called mode-localization. By evaluating the amplitude ratio from resonant peaks, perturbations can be easily measured with high sensitivity, and high Signal-to-Noise-Ratio (SNR) with common-mode rejection [6].

Mode-localization sensing can also be carried out by optical resonators coupled with each others. The parametric perturbation on one of the coupled optical resonators produces mode-localization in optical spectrum. The sensing can be accomplished by evaluating the modal power ratio from resonant peaks, which is the same as MEMS/NEMS mode localization sensing. We name this novel sensing mechanism the optical mode-localization sensing. In this thesis, the optical mode-localization is produced from two optical ring resonators coupled with each other through a directional coupler.

An optomechanical electrometer can be constructed from two coupled optical ring resonators and NOEMS slot modulators. By integrating one or multiple NOEMS slot modulators in one of the coupled ring resonators, the perturbation in electrical charge are transferred to the phase or coupling perturbation in the optical ring resonators. In this way, the electrical charge can be detected by the optical mode-localization. This optomechanical electrometer has a great potential in obtaining ultra-high sensitivity over the existed MEMS/NEMS electrometers.

The project aims to theoretical analyze an optomechanical electrometer constructed from a NOEMS slot modulator based on optical mode-localization sensing mechanism. The fabrication capability and fabrication process development of suspended silicon photonic structures are also discussed.

1.2 Report structure

In chapter 2, the optomechanics and underlying physics are reviewed. The suspended waveguide devices and on-chip electrometers are reviewed in detail. The physics and the optomechanical suspended slot modulator are illustrated in chapter 3. In chapter 4, the theoretical performance of the silicon NOEMS slot modulator with the fully suspended conducted slot or grounded slot configurations is analyzed in detail. In chapter 5, the theory of the optical mode-localization sensing mechanism and the theoretical analysis about the electrometer constructed by integrating the NOEMS slot modulator

with coupled ring resonators are illustrated. The details of fabrication process development and component parameter extraction are illustrated in chapter 6. A summary of contributions and possible works in the future is concluded in chapter 7. The published papers and papers in progress are listed in chapter 8.

Chapter 2

Literature review

Optomechanics is a general term for all devices integrating the optical and mechanical components that its optical properties can be tuned or excited by micro/nano-mechanical structures. The investigation in the optical force and suspended optical structures gives the birth of various optomechanical devices. It has great potential to construct high-performance sensors from the optomechanical actuator and silicon photonic circuitry, including an optomechanical electrometer that has not been developed ever. In this chapter, the physics and publications under the topic of optomechanics are organized and concluded. A detailed illustration of the specific knowledge of related physics is in the rest chapters. The slot waveguide and on-chip electrometer are reviewed in detail.

2.1 The development of optomechanics

In the late 1960s, far before the age of nanoelectronics, engineers recognized the possibility of realizing mechanical devices in microns based on the standard CMOS fabrication on silicon. A hybrid system integrating micromechanical structure and electronics on the same chip was published from the concept of minimization and integration. Such a system was then described as Micro-Electro-Mechanical System (MEMS). Later on, the term Nano-Electro-Mechanical System (NEMS) is given to the birth after CMOS fabrication achieved nanoscale critical dimension (CD). In the late 1980s and mid-1990s, silicon-on-insulator (SOI) is introduced to the industries for reduced parasitic capacitances for ICs, and they are ideal choices for waveguide systems as well [2]. SOI wafer is also considered a good platform for MEMS devices. The earlies research on SOI-based passive waveguides and active waveguide-based devices form the basics of silicon photonics. The integration of photonics with electronics was a popular research direction providing multifunction with improved performance at a low cost from the 1990s to now [2].

With the fact that the development of optoelectronic devices has reached a bottleneck of performance (operating speed, energy consumption, critical dimension, etc.), the possible alternative technologies like MEMS/NEMS and silicon photonics have become attractive topics in both industrial and academic aspects [7]. One common target of the research in MEMS/NEMS and silicon photonics is extending the silicon platform application benefit from mature semiconductor industrial link that provides small volume, low cost and multifunctional devices. Based on similar fabrication platforms, they can be integrated with IC naturally. A mechanically deformable optical device is considered a promising technology for tunable photonics rather than other methods [8].

An optical actuator constructed on a suspended whispering gallery mode (WGM) cavity can magnify or suppress the mechanical resonances from thermal vibrations, which is named dynamic back-action. The kind of the system is given the name of cavity optomechanics with most of its intention on the physics research [9]. The development of cavity optomechanics can be traced back to the 1970s when Braginsky investigated the coupling between optical modes and mechanical mirror vibration in a Fabry-Pérot resonator [10]. Generally, these mechanisms are explored for integrating multi-functional optomechanical systems on chips with excellency in performance and size. However, necessarily high optical energy on WGM cavity needs to be input from tapered optical fibre by evanescent field coupling. The strict requirement on alignment and high power consumption make the system impossible to be integrated on chip.

Later on, the investigation about the optical force generated from suspended waveguides through evanescent coupling demostrated that an optomechanical system can be constructed from suspended waveguide fabricated from SOI platform [11]. The optical applications of MEMS/NEMS electrostatic actuators and switches are also investigated with the intuition of constructing tunable photonic systems through electrostatic actuated suspend waveguides [8]. These integrated optomechanical systems constructed by MEMS/NEMS actuator and optical actuator provide various functionalities requiring external signal to control the system.

2.2 Optomechanical coupling and typical optomechanical devices

The theory of optomechanics comprises a complete feedback loop involving mechanisms on two paths of energy conversion, including optical energy altering mechanical energy (by optical force) and, reversely, mechanical energy altering optical energy (by mechanically induced refractive index change). The whole loop is named as dynamical back-action [12]. The relating mechanisms on the loop are Casimir force, electrostriction/photoelastic effect, radiation pressure. Reviews about these mechanisms can be found in [13].

2.2.1 Casimir Force

The force is firstly predicted as an attractive force between two electrically neutral ideal conductor plates separated with extremely small distance in quantum vacuum state by Casimir. Shortly after, the theory was expanded to dielectric plates separated by any materials by Lifshitz [14]. The theory is constructed on electromagnetic field fluctuation and dissipation of plate materials from their frequency-dependent dielectric permittivities. Now it is derived in the framework of thermal quantum field theory covering both van der Waals (non-retraded) and Casimir (retraded) regimes [15].

2.2.2 Electrostriction

Electrostriction describes the situation in bulk material compressed by the presence of an electric field [16]. When light propagates through the material, the material is applied by gradient force proportional to the gradient of the local optical energy, which is called the electrostrictive force in this case. Electrostrictive forces push polarizable particles toward the high-intensity region, and this compression will lead to a variation of the permittivity of the material, which leads to varied local field strength [16]. Reversely, any altered mass density by local compression/expansion will locally increase/decrease the permittivity of the material, which results in amplification/attenuation of both electrical wave and mechanical wave.

Consequently, electrostriction can enhance both acoustic wave/mechanical vibration and field strength at the same time, such as the self-focusing phenomenon [17]. Electrostriction is considered as one of the origins of third-order nonlinear optical response especially stimulated Brillouin scattering [16]. Electrostrictive force can be quantified by electrical field distribution and photoelastic coefficient of the material according to crystal orientation [18]. It can be predicted by density functional theory [19].

2.2.3 Radiation pressure

Radiation pressure is generated by electromagnetic wave reflection on boundary between different materials [20]. On the edge of the waveguide, the totally reflected light applies force perpendicular to the edge. The radiation pressure can be considered as a simplified model of the total gradient force on the boundary. The significant change in the electric field on the high-index contrast boundary can also be illustrated by Maxwell's continuity conditions [21]. Any movement of the boundary will lead to a variation of radiation pressure by altering the field gradient on the boundary, and it largely depends on device design. Radiation pressure can be calculated from Maxwell stress tensor derived from momentum conservation [20].

2.2.4 Optical microcavities

Optical microcavities frequently occupy in modern optical devices such as lasers, filters, accurate measurement tools and nonlinear optics experiments [9]. With the nature of wavelength selection and light accumulation, enhanced gradient force can be generated by enhanced light intensity gradient. There are two basic types of microcavities used for chip-scale devices: Fabry-Perot (FP) microcavities and whispering gallery modes (WGM) microcavities. One common feature of the optical cavities is that particular optical modes suiting the standing wave condition are strengthened while other modes are filtered out. In optomechanics, microcavities can be used as a tool for field enhancement or used to excite mechanical vibration with critical coupling.

2.2.4.1 Fabry-Perot microcavities

The Fabry-Perot (FP) cavity is named after Charles Fabry and Alfred Perot, who built it in 1897 as an interferometer. The first FP cavity was constructed by two highly reflecting mirrors separated by a distance, and only longitudinal resonances that fulfilments the standing wave condition can be strengthened. Now FP cavity is a generic term for reflective cavities such as photonic crystal cavities and Bragg grating based cavities [22].

2.2.4.2 Whispering gallery modes microcavities

In a whispering gallery modes (WGM) microcavity, the standing wave is formed in a round-trip light path as light propagating in a ring or the edge of a disk. WGMs can be simplified as EM waves circulate and confined within the resonator's structure [9]. High quality factor can be expected by WGM due to minimized reflection losses (low material absorption), thus very high energy density can be achieved [9]. Chip-scale WGMs are usually constructed with a close loop waveguide or disk to confine the light in a round-trip path and a bus waveguide coupled to a round-trip path [23][24].

2.3 Chip-scale optomechanical device

The mechanically movable photonic devices making the exchange between optical energy and kinetic energy possible rather than just thermal dissipation. The optical force from electrostriction and reflection exists in many photonic structures, while the producible optomechanical structures are limited to suspended planar layers for chip-scale devices based on the current semiconductor fabrication platform. The two essential

concepts of the optomechanical device are the dynamic back-action and optical field enhancement.

According to the application, the mechanical actuation is practiced by an appropriate coupling method, and field enhancement may be necessary if a stronger optical force is desired. The system can be designed upon vibration amplification [25], evanescent field coupling [26] and mechanical displacement by MEMS actuator [8][27]. The existing devices can be divided into MEMS/NEMS actuated and optically actuated (optical force) systems depends by how devices are actuated.

2.3.1 MEMS/NEMS actuated system

A MEMS/NEMS actuated system is a kind of tunable photonic device through MEMS/NEMS actuation. For example, with the combination of MEMS/NEMS electrostatic actuation and waveguide, optical switch [28][29], displacement sensing [30], optical filters [31] and optical modulator [32], are able to be constructed. Most of the devices in this category obtained higher performance through a cavity-enhanced field. The most common MEMS/NEMS actuator is the electrostatic force actuator. Detailed information of the related publications is sorted out well and comprehensive in [8].

2.3.2 Optically actuated system

The optical actuator has limited types of designs available considering the principle of light propagation. Currently, evanescent coupling [26] and reflective cavity with moving boundaries [33] are commonly utilised in optical actuators. Optical actuators such as suspended slot waveguide with evanescent mode [34], suspended ring resonator [23] or any other structures with evanescent field coupling [11] can induce the mechanical motion. Based on the theory of optical force, the mechanical structure can be actuated by a specially designed plasmonic device as well [35]. Typical optical actuators configuration and published devices based on evanescent coupling are shown in Figure 2.1 and Figure 2.2.

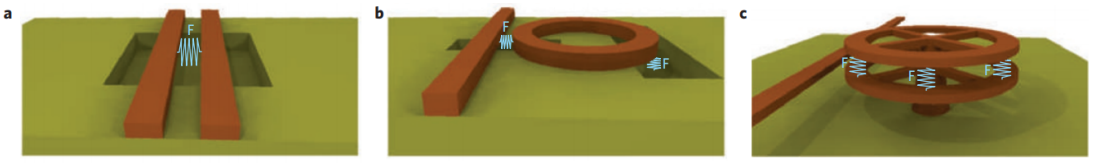

FIGURE 2.1: The optical gradient force acting on integrated waveguide structures. a, The force between two parallel waveguides; b, Force enhancement through the use of an integrated resonator; c, Coupled resonator configuration. [11].

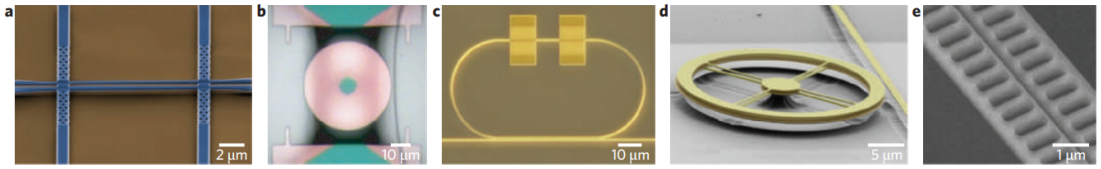

FIGURE 2.2: Typical optomechanically driven nanostructures. a, Two parallel silicon strip waveguides; b, SiNx microdisk coupled to a fibre taper; c, Silicon ring resonator with a photonic-crystal-supported nanomechanical beam; d, Vertically coupled SiN disk resonator; e, Laterally coupled ladder photonic crystal cavities. [11].

Cavity resonators can achieve both static and periodic force actuation. By constructing suspended cavity resonators [36] (ring, toroid and disk resonator), the mechanical vibration of the resonator can be excited by unmodulated light at critical coupling, and this is the unique advantage of the optical actuator. However, the cavity limits the intrinsic optical bandwidth of the system as well [37].

2.3.3 Optomechanical vibration

Periodic force is essential in exciting mechanical vibration more than thermal mechanical vibration. In optomechanics, periodic optical force can be induced by dynamic back-action [24], external feedback construction [37][25] and open loop modulated light/-electrical pulse [38][39]. The mechanical vibration is amplified from thermal vibration except for the open loop system.

2.3.3.1 Optomechanical vibration by external periodic force

By modulating the amplitude of the light input to optical actuators (evanescent wave bonding), mechanical vibration can be generated from the periodic force controlled by a modulated light signal. The optical force generated in such structure is usually weak [39] so high power input and cavity enhancement are necessary to excite the mechanical vibration. Photonic crystal [40] and ring resonator [41] are commonly chosen for the force enhancement. The basic principle for electrostatic actuator is the same.

2.3.3.2 Self-enhanced optomechanical vibration

With dynamic back-action or external feedback, a parametric instability [42] induced by thermal vibration can further enhance (regenerative vibration) or weaken (mechanical cooling) the thermal mechanical vibration [43]. These physical processes are understood from the point of quantum mechanics and concluded as cavity optomechanics [44]. In cavity optomechanics, cooling or amplification of the mechanical vibration is

decided by frequency of the cavity mode and motional sidebands generated by parametric instability as shown in Figure 2.3 [12].

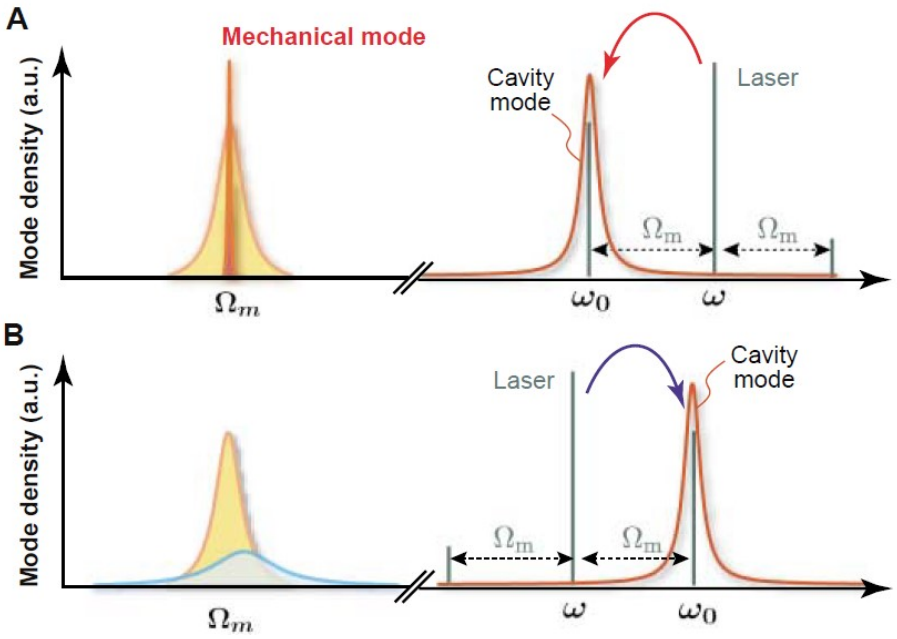

FIGURE 2.3: Dynamical back-action. (A) Mechanical mode amplification proceeds by supressing anti-Stokes scattering; (B) Mechanical cooling proceeds by supressing the Stokes process [12].

In Figure 2.3 (A), if the cavity resonance is pumped red detuned ($\omega > \omega_0$), the scattering from cavity resonance into the stoke sideband will be suppressed, while the anti-Stoke sideband will be enhanced, vice versa. This asymmetry in the motional sidebands contributes to a net power transfer between mechanical mode and light mode due to a periodic optical force in phase/out of phase with the thermal vibration. The asymmetry itself is the result of the bandwidth limitation of the cavity mode. The amplification/cooling is also possible for devices with external feedback [37].

2.4 Slot waveguide devices for sensing

Slot waveguide possesses great potential in applications including optical modulation [32], manipulation of nanoparticles [45] label-free chemical sensing [46] and biosensing [47]. Slot waveguide belongs to evanescent field sensors amongst the most popular sensing methods for high sensitive label-free detection. Matters passing evanescent field or surface bond changing the effective refractive index will cause a resonance shift in the optical spectrum, and it is referred to as refractive index detection.

Slot waveguide was developed from integrated optics based on high-index-contrast waveguides with a guiding mechanism based on total internal reflection (TIR) in a

high-index core surrounded by low-index cladding. While for slot waveguide, the optical field is enhanced and confined in the low-index slot in-between two high-index slots with significant field discontinuity on the high-index-contrast interface [48]. For the silicon platform, the slot waveguide can be simply constructed on SOI where silicon and air are treated as high-index material and low-index material, respectively. In this case, the optical field is mainly confined and enhanced in the form of the evanescent field.

This unique propagating mode makes the slot waveguide attractive for refractive index detection since the slot mode allows most of the mode energy to interact with matters. The sensitivity of the evanescent field sensor depends on the overlap of the sample and the evanescent field. Thus the slot waveguide is considered a good choice for refractive index detection [49]. Moreover, the sensitivity can be improved by further enhancing the field intensity through slot waveguide resonators [47]. Apart from biochemical sensing, mechanical vibration can be detected by refractive index change as well [26]. Any geometrical change of the optical device can induce modal change. For waveguide-based optomechanical systems, mechanical deformation is the main source of the effective refractive index change, which can be analyzed in the spectrum. So far, there are few publications concerning the application of optomechanical electrometer based on slot waveguide.

2.5 Mode-localization sensing mechanism

MEMS (MicroElectroMechanical Systems) is a generic term for all micro technology based systems combining micro-scale mechanics and electronics. It has become an essential topic of discussion for decades in sensor applications with the main advantages of small volume, low fabrication costs and low energy consumption compared with the traditional sensors.

A variety of MEMS sensors are published with a growing market in both defense and commercial products. Among various sensing mechanisms, resonant sensing is regarded as an excellent method with remarkable performance and a high price-performance ratio. Micromechanical resonators have gained increasing interest in the past few decades for their potential as timing references, mass sensors, strain sensors, accelerometers and electrometers. [50].

The resonant sensors detect the measurand (target physical quantities) by making the forced mechanical resonance dependent on the measurand, which is called the coupling between measurand and mechanical resonance [51]. With different coupling mechanisms, MEMS resonators are able to detect varies measurand based on the shift on its resonant frequency and corresponding amplitude.

Based on the MEMS resonator, an advanced sensing system based on constructing weak coupling between identical resonators was introduced to further improve the sensor sensitivity by over two orders of magnitude [5]. Its functionality is accomplished by measuring the normalized amplitude sensitivity based on mode localization phenomenon described as follows: In periodic structures such as two identical resonators coupled to each other, even a small perturbation, which break the system symmetry, will lead to locally vibration energy confinement in small regions [4][52]. A series of mode-localized sensors have been created with incredible sensitivity [4].

There are serval advantages of mode localized sensing. With the help of the mode localization, sensors' sensitivity can be improved by over two orders of magnitude as conventional resonant sensors based on frequency shifting [5]. Since the sensing is achieved by quantifying the relative change between different modes (frequency and amplitude) in the system, it is less susceptible to false-positive readings (reading false reports a moment which does not exist) as the conventional method of frequency shifting [53]. This feature is named as common-mode rejection [6]. The eigenstate or amplitude ratio based sensing allows that both sensitive detection and analytic identification of small perturbation to be achieved at the same time [52].

For two degree-of-freedom (2DoF) mode-localized sensor (two resonators coupled together), the weak coupling between resonators leads to higher sensitivity [54] while it also set a limitation of sensitivity by mode aliasing effect due to finite bandwidth of the modes (finite quality factor) [4], i.e., two modes cannot be identified when they are too close to each other on the frequency spectrum.

2.6 Chip-scale electrometer

One early construction of modern electrometer can be traced back to 1932 when Gunn demonstrated an electrometer designed on a mechanical variable capacitor that could measure charge more than $4fC$ [55]. Throughout the 1970s, vibrating-reed electrometers, which origins from the same concept in 1932, were developed and widely used [56]. Various single electron detection devices are developed with the strong driving force of researching the quantum properties of electrons. The state-of-art electrometers dedicated to single-electron detection are cryogenically cooled (few mK) single-electron transistors (SETs), cryogenically cooled nano-mechanical resonators and graphene resonators [57].

SETs are regarded as the most sensitive electrometers with the capability of sensing a single electron at charge noise of $10^{-5}e/\sqrt{Hz}$ [58]. Apart from the solid-state device, one NEMS resonator was reported to achieve a comparable noise floor at a higher temperature of $4.5K$ [59] and another NEMS resonator was reported to achieve a resolution of $0.1e/\sqrt{Hz}$ in charge detection with the help of mechanical nonlinearity [60]. The

low noise feature of the above devices is obtained under extremely low temperatures. Besides cryogenically cooled devices, single-electron detection at room temperature is possible by Coulomb blockade effect [61] through the nano-scale capacitor. Noise floor of $4 \times 10^{-2} e/\sqrt{Hz}$ was measured at $300K$ with AL SET with minimum feature size of about $10nm$ [62]. The above devices have limited applications with a restricted requirement on the working environment, fabrication method and cost.

Depart from a single-electron electrometer, a wide range of applications for general-propose electrometers operate at room temperature and pressure. MEMS/NEMS time-varying capacitance electrometer or vibrating reed is a good candidate of electrometry with good robustness at different temperatures and pressure. The state-of-art MEMS electrometers operating at room temperature can be divided into three groups, including vibrating-reed electrometer, resonant electrometer and mode-localized electrometer, by their different working principles. The charge is detected by quantifying resonant amplitude response, frequency response and amplitude/frequency ratio from vibrating-reed electrometer, resonant electrometer and mode-localized electrometer, respectively. Resolution of the published micro electrometers here is described as the minimum detectable number of electrons, are listed in Table 2.1.

TABLE 2.1: Resolution and sensitivity of published MEMS electrometers. The unit Hz/fC^2 and ppb/fC^2 is the result of re-position of the zero charge point.

Vibrating-reed electrometer			
By	**Working condition**	**Resolution**	**Sensitivity**
[63]	ambient pressure, room temperature	$6e$	$4.51 \times 10^6 V/C$
[64]	ambient pressure, room temperature	$3e$	$25.11 \times 10^{10} V/C$
[57]	vacuum, room temperature	$23e$	$2.7 \times 10^9 V/C$
Resonant electrometer			
[65]	vacuum, room temperature	$25000e$	$(1.2 \times 10^{-3} Hz) 7.8 ppb/fC^2$
[66]	vacuum, room temperature	$5250e$	$1.03 \times 10^{-2} Hz/fC^2$
[67]	vacuum, room temperature	$203750e$	$(4.4Hz) 7.4 ppb/fC^2$
mode-localized electrometer			
[52]	vacuum, room temperature	$8000e$	$0.034 ppb/fC^2$
[68]	vacuum, room temperature	$10e$	$0.0227/fC$

Usually, the resolution of a sensor is decided by the noise, the sensitivity/responsivity of the sensing element and the resolution of the post-processing unit. The resolution of the electrometers shown in Table 2.1 is obtained from V/C (Voltage/Coulomb), f/C (Frequency shift/Coulomb), AR/C (Amplitude ratio/Coulomb) and ES/C (Eigenstates shift/Coulomb) of the device and minimum detectable voltage of the signal processing circuitry. From Table 2.1, the best resolution is achieved by a vibrating-reed electrometer, which is well-tuned with low noise and parasitic capacitance compensation (chip-scale assembling). The other structures described in [65], [66] and [67] can only achieve relatively poor resolutions without enough tuning. In contrast, mode-localized

electrometer can achieve the resolution at the same level as the vibrating-reed electrometers with less effort on-chip packaging and electronic peripherals. The ultra-high sensitivity improves the charge resolution to ten electrons in a normal noise level.

2.6.1 MEMS vibrating-reed electrometer

The basic structure of the MEMS vibrating-reed electrometer is shown in Figure 2.4 below.

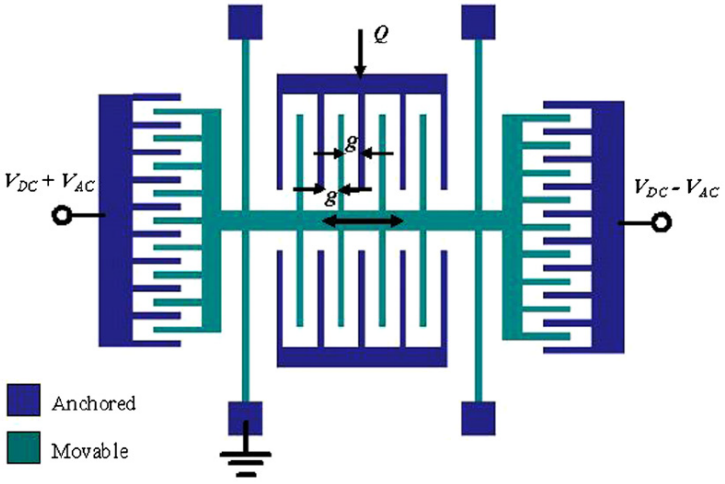

FIGURE 2.4: The configuration of the MEMS vibrating-reed electrometer [63].

Figure 2.4 shows a resonator laterally push-pull actuated resonator with sensing electrodes perpendicular with the direction of actuation. The charge detection is carried out at second harmonic resonant frequency with the consideration of reducing charge feedthrough and 1/f noise from electronic circuit [63]. The charge is detected by measuring the resonant amplitude of the device (Voltage/Coulomb). The resonant amplitude will be enhanced by charge-induced electrical potential difference on the sensing electrodes when it is small [63]. The best resolution among the existed MEMS vibrating-reed electrometer is 3e reported by [64] with good suppression of electronic noise and parasitic capacitance compensation.

2.6.2 MEMS resonant electrometer

The basic structure of the MEMS resonant electrometers are shown in Figure 2.5 and Figure 2.6. The charge is measured from the frequency shift (Frequency shift/Coulomb).

Figure 2.5 shows a resonant electrometer constructed by a Double-Ended Tuning Fork (DETF). In Figure 2.5, the actuation and detection are carried out in the same direction. The charge is detected by measuring the resonant frequency-shift induced by axial force along the longitudinal axis of DETF [65]. Resolution of the electrometer is dominated

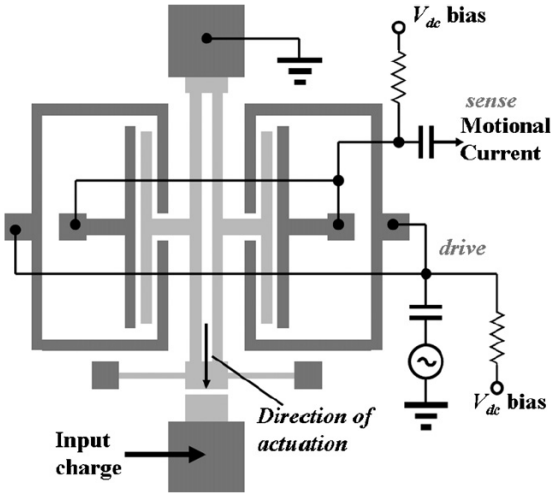

FIGURE 2.5: The configuration of the DETF resonant electrometer in [65]

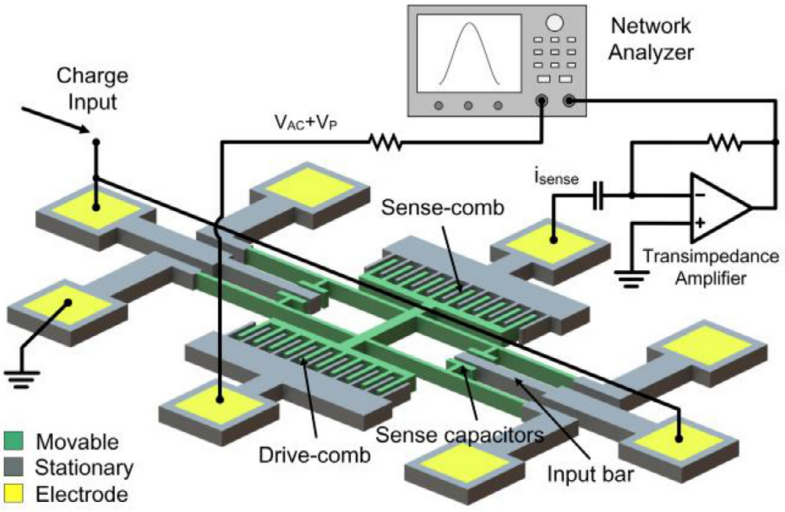

FIGURE 2.6: The configuration of the DETF resonant electrometer in [67]

by electronic noise [65]. In Figure 2.6, the resonant frequency-shift is induced by lateral side stiffness perturbation and this method has higher sensitivity than axial force coupling in Figure 2.5 [67]. However, high frequency fluctuation noise limits the resolution to 202750e, which is much larger than in [65]. The best resolution among the existed MEMS resonant electrometer is 5250e achieved by mechanically amplifying the axial force (positive correlated to sensitivity) through dual micro-levers as shown in Figure 2.7 below.

2.6.3 MEMS mode-localized electrometer

There are many theoretical publications about MEMS mode-localization resonators, while only a few papers published as MEMS mode-localized electrometer with detailed analysis on sensitivity, noise and resolution. Zhang Hemin, et al. developed a

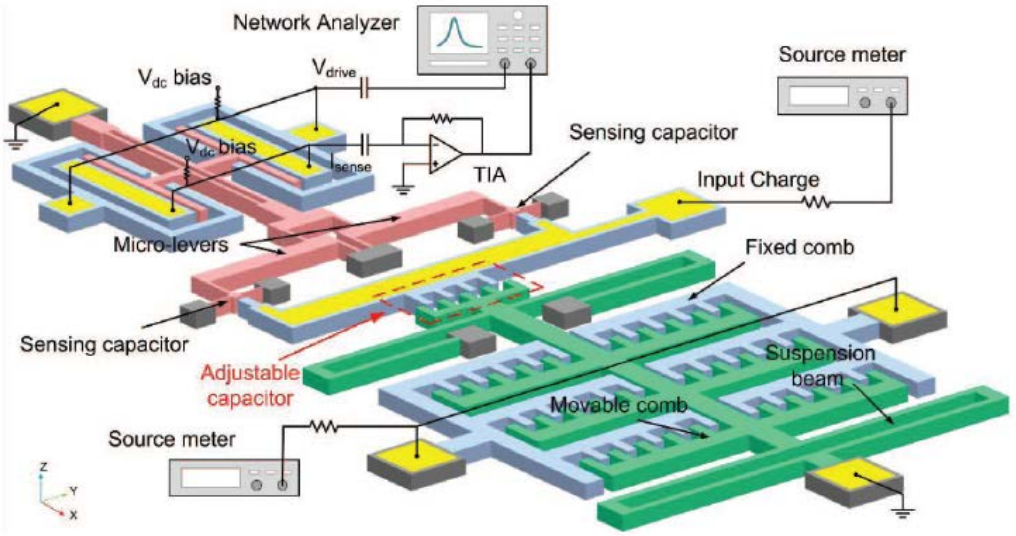

FIGURE 2.7: Optimized electrometer with micro-levers and movable comb that is able to adjust the sensitivity [66].

2 DoF mode-localized electrometer with weak mechanical coupling in 2016 [52]. The construction of the device is shown in figure Figure 2.8.

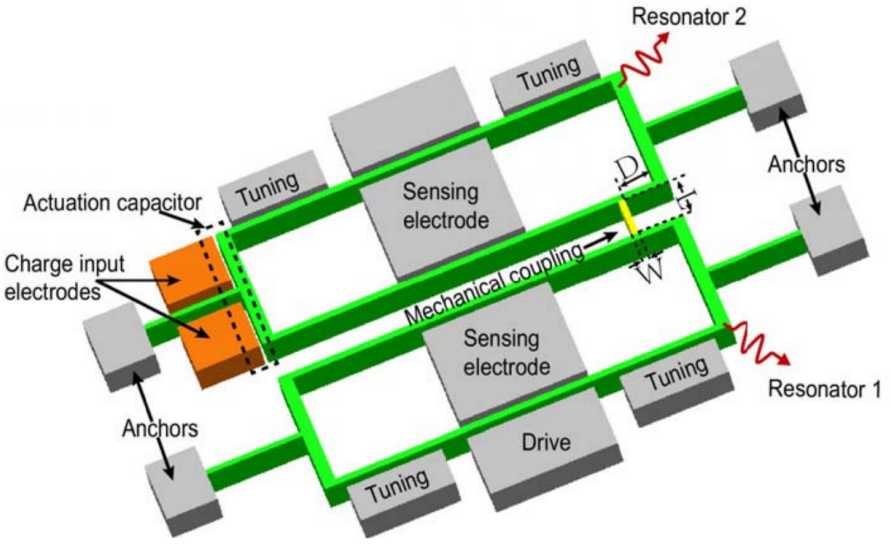

FIGURE 2.8: DoF mode-localized electrometer with weak coupling [52].

Figure 2.8 illustrates a mode-localized electrometer constructed from two identical DETF coupled with mechanical spring. The resolution was reported to be 8000e evaluated from ES/C (Eigenstates shift/Coulomb). Jing Yang, et al. published a 3 DoF mode-localized electrometer with weak mechanical coupling in 2018 [68]. The construction of the electrometer is shown in Figure 2.9.

Figure 2.9 illustrates a mode-localized electrometer constructed from three mechanically coupled resonators. The resolution was reported to be 10e evaluated from AR/C (Amplitude ratio/Coulomb). This significant improvement in resolution is achieved

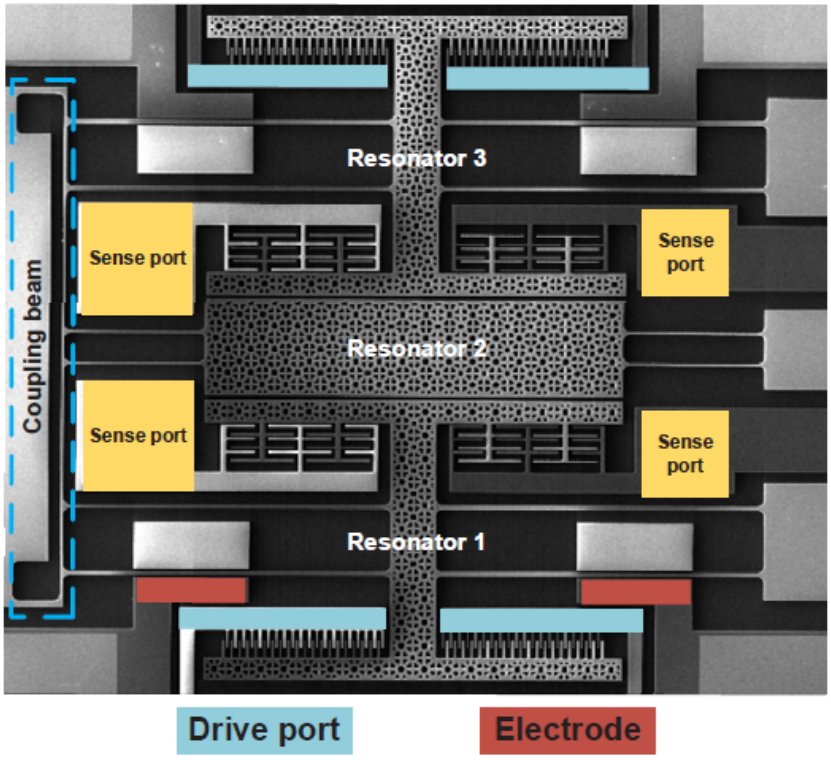

FIGURE 2.9: DoF mode-localized electrometer constructed on a axial symmetrical design [68].

by amplitude ratio output and extra sensitivity enhancement by 3 DoF system rather than 2 DoF.

2.7 Chapter conclusions

The literature reviewed in this chapter covers the research on physics properties and potential applications of the silicon optomechancial devices. The state-of-art MEMS resonant electrometers are reviewed to identify the best on-chip electrometer. The mechanical mode localization by coupled resonators is the key to ultra-high sensitivity. There is a research gap in applying mode localization sensing in the optical and optomechanical systems. It is possible to construct an optical mode localized sensor by coupling multiple optical resonators/cavities, which are the common structures of the reviewed devices. An electrometer can be built from coupled ring resonators and suspended slot waveguide modulators as the first step in discovering the optical mode localized sensing. The coupled ring resonators provide a base for mode localization. The suspended slot waveguide modulator acts as a transducer that converts the charge perturbation into parametric perturbations for mode localized sensing.

Chapter 3

Physical modelling of suspended slot waveguide

This chapter introduces the theoretical background of the suspended slot waveguide and the author's original contribution to the calculation of optomechanical modulator/phase shifter. Specifically, the physical models of the silicon suspended slot applied as a NOEMS device are discussed. The discussion covers the system's optical, electrical and mechanical properties and the interactions between these domains. Specifically, we treat the whole system as a NOEMS actuator that can tune the optical effective index and phase change. Besides the electrostatic force, the existence of Casimir force and optical force reduces the electrical power threshold in controlling the system, limiting the system's tuning ability.

The main origin contributions in this chapter are the analytical approximation of the optomechanical refractive index and phase change. We established an analytical approximation of the index and phase change of the device using the finite element analysis (FEA), including Casimir force, optical force and electrostatic force. The physical models involve the optical mode of slot waveguide; electrostatic, Casimir and optical force in the silicon parallel plate structure; mechanical deformation under uniformly distributed load; pull-in effect; mechanical vibration of coupled resonators; mechanical deformation induced index and phase change of the waveguide.

3.1 Optical mode of slot waveguide

The slot waveguide is constructed on two identical waveguides with a narrow gap between each other. In order to describe the structure of the slot waveguide, the propagating direction of the optical mode is set in the same direction of z-axis. The x-axis is aligned with the direction of evanescent bonding (quasi-TE mode) between slot arms.

The geometrical definition of the slot waveguide in this chapter is shown in Figure 3.1 where w, t, g and L denote the width of the slot arm, the thickness of the silicon layer,

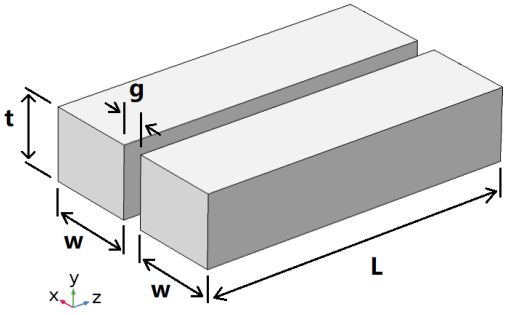

FIGURE 3.1: Slot waveguide structure with infinite height [48].

the separation between slot arms and the suspended length of the waveguide, respectively. For silicon slot waveguides in air or vacuum, high-index-contrast interfaces on the boundary of the waveguide produce large discontinuities with a much higher amplitude electric field in the low index side [48]. This is the result of the continuity of the normal component of electric flux density D from Maxwell's equations. Thus, the optical field can be enhanced and confined in the low-index region when the light is guided by total internal reflection [48]. A simplified theoretical model assuming the slot waveguide structure with infinite height is shown in Figure 3.2 [48]. The numeri-

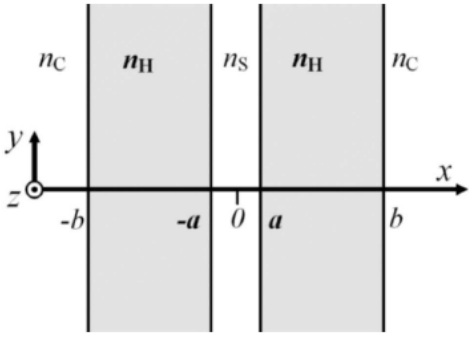

FIGURE 3.2: Slot waveguide structure with infinite height [48].

cal solution of the normalized transverse E-field distribution from this simplified model is shown in Figure 3.3 [48]. From Figure 3.3, discontinuities of the field can be found on the boundaries of the silicon waveguide. The field in between two waveguides is enhanced and confined. In practice, silicon photonics devices for 1550 nm can be fabricated on SOI wafers with 220 nm silicon layer. To ensure the fundamental mode to be a quasi-TE mode, the slots are designed with a width larger than the thickness. The cross-section of the slot waveguide surrounded by air ($n_s = n_c = 1$) is chosen to be $t = 220$nm, $w = 250nm$, $g = 70nm$, limited by the available resolution of the fabrication tools. The corresponding optical mode is shown in Figure 3.4. From Figure 3.4, strong field confinement in between two silicon slots is observed. This mode is named as the

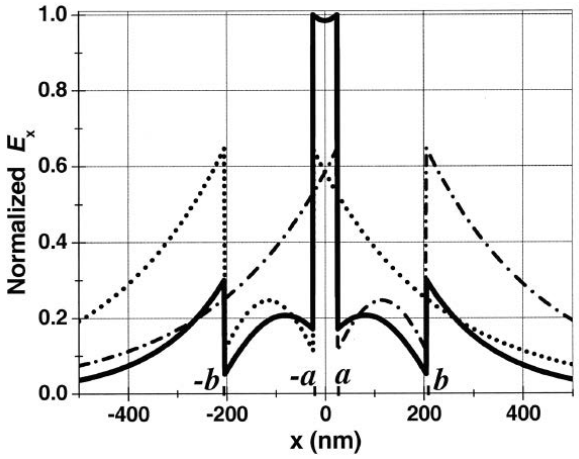

FIGURE 3.3: Normalised transverse E-field distribution at $\lambda_0 = 1.55\mu m$ shown in solid curve, with $n_H = 3.48$, $n_s = n_c = 1.44$, $a = 25nm$ and $b = 205nm$. The field distribution for individual waveguide are shown in dotted and dashed-dotted curves [48].

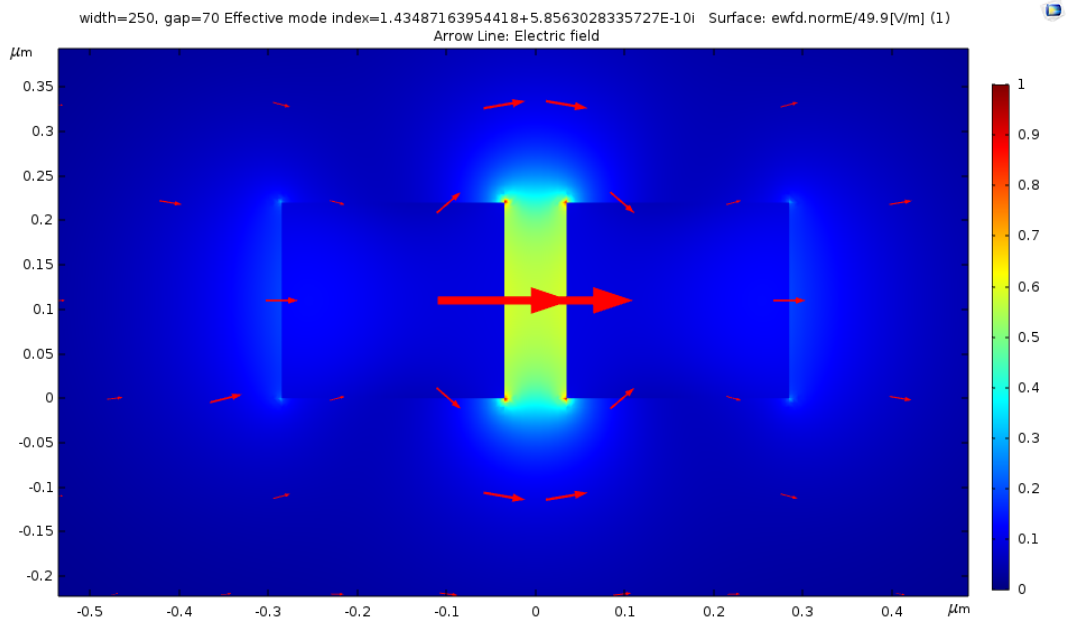

FIGURE 3.4: Normalised optical mode of the slot waveguide; the effective mode index of the waveguide is about 1.44. The red arrow indicates the electrical field at the centre of the arrow, with its size is proportional to field strength.

quasi-TE mode by [48]. The normalized transverse E-field distribution of the quasi-TE mode of the slot waveguide is shown in Figure 3.5. From Figure 3.5, the mode profiles calculated by Lumerical and COMSOL of the device design are slightly different in the magnitude of the field discontinuities on the high index-contrast interface. This is a reasonable difference caused by different numerical solvers (finite-element analysis by COMSOL and finite-difference time-domain method by Lumerical). Both profiles match the theory and simulation result illustrated in [48]. Based on the assumption of perfectly smooth surface, the theoretical propagation loss calculated by Lumerical is smaller than $5 \times 10^{-4} dB/cm$, which is negligible.

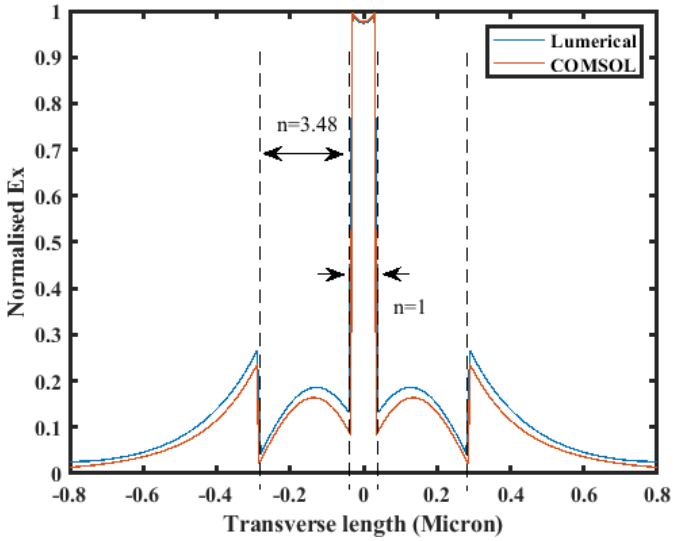

FIGURE 3.5: Quasi-TE mode of the slot waveguide from Lumerical and COMSOL.

3.2 Forces in the optical waveguide

The slot waveguide consists of two parallel plates with electrostatic, optical and Casimir force applied. Optical force and electrostatic force only exist when the electromagnetic field is confined in the waveguide. The theory of Casimir force, electrostatic force and optical force in slot waveguides are illustrated in Section 3.2.2, Section 3.2.3 and Section 3.2.1, respectively.

3.2.1 Optical force in slot waveguide

Generally, sources of optical force in the waveguide are recognized as electrostriction and radiation pressure. The property of optical force strongly depends on the propagating optical mode. For slot waveguide, radiation pressure between the evanescent wave coupled slot is the primary source of the optical force. Electrostriction and radiation pressure is discussed in Section 3.2.1.1, optical force by optical mode in single waveguide and evanescent wave bonding are discussed in Section 3.2.1.2 and Section 3.2.1.3, respectively.

3.2.1.1 Electrostriction and radiation pressure

So far, studies of optical force discovered that nanoscale waveguides and cavities can generate non-ignorable optical force by high field gradient from well-confined field and significant field enhancement techniques [69]. Investigation of the optical force in microscale started from the research in gradient force by Ashkin in 2006, who first

demonstrated the force in small dielectric particles trapped by laser light. The time-averaged energy of the polarized dielectric particle in the field is given by [70]

$$U = -\frac{1}{2}\vec{p}\cdot\vec{E} = -\frac{1}{2}\alpha\left|\vec{E}(\vec{r})\right|^2 \tag{3.1}$$

where $\vec{E}(\vec{r})$ denotes the laser electric field distribution, $\vec{p}$ denotes dipole moment, $\vec{r}$ denotes displacement vector, and α denotes the polarizability of the particle. The gradient force is given by [70]

$$\vec{F} = -\vec{\nabla}U = \frac{1}{2}\epsilon_0\alpha\nabla(E^2) \tag{3.2}$$

The negative sign in the equation indicates that the polarized particles are forced to move into the place where field intensity is stronger. The polarizability of the particle is closely dependent on the property of the particles since the polarization can change the external field distribution as well [16].

Different from individual polarizable particles, optical force in the waveguide originates from electrostriction and radiation pressure. The radiation pressure can be calculated by the Maxwell stress tensor of the field distribution due to energy conservation. Derivation of equations for Maxwell stress tensor can be found in [20]. The expression of the Maxwell stress tensor (T_{ij}) in a dielectric medium at rest is [69]

$$T_{ij} = \epsilon_0\epsilon_r(x,y)\left[E_iE_j - \frac{1}{2}\delta_{ij}|E|^2\right] + \mu_0\mu_r(x,y)\left[H_iH_j - \frac{1}{2}\delta_{ij}|H|^2\right] \tag{3.3}$$

Where $E_k(H_k)$ is the 'k'th (electric/magnetic) field component, $\epsilon_0(\mu_0)$ is the vacuum electric permittivity and magnetic permeability, and $\epsilon(x,y)(\mu)$ is the relative permittivity (permeability) [69]. The full expression for Maxwell stress tensor is:

$$T_{ij} = \begin{bmatrix} \epsilon\left({E_x}^2 - \frac{E^2}{2}\right) + \mu\left({H_x}^2 - \frac{H^2}{2}\right) & \epsilon E_xE_y + \mu H_xH_y & \epsilon E_xE_z + \mu H_xH_z \\ \epsilon E_yE_x + \mu H_yH_x & \epsilon\left({E_y}^2 - \frac{E^2}{2}\right) + \mu\left({H_y}^2 - \frac{H^2}{2}\right) & \epsilon E_yE_z + \mu H_yH_z \\ \epsilon E_zE_x + \mu H_zH_x & \epsilon E_zE_y + \mu H_zH_y & \epsilon\left({E_z}^2 - \frac{E^2}{2}\right) + \mu\left({H_z}^2 - \frac{H^2}{2}\right) \end{bmatrix} \tag{3.4}$$

Force from radiation pressure can be calculated on the boundary calculated by [20]

$$\vec{F} = \oint_S T\cdot\vec{n}\,ds \tag{3.5}$$

where $\vec{n}$ is the outward normal to the closed surface S and T is the sum of T_{ij}. It is the force per unit area transmitted across the surface S, which is the boundary of

the objects in electromagnetic field [20]. Electrostrictive force can be calculated by electrostrictive stress tensor expressed in terms of the material photoelastic coefficients. For isotropic materials and for cubic crystals like silicon the expression of electrostrictive tensor $({\sigma_{kl}}^{es})$ is [69]:

$$\sigma_{kl}^{es} = -\frac{1}{2}\epsilon_0 n^4 p_{ijkl} E_i E_j \tag{3.6}$$

where p_{ijkl} is the photoelastic (or elasto-optic) tensor, which is a fourth-rank tensor used to link the dielectric constant with the refractive index ellipsoid according to Pockel's phenomenological theory of photoelasticity of crystals [71]. Electrostrictive tensor components where the x-direction coincides with the [100] silicon crystal symmetry direction can be calculated by [69]:

$$\sigma_{xx}^{es} = -\frac{1}{2}\epsilon_0 n^4 \left[p_{11}|E_x|^2 + p_{12}(|E_y|^2 + |E_z|^2)\right] \tag{3.7}$$

$$\sigma_{yy}^{es} = -\frac{1}{2}\epsilon_0 n^4 \left[p_{11}|E_y|^2 + p_{12}(|E_x|^2 + |E_z|^2)\right] \tag{3.8}$$

$$\sigma_{zz}^{es} = -\frac{1}{2}\epsilon_0 n^4 \left[p_{11}|E_z|^2 + p_{12}(|E_x|^2 + |E_y|^2)\right] \tag{3.9}$$

here photoelastic coefficients are expressed in contracted notation where $11 \rightarrow 1$, $22 \rightarrow 2$, $33 \rightarrow 3$, $23, 32 \rightarrow 4$, $13, 31 \rightarrow 5$ and $12, 21 \rightarrow 6$. The photoelastic tensor used for calculation is provided from [19] as:

$$p_{ijkl}\mu_{kl} = \left(\frac{\delta a}{a}\right) \begin{bmatrix} p_{11} & 0 & 0 \\ 0 & p_{12} & 0 \\ 0 & 0 & p_{12} \end{bmatrix} \tag{3.10}$$

where a is the lattice constant and $\delta a/a$ is the percentage strain. μ_{kl} is the strain tensor. The expression is valid for uniaxial strain along [100] only [19].

3.2.1.2 Optical force in a single waveguide

The optical force from electrostriction and radiation pressure in the single waveguide can be calculated by Maxwell stress tensor and electrostrictive tensor. The calculation is carried out by COMSOL Multiphysics 5.3. The calculation of the radiation pressure and electrostrictive force on the waveguide is based on the mode profile. The direction of radiation pressure is perpendicular to the boundary of reflection, while electrostrictive force depends on the mode profile. If x-axis is set perpendicular to the direction of light propagation, y-axis is set perpendicular to the silicon layer, and Z axis is aligned with the direction of light propagation, the coordinate will be like as shown in Figure 3.6. Here we only concern about the optical force on the x and y directions as shown in Figure 3.6. In the simulation software, the force should be calculated by integrating the

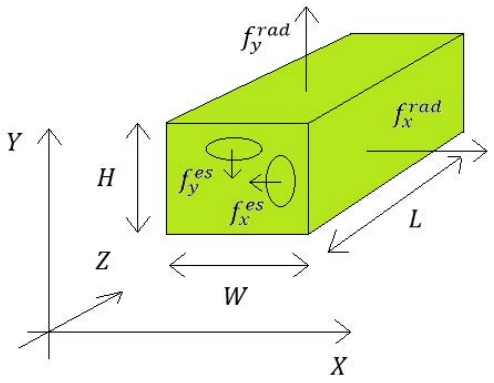

FIGURE 3.6: Reference coordinate setting for the simulation

force density on where the force is applied. The force density is expressed by [69]:

$$F_j^{opt} = F_j^{rad} + F_j^{es} = \partial_i T_{ij} - \partial_i \sigma_{ij}^{es} \tag{3.11}$$

The expressions of $T_x x$ and $T_y y$ from section 3.3.2. are:

$$T_{xx} = \epsilon \frac{1}{2}(E_x^2 - E_y^2 - E_z^2) + \mu \frac{1}{2}(H_x^2 - H_y^2 - H_z^2) \tag{3.12}$$

$$T_{yy} = \epsilon \frac{1}{2}(E_y^2 - E_x^2 - E_z^2) + \mu \frac{1}{2}(H_y^2 - H_x^2 - H_z^2) \tag{3.13}$$

Thus radiation pressure on top and side surface is calculated by:

$$f_x^{rp} = \int_{H*L} \partial_x T_{xx} \cdot dydz \tag{3.14}$$

$$f_y^{rp} = \int_{W*L} \partial_y T_{yy} \cdot dxdz \tag{3.15}$$

If the x-axis is aligned with [100] as described in section 3.3.2., the x component and y component of the electrostrictive tensor are referred to Equation 3.7 and Equation 3.8, respectively. The total electrostrictive force can be estimated by integrating force density with half of the cross-section of the waveguide:

$$f_x^{es} = \int_{W/2*H} -\partial_x \sigma_{xx}^{es} \cdot dxdy \tag{3.16}$$

$$f_y^{es} = \int_{W*H/2} -\partial_y \sigma_{yy}^{es} \cdot dxdy \tag{3.17}$$

Here only the radiation pressure is evaluated since most of the mode energy of the slot waveguide is distributed on the surface of the waveguide, which means electrostriction is ignorable, especially for silicon. In order to standardize the unit of optical force, optical force is described with $pN/\mu m/mW$, which is the load/power since the optical force is evenly distributed along the waveguide length and is proportional with the optical power. The calculation results of the optical force (for silicon waveguide)

in comparison with results in [69] in x-direction are shown in Figure 3.7. From Fig-

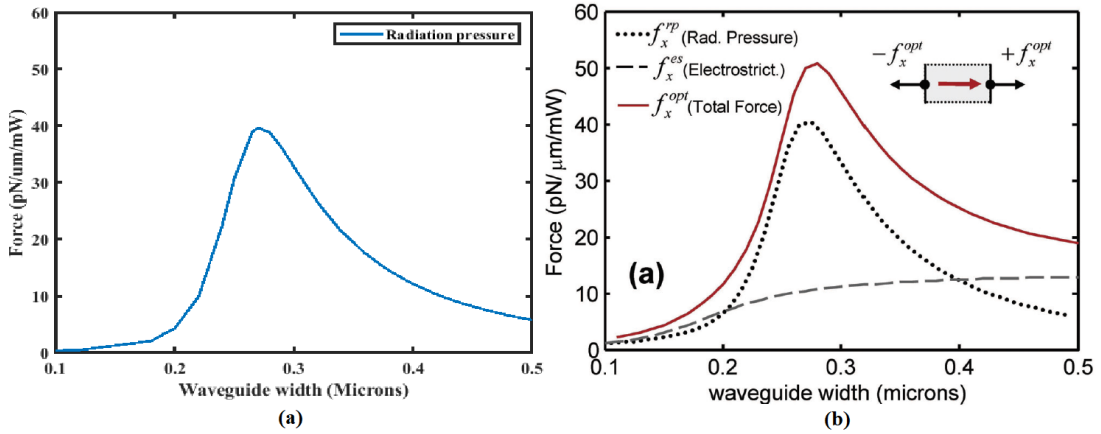

FIGURE 3.7: Optical fore in X-direction with different waveguide width. (a) From COMSOL; (b) From [69].

ure 3.7, the radiation pressure curve calculated by COMSOL is highly agreed with [69]. This means a good agreement between COMSOL and [69] in the electrical field on the boundary can be reached. The calculation results of the optical force in comparison with results in [69] in Y-direction are shown in Figure 3.8. By comparing the simulation

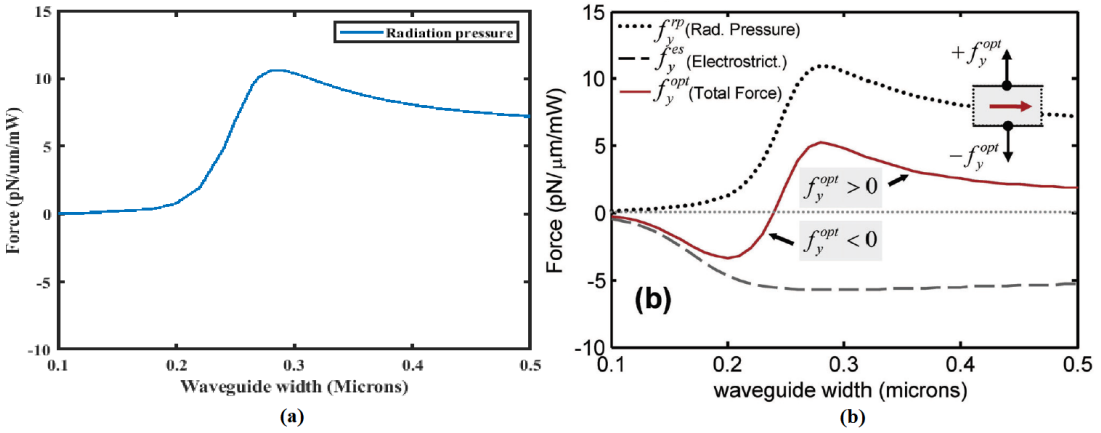

FIGURE 3.8: Optical fore in Y direction with different waveguide width. (a) From COMSOL; (b) From [69].

results between COMSOL and results in [69], it is confirmed that there is no substantial error in results from COMSOL.

3.2.1.3 Optical force in coupled waveguides and a slot waveguide

Optical force in slot waveguide is generated from evanescent wave bonding, which is principally the same as an optical force in the coupled standard waveguide. The force induced by radiation pressure in the coupled waveguides, which is also referred to as directional coupler, can be attractive or repulsive. Since force induced by radiation pressure at the boundary points to the waveguide outwards, the force on the

inner boundary is attractive. In contrast, the force on the outer boundary is repulsive as shown in Figure 3.9. For the coupled waveguides, the asymmetry electric field dis-

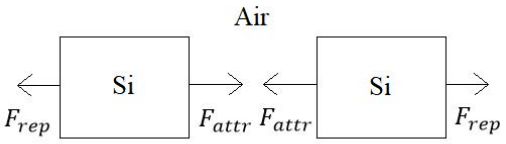

FIGURE 3.9: Force on the boundary of the coupled waveguides.

tribution in each waveguide leads to a different amount of force applied on the inner and outer walls of the waveguides thus, they are pushed close to or pulled away from each other. For the coupled waveguides experiencing symmetric mode that means no phase difference between two waveguides, the total force on the waveguide appears to be attractive. In contrast, the force will be repulsive for asymmetric mode [72]. The radiation pressure between the coupled waveguides can be calculated by [72][38]

$$F_{opt} = -\frac{1}{n_{eff}}\frac{\partial n_{eff}}{\partial g}U = \frac{n_g l}{n_{eff} c}\frac{\partial n_{eff}}{\partial g}P_{opt} \tag{3.18}$$

$$n_g = n_{eff} - \lambda\frac{dn_{eff}}{d\lambda} \tag{3.19}$$

where n_{eff} , n_g, U, P and λ represent the effective refractive index, group refractive index, optical energy, optical power and wavelength, respectively. This simplified model for calculating optical originated from an evanescent field based on kinetic and momentum conservation. The calculation results from the above equations are identical to the force calculated by radiation pressure [72]. The comparison between the calculation results from COMSOL and [72] are shown in Figure 3.10. From Figure 3.10, the radiation pressure-induced force calculated by COMSOL matches the results from [72] for both symmetric mode and asymmetric mode. In Figure 3.10 (b), solid curves are calculated by stress tensor and symbols are calculated from Equation 3.18. Experimental results from [73] proved the validity of the calculation methods in calculating optical force in slot waveguide. By definition of the optical waveguide, If any individual slot arms can support an optical mode, the whole structure will be treated as coupled waveguides rather than an individual waveguide, so the asymmetric mode should not exist in the slot waveguide. As a result, the optical force from quasi-TE mode of a slot waveguide will be attractive between slot arms only.

3.2.2 Casimir Force in silicon parallel plate

From Lifshitz theory, the Casimir force (F_{Cas}) between two real material plates, separated by a gap distance g, is expressed by adding a correction factor to Casimir force

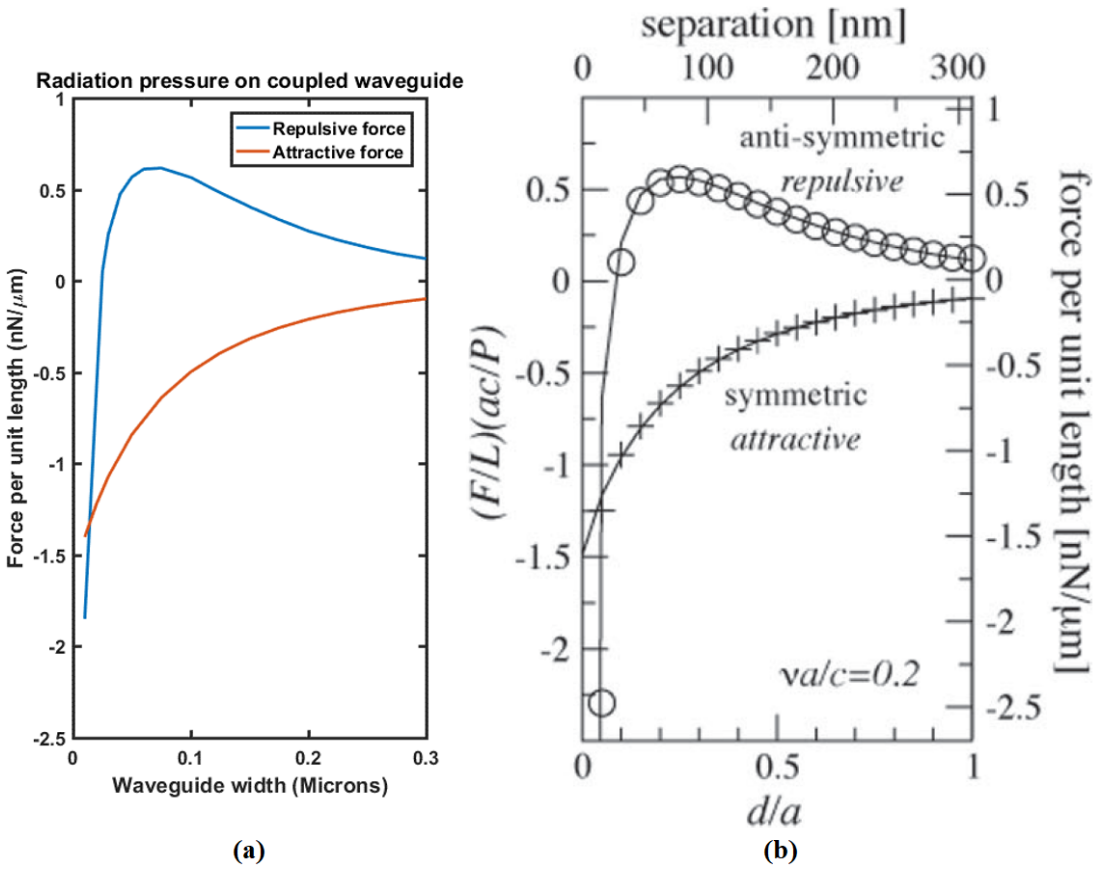

FIGURE 3.10: The calculated force on the coupled waveguides. (a) From COMSOL; (b) From [72]. The limit of the x and y axis are equivalent in (a) and (b).

for ideal conductor plates, which leads to [14]:

$$F_{Cas}(g, A) = -\frac{\hbar c \pi^2}{240} \frac{A}{g^4} \eta \tag{3.20}$$

where $\hbar$ is the reduced Planck constant, A is the area of the plates, and η is the finite conductivity correction factor, which depends on the dielectric permittivities of the material in the system. The influence of the temperature T is usually negligible for a NOEMS, since photon energy dominates the system rather than phonon energy ($g \ll c\hbar/k_B T$), where k_B is the Boltzmann constant [14]. For typical C-band slot-waveguides at room temperature (T = 300 K), $g \ll 7.6\mu m$ satisfy the condition when the separation between arms of slot waveguide is usually around $100nm$. For silicon parallel plate in NOEMS:

$$\eta = \left(\frac{\epsilon - 1}{\epsilon + 1}\right)^2 \left(1 - \frac{1.11}{\sqrt{\epsilon}} \ln \frac{\epsilon}{7.6}\right) \tag{3.21}$$

where ϵ is the dielectric permittivities of the material. For silicon with refractive index equals to 3.475 ($n = \sqrt{\epsilon}$), the correction factor is calculated to be $\eta \approx 0.611$. The Casimir force always exists independently with other forces in the nano/micro system,

for instance, in [74].

3.2.3 Electrostatic force in parallel plate actuator

For electrostatic actuation, the electrical potential energy $P.E.$ stored in the capacitive structure is given by

$$P.E. = \frac{CV^2}{2} \tag{3.22}$$

where C is the capacitance of the structure and V is the potential applied to the structure. The electrostatic force can be derived by differentiating potential energy in space:

$$F_{es} = \frac{dP.E.}{dx} \tag{3.23}$$

For an ideal parallel-plate capacitor, the capacitance is

$$C = \frac{\epsilon_0 \epsilon_r A}{g} \tag{3.24}$$

where A and g represent overlap area and gap (distance between two plates) of the capacitor. $\epsilon_0 (\epsilon_0 = 8.854 * 10^{12} F/m)$ and ϵ_r represent vacuum permittivity and relative permittivity of the material. Thus, the electrostatic force with DC and AC voltage applied on a parallel-plate capacitor is

$$\begin{aligned} F_{es} = \frac{dP.E.}{dx} &= \frac{1}{2} V^2 \frac{\partial C}{\partial x} = \frac{1}{2} \left(V_{DC} + |V_{AC}| \cos \omega t \right)^2 \frac{\partial C}{\partial x} \\ &= \frac{1}{2} \left\{ {V_{DC}}^2 + \frac{|{V_{AC}}^2|}{2} + 2 V_{DC} |V_{AC}| \cos \omega t + \frac{|{V_{AC}}^2|}{2} \cos 2\omega t \right\} \frac{\partial C}{\partial x} \\ &= -\frac{1}{2} \left\{ {V_{DC}}^2 + \frac{|{V_{AC}}^2|}{2} + 2 V_{DC} |V_{AC}| \cos \omega t + \frac{|{V_{AC}}^2|}{2} \cos 2\omega t \right\} \frac{\epsilon_0 \epsilon_r A}{x^2} \end{aligned} \tag{3.25}$$

Using electrostatic actuation, a voltage difference must be applied between the moveable structure and its target deflection direction. To omit the second-order frequency terms, AC voltage is necessary to be smaller than DC voltage. For the case of a slot waveguide, the parallel plate cannot be treated as an ideal capacitor as Equation 3.24 due to its low t/w ratio. The capacitance of the slot waveguide needs to be solved numerically.

3.3 Mechanical deformation and vibration

From the view of material mechanics, each arm of the slot can be treated as a typical clamped-clamped beam structure. The deformation curvature of the beam applied

with uniformly distributed load illustrated in Section 3.3.1, is necessary since it will affect the index and phase change of the waveguide by chang the separation between slot arms. The mechanical vibration analysis, illustrated in Section 3.3.2 and Section 3.3.3, is essential in the transient response of the system and it relates to the modulation speed of the device.

3.3.1 Uniformly distributed load on Euler beam

The displacement of the beams of the slot can be described by the Euler beam equation shown by (residual axial stress neglected) [75]:

$$EI\frac{d^4x}{dz^4} = p_m(z) \tag{3.26}$$

where E is Young's modulus, $p_m(z)$ is the load (N/m) distribution along the beam and I is the beam's area moment of inertia. Coordinate (z, x) described the plane where the beam deformed. In the interested direction, I is defined as:

$$I = \frac{tw^3}{12} \tag{3.27}$$

where w and t are the width and thickness of the beam, respectively. Based on the theory described in previous chapters, electrostatic, optical ,and Casimir force can be treated as uniformly distributed loads along the beam, the arm of the suspended slot waveguide, when displacement is small enough(tens of nano-meters) so $p_m(z)$ can be simplified as a load represented by p_m instead of a function as shown in Figure 3.11

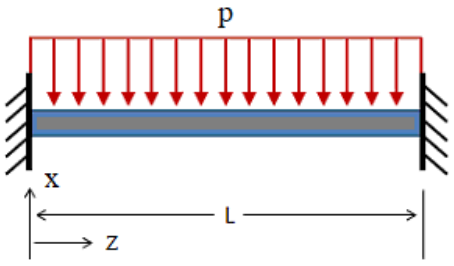

FIGURE 3.11: Fixed-fixed beam with uniform distribute load.

Formula for deflection curvature is described by [76]:

$$\delta x = \frac{p_m z^2}{24EI}(L-z)^2 \tag{3.28}$$

Maximum deformation at the middle of the length is:

$$\delta x_{max} = \frac{p_m L^4}{384EI} \tag{3.29}$$

Beyond elastic range, the structure lacks enough restoring force to balance the external load, thus the system will not reach a steady-state until the structure collapse. The critical load of the fixed-fixed beam can be solved by plastic analysis with the virtual-work method described as [77]:

$$p_{mc} = \frac{16M_p}{L^2} \tag{3.30}$$

where M_p and p_c denotes the plastic moment and critical load of a plastically deformed beam, respectively. For rectangular cross-section M_p can be expressed as [75]:

$$M_p = \sigma_y Z_p = \sigma_y \frac{tw^2}{4} \tag{3.31}$$

where σ_y is the yield stress measured as about $4.9GPa$ at room temperature [78], thus the limitation of the load and deformation are set as:

$$p_{mc} = \frac{4\sigma_y tw^2}{L^2} \tag{3.32}$$

$$\delta x_c = \frac{\sigma_y L^2}{8wE} \tag{3.33}$$

Usually, MEMS/NEMS devices are operated far below this value.

3.3.2 Single degree-of-freedom mechanical vibration

The key elements of all mechanical resonators are mass, spring and damper. MEMS/NEMS resonators may be effectively modelled as single-degree-of-freedom (SDoF) damped oscillators with linear spring (represented by K) and viscous damping (represented by C_m) as shown in Figure 3.12. Systems shown in Figure 3.12(a). can be

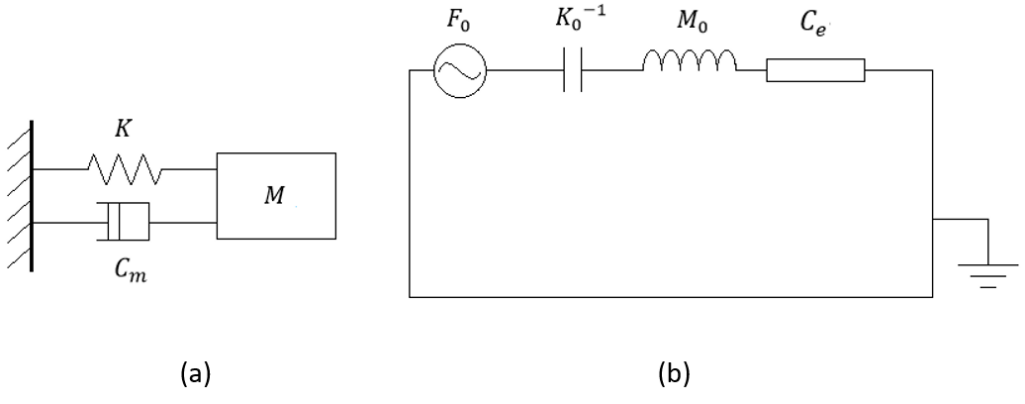

FIGURE 3.12: Damped SDoF oscillator (a); and equivalent circuit model (b).

expressed by equations shown below:

$$M\ddot{x}(t) + C_m\dot{x}(t) + Kx(t) = F(t) \tag{3.34}$$

$$L\ddot{Q}(t) + R\dot{Q}(t) + 1/C_e Q(t) = V(t) \tag{3.35}$$

Equation 3.34 is the motional equation for the mechanical resonator. In Equation 3.34, x denotes the mechanical displacement. Equation 3.35 is the relation between the electrical components and the voltage applied to the LRC circuit. In Equation 3.35, Q denotes the charge accumulated in the capacitor. From the lumped model, mechanical resonators can be described by the LRC circuit equivalently. Accordingly, basic physical parameters of the mechanical resonator can be described by electrical circuit components as shown in Table 3.1 :

TABLE 3.1: Parametric transferring between the mechanical vibration and electrical circuit

Standard unit in mechanical system	**Transferred unit in electrical system**
Energy $J(Fx;1/2Kx^2;1/2Mx^2)$	Energy $J(UIt;1/2CU^2;1/2LI^2)$
Power $P(Nm/s)$	Power $P(Nm/s)$
Force $F(N)$	Voltage $U(V)$
Mass $M(kg)$	Inductance $L(H)$
Displacement $x(m)$	Charge $Q(q)$
Velocity $\dot{x}(m/s)$	Current $I(A)$
Damping $C(Ns/m)$	Resistance $R(\Omega)$
Stiffness/spring factor $K(N/m)$	Capacitance $C = 1/K(F)$

This electrical analogy is name as voltage-force (mass-inductance) analogy [79]. The relation between force and displacement can be expressed by a transfer function of charge and voltage $TF = Q/V$. The system response can be investigated from the transfer function based on control theory. The general form of the transfer function is

$$TF = G(s) = \frac{c(s)}{r(s)} = \frac{K(S+Z_1)(S+Z_2)\dots}{S^n(S+P_1)(S+P_2)\dots} \tag{3.36}$$

where $P_x = R(P_x) + jI(P_x)$ (poles) and $Z_x = R(Z_x) + jI(Z_x)$ (zeros) are the complex roots of $c(s) = 0$ (maximum impedance) and $r(s) = 0$ (minimum impedance) respectively. The physical resonant frequency of the system is the real part of each pole expressed by $\omega_x = R(P_x)$ and the corresponding physical amplitude response is $A_x = |G(s = j\omega_x)|$. To characterise SDOF system, an equivalent RLC serious circuit can be constructed with force-voltage translation $(Q(t) \equiv x(t))$. Its frequency domain transfer function is:

$$TF = \frac{Q_K}{V_{in}} = \frac{1}{MS^2 + CS + K} = \frac{1}{K}\frac{{\omega_n}^2}{S^2 + 2\zeta\omega_n S + {\omega_n}^2} \tag{3.37}$$

The properties of the system are defined by its natural frequency ω_n, damped frequency ω_d, resonant frequency ω_{res}, damping factor ζ, time constant τ and quality factor Q:

$$\omega_n = \sqrt{\frac{K}{M}} \tag{3.38}$$

$$\zeta = \frac{C}{2\sqrt{KM}} \tag{3.39}$$

$$Q = \frac{1}{2\zeta} = \frac{\sqrt{KM}}{C} \tag{3.40}$$

$$\tau = \frac{2M}{C} = \frac{1}{\omega_n \zeta} \tag{3.41}$$

$$\omega_d = \omega_n \sqrt{1-\zeta^2} \tag{3.42}$$

$$\omega_{res} = \omega_n \sqrt{1-2\zeta^2} \tag{3.43}$$

where natural frequency ω_n describes the fundamental system frequency, which is the modulus of a pair of complex poles, and it keeps constant when the system is under-damped or critical damped ($0 < \zeta \leq 1$). The resonance happens within the range of $0 < \zeta \leq \frac{\sqrt{2}}{2}$. The system response at frequency interested (ω) are described by frequency ratio (γ), amplitude response (A) and phase response (ϕ):

$$\gamma = \frac{\omega}{\omega_n} \tag{3.44}$$

$$|A(\gamma,\zeta)| = \frac{1}{K} \frac{1}{\sqrt{(1-\gamma^2)^2 + (2\gamma\zeta)^2}} \tag{3.45}$$

$$\phi(\gamma,\zeta) = \arctan\left(-\frac{2\gamma\zeta}{1-\gamma^2}\right) \in [-\pi, 0] \tag{3.46}$$

The physical amplitude and phase response obtained at resonance frequency ($\gamma = \sqrt{(}1-2\zeta^2)$) are:

$$|A_{res}(\zeta)| = \frac{1}{K} \frac{1}{2\zeta\sqrt{1-\zeta^2}} \tag{3.47}$$

$$\phi_{res}(\gamma,\zeta) = \arctan\left(-\sqrt{\frac{\gamma}{\zeta}}\right) \in [-\pi, 0] \tag{3.48}$$

The displacement of the system from excited amplitude $F_{in}(\omega)$ is

$$x(t) = F_{in}(\omega)|A(\gamma,\zeta)| \sin\left(\omega t - \phi(\gamma,\zeta)\right) \tag{3.49}$$

The transient response of the under damped system with step input ($1(t)$) is expressed by:

$$x(t) = \frac{1}{K}\left[1 - \frac{e^{-t/\tau}}{\sqrt{1-\zeta^2}} \cos\left(\omega_d t - \psi\right)\right] \quad 0 < \zeta < 1 \tag{3.50}$$

where the phase angle $\psi = \arctan\left(\zeta/\sqrt{1-\zeta^2}\right)$. In theory, the vibration of the system is never stopped. In reality, the system is usually regarded to settle within $3\tau - 5\tau$ depending on the tolerable amplitude of vibration.

3.3.3 Two degree-of-freedom mechanical vibration

The two beams of suspended slot waveguide can be treated as two identical mechanical resonators coupled with electrostatic force, optical force and Casimir force acting like spring. It is a typical 2 DoF system constructed as shown in Figure 3.13 where K_C

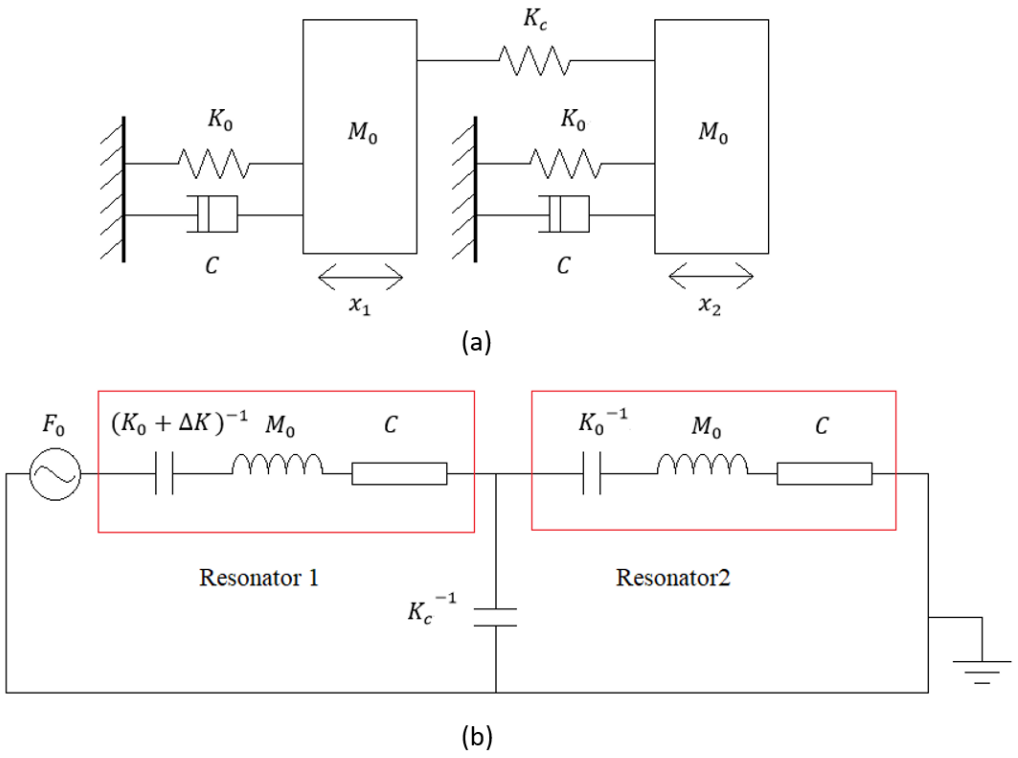

FIGURE 3.13: (a) Mechanical model of coupled resonators with stiffness perturbation; (b) Equivalent circuit of the coupled resonators

represents coupling stiffness. The equivalent circuit is derived from two equations of motion of the system described by [79]:

$$\begin{cases} M_0\ddot{x}_1(t) + C\dot{x}_1(t) + K_0x_1(t) + K_c(x_1 - x_2) = F_0(t) \\ M_0\ddot{x}_2(t) + C\dot{x}_2(t) + K_0x_2(t) + K_c(x_2 - x_1) = F_0(t) \end{cases} \tag{3.51}$$

where x_1 and x_2 are the displacement of the resonator 1 and 2, respectively. These equations are identical to Figure 3.13 if the charge in the first and second capacitors can be represented by x_1 and x_2, respectively. Let $\frac{1}{Z_E}$ and $\frac{1}{Z_C}$ present open-loop transfer function of resonator and coupling:

$$\begin{cases} Z_E = M_0S^2 + CS + K_0 \\ Z_C = K_C \end{cases} \tag{3.52}$$

The transfer functions for resonator 1 and 2 (two different vibrating modes) are

$$TF_1 = \frac{1}{Z_E} \tag{3.53}$$

$$TF_2 = \frac{1}{(Z_E + 2Z_C)} \tag{3.54}$$

The corresponding characteristic equation is

$$Z_E(Z_E + 2Z_C) = 0 \tag{3.55}$$

The analytical solution of the equation is

$$\delta_0{}^{\pm} = -Z_C \pm Z_C \tag{3.56}$$

and at the resonance

$$Z_E = M_0 S^2 + CS + K_0 = \delta_0{}^{\pm} \tag{3.57}$$

$$M_0 S^2 + CS + (K_0 - \delta_0{}^{\pm}) = 0 \tag{3.58}$$

The overall feature of the system is identical to an SDoF system with $K = K_0 - \delta_0{}^{\pm}$. As a result, the two resonant modes can be treated as two resonators with different effective stiffness. They are named the in-phase and out-of-phase modes. As a second-order system, we get:

$$\zeta = \frac{C}{2\sqrt{(K_0 - \delta_0{}^{\pm})M_0}} \tag{3.59}$$

$$Q = \frac{1}{2\zeta} = \frac{\sqrt{(K_0 - \delta_0{}^{\pm})M_0}}{C} \tag{3.60}$$

$$\omega_{res} = \frac{\sqrt{(K_0 - \delta_0{}^{\pm})M_0 - C^2}}{M_0} \tag{3.61}$$

With positive perturbation ($K_0 - \delta_0{}^{\pm} > K_0$), the effective stiffness is increased, which increase Q and ω_{res}. The frequencies of the in-phase (f_{ip}) and out-of-phase (f_{op}) modes under different ΔK and K_c are shown in Figure 3.14.

3.4 Force-induced refractive index and phase change

When suspended slot waveguide is applied with attractive/repulsive force, the effective refractive index and phase of the optical mode will be altered by mechanical deformation. This force-induced refractive index and phase change is determined by how sensitive the optical mode depends on geometrical change and mechanical deformation curvature. The mechanical deformation is limited by the pull-in effect that is a

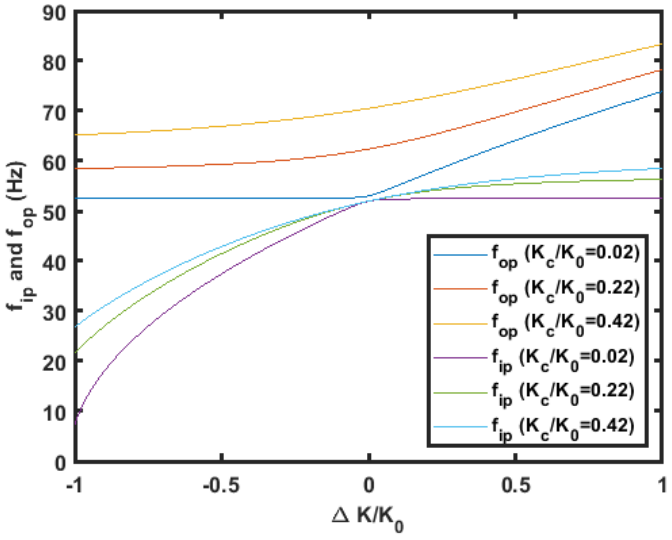

FIGURE 3.14: The resonant frequencies under different ΔK and K_c ($K_0 : M_0 : C = 1000 : 0.37 : 0.001$).

specific effect when the initial force applied can be enhanced during the deformation. This phenomenon involves all three types of forces described above. In the following sections, pull-in effect is described in Section 3.4.1. Effective refractive index and phase of the slot waveguide induced by electrostatic, optical and Casimir force are analyzed.

3.4.1 Optomechanical Pull-in effect

With the constant load in the elastic domain, the structure has enough restoring force to balance the external load thus, the system will reach the steady-state. However, due to the enhanced electromagnetic load with beam separation decreasing according to Equation 3.20, Equation 3.18 and Equation 3.25, the load redistribution happens with beam deformation and further enhanced the electromagnetic load and Casimir load, which forms positive feedback. Rather than initial equilibrium, deformation of the two slot beams induces the load distribution non-uniformly, which eventually enhance the force by decreasing/increasing g as:

$$g(z) = g_0 - 2\delta(z) \tag{3.62}$$

when the voltage is applied directly on two slot arms (fully suspended conducted slot configuration). The expression of g may be different depending on the device configuration and electrical connection. The equilibrium of the restoring force and external load is expressed as:

$$p_m(z) = \frac{F_{opt}(g(z))}{L} + \frac{F_{es}(g(z))}{L} + \frac{F_{cas}(g(z))}{L}, \tag{3.63}$$

will not be able to be kept long before material failure. This is referred to pull-in effect [80] and it sets a critical value (energy limitation) of the system failure. For electrostatic actuation, the maximum voltage allowed for actuation is referred to as the pull-in voltage V_{PI} expressed by [81]:

$$V_{PI} = \sqrt{\frac{8}{27}\frac{{g_0}^2 K}{\epsilon A}} \tag{3.64}$$

where K is the effective mechanical stiffness when the structure is applied with the pull-in voltage, this is an analytical approximation by treating the movable part and its actuator as a linear spring-mass model and an ideal parallel-plate capacitor, respectively. The accurate value of the pull-in voltage needs to be solved numerically. In the later analysis, the suspended slot in the pull-in state is regarded as the 'one' state of the modulator.

3.4.2 Optomachanical refractive index and phase change

Considering the deformation curvature, the effective refractive index distribution along the waveguide is not uniform. Thus effective refractive index change is suitable to be evaluated by integrating index change along the waveguide length. Overall index change can be expressed as:

$$\Delta n_{eff} L = \int_0^L [n_{eff}(g_2(z)) - n_{eff}(g_0)]dz - \int_0^L [n_{eff}(g_1(z)) - n_{eff}(g_0)]dz \tag{3.65}$$

where $g_1(z)$ and $g_2(z)$ is powerless arm separation that only applied with Casimir force and powered arm separation of the waveguide, respectively. An analytical approximation of the index change can be made by combining deformation curvature by Equation 3.28 and equivalent load (p_e) at maximum deformation (δ_{max}) in the middle point ($z = L/2$) of the curvature calculated by quasi-static analysis from FEA software. Treating the $\Delta n_{eff}(g)/\Delta g$ as a constant D in the case of small deformation, the overall index change approximation can be expressed as:

$$\Delta n_{eff} L = (p_{e2} D_2 - p_{e1} D_1)\frac{L^5}{360EI} \tag{3.66}$$

where p_e1, p_e2, $D1$, $D2$ denotes for powerless/powered equivalent load and powerless/powered index change rate, respectively. It can be further simplified by maximum deformation ($\delta^{e1}_{max}, \delta^{e2}_{max}$) expression as:

$$\Delta n_{eff} L = (\delta^{e2}_{max} D_2 - \delta^{e1}_{max} D_1)\frac{49}{45}L \tag{3.67}$$

The phase change of the waveguide response to index change is expressed as:

$$\Delta\phi = \frac{2\pi}{\lambda}\Delta n_{eff} L = (\delta^{e2}_{max} D_2 - \delta^{e1}_{max} D_1)\frac{2\pi L}{\lambda}\frac{49}{45} \tag{3.68}$$

This approximation can be used to evaluate the load distribution by comparing the approximated value with FEA results.

3.5 Chapter conclusions

The formulation and the interactions between the optical, electrical and mechanical properties of the silicon suspended slot applied as a NOEMS device are reviewed and discussed. To be specific, we treat the whole system as a NOEMS actuator that can tune the optical effective index and phase change mainly by electrostatic force. Besides the electrostatic force, the existence of Casimir force and optical force reduces the electrical power threshold in controlling the system, which limits the tuning ability due to the pull-in effect. We established an analytical approximation of the index and phase change of the device using the finite element analysis (FEA), including Casimir force, optical force and electrostatic force.

Chapter 4

Performance analysis of suspended slot modulator

In the previous chapter, theoretical force-induced effective refractive index and phase change of the suspended slot under the electrostatic, optical and Casimir forces are introduced. As a controllable phase shifter, a suspended slot waveguide can be constructed as an optical modulator. The essential part of the suspended slot modulator is the energy efficiency, maximum value of index and phase change and modulating frequency. These parameters are closely related to how the deformation curvature of the waveguide responds to Casimir force, optical force and electrostatic force. Unlike Casimir force and optical force, electrostatic force can be considered separately from the optical performance depending on the electrical configuration of the device. Thus electrostatic controlled suspended slot waveguide is a good choice for optical modulation. This allows the modulator performance to be adjusted by configuring suspended slot settings and associative optical circuitry separately to provide more flexibility in modulator design.

Most of the applications on optical modulations are achieved by the material index dependence on temperature and carrier density. It can also be achieved through adjusting evanescent coupling and reflection by nano-mechanical actuators, which are not commercially available. They are usually referred to as thermo-optical, electro-optical and NOEMS modulators/switches. The thermo-optical modulators/switches can change the index by 10^{-3} with modulating frequency of few KHz [82]. The electro-optical modulators can change the index by 4×10^{-4} with modulating frequency of less than 100 GHz [83]. The energy consumption of the electro-optical modulators are in the range from 0.08 to 3.4 pJ/bit [82]. The NOEMS devices can almost shut down the light propagation with modulating frequency of less than 2 MHz [84][85].

This chapter analyzes possible electro-optical-mechanical configurations and their modulating performance using the FEA method with COMSOL Multiphysics and Lumerical. We theoretically proved that the suspended slot modulator can achieve low energy consumption (0.19 fJ/bit) and impressive tuning ability ($\Delta n = 4 \times 10^{-2}$) with the help of mechanical resonance, which conventional modulators can hardly reach in such a compact size (about 55 μm). On the other hand, the modulating frequency is limited to hundreds of MegaHertz range set by the highest available mechanical resonant frequency of the suspended slot. It covers the gap between existed low speed (thermo-optical) and high speed (carrier-based) modulation.

4.1 Configuration patterns

There are two available electrical configurations: 1) applying a voltage between arms of the slot waveguide; 2) applying a voltage between external electrodes and arms of the slot waveguide. The first method can provide large electrostatic with low power consumption and the latter method allows flexibility of the design since this configuration can adjust electrostatic force independently without interrupting optical mode and force. There are also two available mechanical configurations: 1) suspending only one slot arm; 2) suspending all slot arms. They perform differently by possessing different force/gap curves. By combining the above two electrical and two mechanical configurations, there are four device patterns as shown in Figure 4.1.

As shown in Figure 4.1, Aluminium electrodes for electrostatic actuation are set in the transverse direction of the waveguide. Slots will be grounded or conducted to act as the movable parallel plates. Halfway and fully suspended slot waveguide can be treated as mechanical SDoF and 2 DoF systems, respectively. For the specific setting in slot modulator, the SDoF system (Figure 4.1 (c) and (d)) possesses a loaded slot gap expressed as:

$$g(z) = g_0 - \delta(z) \tag{4.1}$$

the force enhancement is less than 2 DoF (Figure 4.1 (a) and (b)) as Equation 3.62. There are two situations of the force applied on the waveguide depending on if the electrical potential is applied between slot arms (Figure 4.1 (a) and (c)) or electrode and one of slot arms (Figure 4.1 (b) and (d)) as shown in Figure 4.2. The electrostatic force is in the same direction as Casimir force and optical force if the electrical potential is applied between slot arms, while in the inverse direction when the electrical potential is applied between the electrode and one of the slot arms. When electrostatic force is in the same direction as Casimir force and optical force as shown in Figure 4.2 (a), the device can reach the pull-in state with deformation smaller than in Figure 4.2 (b). The specific electrical connections of these four patterns are shown in Figure 4.3.

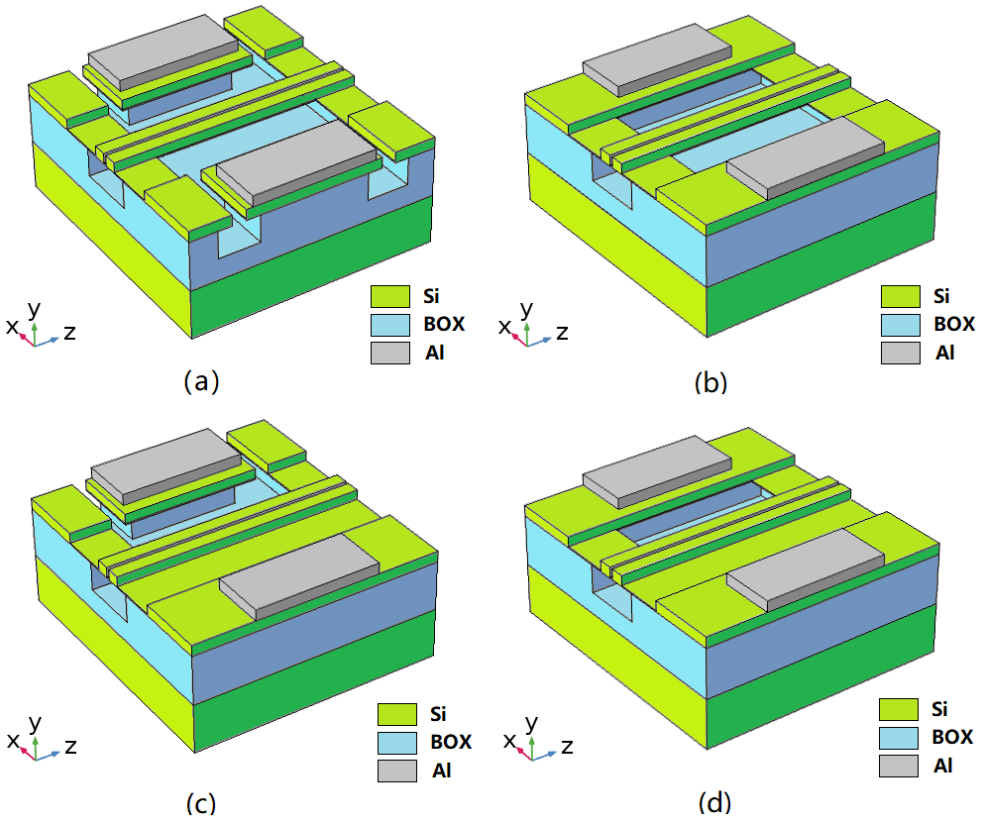

FIGURE 4.1: The electro-optical-mechanical configurations of suspended slot modulator. (a) The fully suspended grounded slot waveguide; (b) The fully suspended conducted slot waveguide; (c) The halfway suspended grounded slot waveguide; (d) The halfway suspended conducted slot waveguide.

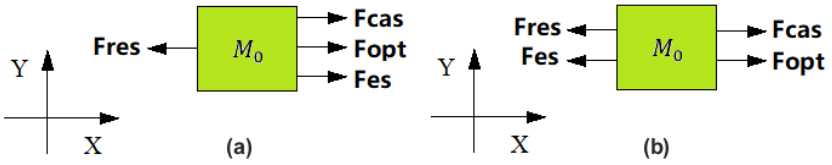

FIGURE 4.2: The forces on cross-section, F_{res}, F_{cas}, F_{es} and F_{opt}, denotes mechanical restoring force, Casimir force, electrostatic force and optical force, respectively. (a) The forces on the cross-section when electrical potential applied between slot arms; (b) The forces on the cross-section when electrical potential applied between slot arm and external electrodes.

The most advantageous configuration among these four patterns is the fully suspended conducted slot waveguide configuration with optimized energy efficiency. This configuration generates the most significant electrostatic force from the narrow gap between slots among the rest configurations. All three types of forces are attractive, so they will not cancel each other like grounded slot waveguide configurations. One problem of the conducted slot configuration is to achieve insulation between slot arms with low optical loss. Currently, the available design shown in [32] consumes a large chip area and requires high-resolution lithography, which makes it hard to be used in practical applications. The grounded slot configurations result in a negligible optical loss if the gaps

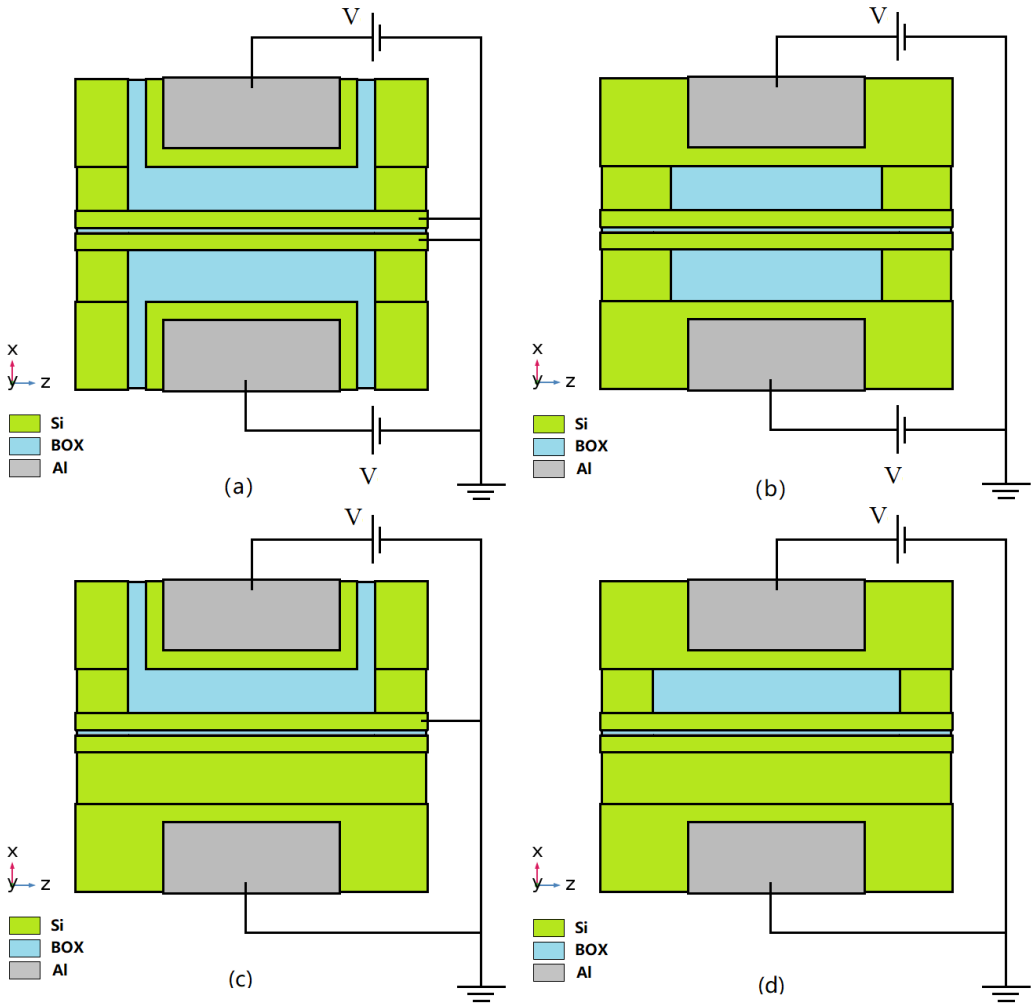

FIGURE 4.3: The electro-optical-mechanical configurations of the suspended slot modulator. (a) The fully suspended grounded slot waveguide; (b) The fully suspended conducted slot waveguide; (c) The halfway suspended grounded slot waveguide; (d) The halfway suspended conducted slot waveguide.

between slots and electrodes are large, while large gaps cause a low energy efficiency during the actuation. The halfway suspended configuration allows the system to be operated with slightly higher frequency, but it is not preferred since the configuration performs worse in all other aspects compared with the fully suspended configuration. In short summary, Figure 4.3 (a) allows the flexible actuating gap but increases the necessary actuating voltage. Figure 4.3 (b) is the most energy sufficient design and suffering the strongest pull-in effect among all configurations. Figure 4.3 (c) and (d) is the degraded version of (a) and (b), respectively. The pull-in effect in Figure 4.3 (c) and (d) is reduced by the halfway suspended waveguide but the tuning ability is reduced as well. So in this chapter, only the performance of fully suspended slot configurations is analyzed.

4.2 Effective refractive index and optical force corresponding to configurations

The effective refractive index and optical force of the waveguide depend on the geometry of the cross-section of the waveguide. Based on four configuration patterns in Section 4.1, there are two geometrical settings of the cross-section resulting from the suspending patterns. The geometrical and fundamental quasi-TE mode of these two geometrical settings are shown in Figure 4.4 and Figure 4.5.

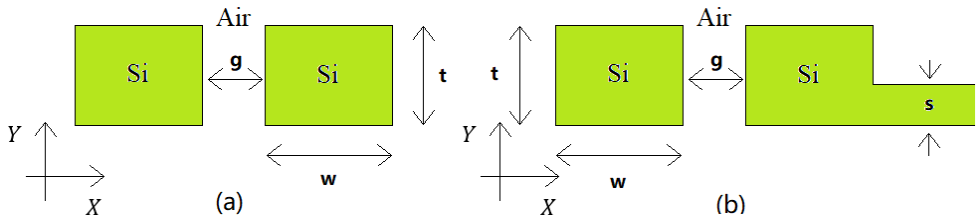

FIGURE 4.4: The cross-section geometry of the suspended slot wavguide. (a) The fully suspended slot waveguide; (b) The halfway suspended slot waveguide.

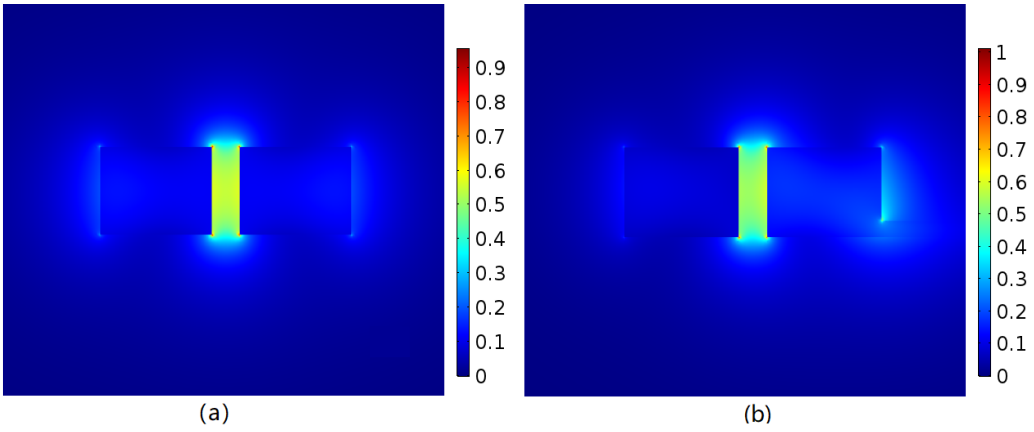

FIGURE 4.5: The optical modes of the suspended slot modulator. (a) The quasi TE mode of the fully suspended slot $t = 220nm$, $w = 280nm$ and $g = 70nm$; (b) The quasi TE mode of the halfway suspended slot $t = 220nm$, $w = 280nm$, $g = 70nm$ and $s = 40nm$

The commercially available thickness of silicon can be chosen to be at 220nm, 340nm and 500nm. Here we choose 220nm SOI as the base of the design to ensure the quasi TE mode is the first-order mode of the slot waveguide at a wavelength of $1550nm$. Layer labelled with thickness s in Figure 4.4 is chosen to have a thickness of $40nm$, to minimize the optical interference from asymmetric geometry of halfway suspended configuration. The effective index of quasi TE mode at different geometrical setting is shown in Figure 4.6 The halfway suspended slot has a larger effective index since it allow more energy propagating in the thin layer of silicon acting as an anchor.

In fundamental quasi-TE mode, electric field distribution in each arm leads to a larger amount of force applied on the inner sidewalls of the slot thus, total force appears to be

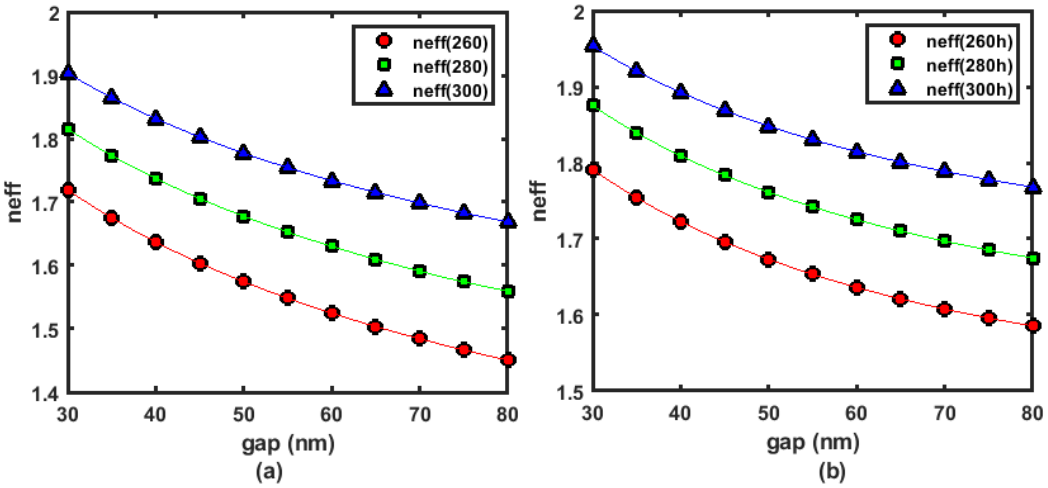

FIGURE 4.6: The refractive index of suspended slot ($t = 220nm$, $g = 70nm$). (a) The effective index of Quasi TE mode of fully suspended slot; (b) The effective index of Quasi TE mode of halfway suspended slot.

attractive. The amount of force is closely related to the confinement of the waveguide, as illustrated in [86]. The optical force from fundamental quasi-TE mode at different g is shown in Figure 4.7 and the positive sign is denoted for the attractive force between slot arms. Total force induced by radiation pressure is always attractive, and the mag-

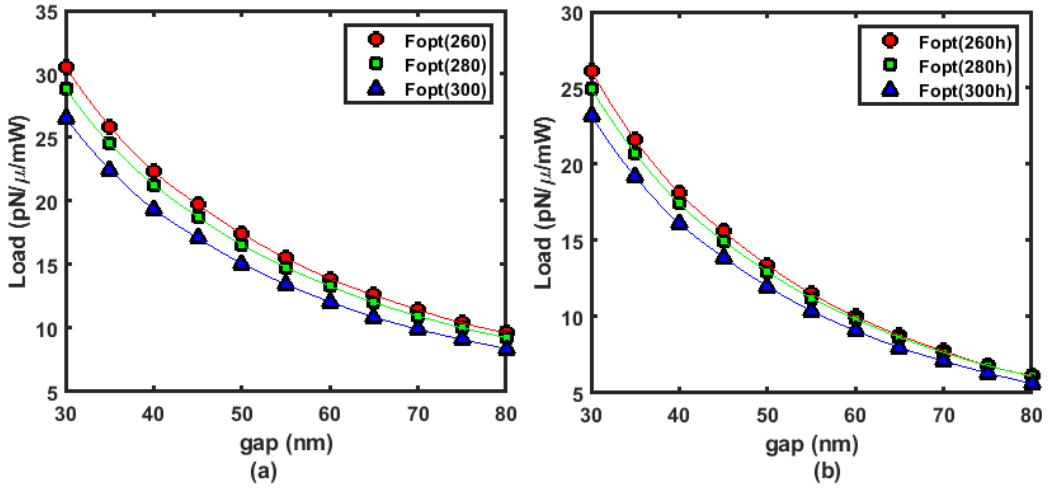

FIGURE 4.7: The optical forces from the suspended slot waveguides ($t = 220nm$, $g = 70nm$). (a) The optical force from the quasi-TE mode of the fully suspended slot $w = 260,\ 280\ and\ 300nm$; (b) The optical force from the quasi-TE mode of the halfway suspended slot $w = 260, 280\ and\ 300nm$, $s = 40nm$.

nitude of the force decreasing dramatically with g increasing. The nonlinear optical stiffness distributed along the waveguide related to this force can be observed in Figure 4.7 as well. Unlike the effective index, the halfway suspended slot has less optical load with the same input power than the fully suspended slot waveguide since energy contributes to radiation pressure on the inner boundary is less. The total load can be

adjusted by changing the length of the suspending area, which means the ratio of mechanical/optical stiffness is able to be adjusted. Calculation results of optical force on different geometrical settings of the fully suspended slot is shown in Figure 4.8.

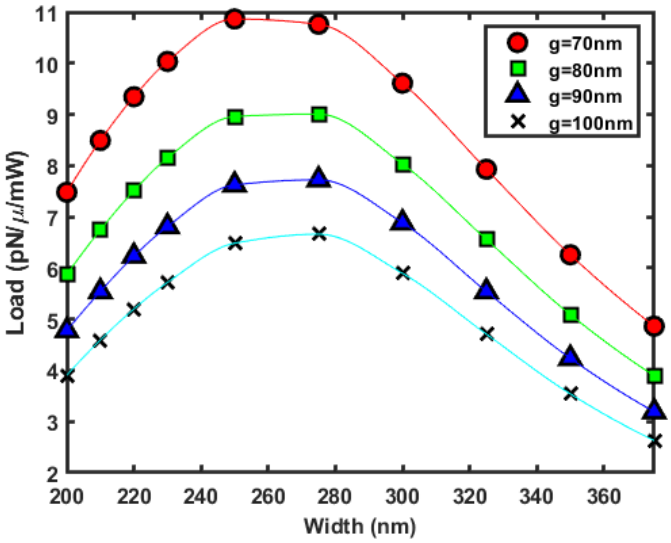

FIGURE 4.8: Optical force of different geometrical settings.

From Figure 4.8, it can be found that the maximum radiation pressure from different gaps locates from 240 nm to 300 nm, which is the region with the maximum confinement of the waveguide as in [86]. The magnitude of the force decreased with the gap increased. This result indicates slot design should be in the range of w from 240 nm to 300 nm with a small gap if the larger optical force is aimed.

4.3 Electrostatic and Casimir force corresponding to configurations

As shown in Figure 4.4, there are two kinds of cross-section settings. Among four configurations shown in Figure 4.1, Figure 4.1(a), Figure 4.1(b) and Figure 4.1(c) can be expressed by Figure 4.4(a) with a different range of g, while Figure 4.1(d) is expressed by Figure 4.4(b). The capacitance of the structure only relates to the aligned surface of the parallel plate, so the influence of w and s in Figure 4.4(b) to electrostatic force is negligible, which means the electrostatic force is almost the same in Figure 4.4(a) and Figure 4.4(b). For conducted slot configuration the gap between parallel plates is small, while the gap is much larger in grounded slot configuration to avoid unexpected optical interruption. The normalized electrostatic force of the two described configurations is shown in Figure 4.9. The positive sign is denoted for attractive force, and the negative sign is denoted for repulsive force. Casimir force is considerable between slot arms only. The magnitude of Casimir force is shown in Figure 4.10.

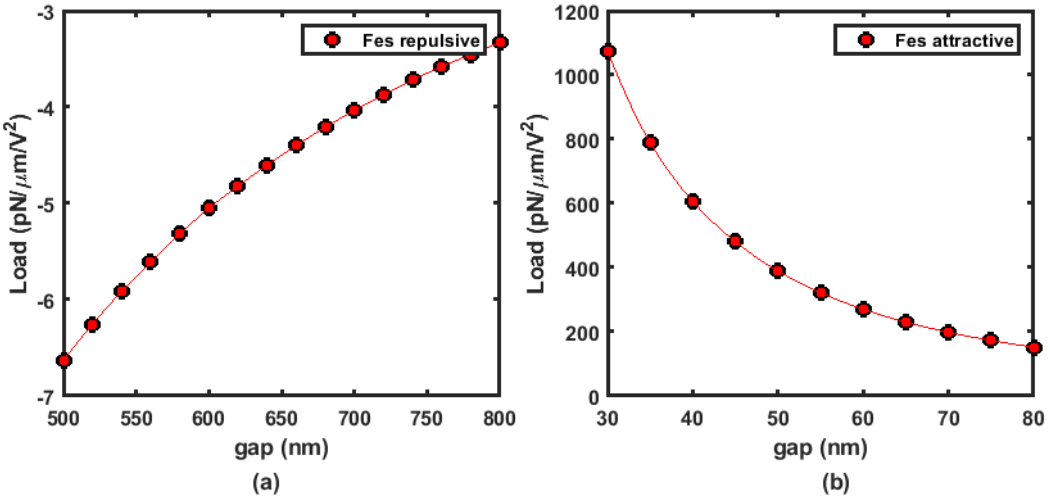

FIGURE 4.9: The electrostatic force based on different electrical configurations ($t = 220nm$, $w = 280nm$) calculated from Maxwell stress tensor by COMSOL Multiphysics. (a) The electrostatic force on the conducted slot configuration; (b) The electrostatic force on the grounded slot configuration.

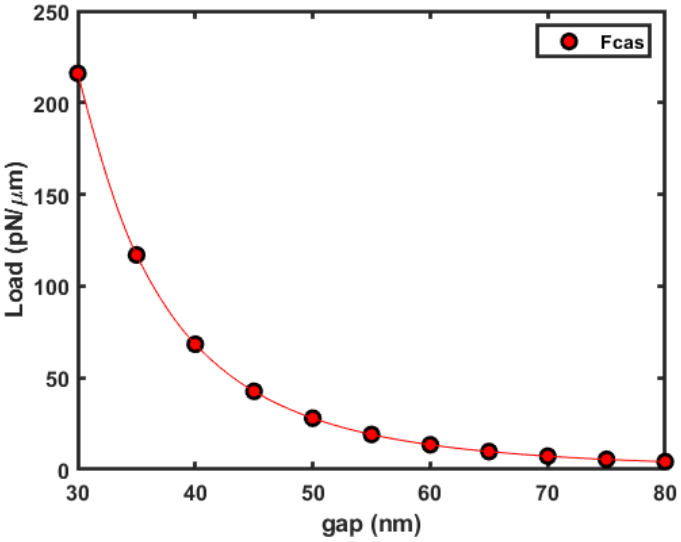

FIGURE 4.10: Casimir force between slots $t = 220nm$, $w = 280nm$.

4.4 Operating mode and state of the modulator

Generally, the modulator can be operated with different waveforms in a frequency range that the system can respond to. Square wave and sinusoidal wave are typical waveforms in digital and analogue electrical and electronic devices. For the dedicated modulator in this thesis, modulation with a square wave is described as pulse mode of the modulation covering frequency ranging from 0 to f_{max}^{pulse} estimated by Equation 4.7. Modulation with a sinusoidal wave is described as the sinusoidal mode of modulation covering frequency ranging from 0 to ω_{res}. The best performance in the sinusoidal

mode can be obtained when the modulator is operated around the mechanical resonant frequency due to significant mechanical amplitude amplification as described in Equation 3.47. This specific case is described as a resonant mode in this thesis.

During the modulation, every bit of the data is presented by high (one) or low (zero) energy level corresponding to maximum index state or minimum index state of the waveguide, respectively, or reversely. If we assume every 'one's and 'zero's correspond to maximum index state and minimum index state of the waveguide, respectively, mechanical deformation curvatures at 'one' and 'zero' in the pulse and sinusoidal mode will be as shown in Figure 4.11. As shown in Figure 4.11, in the pulse mode, 'zero'

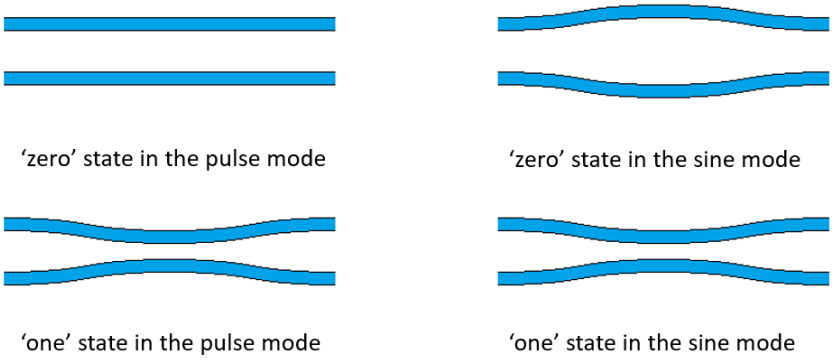

FIGURE 4.11: Top view of 'zero' and 'one' state of the modulator in the pulse mode and sinusoidal mode under the fully suspended conducted slot configuration.

is the state that no actuating voltage applied on waveguide (Casimir force and optical force only), while 'one' is the state that the slot is actuated by electrostatic force. In the sinusoidal mode, 'zero' is the state when two slot arms reach their maximum separation between each other, while 'one' is the state when the separation is minimum. In order to simplify the analysis in the pulse and sinusoidal mode, we treat Equation 3.25 as Equation 4.2 and Equation 4.3 under condition $V_{DC} = 0$ and $V_{AC} = 0$, respectively, described by:

$$F_{es}^{sine} \approx -\frac{1}{2}\left\{\frac{|V_{AC}^2|}{2} + A\frac{|V_{AC}^2|}{2}\cos 2\omega t\right\}\frac{\partial C}{\partial g} \tag{4.2}$$

$$F_{es}^{pulse} \approx -\frac{1}{2}{V_{DC}}^2\frac{\partial C}{\partial g} \tag{4.3}$$

where F_{es}^{sine} and F_{es}^{pulse} are the electrostatic force applied on the device, correspond to the sinusoidal and pulse mode. In Equation 4.2, A denotes for amplitude amplification factor for possible enhancement from mechanical resonance. In the pulse mode, V_{AC} is not involved in the consideration, while in the sinusoidal mode, V_{DC} is ignored in the analysis. The DC term in Equation 4.2 together with Casimir force and optical force

provides a constant bias force that breaks the symmetry of the deformation curvature at the 'zero' and 'one' states to straight slot in the sinusoidal mode.

4.5 Modulation speed

From a typical lump model of single-degree-of-freedom (SDOF) mechanical resonator including mass M, spring K and damper C, the time constant τ of a step input signal can be expressed as:

$$\tau = \frac{1}{\omega_n \zeta} = \frac{2Q}{\omega_n} = \frac{2M}{C} \tag{4.4}$$

$$\omega_n = \sqrt{\frac{K}{M}} \tag{4.5}$$

where ω_n, ζ and Q denotes natural frequency, damping factor and quality factor, respectively. The main damping mechanisms involved in the system can be classified as thermoelastic damping [87], air damping [88] and support loss [89]. For clamped-clamped beams, such as is the case with suspended slot waveguide, thermoelastic damping and support loss are negligible compared with air damping. The natural frequency and thermoelastic quality factor can be solved by COMSOL Multiphysics, while air damping for a double clamped beam can be calculated from [88]:

$$\zeta_{air} = \frac{\alpha \mu L^2}{4.73^2 t^2 w} \sqrt{\frac{3}{E\rho}} \tag{4.6}$$

where α is a constant related to Reynolds number, and μ is the dynamic viscosity of the air. Following [88], $\alpha = 10$ and $\mu = 1.81 * 10^{-5} Ns/m^2$.

For the 2 DoF system, which is exactly the case of the suspended slot modulator, the lump models of identical resonators coupled with a spring (K_c) are shown in Figure 3.13. There are two mechanical resonant modes that exist in a 2 DoF system. The overall feature of the target mode is identical with an SDOF system with $K = K_0 + 2K_c$. In this paper, the electromagnetic spring contributes to negative stiffness, so the resonant frequency will be lower than a single beam. The time constant of the system does not change since it is stiffness independent.

When the modulator is working in the pulse mode, the value of maximum modulating frequency depends on its system response time. If the settling time of the system is regarded as 3τ, corresponding to the step input signal (square wave), the maximum modulation frequency with pulse modulation with 50% duty cycle is expressed as:

$$f_{max}^{pulse} = \frac{1}{6\tau} = \frac{\omega_n \zeta}{6} \tag{4.7}$$

When the modulator is working in the sinusoidal mode, the system is actuated with a sinusoidal signal at frequency ω. Different from the pulse mode, the excited amplitude gain expressed in Equation 3.45 will be larger than the unit gain below the resonant frequency. In the resonant mode, the system is operated around the resonant frequency. The mechanical resonant frequency and corresponding resonant amplitude are described in Equation 3.45. The amount of actuating force required is $|A_{res}(\zeta)|$ times less to reach the same deformation curvature as in pulse mode. As a consequence, resonant modulation can achieve higher operating frequency with less energy consumption (lower voltage) compared with modulators operating in pulse modulation.

To compare the performance between resonant modulation and pulse modulation, we use pull-in displacement as the same as the value in the pulse mode to evaluate the performance in the resonant mode. According to Equation 4.2, actuating voltage at resonance should be described by:

$$\frac{|V_{AC}|^2}{2} + |A_{res}(\zeta)|\frac{|V_{AC}|^2}{2} = (V_{PI})^2 \tag{4.8}$$

By solving the equation, the actuating voltage in resonant mode is described by:

$$|V_{AC}| = V_{PI}\sqrt{\frac{2}{1+|A_{res}(\zeta)|}} \tag{4.9}$$

where $|V_{AC}|$ is always smaller than V_{PI} since A_{res} is always larger than 1 if a resonance exists ($0 < \zeta < \frac{\sqrt{2}}{2}$). Then, the electrostatic force in the 'zero' state can be described by:

$$F_{es0}^{sine} \approx -\frac{1}{2}\left\{\frac{|V_{AC}|^2}{2} - A_{res}\frac{|V_{AC}|^2}{2}\right\}\frac{\partial C}{\partial g} = \frac{1-A_{res}}{1+A_{res}}F_{es1}^{sine} \tag{4.10}$$

where F_{es0}^{sine} and F_{es1}^{sine} denote the electrostatic force in the 'zero' and 'one' state, respectively.

4.6 Performance analysis of the fully suspended conducted slot

The width and the gap of the slot waveguide is chosen to be 280nm and 70nm, respectively. Mechanical properties of the silicon is set as the same as in [89] shown in Table 4.1. The optical force from the fundamental quasi-TE mode only is analyzed in this section. The performance limitations of the design are illustrated for the device in both the pull-in state and initial state, covering the upper and lower limits of the modulation performance. The initial state of the modulator is defined as the state when there is no voltage applied to the device with the light going through the waveguide (Casimir force and optical force), while the pull-in state involves all forces under consideration. The pull-in state is regarded as 'one' state and the initial state is regarded as

TABLE 4.1: Material properties of highly-doped single-crystal silicon

Property	**Symbol**	**Value**
Density (kg/m^3)	ρ	2330
Young's modulus for Si[1 0 0] (Pa)	E	$1.3 \cdot 10^{11}$
Poisson's ratio for Si[100]	v	0.28
Thermal expansion coefficient (K)	α_T	$2.6 \cdot 10^{-6}$
Specific heat ($J/(Km^3)$)	C_T	$1.63 \cdot 10^6$
Thermal conductivity ($W/(mK)$)	κ	90
Environmental temperature (K)	T	293.15

'zero' state of the modulator to describe the theoretical maximum tuning range of the device. Casimir force is calculated from Equation 3.20 and Equation 3.21. Optical force and electrostatic force are calculated using the wave optics module and electrostatic module of COMSOL multiphysics, respectively.

The attractive forces between the two slot arms are equivalent to a nonlinear mechanical connection with negative stiffness. The three types of force analysed in this model have individual force-gap (spring) features that change the load distributions in different ways as shown in Figure 4.9, Figure 4.10 and Figure 4.7. Thus, the composition of the force affects the performance of the modulator and some limitations are set by the pull-in effect of the actuator. To simplify the analysis, the optical power is set to be a constant of 100 μW, so the only variable quantity in the system is the actuation voltage. The modulator performance will be analysed in the pulse mode, sinusoidal mode and resonant mode. The 'one' and 'zero' states of each mode will be analysed as well.

4.6.1 Performance in the pulse mode

The performance of the modulator in the pull-in and initial states, with no electrostatic force applied, are investigated to figure out the maximum modifiable index range of the device. Here the pull-in state is regarded as the 'one' state, and initial state is regarded as the 'zero' state. The pull-in voltage of the modulator in the pulse mode is shown in Figure 4.12. From this plot, the allowed amount of voltage is dramatically decreased when the length of suspension (L) increased. This is the result of increased mass (M) and decreased stiffness (K) with a longer suspended section. This decreased stiffness indicates a smaller δ_{max} in the pull-in state with longer suspension length considering the equilibrium of the restoring force ($K \cdot x$), Casimir load and electromagnetic load. On the other hand, this decreased stiffness also indicates larger δ_{max} in the initial state with a longer suspended section as shown in Figure 4.13.(a). From Figure 4.13.(a), δ_{max} in the initial state and pull-in state intersect at a suspended length between 52 μm and 53 μm, which indicates the limits of the suspended length since the system collapse no matter what voltage is applied. In this case, modulation is impossible.

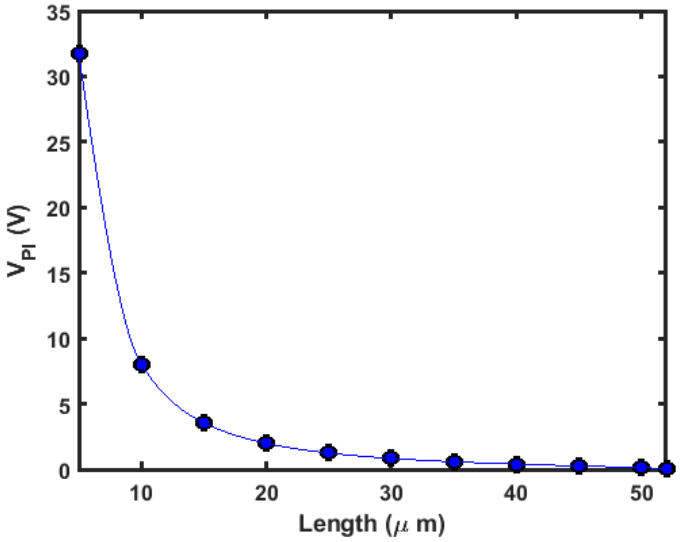

FIGURE 4.12: Pull-in voltage (V_{PI}) of the modulator in the pulse mode with different suspended lengths

The corresponding effective index changes in the 'one' state and 'zero' state are shown in Figure 4.13.(b). The plot shows a larger value of Δn_{eff} with longer suspended lengths in the initial state when the waveguide has Casimir and optical forces applied. By comparing the 'modifiable' and 'zero state' curves, it is proved that the load re-distribution on the waveguide is negligible with a short suspended length ($\leq$ 35 μm) due to the higher stiffness compared with longer suspended lengths. This non-linearly index change/suspended length curve degrades the modifiable effective index of the modulator with longer suspended lengths ($\geq$ 35μm). As the suspended length is increased, 35 μm is the point at which the influence of Casimir and optical forces on the deformation curvature of the waveguide becomes comparable with the influence of the electrostatic force. Casimir and optical forces contribute to a large initial effective index change and degrade the tuning ability of the modulator for suspended lengths longer than 35 μm. As a consequence, the modifiable effective index change reaches a maximum of about 0.065 with a length of 5 μm and almost 0 with a length of 52 μm in Figure 4.13.(b). The index changes shown in Figure 4.13.(b) are one order of magnitude higher than the typical values of index change shown in [90], which means the described suspended slot modulator consumes much less chip area compared with most active modulators.

The results of analytical approximations from Equation 3.67, Equation 3.68 and numerical solution from FEA software are shown in Figure 4.14. The maximum effective index change and phase change of the device are 0.0649 and 388.4° with a suspended length of 5 μm and 30 μm, respectively. It can be found that the analytical solution of the effective index and phase change are always larger than from FEA software as shown in Figure 4.14, which means that the enhanced force applied to the structure deforms the waveguide in a different way to that in Equation 3.28 and it contributes to a smaller

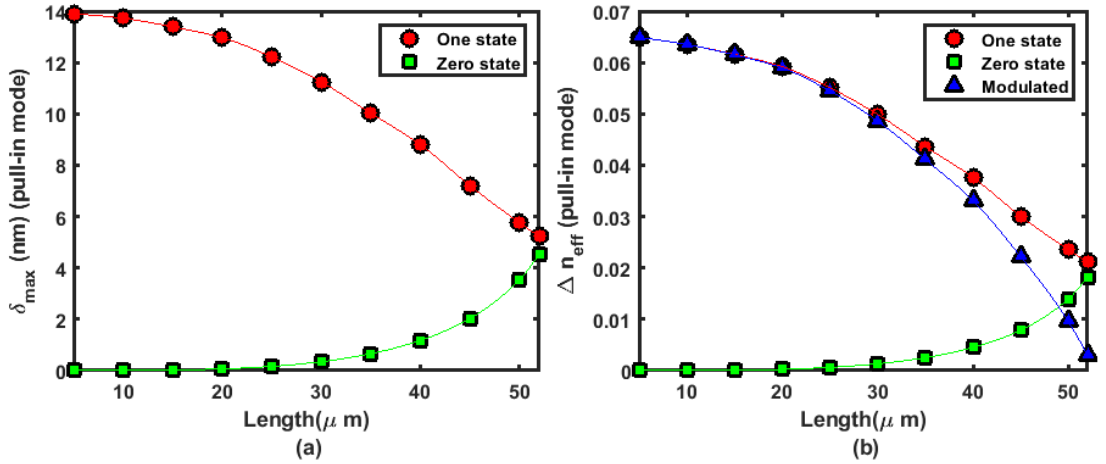

FIGURE 4.13: (a) The maximum displacement (δ_{max}) on the deformation curves in the 'one' state and 'zero' state with different suspended lengths; (b) Effective refractive index change (Δn_{eff}) in the 'one' state and 'zero' state with different suspended lengths. The curve 'Modulated' is the is the index difference between the 'one' state and 'zero' state in the pulse mode, which is the maximum modifiable index change of the modulator. Both Figure 4.13.(a) and (b) are calculated by COMSOL Multiphysics

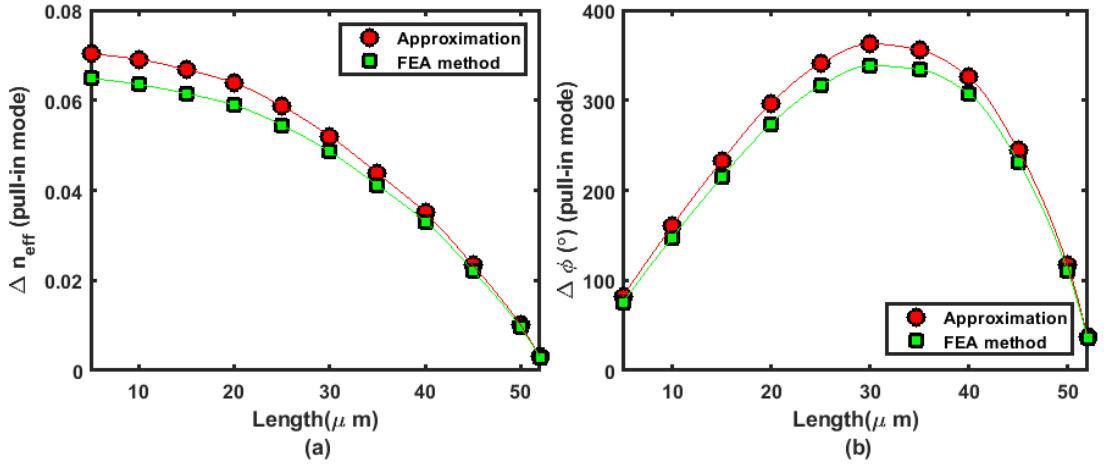

FIGURE 4.14: The comparison of the index and phase changes (Δn_{eff}, $\Delta\phi$) between the theoretical approximation given by Equation 3.67 Equation 3.68 and the FEA method in the pulse mode with different suspended lengths; (a) The curve 'Approximation' is given by Equation 3.67 and the curve 'FEA method' is the same as the curve 'Modulated' in Figure 4.13.(b); (b) The curve 'Approximation' is given by Equation 3.68 and the curve 'FEA method' is calculated from the curve 'Modulated' in Figure 4.13.(b).

index and phase change. The analytical approximation only shows a maximum difference of 7 % to 8 % in the pull-in state compared to the result from the FEA software. This small error indicates that the load re-distribution caused by the force enhancement is not significant in the pulse mode. From Figure 4.14, any suspended length between 12 μm and 47 μm can achieve a π shift in the normal state.

The forces applied in the system also affect the maximum allowable modulation frequency as shown in Figure 4.15. Under the influence of both negative spring and air damping, the modulation frequency limit in the pull-in state is increased with increased

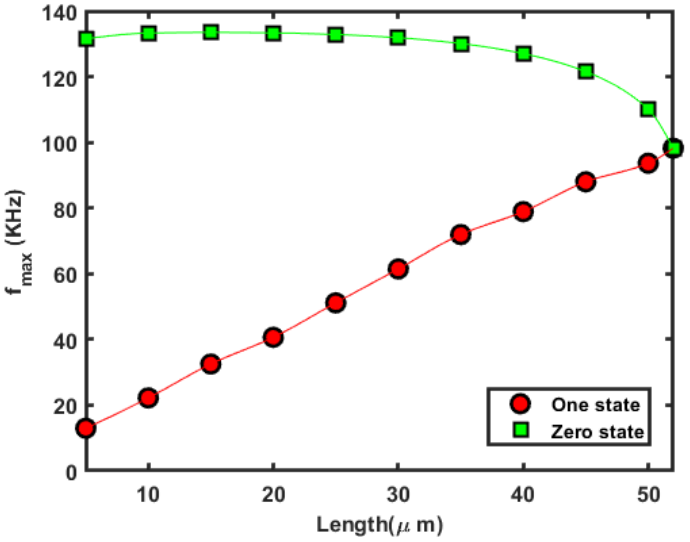

FIGURE 4.15: The pulse modulation frequency limitation (f_{max}) at the initial ('zero') state and pull-in ('one') state with different suspended lengths

length, while the frequency limit in the initial state experiences a ramp and drop with a maximum of about 133 KHz. These two curves are the results of the product of decreased vibration frequency and increased air damping with increased length. The intersection of these two curves indicates that the frequency limitation (low) of the described modulator is about 100 KHz. The actual operational frequency is in the region between the 'one' state and 'zero' state. According to Equation 4.7, the modulation frequency can be further improved by increasing mechanical resonant frequency and air damping. A higher mechanical resonant frequency can be achieved by slot design with higher mechanical stiffness or by replacing the silicon with other materials with higher mechanical stiffness, such as silicon nitride. Slot arms with larger width will increase mechanical resonant frequency while total index change and air damping are decreased. Higher air damping can be achieved by replacing air with other mediums with higher viscosity such as water or having a longer suspending length according to Equation 4.6. To allow for a longer suspended slot, a slot design with weaker optical force, weaker Casimir force and stronger restoring force is required, which can be achieved by using different optical and electrical configurations.

4.6.2 Performance in the resonant mode

The modulator performance in the resonant mode is analysed using a sinusoidal drive since it presents the best modulator performance in the regime of sinusoidal mode. To make the parameters in the sinusoidal mode comparable with the pulse mode, the maximum displacement on the deformation curvature in the 'one' state of the modulator in the sinusoidal mode is chosen to be the same as in the 'one' state of the modulator in the pulse mode. With the same maximum displacement on the deformation curvature as

in the pulse mode 'one' state, the actuating voltage of the modulator for all considered suspended lengths is significantly decreased in the resonant mode due to resonance-based amplification. The equivalent actuating voltage amplitude from Equation 4.9 in the 'one' state and the corresponding amplification factor for the different suspended lengths considered are shown in Figure 4.16. From this plot, the amplification factor of

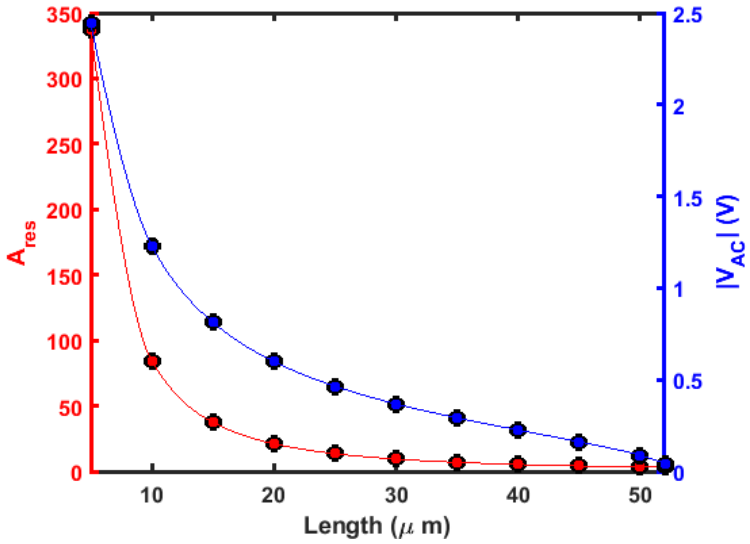

FIGURE 4.16: Equivalent actuation voltage ($|V_{AC}|$) and force amplification factor (A_{res})in the resonant mode with different suspended lengths.

the modulator decreases with increasing suspended length. The amplification factors for the shorter lengths are extremely high due to decreased air damping according to Equation 4.6 and Equation 3.47. The maximum actuating voltage amplitude of the 'one' state is 2.45 V with a length of 5 μm. A typical value for the actuating voltage amplitude is 0.39 V with a length of 30 μm. The DC electrostatic, Casimir and optical forces apply a bias force on the suspended slot, which makes the beams deform differently in the 'one' state and the 'zero' state. The maximum displacement on the deformation curvature for the 'one' and 'zero' state and corresponding index changes are shown in Figure 4.17. In the 'one' state of the resonant mode, the maximum displacement of different suspended lengths is the same as with the 'one' state of the pulse mode. Negative values of the maximum displacement in the 'zero' state are calculated based on Equation 4.10. The comparison of the modulated index and phase change between the theoretical approximation and FEA method for different lengths of the slot waveguide are shown in Figure 4.18. In Figure 4.18, the modulated index and phase changes solved by the FEA method are slightly increased compared with those in Figure 4.14. The negative deformation curvature caused by repulsive electrostatic force in the 'zero' state contributes to the increased part of the modulated index and phase changes. The maximum effective index change and phase change of the device is 0.0828 and 437.9° with a suspended length of 5 μm and 35 μm, respectively. The numerical difference between the theoretical approximation and the FEA method is always less than 6 %.

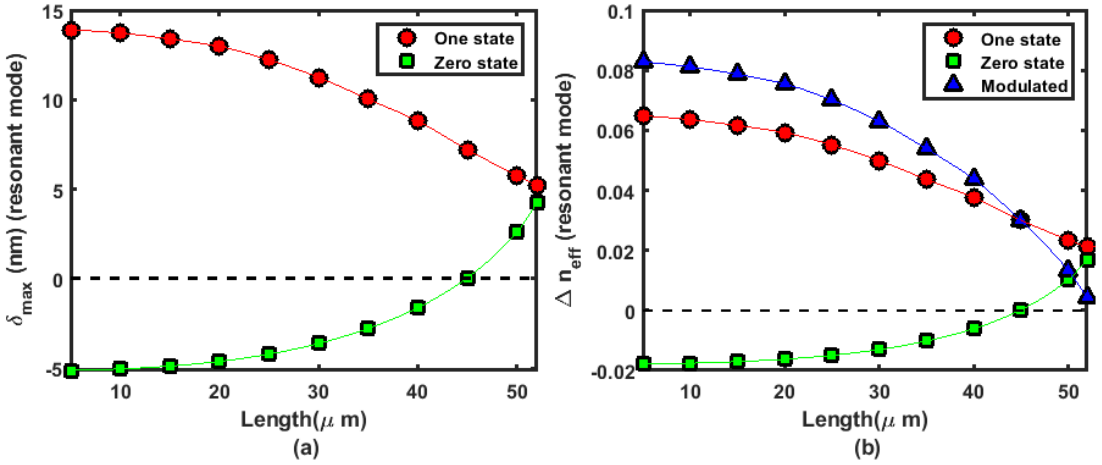

FIGURE 4.17: (a) The maximum displacement (δ_{max}) on the deformation curves in the 'one' state and 'zero' state in the resonant mode with different suspended lengths; (b) Effective refractive index change (Δn_{eff}) in the 'one' state and 'zero' state with different suspended lengths. The curve 'Modulated' is the is the index difference between the 'one' state and 'zero' state in the resonant mode, which is the maximum modifiable index change of the modulator. Both Figure 4.17.(a) and (b) are calculated by COMSOL Multiphysics

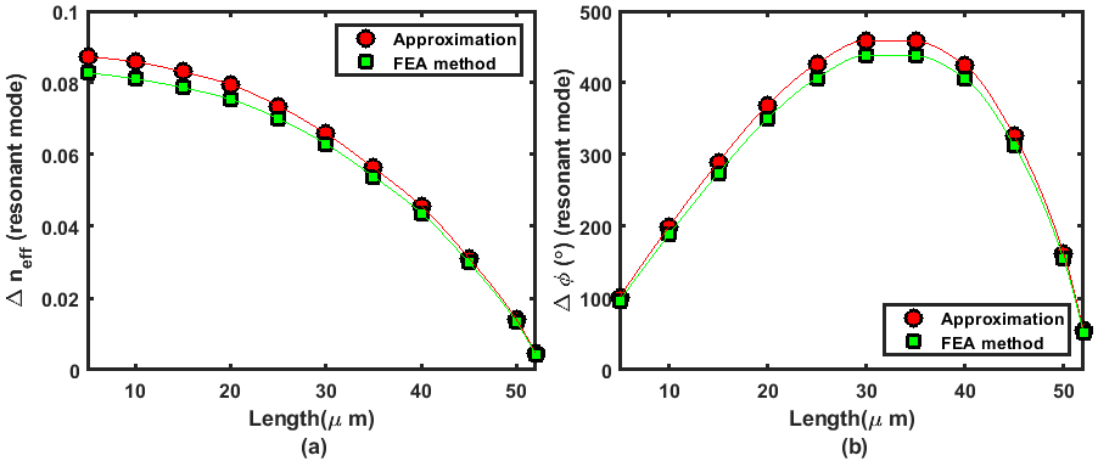

FIGURE 4.18: The comparison of the index and phase changes ($\Delta n_{eff}, \Delta\phi$) between the theoretical approximation given by Equation 3.67 Equation 3.68 and the FEA method in the resonant mode with different suspended lengths; (a) The curve 'Approximation' is given by Equation 3.67 and the curve 'FEA method' is the index difference between the 'one' state and 'zero' state of the modulator in the resonant mode by COMSOL Multiphysics; (b) The curve 'Approximation' is given by Equation 3.68 and the curve 'FEA method' is calculated from the curve 'FEA method' in Figure 4.18.(a).

The resonant frequency of the suspended slot for different lengths as calculated using Equation 3.43 is shown in Figure 4.19. The resonant frequency of the modulator is much higher than the modulating frequency shown in Figure 4.15. In the pulse mode, the modulating frequency is limited by τ to avoid distortion of the waveform (dispersion). While in the resonant mode, the modulator is excited with single frequency rather than a package of signals with different frequencies so the system settling time will not influence the modulating frequency of the device. In Figure 4.19, the highest

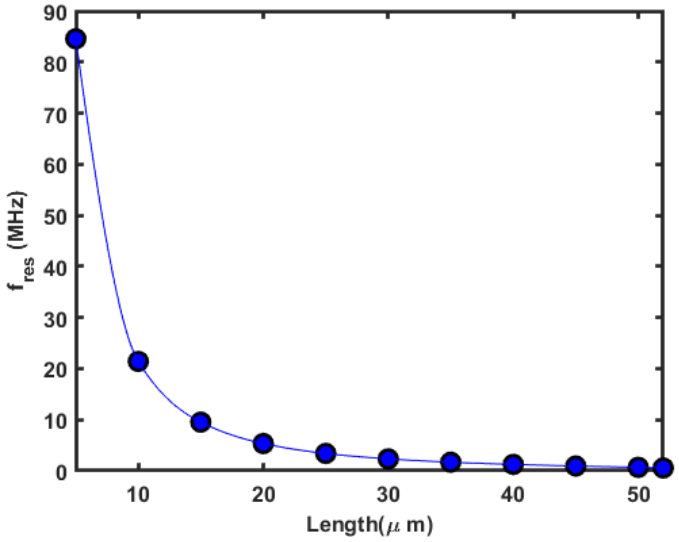

FIGURE 4.19: Resonant frequency (f_{res}) of the modulator with different suspended lengths

resonant frequency is 84.6 MHz with a length of 5 μm. A typical resonant frequency value is 2.33 MHz with a length of 30 μm. Even the smallest resonant frequency at 0.583 MHz with a length of 52 μm is almost 4.4 times larger than the maximum modulating frequency shown in Figure 4.15.

4.6.3 Power consumption

The power consumption of the modulation evaluated by fJ/bit can be calculated by [91]:

$$E_{bit} = \frac{CV^2}{4} \tag{4.11}$$

One unique feature of the suspended slot modulator is that the capacitance will be changed by deformation of the slot arms, so it closely relates to the actuation voltage, and it is independent of the frequency of the square wave signal below f_{max}^{pulse}. The power consumption at the pull-in state of the pulse and resonant modes with the same modulation depth are shown in Figure 4.20. In the pulse mode, the energy required per bit is always less than 32 fJ/bit and decreases as the suspended length is increased. We can find an impressive value of 0.13 fJ/bit with a length of 30 μm. In the resonant mode, the energy required per bit is always less than 0.19 fJ/bit. The energy consumption with a length of 30 μm is further decreased to 0.025 fJ/bit. The energy consumption in the resonant mode is even less than that in the pulse mode for all lengths, reaching levels that are unachievable using most other active modulators such as described in [90], [92] and [93]. Moreover, there is no optical absorption contributing to excess loss during the modulation as with plasma dispersion based approaches.

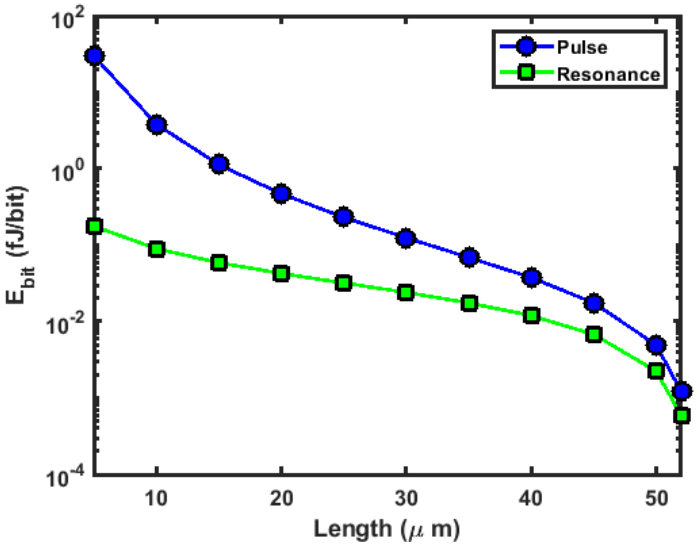

FIGURE 4.20: The energy cost of the modulation (E_{bit}) in the pulse and resonant mode with different suspended lengths

4.7 Performance analysis of the fully suspended grounded slot

In order to compare the performance between the fully suspended grounded slot and conducted slot, the geometrical parameters and material properties are set the same as in Section 4.6. The gap between the waveguide (ground) and external electrode for actuation is 300nm, which needs to be large enough to avoid the unexpected optical perturbation beyond the deformation of the waveguide. For grounded slot waveguide, The one and zero states of the modulator is reversed as in Section 4.6 since the electrostatic force will decrease the effective index of the waveguide.

4.7.1 Performance in the pulse mode

The pull-in voltage of the modulator in the pulse mode in grounded slot configuration is shown in Figure 4.21. The pull-in voltage in grounded slot configuration is about ten times as large as the one in conducted slot configuration from this plot. The ability of the electrostatic force generation in two different configurations is essential. The conducted slot configuration set two slot arms as electrodes, so the actuating gap is identical to slot separation decided by wave optics, which is 70 nm in this case. On the other hand, the grounded slot configuration use external electrodes with flexible and larger actuating gap to avoid optical loss, which is 300 nm in this case. As an electrostatic actuator, in the same condition, a narrow actuating gap brings larger force while the corresponding pull-in voltage and displacement are smaller.

One beneficial feature of the slot modulator in grounded configuration is its adjustable index change limitation from flexible actuating gap and δ_{max} as shown in Figure 4.22.

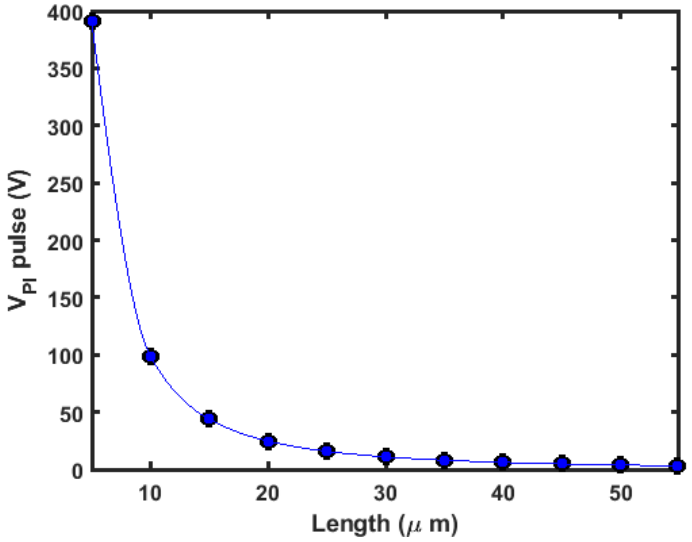

FIGURE 4.21: Pull-in voltage (V_{PI}) of the modulator in the pulse mode with different suspended lengths

(a). From Figure 4.22.(a), δ_{max} in the zero state (pull-in state) ranges from 140 nm to

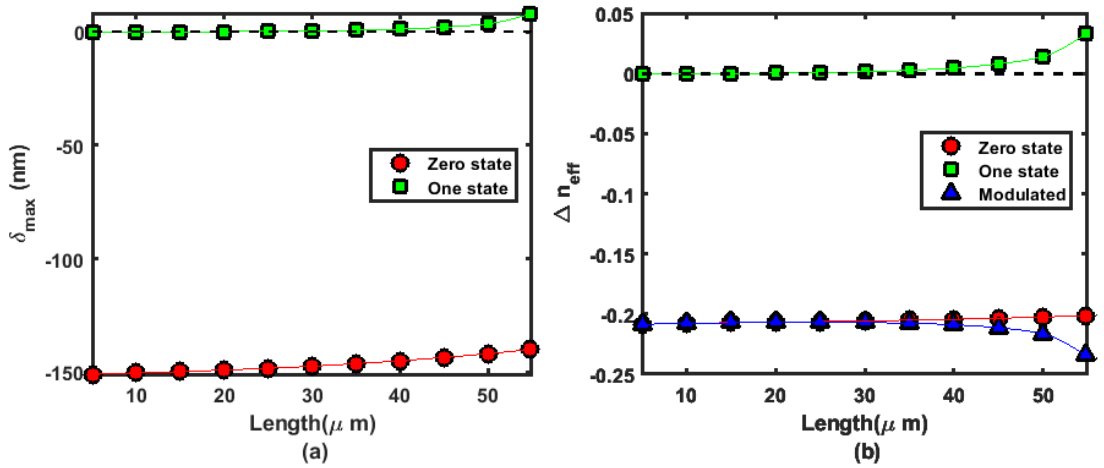

FIGURE 4.22: (a) The maximum displacement (δ_{max}) on the deformation curves in the 'one' state and 'zero' state with different suspended lengths; (b) Effective refractive index change (Δn_{eff}) in the 'one' state and 'zero' state with different suspended lengths. The curve 'Modulated' is the is the index difference between the 'one' state and 'zero' state in the pulse mode, which is the maximum modifiable index change of the modulator. Both Figure 4.22.(a) and (b) are calculated by COMSOL Multiphysics

150 nm at a suspended length between 5 μm and 55 μm, which is about half of the actuating gap. Usually, the δ_{max} at the pull-in voltage of a parallel-plate actuator is about one-third of the actuating gap, while optical force and Casimir force contributes to a higher restoring force/stiffness in grounded slot configuration, so the pull-in δ_{max} is enlarged to half of the actuating gap in this specific case. The tuning limitation is largely improved with the drawback of higher actuating voltage and power consumption. The

index change corresponding to grounded slot configuration in the zero and one states are shown in Figure 4.22.(b).

The corresponding effective index changes in the 'one' state and 'zero' state are shown in Figure 4.13.(b). The negative index change in the plot is the result of the repulsive electrostatic force from grounded slot configuration and negative effective/gap slop of the slot waveguide. The amount of index change is about three times as large as the one in conducted slot configuration. In Figure 4.13.(b), the index changes in the one state are not strongly related to the suspended length of the waveguide as in conducted slot configuration, which means the load re-distribution effect is not significant. This is the result of weaker repulsive electrostatic force and the enhanced restoring force by attractive optical and Casimir force, which further degrade the load re-distribution effect.

The results of analytical approximations from Equation 3.67, Equation 3.68 and numerical solution from FEA software are shown in Figure 4.14. The maximum effective

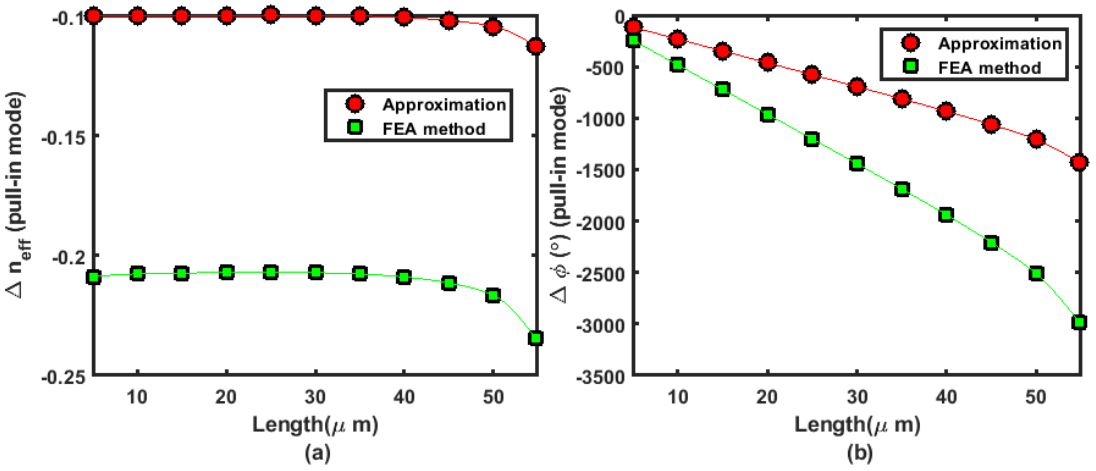

FIGURE 4.23: The comparison of the index and phase changes (Δn_{eff}, $\Delta\phi$) between the theoretical approximation given by Equation 3.67, Equation 3.68 and the FEA method in the pulse mode with different suspended lengths; (a) The curve 'Approximation' is given by Equation 3.67 and the curve 'FEA method' is the same as the curve 'Modulated' in Figure 4.22.(b); (b) The curve 'Approximation' is given by Equation 3.68 and the curve 'FEA method' is calculated from the curve 'Modulated' in Figure 4.22.(b).

index change and phase change of the device are -0.235 and -3010.36° with a suspended length of 30 μm, which is about four times and eight times of maximum index and phase change under conducted slot configuration, respectively. It can be found that the analytical solution of the effective index and phase change is about half of the FEA solution as shown in Figure 4.23, which means that the analytical approximation is only valid when displacement is small. This significant error indicates that the deformation curvatures caused by the combination of repulsive electrostatic force, attractive optical and Casimir force are unpredictable by current analytical approximation rather than the case that all forces are attractive. This specific load condition also results in that the phase changes shown in Figure 4.23 (b) has no local maximum like the one

under conducted slot configuration. From Figure 4.23, any suspended length between 10 μm and 55 μm can achieve a π shift in the normal state.

The forces applied in the system also affect the maximum allowable modulation frequency as shown in Figure 4.24. The modulation frequency limit in the pull-in state

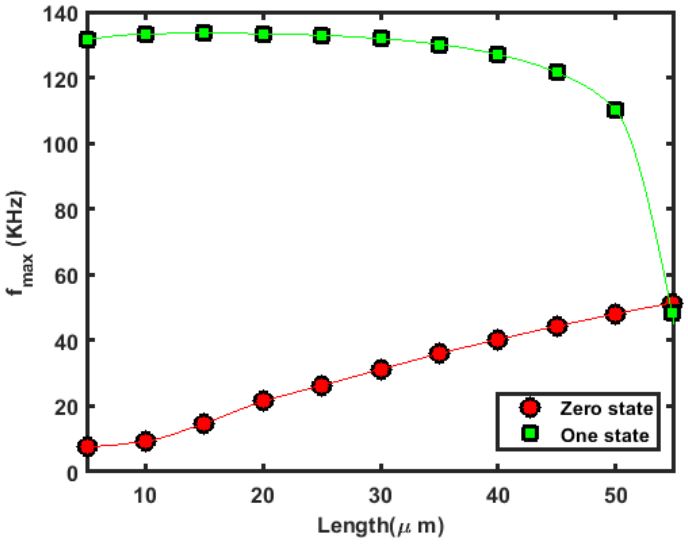

FIGURE 4.24: The pulse modulation frequency limitation (f_{max}) at the initial ('one') state and pull-in ('zero') state with different suspended lengths

is increased with increased length, while the frequency limit in the initial state experiences a ramp and drop with a maximum of about 133 KHz. The intersection of these two curves indicates that the frequency limitation (low) of the described modulator is about 50 KHz, which is half of the one in conducted slot configuration.

4.7.2 Performance in the resonant mode

The performance described in Section 4.6.2 touches the physical limitation of the suspended slot modulator operating under the maximum electrostatic force allowed. In the resonant mode of a fully suspended grounded slot modulator, electrostatic force at the one-state should not exceed the limitation solved in Section 4.6.2 since they are identical models in the one state. Based on the relationship between electrostatic force described in Equation 4.10, grounded slot configuration experiences the same force limitation as conducted slot configuration in the zero state as well. As a consequence, performance limitations in the resonant mode of the fully suspended grounded has no difference with performance limitations described in Section 4.6.2. However, the capacitance and actuating voltage is significantly changed due to different electrical configuration of the device. The maximum actuating voltage allow is shown in Figure 4.25. From Figure 4.25, actuating voltage required for grounded configuration is

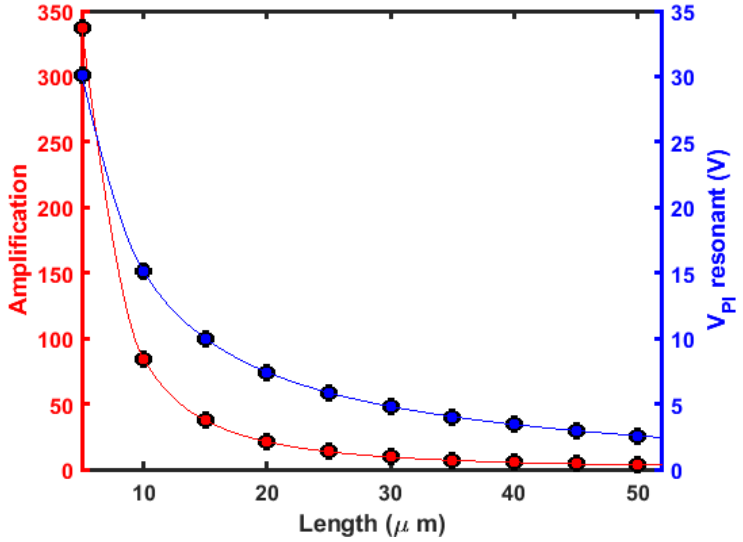

FIGURE 4.25: Equivalent actuation voltage ($|V_{AC}|$) and force amplification factor (A_{res})in the resonant mode with different suspended lengths of the fully suspended grounded configuration

about ten times as large as the one in conducted configuration due to the smaller electrostatic force generated from side electrodes. The different voltage and capacitance lead to different power consumption features analyzed in Section 4.7.3.

4.7.3 Power consumption

The power consumption at the pull-in state of the pulse and resonant modes with the same modulation depth is shown in Figure 4.26. From Figure 4.26, energy consump-

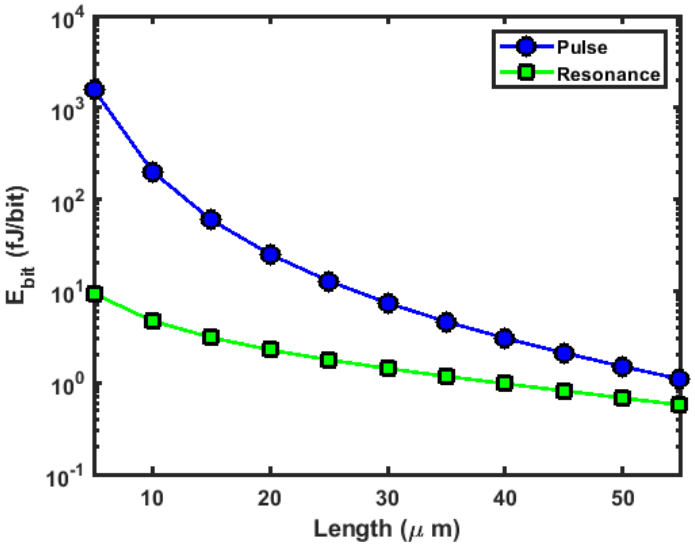

FIGURE 4.26: The energy cost of the modulation (E_{bit}) in the pulse and resonant mode with different suspended lengths in fully suspended grounded configuration

tion under the grounded slot configuration (gap=300nm) is about 10 to 1000 times as much as the one under the conducted slot configuration. The difference in energy consumption is increasing with the suspending length increasing. In the pulse mode, the energy required per bit is always less than 1.58 pJ/bit and decreases as the suspended length is increased. The energy consumption is 7.4 fJ/bit with a length of 30 μm. In the resonant mode, the energy required per bit is always less than 9.34 fJ/bit. The energy consumption with a length of 30 μm is decreased to 1.43 fJ/bit. The energy consumption in the resonant mode is less than that in the pulse mode for all lengths.

4.8 Modulator construction

The modulator can be constructed by cascading multiple suspended slot waveguide segments into a Mach-Zhender Interfrometer (MZI) or a ring resonator modulator. Multiple identical segments can effectively decrease the actuating voltage with a given value of total effective index change and phase change thus, lower power consumption can be achieved. Furthermore, the active modulator can be constructed with segments having different suspended lengths providing more flexibility in the design. Fortunately, the length of a single segment of the suspended slot will not exceed 52 μm based on the calculations above, so the size of the modulator is easily controlled. This optomechanical modulation does not induce additional light absorption in the C-band, so the propagating loss during modulation is extremely low. The most significant cause of loss is likely to result from the mode conversion between suspended and supported slot waveguides.

The simulation results show that the best modulator performance is obtained by operating in the resonant mode at the mechanical resonant frequency. Power dependent optical forces can significantly influence the system with a high power input (mW level) as measured in [34] or field enhancement [11]. For a specific mode shape with a specific suspended length of the suspended slot, mechanical resonance provides very narrow modulating bandwidth. Non-identical suspended lengths on different segments must be considered to expand modulating bandwidth. The mechanical resonant frequency of each segment can be tuned by using an offset voltage or different input optical power to adjust modulating bandwidth. A higher modulating frequency in the resonant mode can be achieved by exciting mechanical resonance at higher frequencies. However, the mode shape (deformation curvature) of higher-order mechanical resonant modes must degrade the index and phase change of the modulation. In this case, a trade-off between the modulating frequency and modulation depth is required.

The geometrical parameters defining the cross-section of the suspended slot can be adjusted to optimize the performance depending on the specific requirements. The larger the separation between the slot arms, the lower the Casimir and optical forces.

Therefore, the critical displacement of the slot arms is enlarged, allowing for a better modulation depth to be expected. A thicker slot waveguide can generate a larger optical force, Casimir force and electrostatic force, so less energy is required in actuation. A wider slot waveguide changes the magnitude of the optical force and effective index dependence on the separation between slots arms. Moreover, the mechanical resonant frequency is increased with higher mechanical stiffness as measured in [26]. In this case, a higher modulating frequency is obtained along with a higher modulation depth in the pull-in state with higher power consumption in modulation. As a result, any geometrical changes will affect the performance of the modulator. Generally, the overall performance of the modulator will be in a region between a carrier-based approach and the MOEMS approach and could serve a number of niche applications for which its performance is well suited.

4.9 Chapter conclusions

As a controllable phase shifter, a suspended slot waveguide can be constructed as an optical modulator. The essential part of the suspended slot modulator is the energy efficiency, maximum value of index and phase change and modulating frequency. Electrostatic controlled suspended slot waveguide is a good choice for optical modulation and electro-optical transduction. This allows the modulator performance to be adjusted by configuring suspended slot settings and associative optical circuitry separately to provide more flexibility in modulator design.

The modulator performance under the fully suspended conducted and grounded slot configurations are analyzed using FEA method with COMSOL Multiphysics and Lumerical. We theoretically proved that the suspended slot modulator with conducted slot configuration can achieve low energy consumption (0.19 fJ/bit) and impressive tuning ability ($\Delta n = 4 \times 10^{-2}$) with the help of mechanical resonance, which can be hardly reached by conventional modulators in such a compact size limited by pull-in effect (less than 55 μm). However, the modulating frequency is limited to hundred's of Mega Hertz range set by highest available mechanical resonant frequency of the suspended slot. It covers the gap between existed low speed (thermo-optical) and high speed (carrier based) modulation. The performance of the modulators with grounded slot configuration are inferior to one from conducted slot configuration with the same suspended length. Nevertheless, the flexible design allowed under grounded slot configuration to be a potentially good electro-optical transducer for optical mode-localization sensing as well.

Chapter 5

NOEMS electrometer based on optical mode-localization

By monitoring the resonances in a weakly coupled mechanical resonant system from parametric perturbation, mode-localization MEMS sensors achieve several advantages such as high sensitivity and common-mode rejection. The core concept of such a system is to construct weak couplings between mechanical resonators and quantify the external perturbations (measurand) from resonant peaks on the spectrum. The mode-localization of the coupled resonators is the result of the perturbation, which gives high sensitivity. This concept can be embedded in optical guided wave systems to develop ultra-sensitive sensors based on mode-localization in optically coupled ring resonators, where the perturbation is induced by the NOEMS slot modulator integrated on one of the rings.

Based on the NOEMS slot modulator discussed in chapter 4, a perturbation in voltage can induce a phase perturbation to the structure. For the capacitive actuator applied in the modulator, a perturbation in electric charge changes the actuating voltage through capacitance thus, the charge perturbation can be transferred to the phase perturbation. Therefore, an optomechanical slot modulator can sense the electric charge on the structure to construct an electrometer. Making use of the mode-localization in optically coupled ring resonators with integrated optomechanical slot modulator, ultra-high sensitivity can be achieved in measuring the electronic charge.

For optical systems, resonant mode splitting happens when multiple identical resonators are identically coupled together. Localized perturbation in resonators and couplers will cause the asymmetry in mode splitting. In this case, the total energy in the spectrum will not be evenly confined in all resonant modes, resulting in different modal amplitudes. This is the mode localization phenomenon. The symmetry of the mode splitting can be evaluated by the modal power ratio between different modes that depend on the localized perturbation in effective index and coupling coefficient, thus the

localized perturbation can be detected by examining the modal power ratio. Here we name this sensing mechanism as optical mode localized sensing.

This sensing mechanism can be embedded in optical waveguide/fiber systems to develop ultra-sensitive sensors based on mode localization in optically coupled ring resonators. The sensing element of the optical mode localization sensor can be chosen to be constructed from optical ring resonators coupled with each other by directional couplers. The optical structure constructed with coupled ring resonators is referred to as coupled resonator optical waveguide system (CROW) [94]. The existing applications of CROW covers electromagnetic induced transparency, slow light/delay line, gyroscope[95], biosensor and optical communication [96][97].

The transfer matrix method is widely used in analyzing the spectrum of CROW with identical ring resonators [94][98]. The numerical computation of the spectrum is effectively simplified by identical electric intensity eigenvectors between adjacent resonators. However, hard work is required to derive the analytical expressions for electrical properties in CROW with non-identical ring resonators. Here we use feedback theory [99] [100] (also referred to as Mason's rule [101][102]), which makes the analytical derivation easier, to analyze the coupled ring resonators for optical mode localized sensing.

The theoretical model is validated by comparing the calculation results from the theoretical model and simulation (Lumerical connection). There are four parametric configurations with different output characteristics. After the spectrum analysis, the mode localization caused by index perturbation (configuration C.) is considered a good choice for constructing the sensing element among the four parametric configurations. We also model the optical mode localized sensor assuming an imperfect CROW with fabrication imperfection induced randomly disordered coupled resonators. The mode aliasing, signal-to-noise ratio and dual-channel calibration are discussed when the sensor is configured as a dispersive sensor. It is proved by calculation that the sensitivity is optimized by at least 17.6 times by optical mode localized electrometer compared with mechanical one ($0.0227\ fC^{-1}$) [68].

In this chapter, the basics of the optical resonator based on guided wave circuitry are introduced in Section 5.2 and Section 5.3. The theory of MEMS mode-localization sensor and its principle of performance evaluation is introduced in Section 5.1. Following the same method, the performance of the optical mode-localization circuitry is evaluated theoretically, which is our original contribution. As an outcome, the electrometer designed from coupled ring resonators and NOEMS slot modulator is proved to have a theoretical ultra-high sensitivity, discussed in Section 5.4.

5.1 Mechanical mode-localization sensing mechanism

The existing mode-localized sensors are constructed on 2 DoF and 3 DoF mechanical resonators. To introduce the common feature of mode-localized sensors, the theoretical model of a 2 DoF mode-localized sensor is illustrated here. For 2 DoF mechanical system, the lump models of coupled identical resonators with stiffness perturbations are shown in Figure 5.1

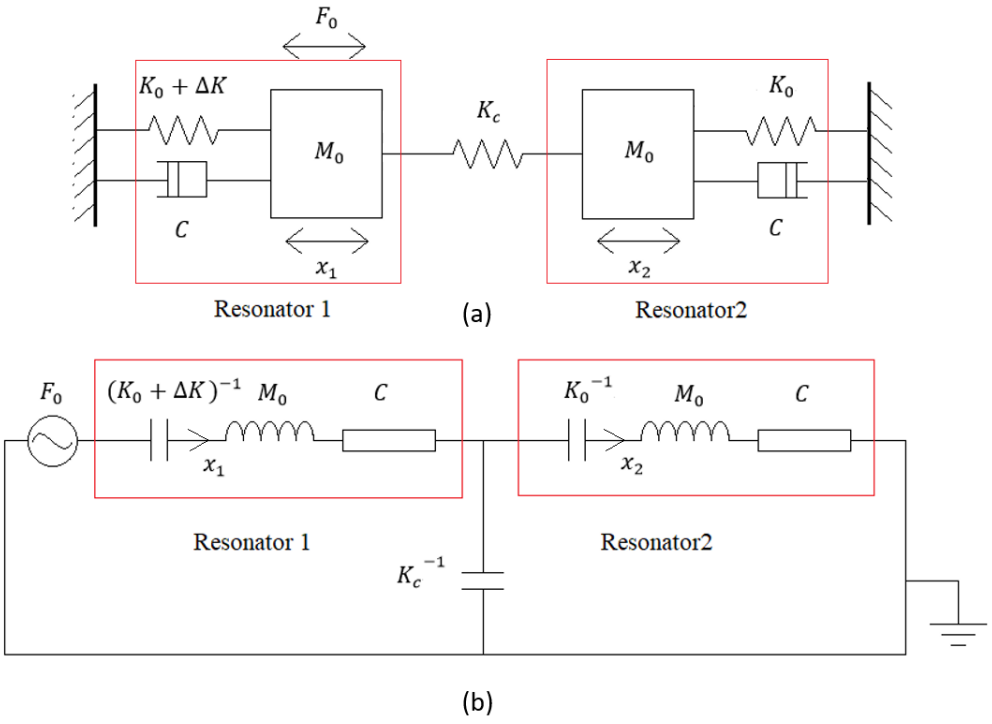

FIGURE 5.1: Fundamental model of mode localization based on spring mass model and its equivalent circuit. K_0, M_0, C, ΔK and x are stiffness, mass, damper, stiffness perturbation and mechanical displacement, respectively. (a). The mechanical model of coupled resonators with stiffness perturbation. (b). The equivalent circuit of (a).

This equivalent circuit is derived from two equations of motion of the system described by [79]:

$$\begin{cases} F_0(t) = M_0\ddot{x}_1(t) + C\dot{x}_1(t) + (K_0 + \Delta K)x_1(t) + K_c(x_1 - x_2) \\ F_0(t) = M_0\ddot{x}_2(t) + C\dot{x}_2(t) + K_0x_2(t) + K_c(x_2 - x_1) \end{cases} \tag{5.1}$$

where x_1 and x_2 are the displacement of the resonator 1 and 2, respectively. These equations are identical to Figure 5.1 if the charge in the first and second capacitors can be represented by x_1 and x_2, respectively. Let $\frac{1}{Z_E}$ and $\frac{1}{Z_C}$ present open-loop transfer function of resonator and coupling:

$$\begin{cases} Z_E = M_0S^2 + CS + K_0 \\ Z_C = K_C \end{cases} \tag{5.2}$$

The transfer functions for resonator 1 and 2 are

$$TF_1 = \frac{Z_E + 2Z_C}{(Z_E + \Delta K)(Z_E + Z_C) + Z_E Z_C} = \frac{Z_E + 2Z_C}{{Z_E}^2 + (2Z_C + \Delta K)Z_E + \Delta K Z_C} \tag{5.3}$$

$$TF_2 = \frac{Z_E}{(Z_E + \Delta K)(Z_E + Z_C) + Z_E Z_C} = \frac{Z_E}{(Z_E + \Delta K)(Z_E + Z_C) + Z_E Z_C} \tag{5.4}$$

The corresponding characteristic equation is

$${Z_E}^2 + (2Z_C + \Delta K)Z_E + \Delta K Z_C = 0 \tag{5.5}$$

The analytical solution of the equation is

$${\delta_0}^{\pm} = \frac{-(2Z_C + \Delta K) \pm \sqrt{(2Z_C + \Delta K)^2 - 4\Delta K Z_C}}{2} = \frac{-(2Z_C + \Delta K) \pm (2Z_C - \Delta K)}{2} \tag{5.6}$$

and at the resonance

$$Z_E = M_0 S^2 + CS + K_0 = {\delta_0}^{\pm} \tag{5.7}$$

$$M_0 S^2 + CS + (K_0 - {\delta_0}^{\pm}) = 0 \tag{5.8}$$

The overall feature of the system is identical with an SDOF system with $K = K_0 - {\delta_0}^{\pm}$. As a result, the two modes can be modelled as two nearly identical resonators with the only difference in effective stiffness. The damping factor, quality factor and resonant frequency are expressed as:

$$\zeta = \frac{C}{2\sqrt{(K_0 - {\delta_0}^{\pm})M_0}} \tag{5.9}$$

$$Q = \frac{1}{2\zeta} = \frac{\sqrt{(K_0 - {\delta_0}^{\pm})M_0}}{C} \tag{5.10}$$

$$\omega_{res} = \frac{\sqrt{(K_0 - {\delta_0}^{\pm})M_0 - C^2}}{M_0} \tag{5.11}$$

With positive perturbation ($K_0 - {\delta_0}^{\pm} > K_0$), the effective stiffness is increased and it will increase Q and ω_{res}, accordingly. An example of the power spectrum mode-localized system is shown in Figure 5.2. The modal amplitude and frequency shown in Figure 5.2 differ with different parametric perturbation (ΔK or ΔM). The system output and sensitivity can be evaluated from eigenstates shift [54] or modal amplitude ratio [103]. Quantifying the modal amplitude ratio (the ratio of the magnitude of the two eigenstates) results in a much higher sensitivity [103]. The sensing measurements are a function of modal amplitude ratio that corresponds to the parametric perturbation.

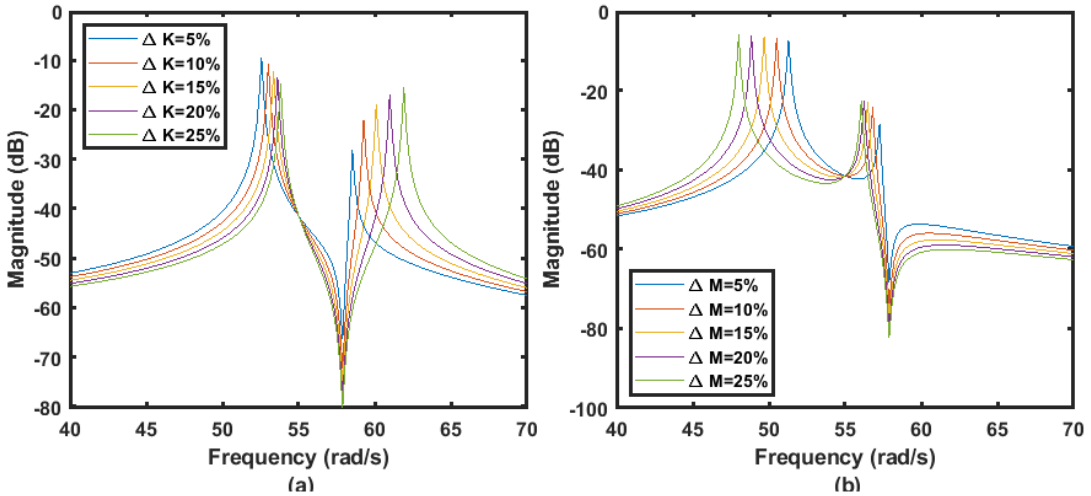

FIGURE 5.2: Power spectrum of the mode localized system under different stiffness perturbations. ($K_0 : M_0 : K_C : C = 1000 : 0.37 : 120 : 0.05$).

5.1.1 Mode aliasing effect

The overlap of the in-phase and out-of-phase modes disrupts the recognition of the modal amplitudes of the two resonant modes if the modes' frequencies are close to each other. The failure of the mode recognition produces a 'sensing dead zone' around the point of zero perturbation. The sensitivity gets worse when the resonant line-width is enlarged by damping. The overlap of these two modes is referred to as the mode aliasing effect [103]. If we recognize an individual mode through the existence of 3 dB frequencies of both resonant peaks, the following anti-aliasing condition has to be satisfied:

$$\Delta f > \Delta f_{3dB-ip} + \Delta f_{3dB-op} \tag{5.12}$$

where Δf is the acceptable modal frequency difference during the measurement. Δf_{3dB-ip} and Δf_{3dB-op} is the 3 dB bandwidth of the in-phase and out-of-phase mode. By definition, the 3 dB bandwidth can be derived as:

$$\Delta f_{3dB} = f/Q \tag{5.13}$$

The frequencies of the in-phase (f_{ip}) and out-of-phase (f_{op}) modes are given by Equation 5.11. The quality factors of the in-phase and out-of-phase modes are given by Equation 5.10. Then the smallest acceptable modal frequencies difference during the measurement is derived as:

$$\Delta f = \frac{f_{ip}}{Q_{ip}} + \frac{f_{op}}{Q_{op}} = \frac{C}{2\pi M_0}\left(\sqrt{1-\frac{C^2}{(K_0+\Delta K)M_0}} + \sqrt{1-\frac{C^2}{(K_0+2K_c)M_0}}\right) \tag{5.14}$$

Here, positive ΔK can increase the difference in modal frequency Δf to mitigate mode aliasing. The two modes can be recognized when Equation 5.14 is satisfied. The existence of the 'sensing dead zone' around the zero perturbation point will also affect the resolution of the sensor. Experimental results related to the mode aliasing effect in mode-localized sensing can be found in [103].

5.1.2 Signal-to-noise ratio, sensitivity and resolution

When the modal amplitude ratio is utilized to quantify the measurement, the signal-to-noise ratio (SNR) is defined as [103]:

$$\mathrm{SNR} = \left|\frac{x_2}{x_1}\right|^2 \Big/ \left|\frac{x_2}{x_1}\right|^2_{noise} = \frac{\mathrm{SNR}_1 \times \mathrm{SNR}_2}{\mathrm{SNR}_1 + \mathrm{SNR}_2} \tag{5.15}$$

where x_1 and x_2 represent the modal amplitudes of the resonators 1 and 2, respectively. SNR_1 and SNR_2 are the SNR of resonator 1 and 2, respectively. The individual SNR denoted by $\mathrm{SNR_i}$ is described as [103] :

$$\mathrm{SNR_i} = \frac{\mathrm{SNR}_{m,i} \times \mathrm{SNR}_{e,i}}{\mathrm{SNR}_{m,i} + \mathrm{SNR}_{e,i}},\ i = 1\ or\ 2 \tag{5.16}$$

where $\mathrm{SNR}_{m,i}$ and $\mathrm{SNR}_{e,i}$ are the mechanical and electrical SNR of the ith resonator, respectively, limited by the mechanical-thermal noise of the resonator and the electrical-thermal noise of the interface electronics [104]. For measurand X, the sensitivity is defined by:

$$\text{Sensitivity} = \frac{\partial(\text{Amplitude Ratio})}{\partial X} \tag{5.17}$$

The resolution is evaluated by the minimum resolvable X of the sensor near the point where $X = 0$, described as:

$$\langle X \rangle_{min} = \frac{\langle \text{Amplitude Ratio} \rangle_{\min}}{Sensitivity} \tag{5.18}$$

where $\langle \text{Amplitude Ratio} \rangle_{\min}$ is the noise power spectral density of the amplitude ratio.

5.2 Modelling of the all-pass optical ring resonator

The optical guided wave circuitry considered in this section consists of waveguides and a directional coupler. The physical phenomenons, including resonant spectrum, power enhancement, thermal-optic effect and optomechanical frequency shift, are illustrated based on the all-pass configuration of the single ring circuitry.

5.2.1 Spectrum analysis of the all-pass optical ring resonator

A simple form of the ring resonator consists of a ring and bus waveguide is shown in Figure 5.3 [105]. In Figure 5.3, E represents normalised complex mode amplitudes so

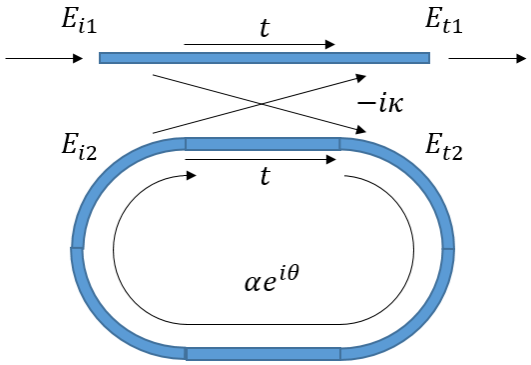

FIGURE 5.3: The generic model of single waveguide coupled ring resonator. [105]

the modal power is E^2. t is the straight-through coefficient and κ the cross-coupling coefficient. α is the loss coefficient of the ring and zero loss is expressed by $\alpha = 1$. Electromagnetic field in the ring couples the field from the bus waveguide through the directional coupler with symmetric and anti-symmetric mode exists simultaneously. The straight-through coefficient, t, and the cross-coupling coefficient, κ, are given by [106][107]:

$$t = \cos\left(\frac{\pi\Delta n}{\lambda}L_c\right);\ \kappa = \sin\left(\frac{\pi\Delta n}{\lambda}L_c\right) \tag{5.19}$$

where Δn is the effective index difference between symmetric and anti-symmetric modes. L_c is the length of the coupler. The simplified coupling matrix of a directional coupler in the complex form shown in Figure 5.3 is described by:

$$C = \begin{pmatrix} t & -i\kappa \\ -i\kappa & t \end{pmatrix} \tag{5.20}$$

This specific configuration is also named as the all-pass ring resonator [108]. The coupling between the waveguide and ring resonator can be described by the following matrix:

$$\begin{pmatrix} E_{t1} \\ E_{t2} \end{pmatrix} = \begin{pmatrix} t & -i\kappa \\ -i\kappa & t \end{pmatrix} \begin{pmatrix} E_{i1} \\ E_{i2} \end{pmatrix}. \tag{5.21}$$

If the coupling is lossless:

$$\left|\kappa^2\right| + \left|t^2\right| = 1 \tag{5.22}$$

The complex mode amplitudes (waveguide mode) E are normalized so that their squared magnitude corresponds to the modal power. To further simplify the analysis, E_{i1} is chosen to be equal to 1. Then the round trip in the ring is given by

$$E_{i2} = \alpha \cdot e^{-i\theta} E_{t2} \tag{5.23}$$

These modal amplitudes can be obtained from Equation 5.21, Equation 5.22 and Equation 5.23 by

$$E_{t1} = \frac{-(\kappa^2 + t^2)\alpha + t \cdot e^{i\theta}}{-\alpha t + e^{i\theta}} = \frac{-\alpha + t \cdot e^{i\theta}}{-\alpha t + e^{i\theta}} \tag{5.24}$$

$$E_{i2} = \frac{-i\kappa\alpha}{-\alpha t + e^{i\theta}} \tag{5.25}$$

$$E_{t2} = \frac{-i\kappa e^{i\theta}}{-\alpha t + e^{i\theta}} \tag{5.26}$$

Take the phase (φ_t) of the bus waveguide into consideration, the coupling coefficient is expressed as $t = |t|\exp(-i\varphi_t)$. The corresponding power from the derived modal amplitudes can be expressed as:

$$P_{t1} = |E_{t1}|^2 = \frac{\alpha^2 + t^2 - 2\alpha t\cos(\theta + \varphi_t)}{1 + \alpha^2 t^2 - 2\alpha t\cos(\theta + \varphi_t)} \tag{5.27}$$

$$P_{i2} = |E_{i2}|^2 = \frac{\alpha^2\kappa^2}{1 + \alpha^2 t^2 - 2\alpha t\cos(\theta + \varphi_t)} \tag{5.28}$$

On resonance, $(\theta + \varphi_t) = 2\pi m$, where m is an integer, the power can be simplified as:

$$P_{t1} = |E_{t1}|^2 = \left(\frac{\alpha - t}{1 - \alpha t}\right)^2 \tag{5.29}$$

$$P_{i2} = |E_{i2}|^2 = \left(\frac{\alpha\kappa}{1 - \alpha t}\right)^2 \tag{5.30}$$

The extinction ratio (ER), the free spectrum range (FSR) and the full width at half maximum (FWHM) useful to analysis the power versus wavelength spectrum. The input phase for the power transmission function can be derived as:

$$\lambda = \frac{2\pi n_g L_0}{2m\pi + \theta - (dn_{eff}/d\lambda)2\pi L_0} \tag{5.31}$$

where m denotes the order of the resonant harmonics expressed in Equation 5.33. The figure of merits is shown in Figure 5.4. The extinction ratio is defined as the ratio between resonant and background power in the spectrum decribed by:

$$ER = \frac{P_{t1}(\pi)}{P_{t1}(2\pi)} = \left[\frac{(\alpha + t)(1 - \alpha t)}{(\alpha - t)(1 + \alpha t)}\right]^2 \tag{5.32}$$

In the case of critical coupling ($\alpha = t$), the transmitted power turns to be zero and energy is completely circulated in the round trip path of the ring. From Equation 5.32, the extinction ratio becomes infinity in the case of critical coupling. Based on standing wave condition on the round trip path of the ring expressed as:

$$\theta = \beta L_0 = k \cdot neff \cdot L_0 = \frac{2\pi n_{eff} L_0}{\lambda} = 2m\pi, \qquad m = 1, 2, 3..., \tag{5.33}$$

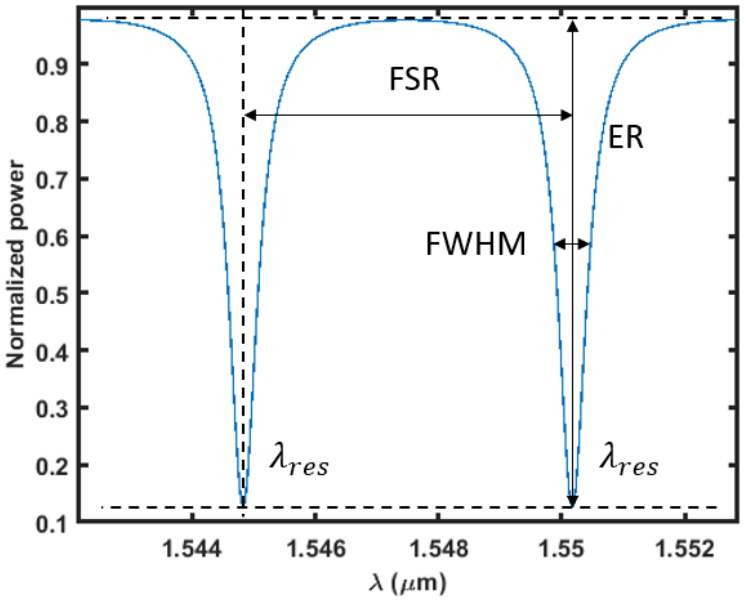

FIGURE 5.4: Illustration of the extinction ratio (ER), the free spectrum range (FSR) and the full width at half maximum (FWHM). ($\alpha = 0.8$, $t = 0.9$, $n_eff = 1.6$, $dn_eff/d\lambda = 0$)

where L_0 denotes the round trip path of the ring. β denotes the propagation constant of the waveguide. k denotes the vacuum wavenumber of the light. m denotes the corresponding order of the resonant harmonics, and it presents the number of resonance peaks within the range from 0 to λ_{res}. The wavelength at the resonance is described by:

$$\lambda_{res} = \frac{n_{eff} L_0}{m}, \qquad m = 1, 2, 3... . \tag{5.34}$$

Distance between resonance peaks is termed as the free spectral range (FSR). It is the separation between the adjacent resonant peaks described by wavelength. Free spectral range with a first-order approximation of the dispersion is expressed as:

$$FSR = \frac{\lambda}{N} = \frac{\lambda^2}{n_g L_0} \tag{5.35}$$

where N represents the number of resonant peaks within the range from 0 to λ. If the phase difference between resonance peak and half maximum of the resonance is represented by $\theta_{FWHM}/2$, the full width at half maximum (FWHM) of the resonance spectrum derived from Equation 5.28 is given by:

$$FWHM = \theta_{FWHM} . \frac{FSR}{2\pi} \tag{5.36}$$

$$\sin \frac{\theta_{FWHM}}{4} = \frac{1 - \alpha t}{2\sqrt{\alpha t}} \tag{5.37}$$

Here $\theta_{FWHM}/4$ is assumed to be small enough to hold ($\sin\frac{\theta_{FWHM}}{4} \approx \frac{\theta_{FWHM}}{4}$), thus:

$$FWHM \approx \frac{(1-\alpha t)\lambda_{res}^2}{\pi n_g L_0 \sqrt{\alpha t}} \tag{5.38}$$

The finesse, which describes the spectrum occupation of the resonances, is defined as the ratio of FSR and resonance width:

$$Finesse = \frac{FSR}{FWHM} = \frac{2\pi}{\theta_{FWHM}} \approx \frac{\pi\sqrt{\alpha t}}{(1-\alpha t)} \tag{5.39}$$

The quality factor of the resonance is derived by:

$$Q = \frac{\lambda_{res}}{FWHM} \approx \frac{\pi n_g L_0 \sqrt{\alpha t}}{(1-\alpha t)\lambda_{res}}\,. \tag{5.40}$$

If the input power of the ring is regarded as 1 so the intensity enhancement factor B of the ring can be simply defined by:

$$B = \frac{P_{i2}}{P_{i1}} = \frac{(\alpha\kappa)^2}{(1-\alpha t)^2} \tag{5.41}$$

It is determined from coupling ratio and energy loss on the ring.

5.2.2 Thermal-optic effect

Thermal-optical spectrum shift for a waveguide can be calculated from Equation 5.42 [109].

$$\frac{\delta\lambda}{\delta T} = \frac{\lambda_0}{n_{group}}\left(\frac{\delta n_{eff}}{\delta T}\right) = \frac{\lambda_0}{n_{group}}\left(\frac{\delta n_{eff}}{\delta n_{core}}\frac{\delta n_{core}}{\delta T} + \frac{\delta n_{eff}}{\delta n_{clad}}\frac{\delta n_{clad}}{\delta T}\right) \tag{5.42}$$

The thermal shift of resonant peaks described by Equation 5.34 is directly related to Equation 5.42 since it is only related to effective refractive index and group index. Thermal-optic coefficient $\delta n/\delta T$ for silicon and silicon dioxide at 1550 nm is 1.87E-04 [110] and 8.44E-06 [111] at room temperature respectively. The corresponding refractive index of silicon and silicon dioxide is 3.48314 [110] and 1.444 [111] respectively. The theoretical wavelength shift can be solved by the combination of simulation software and Equation 5.42. Based on the theory, a slab waveguide (1.55 μm) ring resonator with a radius of 50 um produce a wavelength shift of $76pm/K$ approximately due to the thermal-optic effect. According to Equation 5.42, different waveguide/structure designs will produce different thermal-optic spectrum shifts, so a referencing for each device will be necessary if this spectrum shift is concerned.

5.2.3 Resonant wavelength shift by modulator/phase shifter

Any phase on the optical ring resonator shifts the resonant frequency. The resonant frequency shift is described as:

$$\Delta\lambda_{res} = \frac{\lambda}{2m\pi}\Delta\theta, \qquad m = 1, 2, 3... , \tag{5.43}$$

where $\Delta\theta$ is the phase change on the ring resonator. m denotes the corresponding order of the resonant harmonics, and it presents the number of resonance peaks within the range from 0 to λ_{res}. Recalling the phase change induced by the suspended slot modulator in Section 4.6:

$$\Delta\theta = \frac{2\pi}{\lambda}\Delta n_{eff} L = (\delta^{e2}_{max} D_2 - \delta^{e1}_{max} D_1)\frac{2\pi L}{\lambda}\frac{49}{45} \tag{3.68}$$

where δ^{e1}_{max} and δ^{e2}_{max} denotes the maximum deformation at the zero and one state, respectively. D_1 and D_2 denotes for powerless/powered index change rate, respectively. L denotes the suspended length of the waveguide. If the suspended slot modulator is applied on the ring resonator to produce a resonant wavelength shift, the resonant wavelength shift is expressed as:

$$\Delta\lambda_{res} = (\delta^{e2}_{max} D_2 - \delta^{e1}_{max} D_1)\frac{L}{m}\frac{49}{45}, \qquad m = 1, 2, 3... , \tag{5.44}$$

5.3 Optical mode-localization sensing mechanism

The sensing element of the optical mode-localization sensor is chosen to be constructed from optical ring resonators coupled with each other by directional couplers. It is a four-port system containing two coupled ring resonators, which is usually investigated as wavelength-division multiplexed (WDM) optical signal channel dropping filters [112]. The index or coupling perturbation induces the optical mode-localization on the output power-wavelength spectrum. Following the same principle of the mechanical mode-localization sensing mechanism, the output of the sensing element is determined by the power ratio between localized resonant peaks on the spectrum.

The feedback theory (Mason's rule) based on the signal flow graph is used to derive the transfer functions between the input and output port of the sensing element. The theoretical model is validated by comparing the calculation results from the theoretical model and simulation (Lumerical connection). There are four parametric configurations with different output characteristics. The mode-localization caused by index perturbation (configuration C.) is considered a good choice for constructing the sensing element among the four parametric configurations after the spectrum analysis. The

mode aliasing, noise immunity, signal-to-noise ratio and dual-channel calibration are discussed when the sensor is configured under configuration C.

The spectrum of the coupled ring resonators is analysed in from Section 5.3.1 to Section 5.3.6. The output characteristics of the coupled ring resonator under condition C. are discussed in Section 5.3.7. The mode aliasing effect and noise immunity are discussed in Section 5.3.9. The signal-to-noise ratio and dual-channel calibration of the sensor are discussed in Section 5.3.10.

5.3.1 Transmission of the coupled ring resonators (mode-localizer)

By coupling two optical ring resonators together, a four-port system usually applied as the optical add-drop filter is constructed. The structure of a four-port system with two coupled ring resonators is shown in Figure 5.5.

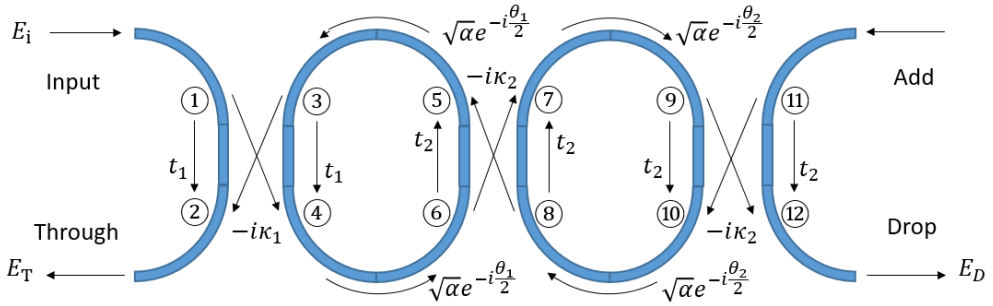

FIGURE 5.5: A four port system constructed with two bus waveguide and two coupled ring resonators

In Figure 5.5, every coupler is labelled with different numbered nodes to identify the details of the coupling between the bus waveguides and ring resonators. The two rings are constructed from waveguides with different propagation constant, and coupled differently with bus waveguide. The relation of the electrical field between different nodes shown in Figure 5.5 can be expressed by signal flow graph as shown in Figure 5.6. In Figure 5.6, different phase shift (θ_1, θ_2) of the waveguide between numbered

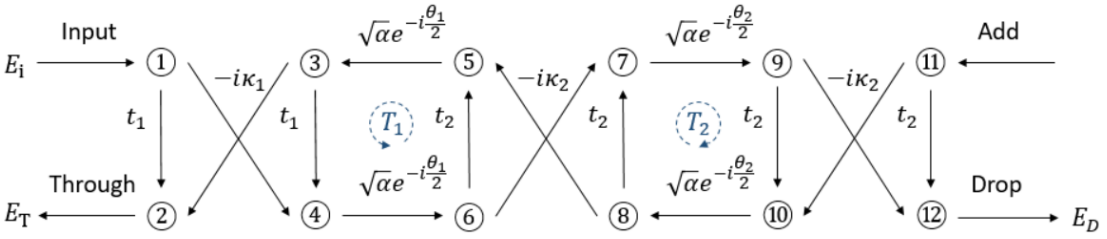

FIGURE 5.6: Electrical field flow graph between numbered nodes in Figure 5.5

nodes may result from different propagation constant of the waveguide or different light travel path length of the ring. In this chapter, only the phase shift caused by different propagation constant of the waveguide is considered. For the ease of analysis,

an equivalent graph shown in Figure 5.7 is converted from flipping the ring labelled from node 3 to 5 and bus waveguide labelled from node 11 to 12 in Figure 5.6 to give a better view of the coupling.

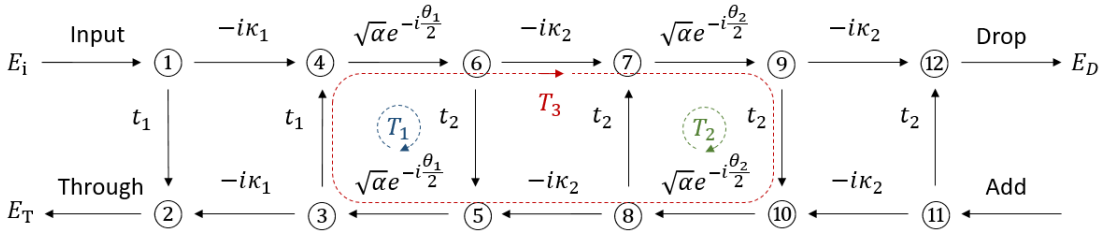

FIGURE 5.7: Equivalent flow graph of Figure 5.6

According to the feedback theory [99] [100] (also referred to as Mason's rule [101][102]), the transfer function between the input and output of the system can be derived from:

$$G = \frac{\sum_j G_j \Delta_j}{\Delta} \tag{5.45}$$

$$\Delta = 1 - \sum_m P_{m1} + \sum_m P_{m2} - \sum_m P_{m3} + ... \tag{5.46}$$

where G_j, P_{mr} and Δ_j are the gain of the jth forward path, gain product of the mth possible combination of r nontouching loops, and the value of Δ for that part of the graph not touching the jth forward path, respectively. Δ is called the determinant of the graph, and Δ_j is called the cofactor of forwarding path j [113]. The determinant of a complete flow graph is equal to the product of the determinants of each of the nontouching parts in its loop subgraph [113]. In Figure 5.7, there are three individual loops denoted by T_1, T_2 and T_3 expressed by:

$$T_1 = t_1 t_2 \alpha e^{-i\theta_1};\ T_2 = {t_2}^2 \alpha e^{-i\theta_2};\ T_3 = -\kappa_2^2 t_1 t_2 \alpha^2 e^{-i(\theta_1+\theta_2)} \tag{5.47}$$

According to [99] and [113], the determinant of the Figure 5.7 is expressed by:

$$\begin{aligned} \Delta &= 1 - T_1 - T_2 - T_3 + T_1 T_2 \\ &= 1 - t_1 t_2 \alpha e^{-i\theta_1} - t_2^2 \alpha e^{-i\theta_2} + (t_1 t_2^3 \alpha^2 + \kappa_2^2 t_1 t_2 \alpha^2) e^{-i(\theta_1+\theta_2)} \end{aligned} \tag{5.48}$$

Here we only concern the transmission from input to through or drop ports (only one input). The transfer function of the electric field from the input to the drop port and through port of the system ($G_D = E_D/E_i$; $G_T = E_T/E_i$) are expressed by:

$$\begin{aligned} G_D &= \frac{G_{1\to 12}}{\Delta} \\ &= \frac{-i\kappa_1 \kappa_2^2 \alpha e^{-i(\theta_1+\theta_2)/2}}{1 - a e^{-i\theta_1} - b e^{-i\theta_2} + (ab - c) e^{-i(\theta_1+\theta_2)}} \end{aligned} \tag{5.49}$$

and

$$\begin{aligned} G_T &= \frac{G_{1\to2}\Delta + G_{1\to9\to10\to2} + G_{1\to6\to5\to2}(1-be^{-i\theta})}{\Delta} \\ &= \frac{t_1 + (d-t_1a)e^{-i\theta_1} - t_1be^{-i\theta_2} + (t_1ab + f - t_1c - db)e^{-i(\theta_1+\theta_2)}}{1 - ae^{-i\theta_1} - be^{-i\theta_2} + (ab-c)e^{-i(\theta_1+\theta_2)}} \end{aligned} \tag{5.50}$$

where G_D and G_T are electric transfer function from the input to the drop port and through port, respectively. Parameter a, b, c, d, f are expressed by:

$$a = t_1t_2\alpha;\ b = t_2^2\alpha;\ c = -\kappa_2^2t_1t_2\alpha^2;\ d = -k_1^2t_2\alpha;\ f = k_1^2k_2^2t_2\alpha \tag{5.51}$$

The power transmission from the input to the drop port and through port are expressed by:

$$|G_D|^2 = \frac{\kappa_1^2\kappa_2^4\alpha^2}{D_1 + D_2\cos(\theta_1) + D_3\cos(\theta_2) + D_4\cos(\theta_1)\cos(\theta_2) + D_5\cos(\theta_1+\theta_2)} \tag{5.52}$$

and

$$|G_T|^2 = \frac{N_1 + N_2\cos(\theta_1-\theta_2) + N_3\cos(\theta_2) + N_4\cos(\theta_1) + N_5\cos(\theta_1+\theta_2)}{D_1 + D_2\cos(\theta_1) + D_3\cos(\theta_2) + D_4\cos(\theta_1)\cos(\theta_2) + D_5\cos(\theta_1+\theta_2)} \tag{5.53}$$

where $|G_D|^2$ and $|G_T|^2$ are power transmission from the input to the drop port and through port, respectively. Parameter N_x and D_x are expressed by:

$$\begin{aligned} &N_1 = (d-t_1a)^2 + (-t_1b)^2 + (f-db-t_1c+t_1ab)^2 + t_1^2; \\ &N_2 = -2(d-t_1a)t_1b;\ N_3 = 2[(d-t_1a)(f-db-t_1c+t_1ab) - (t_1b)t_1]; \\ &N_4 = 2((d-t_1a)t_1 - t_1b(f-db-t_1c+t_1ab));\ N_5 = 2(f-db-t_1c+t_1ab)t_1; \end{aligned} \tag{5.54}$$

and

$$\begin{aligned} &D_1 = a^2b^2 + a^2 + b^2 + c^2 - 2abc + 1;\ D_2 = -2ab^2 + 2bc - 2a; \\ &D_3 = -2a^2b + 2ac - 2b;\ D_4 = 4ab;\ D_5 = -2c; \end{aligned} \tag{5.55}$$

The power transmission of the left and right resonant peaks from $|G_T|^2$ are represented by P_T^- and P_T^+ within $-\pi < \theta < \pi$ in the transmission-phase spectrum, respectively. The power transmission of the resonant peaks from $|G_D|^2$ is represented by $P_D^\pm$. An illustration of the spectrum is shown in Figure 5.8.

To find the phase ($\theta_d^\pm$ and $\theta_t^\pm$) of the resonant peaks on the spectrum, the extreme value of the $|G_T|^2$ and $|G_D|^2$ needs to be solved from $d(|G_x|^2)/d(\theta) = 0$. For $|G_D|^2$, the extreme values are determined from $d(|\Delta|^2)/d(\theta) = 0$, while for $|G_T|^2$, the extreme values are determined from both the denominator ($|\Delta|^2$) and numerator of Equation 5.53 denoted by $|\Delta_T|^2$. $d(|\Delta|^2)/d(\theta) = 0$ and $d(|\Delta_T|^2)/d(\theta) = 0$ are expressed as:

$$D_2\sin(\theta_1) + (D_4 + 2D_5)\sin(\theta_1+\theta_2) = -D_3\sin(\theta_2) \tag{5.56}$$

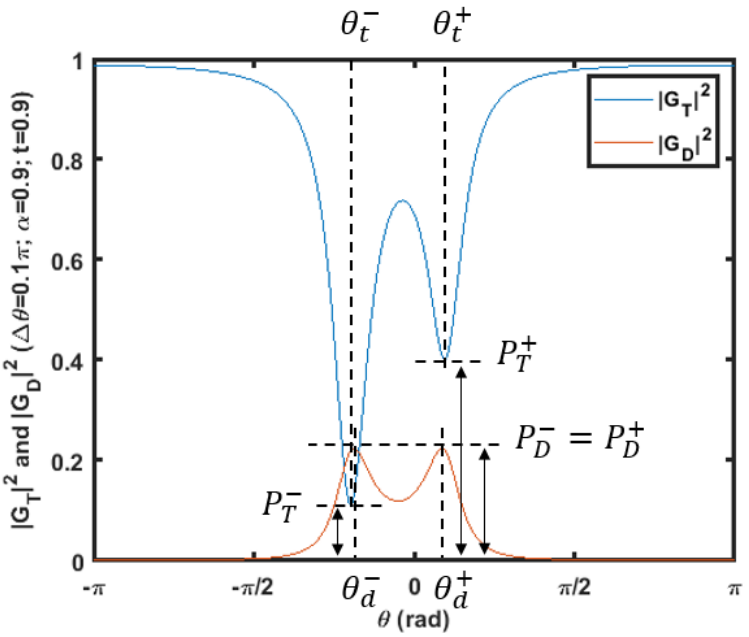

FIGURE 5.8: Notations for resonant peaks in $|G_T|^2$ and $|G_D|^2$ with $\Delta\theta = 0.1\pi$. The power transmission of the resonant peaks are denoted by $P^{\pm}$ to describe resonant peaks on the left $(-)$ and right $(+)$ hand side. $\theta^{\pm}$ denotes the phase of the resonant peaks.

and

$$N_4 \sin(\theta_1) + 2N_5 \sin(\theta_1 + \theta_2) = -N_3 \sin(\theta_2) \tag{5.57}$$

The solutions from Equation 5.56 are denoted by θ_d and θ_b, respectively. They correspond the local minimum and maximum of $|\Delta|^2$ solved from Equation 5.56. The phase correspond to local maximum of $|\Delta|^2$ solved from Equation 5.57 are denoted by θ_n.

These two equations can be treated differently corresponding to how system is arranged. The system can be arranged into four different conditions including: A. system with zero perturbation ($t_1 = t_2, \theta_1 = \theta_2$), B. system with coupling perturbation ($t_1 \neq t_2, \theta_1 = \theta_2$), C. system with phase perturbation ($t_1 = t_2, \theta_1 \neq \theta_2$), and D. system with coupling and phase perturbation ($t_1 \neq t_2, \theta_1 \neq \theta_2$).

5.3.2 Condition A. System with zero perturbation

Based on the system constructed with $t_1 = t_2 = t$ and $\theta_1 = \theta_2 = \theta$, the spectrum of $|G_D|^2$ can be analyzed from the denominator $|\Delta|^2$. For $d(|\Delta|^2)/d(\theta) = 0$, Equation 5.56 can be expressed as:

$$\sin(\theta)\left[D_2 + (D_4 + 2D_5)\cos(\theta)\right] = 0 \tag{5.58}$$

When $\sin(\theta) = 0$, the phase corresponding to the local minimums of $|\Delta|^2$ is solved as:

$$\theta_b = m\pi, m \in Z \tag{5.59}$$

where θ_b denotes the phase corresponding to the background transmission (power transmission between resonant peaks) of $|G_D|^2$. When $\sin(\theta) \neq 0$, the phase corresponding to the local maximums of $|\Delta|^2$ is solved as:

$$\begin{aligned}\theta_d &= 2m\pi \pm \left|\arccos\left[-\frac{D_2}{(D_4+2D_5)}\right]\right|, m \in Z \\ &= 2m\pi \pm \left|\arccos\left[\frac{t^2\alpha^2(1-\gamma)+1}{2\alpha(1-\gamma)}\right]\right|, m \in Z\end{aligned} \tag{5.60}$$

where θ_d denotes the phase corresponding to the resonant peaks of $|\Delta|^2$ and $\gamma = 1 - t^2 - \kappa^2$ denotes the loss of the coupler. This result indicates that two resonant peaks has the same value of $cos(\theta_d)$ and $|G_D|^2$ in a symmetrical system. The magnitude of the resonant peaks is expressed by:

$$|G_D(\theta_d)|^2 = \frac{\kappa^6\alpha^2(D_4+2D_5)}{(D_1-D_5)(D_4+2D_5)-D_2^2} \tag{5.61}$$

The extinction ratio of the resonant peak is expressed by:

$$ER = \frac{|G_D(\theta_d)|^2}{|G_D(\theta_b)|^2} = \frac{(D_4+2D_5)(D_1-2D_2+D_4+D_5)}{(D_1-D_5)(D_4+2D_5)-D_2^2} \tag{5.62}$$

To find out the θ_{FWHM}, the phase corresponding to the half-power of the resonant peak needs to be solved. Based on the approximation that resonant spectrum shape is symmetrical to $\theta = \theta_d$:

$$|G_D(\theta_d)|^2/2 = |G_D(\theta_d \pm \theta_{FWHM}/2)|^2 \tag{5.63}$$

then:

$$\cos(\theta_d \pm \theta_{FWHM}/2) = \frac{-D_2 \pm \sqrt{(D_1-D_5)(D_4+2D_5)-D_2^2}}{D_4+2D_5} \tag{5.64}$$

The numerical solution of θ_{FWHM} can be solved out from:

$$\theta_{FWHM} = \arccos(\theta_d + \theta_{FWHM}/2) - \arccos(\theta_d - \theta_{FWHM}/2) \tag{5.65}$$

If the FSR of the system is defined in the same way as Equation 5.35, FWHM, Finesse and Q of the $|G_D|^2$ can be solved numerically.

The spectrum of $|G_T|^2$ needs to be analyzed from denominator $|\Delta|^2$ and numerator $|\Delta_T|^2$. For $d(|\Delta_T|^2)/d(\theta) = 0$, Equation 5.57 is expressed as:

$$\sin(\theta)\left[N_3 + N_4 + 4N_5\cos(\theta)\right] = 0 \tag{5.66}$$

when $\sin(\theta) \neq 0$, the phase corresponding to the extreme value of $|\Delta_T|^2$ is solved as:

$$\begin{aligned}\theta_n &= 2m\pi \pm \left|\arccos\left[-\frac{N_3+N_4}{4N_5}\right]\right|, m \in Z \\ &= 2m\pi \pm \left|\arccos\left[\frac{(\kappa^2+2t^2)[\kappa^2\alpha(\kappa^2+t^2\alpha)+t^2\alpha^2(\kappa^2+t^2)+1]}{4[\kappa^2(\kappa^2+t^2\alpha^2)+t^2\alpha(\kappa^2+t^2)]}\right]\right|, m \in Z\end{aligned} \tag{5.67}$$

where θ_n denotes the phase corresponding to the extreme value of $|\Delta_T|^2$. Equation 5.67 is different from Equation 5.60 so the phase (θ_t) corresponding to the extreme value of $|G_T|^2$ exists between θ_d and θ_n. This result indicates that two resonant peaks has the same value of $|G_T|^2$ in a symmetrical system and there is no analytical solution for θ_t.

In a lossless system ($\alpha = 1$ and $\gamma = 0$), the expression can be simplified as:

$$\theta_n = \theta_d = 2m\pi \pm \left|\arccos\left(\frac{t^2+1}{2}\right)\right|, m \in Z \tag{5.68}$$

In this case, $|G_T|^2$ and $|G_D|^2$ can be regarded as mirror images of each other from the point of energy conservation, expressed by:

$$|G_T|^2 = 1 - |G_D|^2 \tag{5.69}$$

The power spectrum within single period for both $|G_D|^2$ and $|G_T|^2$ in case A with different values of α and t are shown in Figure 5.9 and Figure 5.10. To illustrate the spectrum difference between the lossless system and normal system, Figure 5.9 is plotted with $\alpha = 1$ and Figure 5.10 is plotted with $\alpha = 0.97$. To illustrate the spectrum difference between different value of t, each of Figure 5.9 and Figure 5.10 is plotted with three sub-figures with $t = 0.7, 0.8$ & 0.9.

From Figure 5.9, all three plots show the feature of the lossless system described in Equation 5.68 and Equation 5.69. The resonant peaks from $|G_D|^2$ or $|G_T|^2$ have the same magnitude, and they are symmetrical to $\theta = 0$. As described in Equation 5.60, phase difference between two resonant peaks and line width (FWHM) are decreasing with t increasing, shown in Figure 5.9 (a). (b). and (c). $|G_D|^2$ and $|G_T|^2$ can be regarded as critical coupling from the magnitude of resonant peaks.

The only difference between Figure 5.9 and Figure 5.10 is the propagation loss set with $\alpha = 0.97$. From Figure 5.10, the resonant peaks from $|G_D|^2$ are dropped significantly rather than the resonant peaks from $|G_T|^2$, which indicates the resonant peaks from $|G_D|^2$ are more sensitive to the propagation loss change in the system. For both $|G_T|^2$ and $|G_D|^2$, the extinction ratio become weaker with higher value of t.

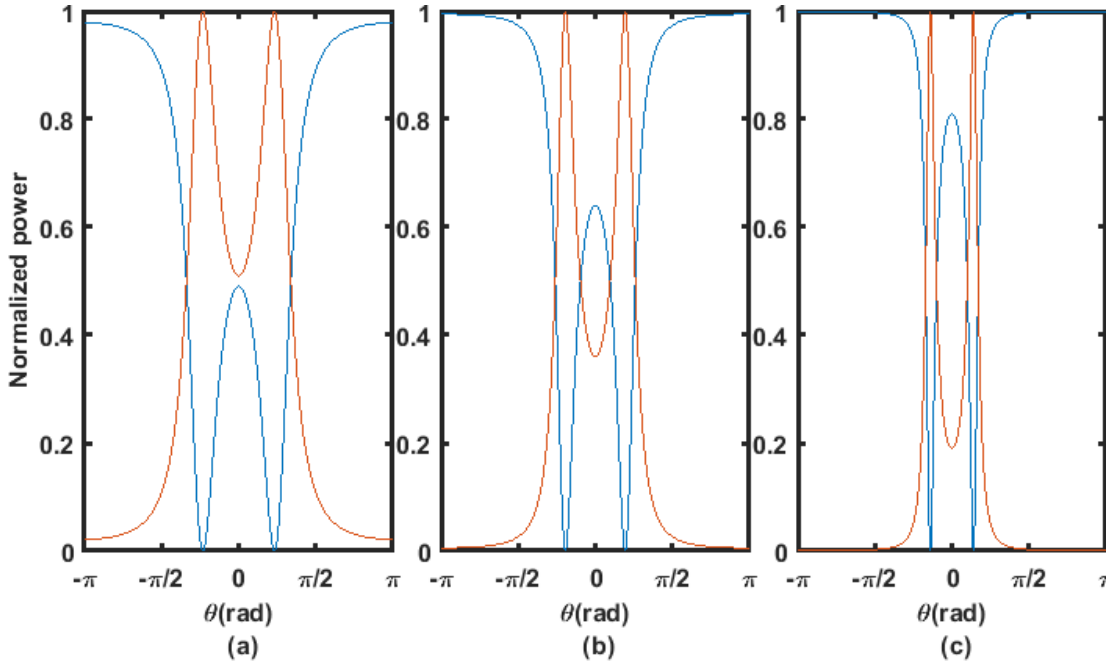

FIGURE 5.9: Power spectrum from $|G_D|^2$ (red curve) and $|G_T|^2$ (blue curve). (a). $\alpha = 1$, $t = 0.7$; (b). $\alpha = 1$, $t = 0.8$; (c). $\alpha = 1$, $t = 0.9$.

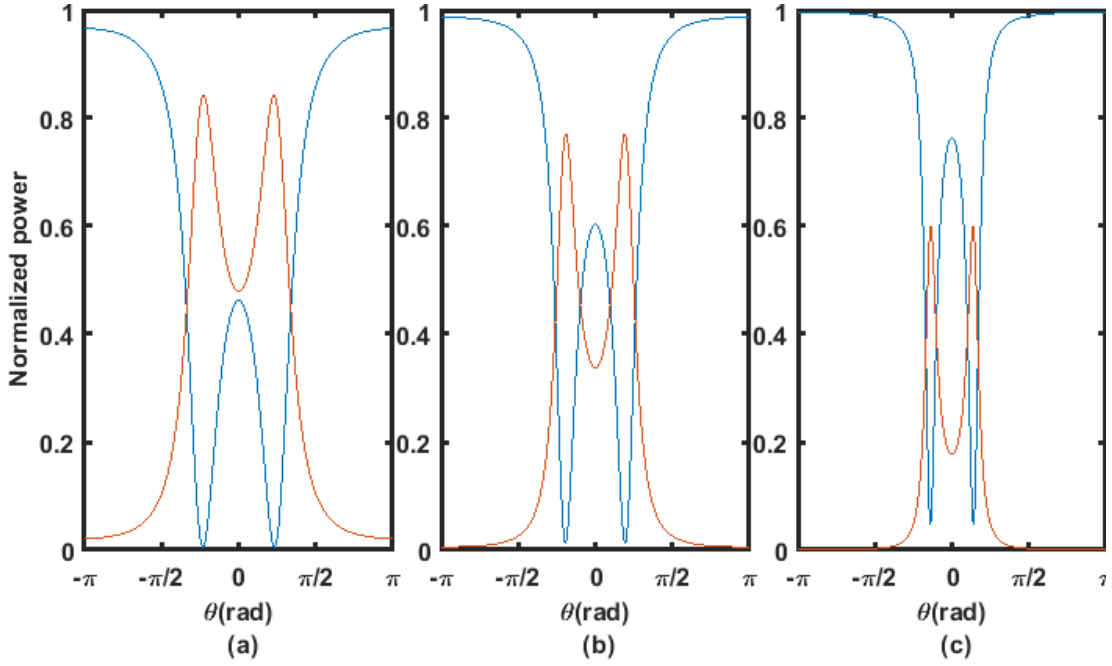

FIGURE 5.10: Power spectrum from $|G_D|^2$ (red curve) and $|G_T|^2$ (blue curve). (a). $\alpha = 0.97$, $t = 0.7$; (b). $\alpha = 0.97$, $t = 0.8$; (c). $\alpha = 0.97$, $t = 0.9$.

5.3.3 Condition B. System with coupling perturbation

Based on system constructed from $t_1 \neq t_2$ and $\theta_1 = \theta_2 = \theta$, the spectrum of $|G_D|^2$ can be analyzed from the denominator $|\Delta|^2$. For $d(|\Delta|^2)/d(\theta) = 0$, Equation 5.56 can be

expressed as:

$$\sin(\theta)[D_2 + D_3 + 2(D_4 + 2D_5)\cos(\theta)] = 0 \tag{5.70}$$

when $\sin(\theta) \neq 0$, the phase corresponding to the extreme value of $|\Delta|^2$ is solved as:

$$\begin{aligned} \theta_d &= 2m\pi \pm \left|\arccos\left[-\frac{D_2 + D_3}{2(D_4 + 2D_5)}\right]\right|, m \in Z \\ &= 2m\pi \pm \left|\arccos\left[\frac{(t_1 + t_2)[t_1 t_2 \alpha^2(1 - \gamma_2) + 1]}{4\alpha t_1(1 - \gamma_2)}\right]\right|, m \in Z \end{aligned} \tag{5.71}$$

This result indicates that two resonant peaks have the same magnitude since the two peaks have the same value of $cos(\theta_c)$ when identical rings coupled with bus waveguide differently. The magnitude of the resonant peaks is expressed as:

$$|G_D(\theta_d)|^2 = \frac{4\kappa_1^2\kappa_2^4\alpha^2(D_4 + 2D_5)}{4(D_1 - D_5)(D_4 + 2D_5) - (D_2 + D_3)^2} \tag{5.72}$$

The extinction ratio of the resonant peak is expressed by:

$$ER = \frac{|G_D(\theta_d)|^2}{|G_D(\pi)|^2} = \frac{4(D_4 + 2D_5)(D_1 - D_2 - D_3 + D_4 + D_5)}{4(D_1 - D_5)(D_4 + 2D_5) - (D_2 + D_3)^2} \tag{5.73}$$

According to Equation 5.63, numerical solution of θ_{FWHM} can be solved out from:

$$\begin{aligned} \theta_{FWHM} = &\arccos\left(\frac{-(D_2 + D_3) + \sqrt{4(D_1 - D_5)(D_4 + 2D_5) - (D_2 + D_3)^2}}{2(D_4 + 2D_5)}\right) \\ &- \arccos\left(\frac{-(D_2 + D_3) - \sqrt{4(D_1 - D_5)(D_4 + 2D_5) - (D_2 + D_3)^2}}{2(D_4 + 2D_5)}\right) \end{aligned} \tag{5.74}$$

The spectrum of $|G_T|^2$ needs to be analyzed from denominator $|\Delta|^2$ and numerator $|\Delta_T|^2$. For $d(|\Delta_T|^2)/d(\theta) = 0$, Equation 5.57 is expressed as Equation 5.66. When $\sin(\theta) \neq 0$, the phase corresponding to the extreme value of $|\Delta_T|^2$ is solved as:

$$\theta_n = 2m\pi \pm \left|\arccos\left[\frac{(1 - \gamma_1 + t_1 t_2)[\kappa_1^2 t_2 \alpha(\kappa_2^2 + t_2^2\alpha) + t_1^2 t_2 \alpha^2(1 - \gamma_2) + t_1]}{4[\kappa_1^2(\kappa_2^2 + t_2^2\alpha^2) + t_1^2\alpha(1 - \gamma_2)]t_1}\right]\right|, m \in Z \tag{5.75}$$

Equation 5.75 is different from Equation 5.71 so the phase corresponding to the extreme value of $|G_T|^2$ exists between θ_d and θ_n. This result indicates that two resonant peaks has the same value of $|G_T|^2$ in a symmetrical system.

If the system is lossless ($\alpha = 1$ and $\gamma = 0$), the expression can be simplified as:

$$\theta_n = \theta_d = 2m\pi \pm \left|\arccos\left(\frac{(1 + t_1 t_2)(t_1 + t_2)}{4t_1}\right)\right|, m \in Z \tag{5.76}$$

In this case, $|G_T|^2$ and $|G_D|^2$ can be regarded as mirror images of each other as shown in Equation 5.69.

The power spectrum within single period for both $|G_D|^2$ and $|G_T|^2$ in case B with different values of α and t are shown in Figure 5.11 and Figure 5.12. To illustrate the spectrum difference between the lossless system and normal system, Figure 5.11 is plotted with $\alpha = 1$ and Figure 5.12 is plotted with $\alpha = 0.97$. To illustrate the spectrum difference between different value of Δt, each of Figure 5.11 and Figure 5.12 is plotted with three sub-figures with $\Delta t = t_2 - t_1 = -0.1, 0$ & 0.1. t_1 is chosen to be 0.75.

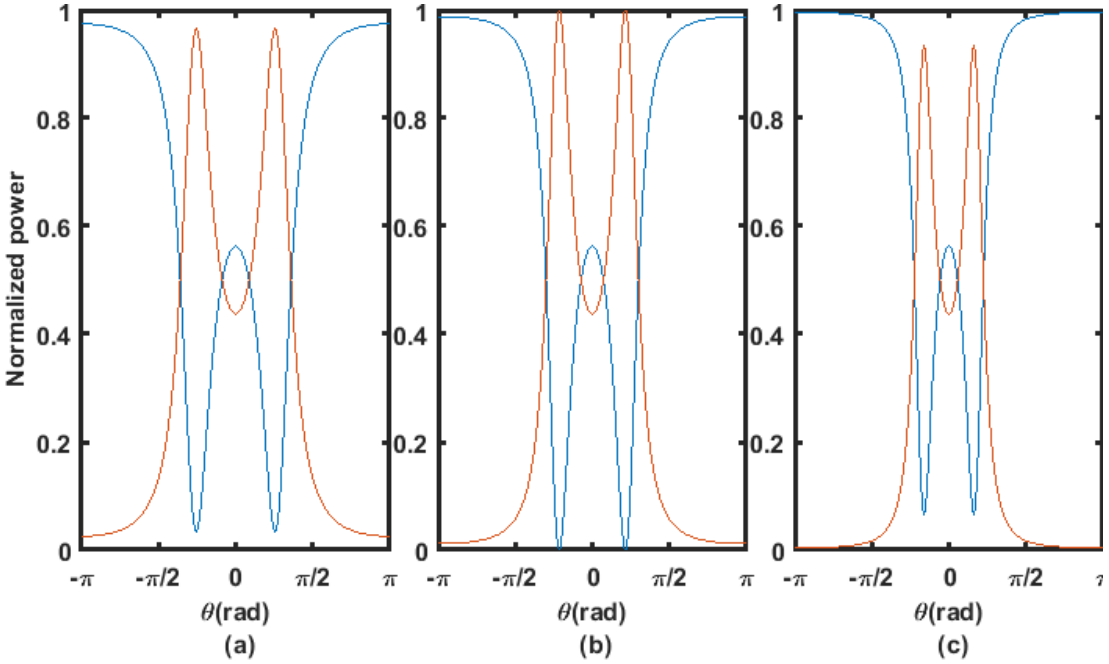

FIGURE 5.11: Power spectrum from $|G_D|^2$ (red curve) and $|G_T|^2$ (blue curve). (a). $\alpha = 1$, $t = 0.75$ and $t = 0.65$; (b). $\alpha = 1$, $t_1 = 0.75$ and $t_2 = 0.75$; (c). $\alpha = 1$, $t_1 = 0.75$ and $t_2 = 0.85$.

From Figure 5.11, all three plots show the feature of the lossless system described in Equation 5.76 and Equation 5.69. The features of the resonant symmetry, the relationship between line width and t, and the relationship between resonant magnitude and t is similar to Figure 5.9. By comparing Figure 5.11.(a)., (b). and (c)., critical coupling can be achieved only when $\Delta t = 0$ (Case A).

Generally, the spectrum feature in case B, is similar in case A except for critical coupling and enhanced resonance from $|G_T|^2$ with a higher value of t shown in Figure 5.12.

5.3.4 Condition C. System with phase perturbation

Based on system constructed from $t_1 = t_2 = t$, $\theta_1 = \theta + \Delta\theta$ and $\theta_2 = \theta$, the spectrum of $|G_D|^2$ can be analyzed from the denominator $|\Delta|^2$. For $d(|\Delta|^2)/d(\theta) = 0$, Equation 5.56 can be expressed as:

$$\sin\left(\frac{2\theta + \Delta\theta}{2}\right)\left[2D_2\cos\left(\frac{\Delta\theta}{2}\right) + 2(D_4 + 2D_5)\cos\left(\frac{2\theta + \Delta\theta}{2}\right)\right] = 0 \tag{5.77}$$

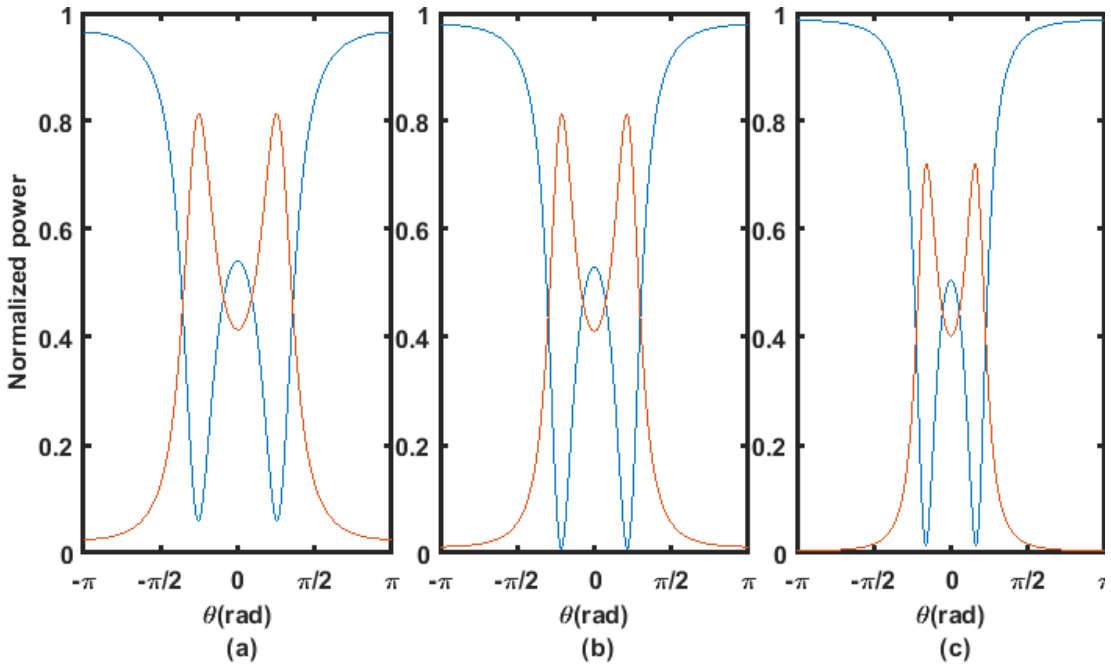

FIGURE 5.12: Power spectrum from $|G_D|^2$ (red curve) and $|G_T|^2$ (blue curve). (a). $\alpha = 0.97$, $t = 0.75$ and $t = 0.65$; (b). $\alpha = 0.97$, $t_1 = 0.75$ and $t_2 = 0.75$; (c). $\alpha = 0.97$, $t_1 = 0.75$ and $t_2 = 0.85$.

when $\sin(\frac{2\theta+\Delta\theta}{2}) \neq 0$, the corresponding phase of the resonant peaks is solved as:

$$\begin{aligned}\theta_d &= 2m\pi - \frac{\Delta\theta}{2} \pm \left|\arccos\left[-\frac{D_2}{D_4+2D_5}\cos\left(\frac{\Delta\theta}{2}\right)\right]\right|, m \in Z \\ &= 2m\pi - \frac{\Delta\theta}{2} \pm \left|\arccos\left[\left(\frac{t^2\alpha^2(1-\gamma)+1}{2\alpha(1-\gamma)}\right)\cos\left(\frac{\Delta\theta}{2}\right)\right]\right|, m \in Z\end{aligned} \tag{5.78}$$

According to Equation 5.77, two resonant peaks of $|G_D|^2$ has the same magnitude when non-identical rings coupled with bus waveguide identically. The magnitude of the resonant peaks is expressed as:

$$|G_D(\theta_d)|^2 = \frac{4\kappa^6\alpha^2(D_4+2D_5)}{[D_1-D_5+D_4(\cos^2(\Delta\theta/2)-1)](D_4+2D_5)-D_2^2\cos^2(\Delta\theta/2)} \tag{5.79}$$

The extinction ratio of the resonant peak is expressed by:

$$ER = \frac{D_1+D_5-2D_2\cos(\Delta\theta/2)+D_4\cos^2(\Delta\theta/2)}{[D_1-D_5+D_4(\cos^2(\Delta\theta/2)-1)](D_4+2D_5)-D_2^2\cos^2(\Delta\theta/2)} \tag{5.80}$$

According to Equation 5.63, numerical solution of θ_{FWHM} can be solved out from:

$$\begin{aligned}\theta_{FWHM} = &\arccos\left(\sqrt{\frac{2\cos^2(\Delta\theta/2)}{(D_4+2D_5)^2}+\frac{D_4+D_5-D_1}{(D_4+2D_5)(D_2^2-D_4^2-2D_4D_5)}}\right) \\ &-\arccos\left(-\sqrt{\frac{2\cos^2(\Delta\theta/2)}{(D_4+2D_5)^2}+\frac{D_4+D_5-D_1}{(D_4+2D_5)(D_2^2-D_4^2-2D_4D_5)}}\right)\end{aligned} \tag{5.81}$$

The spectrum of $|G_T|^2$ needs to be analyzed from denominator $|\Delta|^2$ and numerator $|\Delta_T|^2$. For $d(|\Delta_T|^2)/d(\theta) = 0$, it is hard to find analytical solutions for Equation 5.57 when $\theta_1 \neq \theta_2$. If propagation and coupling loss is small ($\alpha^2 \approx \alpha$, $1-\gamma \approx 1$), an approximation can be made from Equation 5.82, expressed as:

$$\theta_n \approx 2m\pi - \frac{\Delta\theta}{2} \pm \left|\arccos\left[\frac{(1-\gamma_1+t_1t_2)\alpha}{2}\cos\left(\frac{\Delta\theta}{2}\right)\right]\right|, m \in Z \tag{5.82}$$

If the system is lossless ($\alpha = 1$, $\gamma = 0$ and $N_3 = N_4$), Equation 5.57 can be simplified as:

$$\cos\left(\theta + \frac{\Delta\theta}{2}\right) = -\frac{N_3}{4N_5}\cos\left(\frac{\Delta\theta}{2}\right) \tag{5.83}$$

so

$$\theta_n = \theta_d = 2m\pi - \frac{\Delta\theta}{2} \pm \left|\arccos\left[\left(\frac{t^2+1}{2}\right)\cos\left(\frac{\Delta\theta}{2}\right)\right]\right|, m \in Z \tag{5.84}$$

In this case, $|G_T|^2$ and $|G_D|^2$ can be regraded as mirror images of each other as shown in Equation 5.69.

The power spectrum within single period for both $|G_D|^2$ and $|G_T|^2$ in case C with different parametric settings are shown in Figure 5.13 and Figure 5.14. To illustrate the spectrum difference between the lossless system and normal system in case C., Figure 5.13 is plotted with $\alpha = 1$ and Figure 5.14 is plotted with $\alpha = 0.97$. To illustrate the spectrum difference between different value of $\Delta\theta$, each of Figure 5.13 and Figure 5.14 is plotted with three sub-figures with $\Delta\theta = -\pi/5, 0$ & $\pi/5$.

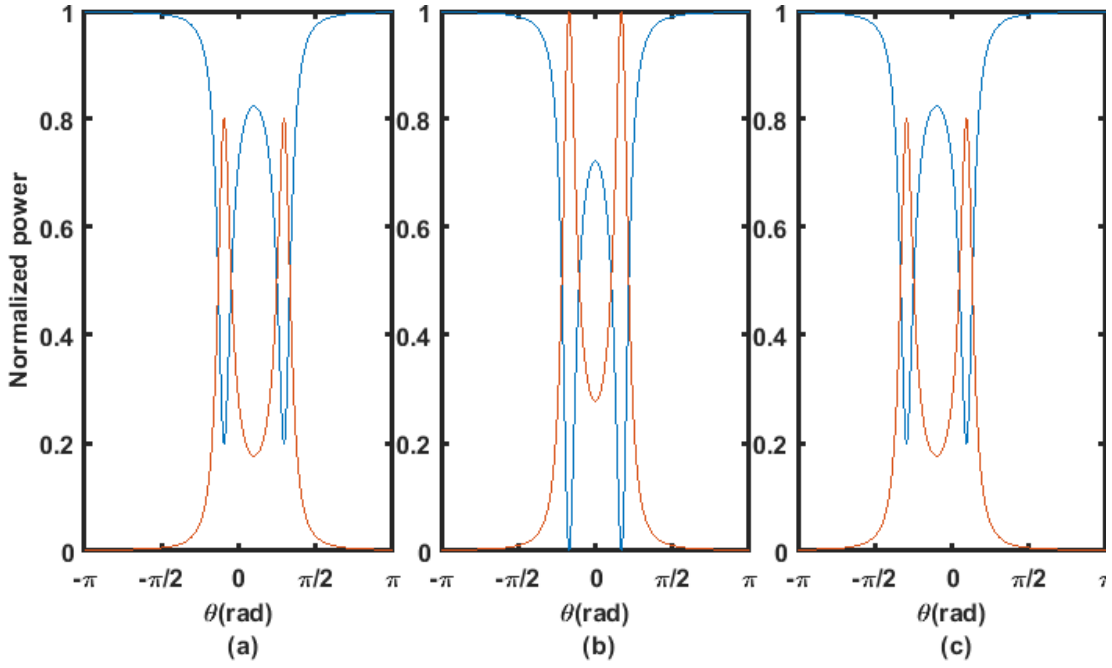

FIGURE 5.13: Power spectrum from $|G_D|^2$ (red curve) and $|G_T|^2$ (blue curve). (a). $\alpha = 1$, $t = 0.85$ and $\Delta\theta = -\pi/5$; (b). $\alpha = 1$, $t = 0.85$ and $\Delta\theta = 0$; (c). $\alpha = 1$, $t = 0.85$ and $\Delta\theta = \pi/5$.

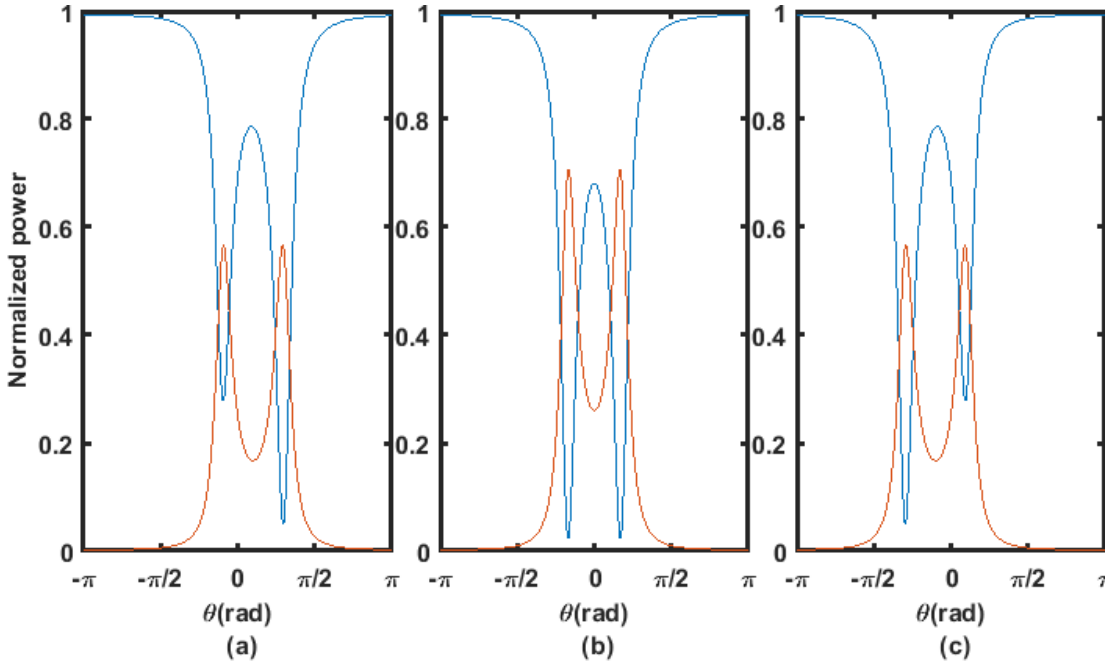

FIGURE 5.14: Power spectrum from $|G_D|^2$ (red curve) and $|G_T|^2$ (blue curve). (a). $\alpha = 0.97$, $t = 0.85$ and $\Delta\theta = -\pi/5$; (b). $\alpha = 0.97$, $t = 0.85$ and $\Delta\theta = 0$; (c). $\alpha = 0.97$, $t = 0.85$ and $\Delta\theta = \pi/5$.

From Figure 5.13, all three plots show the feature of the lossless system described in Equation 5.84 and Equation 5.69. The resonant peaks is symmetric to $\theta = -\Delta\theta/2$. By comparing Figure 5.13.(a)., (b). and (c)., critical coupling can be achieved only when $\Delta t = 0$ (Case A).

From $\alpha = 0.97$ shown in Figure 5.14, the magnitude of resonant peaks from $|G_T|^2$ are different and two resonant phase are not strictly symmetric to $\theta = -\Delta\theta/2$. When $\Delta\theta < 0$, peaks from $|G_T|^2$ with negative resonant phase has smaller resonant magnitude than peaks with positive resonant phase. When $\Delta\theta > 0$, peaks from $|G_T|^2$ with negative resonant phase has larger resonant magnitude than peaks with positive resonant phase. However, the resonant peaks from $|G_D|^2$ are still symmetric to $\theta = -\Delta\theta/2$ as described in Equation 5.78.

5.3.5 Condition D. System with coupling and phase perturbation

Based on the system constructed from $t_1 \neq t_2$ and $\theta_1 \neq \theta_2$, there are no analytical solutions for $d(|\Delta|^2)/d(\theta) = 0$ and $d(|\Delta_T|^2)/d(\theta) = 0$. The resonant peaks of $|G_T|^2$ are no longer symmetric to $\Delta\theta/2$, so as to $|G_T|^2$. When $\Delta\theta$ is small, θ_d and θ_n can be approximated as:

$$\theta_d \approx 2m\pi - \frac{\Delta\theta}{2} \pm \left|\arccos\left[\frac{(t_1+t_2)[t_1t_2\alpha^2(1-\gamma_2)+1]}{4\alpha t_1(1-\gamma_2)}\cos\left(\frac{\Delta\theta}{2}\right)\right]\right|, m \in Z \tag{5.85}$$

and

$$\theta_n \approx 2m\pi - \frac{\Delta\theta}{2} \pm \left|\arccos\left[\frac{(1-\gamma_1+t_1t_2)[\kappa_1^2t_2\alpha(\kappa_2^2+t_2^2\alpha)+t_1^2t_2\alpha^2(1-\gamma_2)+t_1]}{4[\kappa_1^2(\kappa_2^2+t_2^2\alpha^2)+t_1^2\alpha(1-\gamma_2)]t_1}\cos\left(\frac{\Delta\theta}{2}\right)\right]\right|, m \in Z \tag{5.86}$$

If the system is lossless ($\alpha = 1, \gamma = 0$),

$$\theta_n = \theta_d \approx 2m\pi - \frac{\Delta\theta}{2} \pm \left|\arccos\left(\frac{(1+t_1t_2)(t_1+t_2)}{4t_1}\cos\left(\frac{\Delta\theta}{2}\right)\right)\right|, m \in Z \tag{5.87}$$

In this case, $|G_T|^2$ and $|G_D|^2$ can be regarded as mirror images of each other as shown in Equation 5.69.

The power spectrum within single period for both $|G_D|^2$ and $|G_T|^2$ in case D. with different parametric settings are shown in Figure 5.15 and Figure 5.16. To illustrate the spectrum difference between the lossless system and normal system in case D., Figure 5.15 and Figure 5.16.(a). are plotted with $\alpha = 1$. Figure 5.16.(b). and Figure 5.16.(c). is plotted with $\alpha = 0.97$. To illustrate the spectrum difference between different value of $\Delta\theta$ and Δt, Figure 5.15 and Figure 5.16 are plotted with $\Delta\theta = -\pi/5, \pi/5$ and $\Delta t = -0.1, 0.1$.

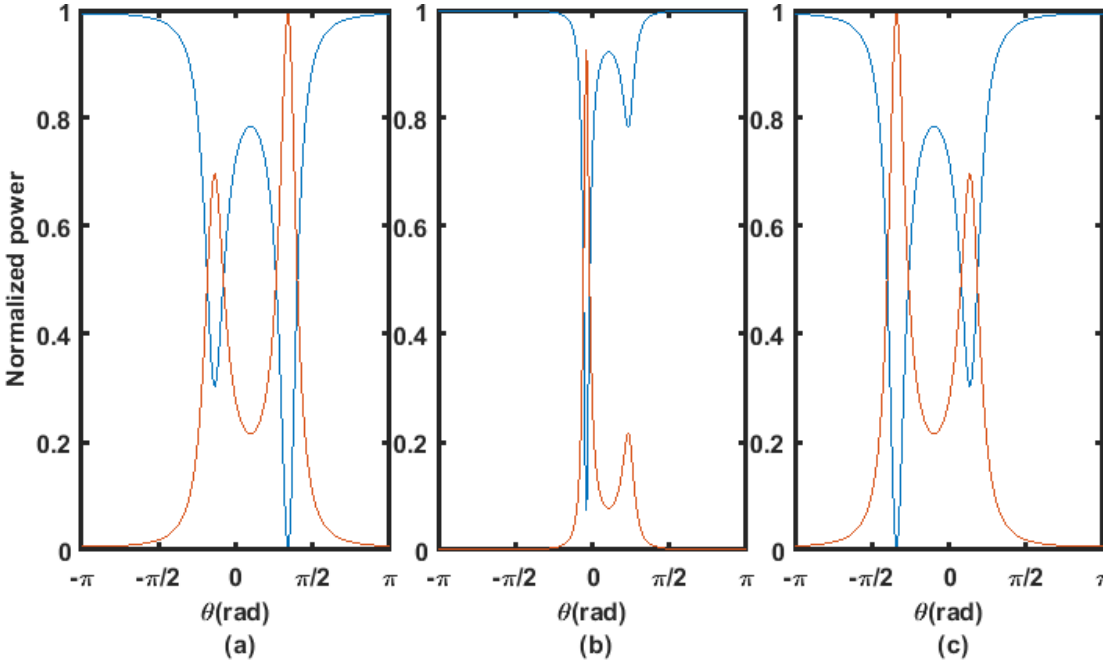

FIGURE 5.15: Power spectrum from $|G_D|^2$ (red curve) and $|G_T|^2$ (blue curve). (a). $\alpha = 1$, $t_1 = 0.85$, $t_2 = 0.75$ and $\Delta\theta = -\pi/5$; (b). $\alpha = 1$, $t_1 = 0.85$, $t_2 = 0.95$ and $\Delta\theta = -\pi/5$; (c). $\alpha = 1$, $t_1 = 0.85$, $t_2 = 0.75$ and $\Delta\theta = \pi/5$.

From Figure 5.15 and Figure 5.16.(a)., all four plots show the feature of the lossless system described in Equation 5.69. In both Figure 5.15 and Figure 5.16, the magnitude of resonant peaks from $|G_T|^2$ or $|G_T|^2$ are different and two resonant phase are not strictly

symmetric to $\theta = -\Delta\theta/2$. The magnitude of resonant peaks from $|G_D|^2$ or $|G_T|^2$ are no longer the same. When $t_1 > t_2$ and $\Delta\theta < 0$, peaks from $|G_D|^2$ with negative resonant phase has smaller resonant magnitude than peaks with positive resonant phase and this is opposite for peaks from $|G_T|^2$. The inverse condition of t and $\Delta\theta$ leads to inverse shape of $|G_D|^2$ and $|G_T|^2$.

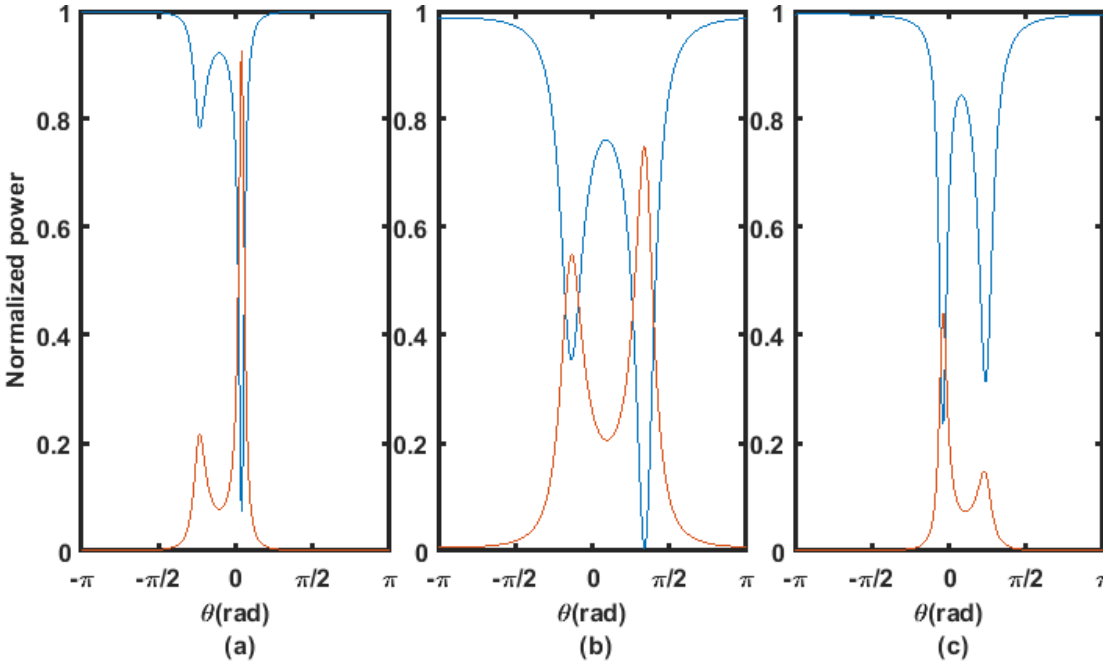

FIGURE 5.16: Power spectrum from $|G_D|^2$ (red curve) and $|G_T|^2$ (blue curve). (a). $\alpha = 1$, $t_1 = 0.85$, $t_2 = 0.95$ and $\Delta\theta = \pi/5$; (b). $\alpha = 0.97$, $t_1 = 0.85$, $t_2 = 0.75$ and $\Delta\theta = -\pi/5$; (c). $\alpha = 0.97$, $t_1 = 0.85$, $t_2 = 0.95$ and $\Delta\theta = -\pi/5$.

By comparing Figure 5.15.(a). and (b). with Figure 5.16.(b). and (c)., the loss in the system makes resonances weaker and $|G_D|^2$ is more sensitive to the loss compared with $|G_T|^2$.

5.3.6 General feature of the power transmission under phase and coupling perturbations

A qualitative analysis about the resonant peaks in different loss, phase and coupling conditions are shown in Table 5.1. This table is a summary from Figure 5.9 to Figure 5.16.

From Table 5.1, $|G_D|^2$ can be precisely solved in configurations A., B. and C., while precise solution of $|G_T|^2$ only exists when system is lossless ($|G_T|^2 + |G_D|^2 = 1$). Among the four configurations, the precise expressions of the resonant power transmission and corresponding phases of $|G_D|^2$ only exist when the magnitude of the two resonant peaks from $|G_D|^2$ are the same. $|G_T|^2$ can be solved numerically only unless the system is lossless.

TABLE 5.1: Summary of spectrum of $|G_D|^2$ and $|G_T|^2$ under different configurations. $\Delta\theta = \theta_1 - \theta_2$; $\Delta t = t_1 - t_2$; $\Delta P_D = P_D^- - P_D^+$; $\Delta P_T = P_T^- - P_T^+$. Column labelled with 'Analytical $P_D^{\pm}$' or 'Analytical $P_T^{\pm}$' indicates whether analytical solution existed for resonant peaks from $|G_D|^2$ or $|G_D|^2$, respectively.

Configuration	α	$\Delta\theta$	Δt	ΔP_D	ΔP_T	**Analytical** $P_D^{\pm}$	**Analytical** $P_T^{\pm}$
A	1	0	0	0	0	✓	✓
	0.97	0	0	0	0	✓	×
B	1	0	>0	0	0	✓	✓
	1	0	<0	0	0	✓	✓
	0.97	0	>0	0	0	✓	×
	0.97	0	<0	0	0	✓	×
C	1	<0	0	0	0	✓	✓
	1	>0	0	0	0	✓	✓
	0.97	<0	0	0	>0	✓	×
	0.97	>0	0	0	<0	✓	×
D	1	<0	>0	<0	>0	×	×
	1	<0	<0	>0	<0	×	×
	1	>0	>0	>0	<0	×	×
	1	>0	<0	<0	>0	×	×
	0.97	<0	>0	<0	>0	×	×
	0.97	<0	<0	>0	<0	×	×
	0.97	>0	>0	<0	>0	×	×
	0.97	>0	<0	>0	<0	×	×

If the system is lossless ($\alpha = 1$ and $\gamma = 0$), for any configurations, $|G_D|^2$ and $|G_T|^2$ have the same resonant phase ($\theta_d = \theta_b$), and they can be regarded as mirror image of each other ($|G_D|^2 + |G_T|^2 = 1$). In configurations A., B. and C. (partial symmetry breaking), the two resonant peaks from $|G_D|^2$ or $|G_T|^2$ have the same power transmission. However, in configuration D. (all symmetry breaking) the transmission of the two resonant peaks is different.

For a system with loss in configurations C. and D., the transmission of the resonant peaks from $|G_D|^2$ or $|G_T|^2$ are different depends on the specific relation between the phase (θ_1, θ_2) and coupling coefficient (t_1, t_2).

Systems in configurations B., C. and D. can be applied as sensors if the perturbation of measurand can be coupled to the perturbation in phase or coupling coefficient. The different resonant magnitude of two peaks makes it possible to be applied as an optical mode-localizer that evaluates the coupling and phase symmetry by analysing the modal phases and powers in the spectrum. The system with phase perturbation is better than other configurations since the asymmetric mode-splitting in $|G_T|^2$ and the symmetric mode-splitting in $|G_D|^2$ provide good sensitivity and noise immunity at the same time. The analytical solutions for resonant peaks in $|G_D|^2$ make the system easy to be analyzed from the measurement.

5.3.7 Output characteristics of the sensing based on phase perturbation

In practice, thermal-optic effect (Section 5.2.2) and dispersion will affect resonant wavelength and magnitude of resonant peaks in silicon photonics devices, respectively. For ring resonators, the spectrum shift caused by the thermal-optic effect is not negligible as a result of the enhanced circulating power in the ring. Dispersion in the waveguide will influence the resonant wavelength in the spectrum as described in Equation 5.31 as well. Meanwhile, the magnitude of resonant peaks will not be affected by the thermal-optic effect and dispersion, which means the output characteristics defined by resonant modal power ratio will not be affected by the thermal-optic effect and dispersion.

Here the circuitry constructed under configuration C. is chosen to be the core sensing element. In configuration C. the magnitude of the resonant peaks of the sensing element is altered by the change of the phase change in one of the resonators. Both symmetric mode-splitting from $|G_D|^2$ and asymmetric mode-splitting from $|G_T|^2$ in the spectrum are helpful to simplify the post-analysis and achieve high sensitivity at the same time. The precise solutions of resonance in $|G_D|^2$ allow the propagation loss α to be measured from the magnitude of resonant peaks. The magnitude of the left and right resonant peaks from $|G_T|^2$ are represented by P_T^- and P_T^+ within $-\pi < \theta < \pi$. In the power-phase spectrum, respectively. The magnitude of the resonant peaks from $|G_D|^2$ is represented by $P_D^{\pm}$. The output of the sensing element is evaluated by the power ratio P_T^- / P_T^+. The characteristics of the circuitry with $t = 0.75$ in the range of $|\Delta\theta| < \pi$ are shown in Figure 5.17 and Figure 5.18.

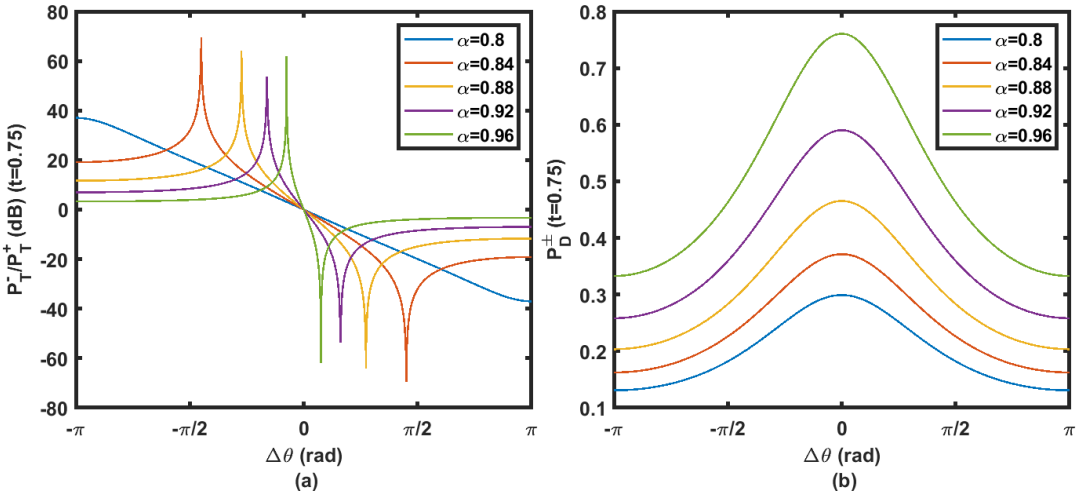

FIGURE 5.17: (a). Power ratio (dB) between resonant peaks from $|G_T|^2$ at different values of α; (b). Normalised magnitude of resonant peaks from $|G_D|^2$.

In Figure 5.17 (a)., the power ratio curve is symmetrical about the origin point. Impressive values of power ratio between 50 to 70 dB are obtained from the local maximum of the curve. The accuracy of the calculated extreme values on the power ratio curves is hardly affected by numerical errors. In practice, the recognition of the local maximum

and minimum of the curve are closely related to noise floor from the environment (see Section 5.3.9). It can be observed that the propagation loss coefficient α closely relates to the curve shape of power ratio P_T^- / P_T^+. The local maximum and minimum approaches to each other when the α becomes larger. The system sensitivity (slope of output) is magnified in the region between the local maximum and minimum, and it is further increased by larger α. With different values of t and α, the curve of power ratio can be negatively correlated to the phase change applied on the ring or experiencing a local maximum and minimum when phase change is negative and positive, respectively. This feature brings a problem in identifying the phase perturbation on the ring from the measured power ratio since a single value of power ratio might be corresponding to two values of the phase perturbation.

For $P_D^{\pm}$ shown in Figure 5.17 (b)., curves are symmetrical to $\Delta\theta = 0$. $P_D^{\pm}$ can be used to solve the value of α from the analytical solution described in Equation 5.78 and Equation 5.79. Moreover, $P_D^{\pm}$ is monotonic in the region of $-\pi < \Delta\theta < 0$ or $0 < \Delta\theta < \pi$, so the combination of P_T^- / P_T^+ and $P_D^{\pm}$ is necessary to obtain the right value of phase perturbation.

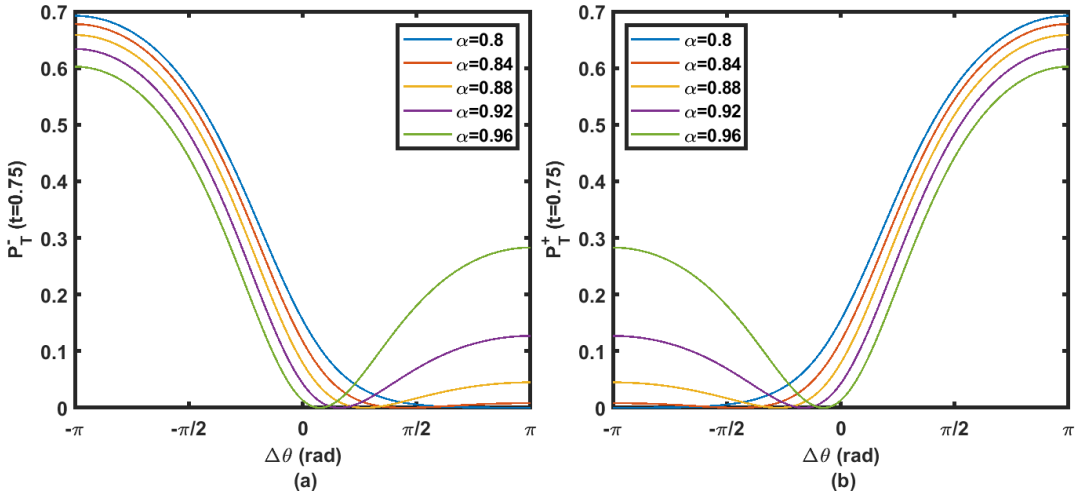

FIGURE 5.18: (a). Normalized magnitude of P_T^- under α from 0.8 to 0.96; (b). Normalised magnitude of P_T^+ under α from 0.8 to 0.96.

From Figure 5.18 (a). and (b)., one local minimum can be found on each curve of P_T^- and P_T^+. For a specific combination of t and α, P_T^- and P_T^+ are symmetrical to $\Delta\theta = 0$. Local maximums and minimums in Figure 5.17 (a). are the result from local minimums on the P_T^- and P_T^+ curves.

When $|\Delta\theta| > \pi$, one of the resonant peaks is shifted out from the observed phase range. In this case, the P_T^- or P_T^+ from other period enters the observed phase range and relabelled as P_T^+ or P_T^-, while the previous P_T^+ or P_T^- will be relabelled as P_T^- or P_T^+ following the definition of P_T^- and P_T^+. The exchange of P_T^- and P_T^+ cause a sudden drop/raise can be observed at $\Delta\theta = \pm\pi$ in Figure 5.17 (a). and Figure 5.18.

The power ratio P_T^- / P_T^+ and normalised power $P_D^{\pm}$ at different t are shown in Figure 5.19 and Figure 5.20.

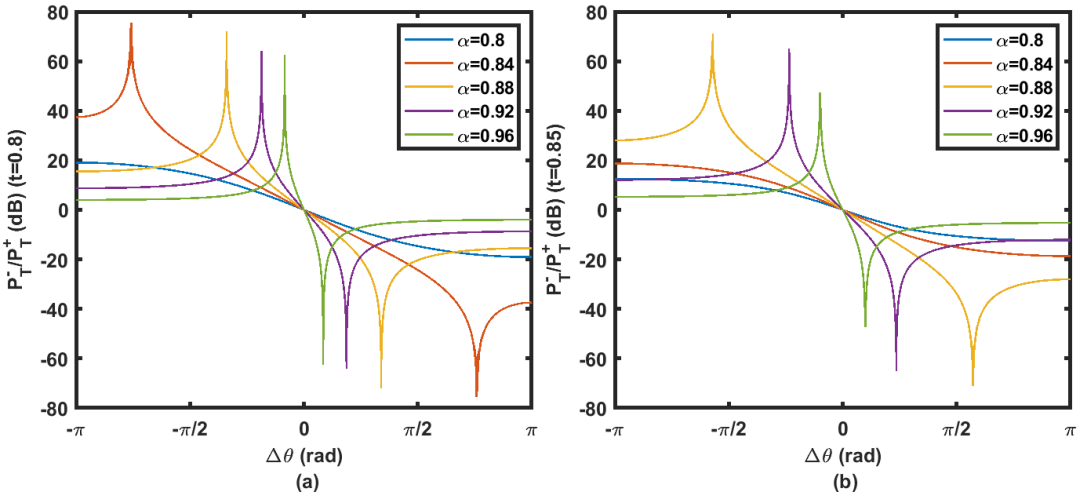

FIGURE 5.19: Power ratio from P_T^- and P_T^+ at α from 0.8 to 0.96. (a). Power ratio (dB) ($t = 0.8$); (b). Power ratio (dB) ($t = 0.85$).

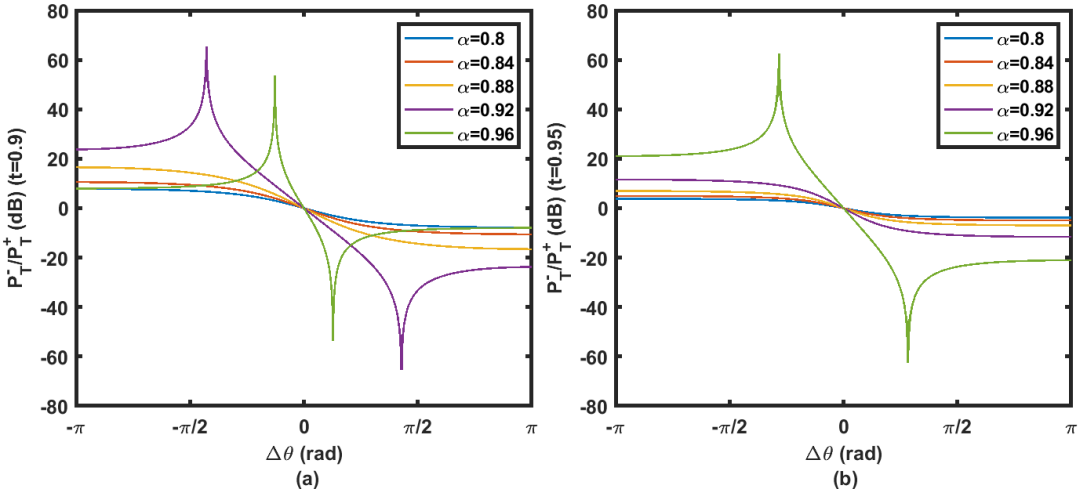

FIGURE 5.20: Power ratio from P_T^- and P_T^+ at α from 0.8 to 0.96. (a). Power ratio (dB) ($t = 0.9$); (b). Power ratio (dB) ($t = 0.95$).

By observing the power ratio P_T^- / P_T^+ under different coupling coefficients from $t = 0.75$ to $t = 0.95$, local maximum and minimum on the curve disappear when the coupling coefficient is high for a fixed value of loss coefficient. The system sensitivity can be adjusted according to the specific requirement on the range of $\Delta\theta$ and sensitivity.

5.3.8 Model validation by applying Lumerical interconnection module

The transmission spectrum analysis of the coupled ring resonators can also be carried out by the Lumerical interconnection module, which is capable of analyzing complicated photonic circuitry, including ring resonators. The theoretical calculation according to the signal flow graph method can be examined and validated by the simulation

result. In order to compare the theoretical model with the simulation result, a conversion between the phase change and effective index change is necessary. If the dispersion is not involved in the consideration, the conversion can be expressed as:

$$\Delta\theta = \frac{2\pi L_0}{\lambda}\Delta n \tag{5.88}$$

From Equation 5.88, the phase perturbation ($\Delta\theta$) is not a constant in the spectrum with a constant index change (Δn), so the curve of the power ratio (P_T^- / P_T^+) versus phase perturbation must be different from the curve of power ratio versus index change (Δn). The parameters of the model used for theory validation are shown in Table 5.2.

TABLE 5.2: Model parameters chosen for theory validation

Case	n_{eff}	$L_0(\mu m)$	α	t	Loss $(1/m)$
C	1.8	280	0.96	0.9	280

The propagation loss is calculated based on α and L_0. Please be noticed that t in the table is the coupling coefficient for the electrical field and the power coupling coefficient is t^2. The detail of the system construction in the Lumerical user interface is shown in Figure 5.21.

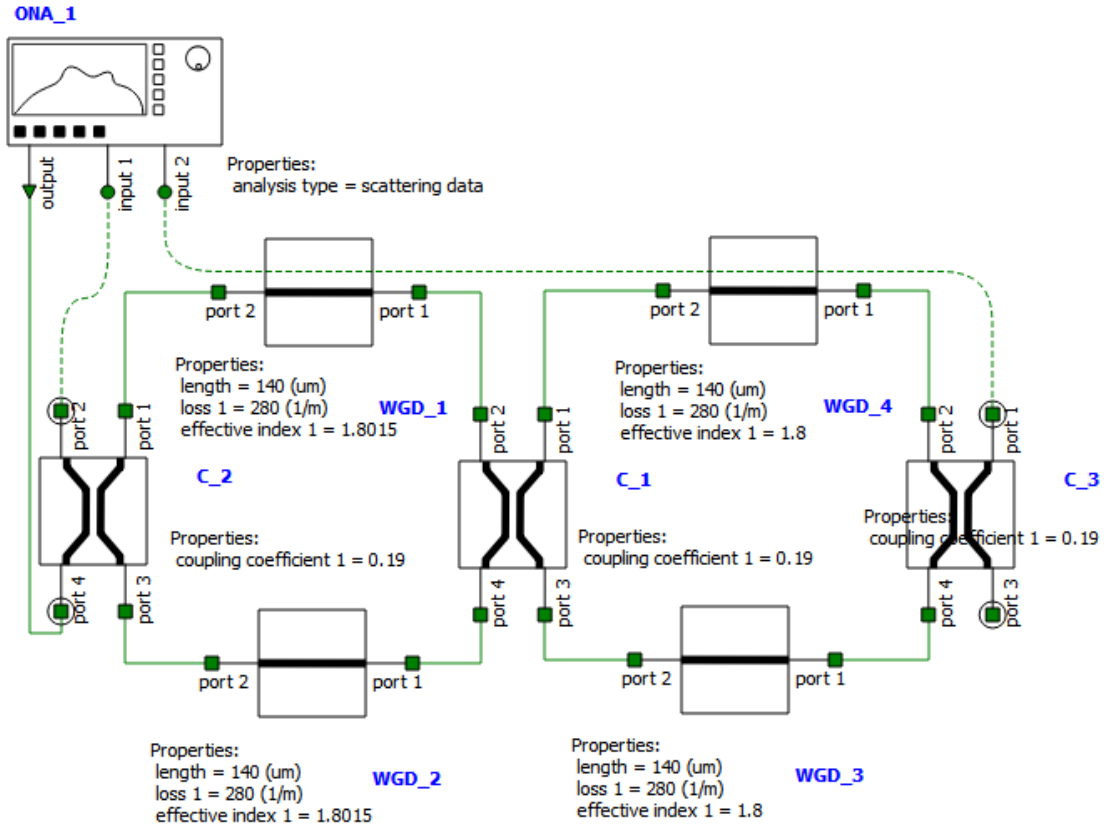

FIGURE 5.21: System construction in the schematic interface of the Lumerical interconnection module.

From Figure 5.21, it can be seen that ideal couplers and waveguides components are

selected to construct the system in order to be consistent with the theoretical model. The calculation result from the signal flow graph and Lumerical simulation are shown in Figure 5.22. The calculated spectrum from signal flow graph and Lumerical simu-

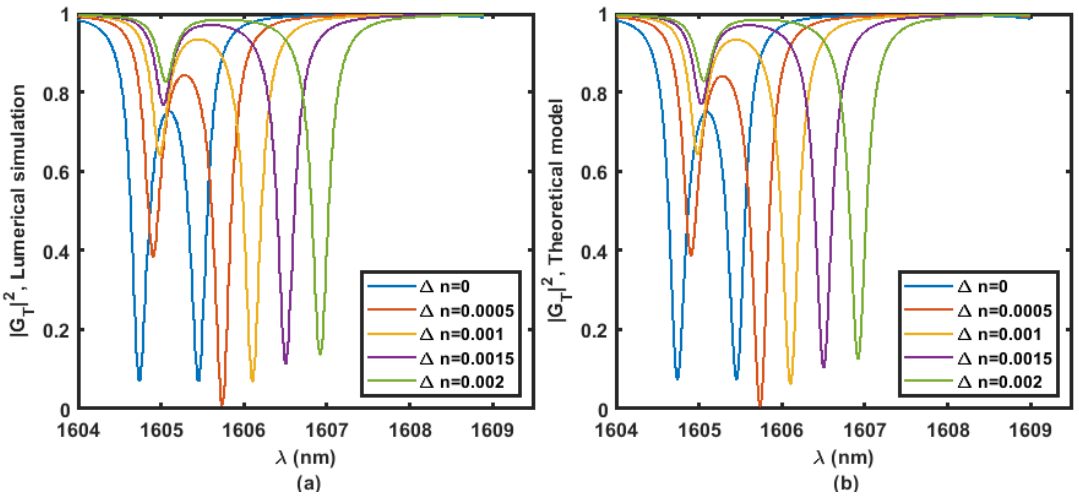

FIGURE 5.22: $|G_T|^2$ from $\alpha = 0.96$ and $t = 0.9$ calculated by theory model (Matlab) and Lumerical interconnection module from Δn= 0 to 0.002. (a). Lumerical simulation; (b). Theory.

lation shows almost no visible difference in resonant frequency and amplitude in Figure 5.22. The minor difference between signal flow graph and Lumerical simulation can be evaluated by comparing the power ratio (P_T^- / P_T^+) from resonant peaks shown in Figure 5.23.

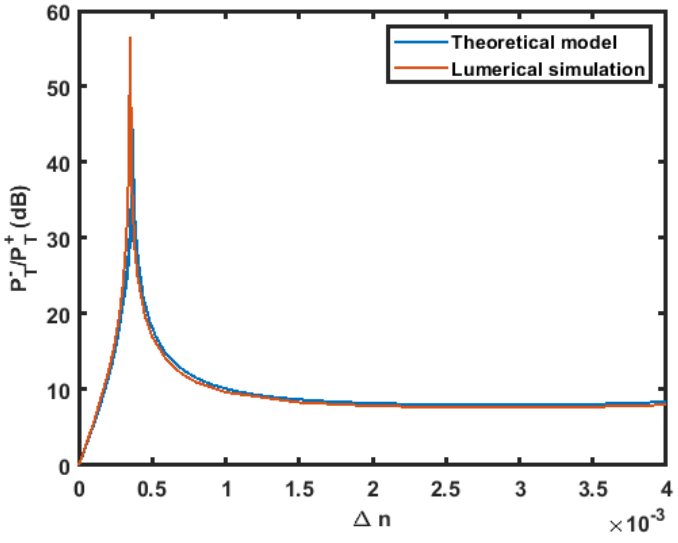

FIGURE 5.23: Power ratio (dB) from P_T^- and P_T^+ at Δn from 0 to 0.004 (0 to π).

There is a slight difference between curves in Figure 5.23 except the region near the peak of the power ratio. Generally, the analysis from both methods is consistent with

each other. The simulation result appears to be less affected by the numerical errors during the calculation rather than the calculation result from Matlab. The Lumerical interconnect module simulates the light travelling in the given photonic circuitry until the energy in the circuitry attenuates to a preset value (approaching zero). The process allows the calculation to be carried out with less numerical approximation than the derived transfer function that contains few exponential terms (Taylor expansion required). This unique feature of the Lumerical interconnection can be understood as an advantage when high accuracy analysis is required in a complex photonic circuitry.

5.3.9 Mode aliasing and noise immunity in configuration C.

As described in Section 5.1.1, the mode aliasing effect set a 'sensing dead zone' in coupled ring circuitry as well. Unlike mechanical mode localized sensor, the mode aliasing only happens when the sensor is constructed with some specific combination of t and α. Recalling the modal phase of $|G_D|^2$ in configuration C.:

$$\theta_d = 2m\pi - \frac{\Delta\theta}{2} \pm \left|\arccos\left[\left(\frac{t^2\alpha^2(1-\gamma)+1}{2\alpha(1-\gamma)}\right)\cos\left(\frac{\Delta\theta}{2}\right)\right]\right|, m \in Z \tag{5.78}$$

A small phase difference between two resonant modes is obtained from high t and low α. Therefore, the mode aliasing can be avoided by selecting a suitable value of t and α within the whole spectrum. However, the 'sensing dead zone' still exists when any one of P_T^- and P_T^+ approaches zero (local maximum and minimum on the power ratio plot), where the modal power is drowning in the noise floor since one of the modal powers is undetectable. This kind of 'sensing dead zone' can be avoided by selecting a suitable value of t and α to eliminate the local maximum and minimum of the power ratio. Both of the modal power can be enlarged to obtain good noise immunity against noise floor with a cost of lower power ratio and sensitivity such as t and α setting in Figure 5.20. The corresponding P_T^- and P_T^+ are shown in Figure 5.24. This plot illustrates that systems constructed from high t and low α can tolerate high noise during the sensing. The system with $t = 0.95$ and $\alpha = 0.8$ have a normalized power of 0.4 that relax the SNR requirement of the post-processing unit to recognized the resonances. Meanwhile, a low power ratio of about 3 dB is obtained. An appropriate combination of t and α needs to be considered to achieve the balance between the sensitivity, mode-aliasing and noise immunity of the sensor.

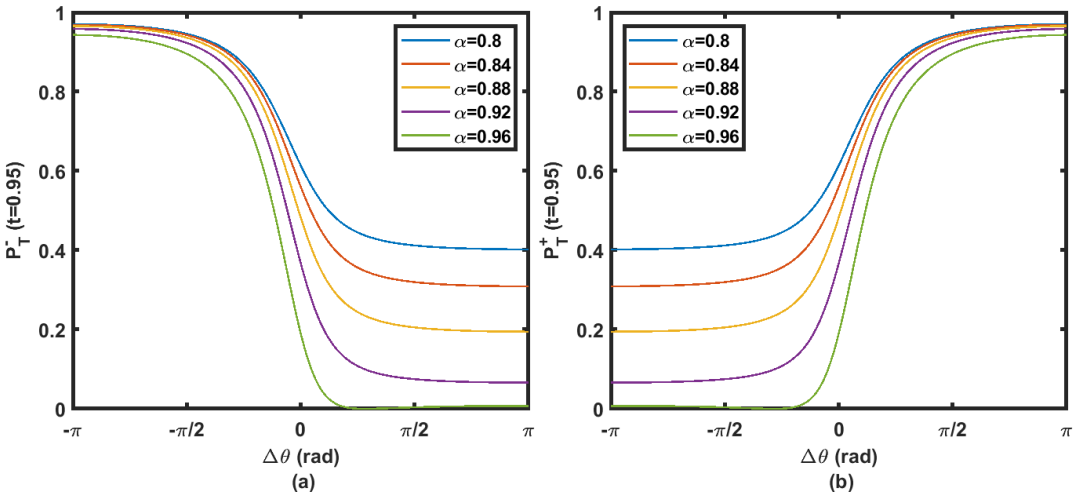

FIGURE 5.24: (a). Normalized magnitude of P_T^- under α from 0.8 to 0.96; (b). Normalised magnitude of P_T^+ under α from 0.8 to 0.96.

5.3.10 Signal-to-noise ratio and dual-channel calibration in configuration C.

The detectable value of the maximum and minimum power ratio in the system is determined by SNR from $|G_T|^2$ and $|G_D|^2$. Following the definition of SNR:

$$\mathrm{SNR_T} = \frac{P_T^-}{P_T^+} / \frac{P_n^-}{P_n^+} \tag{5.89}$$

$$\mathrm{SNR_D} = 1 / \frac{P_n^-}{P_n^+} \tag{5.90}$$

where P_n^- and P_n^+ represent the noise on the resonant peaks. From Equation 5.89, $\mathrm{SNR_T}$ is getting worse when $P_T^- < P_T^+$, while Equation 5.90 indicates that $\mathrm{SNR_D}$ only depends on the noise power ratio. The combination of the resonant peaks in $|G_T|^2$ and $|G_D|^2$ can improve the SNR of the sensor when $P_T^- < P_T^+$. This SNR compensation technique is the unique feature of the optical mode-localization rather than a mechanical one. The measured power of the two resonant peaks from $|G_T|^2$ and $|G_D|^2$ are expressed as:

$$P_{Tm}^{\pm} = P_T^{\pm} + P_n^{\pm} \tag{5.91}$$

$$P_{Dm}^{\pm} = P_D^{\pm} + P_n^{\pm} \tag{5.92}$$

where $P_{Tm}^{\pm}$ and $P_{Dm}^{\pm}$ represent the measured power of resonant peaks in $|G_T|^2$ and $|G_D|^2$, respectively. By resolving the measured resonant peaks in $|G_T|^2$ and $|G_D|^2$ separately, two different phase perturbation values can be solved out. These two values define a range where the noiseless phase perturbation locates, thus the sensing accuracy is improved. A real-time measurement error is quantified as well.

Here we name this unique technique dual-channel calibration. This dual-channel calibration of the optical mode-localization sensing mechanism makes it better than the

mechanical mode-localization sensing mechanism in a noisy environment.

5.4 Sensitivity analysis of the NOEMS mode-localized electrometer

An electrometer can be constructed from the optical mode-localization sensing element in configuration C. The structure of the electrometer is illustrated in Figure 5.25. A mode converter is necessary if the optical mode of the waveguide and phase shifter is different.

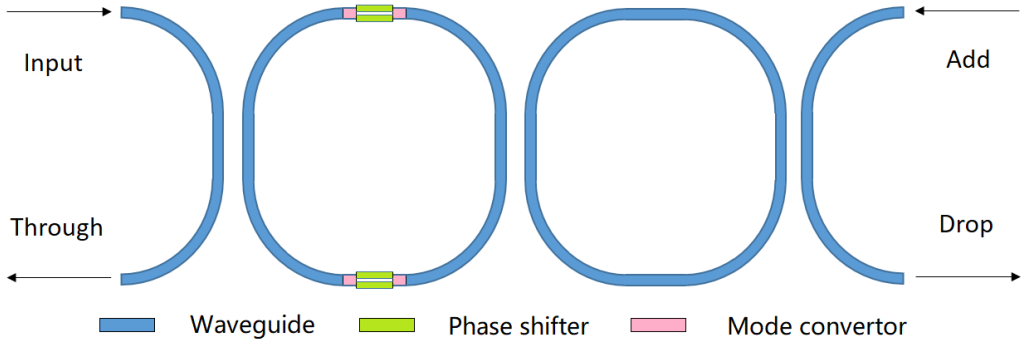

FIGURE 5.25: Optical phase symmetry scale constructed based on Case C.

By applying a NOEMS slot modulator described in Section 4.6 (fully suspended conducted configuration) as phase shifter, the charge/electrical potential between electrostatic actuators will be detected by optical parametric symmetry scale from its corresponding index and phase change by electrostatic actuation.

By cascading the NOEMS slot phase shifters into the phase symmetry scale, charges can be detected by evaluating modal power ratio from through port. The sensing sensitivity of the electrometer is described by the slope of the modal power ratio expressed by:

$$Sensitivity = \frac{\partial(P_T^- / P_T^+)}{\partial\, Q} \tag{5.93}$$

The measurement range of the charge depends on pull-in voltage and $Q/\Delta\theta$ ratio from the phase shifter and the measurement range of the symmetry scale ($-\pi < \Delta\theta < \pi$). If $t = 0.75$ and $L = 30\ \mu m$, the relationship between modal power ratio, charge and phase change obtained by applying conducted slot modulator are shown in Figure 5.26.

Compared with the output from the coupled rings with phase perturbation, the nonlinear $Q/\Delta\theta$ response produced from slot modulator induces worse linearity in Q/PR curves. The shapes of the curve are independent of the suspended length of the slot modulator, but the maximum number of detectable electrons is not. The maximum number of detectable electrons at different suspended lengths are shown in Table 5.3.

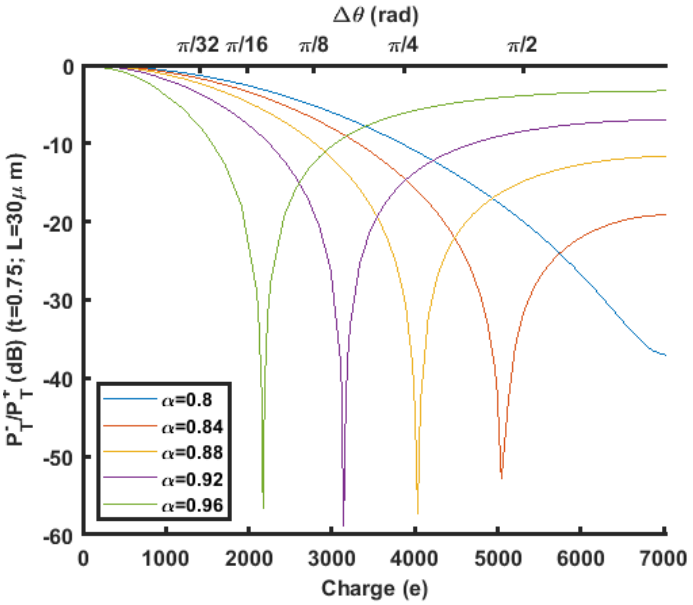

FIGURE 5.26: Electrometer output (power ratio/charge and phase change) when α from 0.8 to 0.96

TABLE 5.3: Maximum detectable electron numbers and its corresponding charge (fC) at different suspended lengths of the conducted fully suspended slot modulator

$L(\mu m)$	**5**	**10**	**15**	**20**	**25**	**30**	**35**	**40**	**45**	**50**
$Q(e)$	56663	28533	18119	12451	9158	7029	5508	4380	3414	2058
$Q(fC)$	9.07	4.57	2.90	2.00	1.47	1.13	0.882	0.702	0.547	0.330

From Table 5.3, the sensing range of the electrometer is small. The design of the slot modulator needs to be optimized to achieve the larger detecting range. For the electrometer described in this section, the sensitivities are different in every point on a single curve and different in curves with different α. In this case, the minimum sensitivity of a curve at $\Delta\theta = 0$ is evaluated in order to compare the sensitivity from a curve to the other curves. The minimum sensitivity of at different L and α are shown in Figure 5.27.

These minimum sensitivities in Figure 5.27 are outstanding compared with mechanical mode-localized electrometers in [68] with a measured linearity sensitivity of 0.0227 fC^{-1}. It gives the theoretical support that a state-of-art ultra-high sensitivity electrometer is possible to be constructed on coupled ring resonators and conducted slot modulator. The sensitivity is optimized by at least 17.6 times by comparing the largest sensitivity of 0.4 fC^{-1} in Figure 5.27 and the measured linearity sensitivity of 0.0227 fC^{-1} in [68].

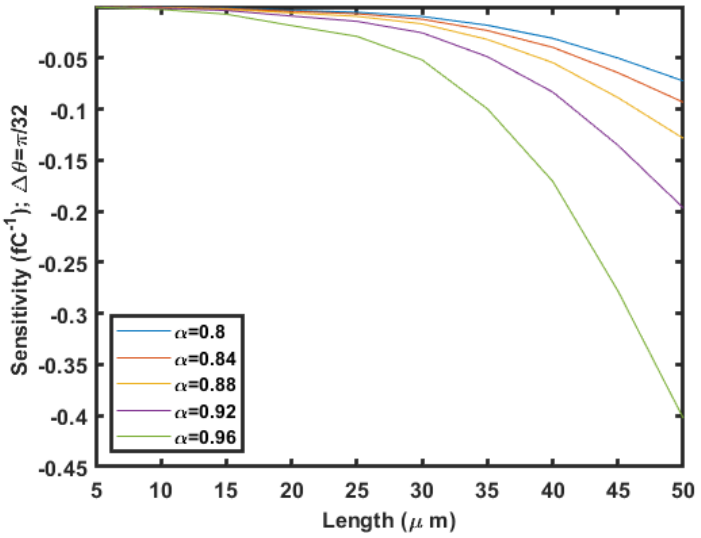

FIGURE 5.27: Electrometer output (power ratio/charge and phase change) when α from 0.8 to 0.96

5.5 Chapter conclusions

The basics of the ring resonators and mechanical mode-localization sensing are reviewed. The theoretical model of optical mode-localized sensing realized by coupled resonator optical waveguide system (CROW) are established. Here we use feedback theory (also referred to as Mason's rule), which makes the analytical derivation easier, to analyze the coupled ring resonators for optical mode localized sensing. The model is validated by simulation (Lumerical interconnection). The mode-localized achieved by index and coupling perturbation are analyzed in four different configurations. Among these configurations, dispersive sensing accomplished by detecting the index perturbation is considered the best choice for optical mode-localized electrometer. The output characterization, signal-to-noise ratio, mode aliasing and dual-channel calibration feature of the optical mode localizer are analysed in detail.

The optical mode-localized electrometer can be constructed by dispersive mode localizer with an electro-optical transducer that transfer the change in the number of electrons to effective index. It is achieved by suspended slot modulator analyzed in the previous chapter. We proved that ultra-high sensitivity can be obtained from optical mode-localized electrometer more than mechanical mode-localized electrometer. The sensitivity is optimized at least 17.6 times by optical mode localized electrometer compared with mechanical one (0.0227 fC^{-1}).

Chapter 6

Fabrication flow development and analysis

To investigate the feasibility of fabricating optical mode localized electrometer based on the specific fabrication conditions of the available equipment, fabrication flow development and analysis is carried out with originally designed test devices dedicated to extracting parameters for electrometer design. The fabrication flow is designed with reference to the mature fabrication process from the silicon photonics group except for HF vapour etching that releases the suspended structure on chip. The content in this chapter is an illustration of the progress of the sample fabrication and problems encountered during the fabrication flow development and analysis. Considering the existing equipment and status of the clean room, there is no means to challenge the state of art semiconductor fabrication technology.

The hybrid of the silicon photonic circuit and NEMS structure not only increases the complexity of the fabrication flow but also brings the concern about the design and fabrication compatibility between the suspended waveguide and waveguide that is mechanically stable. In order to target and solve the problems in the device fabrication capability and measurement, several test runs were carried out with different testing structures. For the electrometer described in Section 5.4, the background noise, loss and coupling are necessary for evaluating the performance of the electrometer. The analysis needs to be carried out by characterizing the spectrum from the specific test devices with the same basic components (waveguide and coupler) to provide references for designing the electrometer.

The fabrication processes for optomechanical devices are investigated in specific fabrication conditions of Zepler Institute (semiconductor fabrication facilities of the University of Southampton). Experimental results showed that the surface roughness during the etching seriously affects the output spectrum with unexpected mode splitting from

waveguide mode reflection in the ring resonator. The propagation loss of the waveguide or addition optical loss is induced by surface roughness that can hardly be considered during the design. The critical damage of the structure or additional optical loss is induced after the structural releasing as well. The performances of the devices are also affected by the quality of the deposited silicon dioxide hard mask and misalignment between layers. As a consequence, dedicated grating and testing structure designs are required to compensate for the fabrication imperfections in the future.

In this chapter, the design of the test devices (Section 6.1) and general fabrication flow (Section 6.2) are described in detail. The discussion of essential fabrication imperfections on specific designs is analyzed according to the scanning electron microscopy (SEM) inspection and output spectrum. The experimental setup and device analysis are described in Section 6.4.

6.1 Test device design

The devices fabricated by test runs aim to find out how the process flow for NOEMS influences the loss and conformity of production in the silicon photonics circuitry. The optical transmission spectrum needs to be obtained from experimental tools to analyse the device. During the test, not only the device but also the features of necessary discrete components are involved in the transmission spectrum, for instance, loss in the fiber connection.

For electrometer design described in Section 5.4, thermo-optic spectrum shift described in Section 5.2.2 and other possible perturbations from fabrication can influence the spectrum. One method for suppressing the unexpected spectrum change except from the NOEMS actuator is to integrate a reference ring nearby the target structure with the NOEMS actuator in the same optical circuits. The general concept of the test device is shown in Figure 6.1. The target ring and reference ring need to be different in their light travel path to avoid the overlap between resonant peaks. By comparing the target resonant peaks and reference resonant peaks, spectrum shift and loss caused by the mechanical actuator is possible to be identified with influences from other factors such as thermo-optic effect, waveguide dispersion and waveguide loss.

The target parameters for designing an electrometer described in Section 5.4 are the propagation loss in the ring (α) and coupling coefficient t. Recalling the extinction ratio of all-pass ring resonator:

$$ER = \left[\frac{(\alpha + t)(1 - \alpha t)}{(\alpha - t)(1 + \alpha t)}\right]^2 \tag{5.32}$$

where we can know that higher extinction ratio only exist around critical coupling ($\alpha = t$). The propagation loss can be estimated by measuring the extinction ratio of a series of devices with ring resonators that only different in coupling. The resonator with the

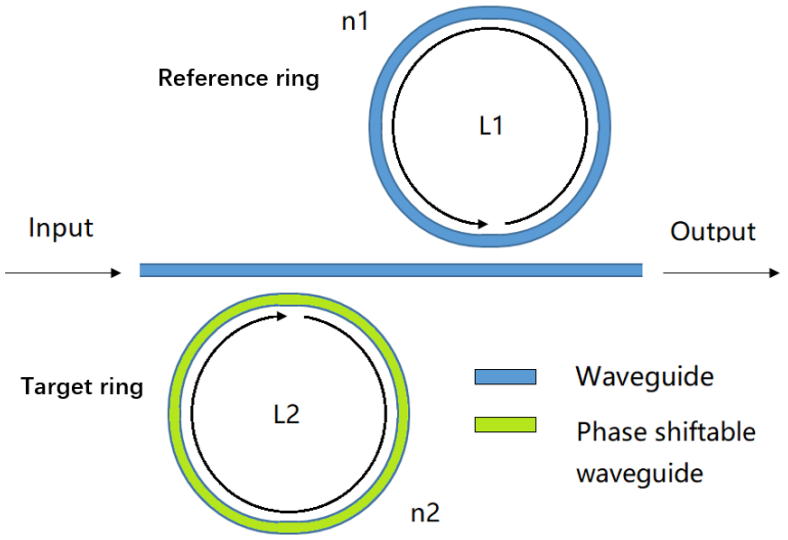

FIGURE 6.1: General concept of the test device for phase shiftable ring resonator. The target ring is the ring that can change the waveguide mode phase by embedding modulators on the ring structure. The reference ring is constructed by waveguide only.

value of α approach the value of t ($\alpha \approx t$) has the most significant extinction ratio. For each device, an extra plain ring resonator with slightly different light travel path length is coupled to the same bus waveguide to produce a reference spectrum to find out the how the phase shifter change the spectrum. To be more specific for NOEMS electrometer, mode converters are necessary for NEMS actuators shown in Figure 6.2. Optical mode conversion is technically essential to achieve suspension and electrical

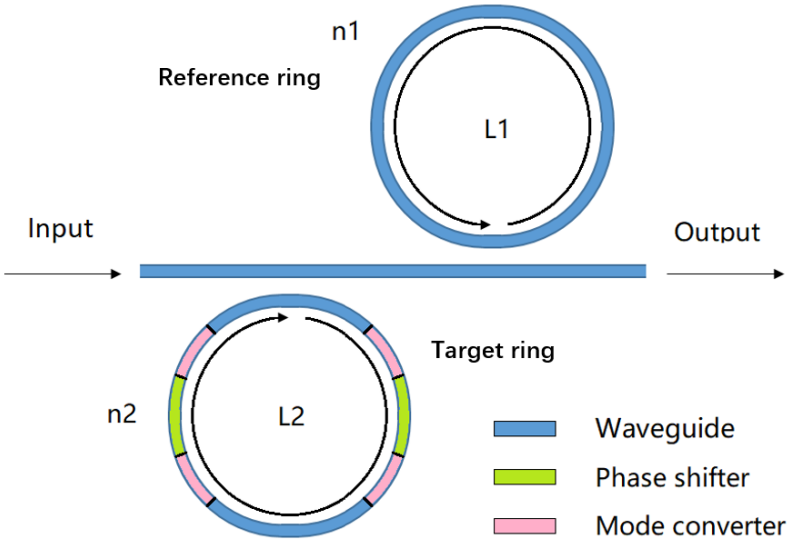

FIGURE 6.2: Concept of the test device for NOEMS electrometer. The construction of the target ring is more realistic with the mode converter to reduce the insertion loss during the waveguide mode conversion.

isolation for electrostatic actuation. There must be geometrical differences between supporting structure and suspending structure so as to their optical mode. In order

to minimize insertion loss between supporting and suspension, the mode converter is necessary. Mode conversion is also required between the standard waveguide and slot waveguide to allow flexibility in device design. To exam the product quality of the slot waveguide, the rings shown in Figure 6.2 are chosen to be constructed from slot waveguide, so mode conversions are required for three optical modes include rib, slot and suspended slot mode. Mode converter between slot and suspended slot mode must consider the electrical insulation between two slot arms for electrometer.

The two specific mask designs following the concept in Figure 6.2 are illustrated in Figure 6.3 and Figure 6.4. The width of the rib waveguide is 450 nm. The width of the slot arms is 280 nm and the gap between the slot arms is 70 nm. In theory, the device design illustrated in Figure 6.3 is capable of extracting the coupling coefficient and propagating loss of the slot waveguide. Device design illustrated in Figure 6.4 is capable of examining the mode converter design for electrometer. In the following contents, the two test device designs in Figure 6.3 and Figure 6.4 are referred to as 'Test design A' and 'Test design B', respectively. In both figures, the light blue and dark blue layers

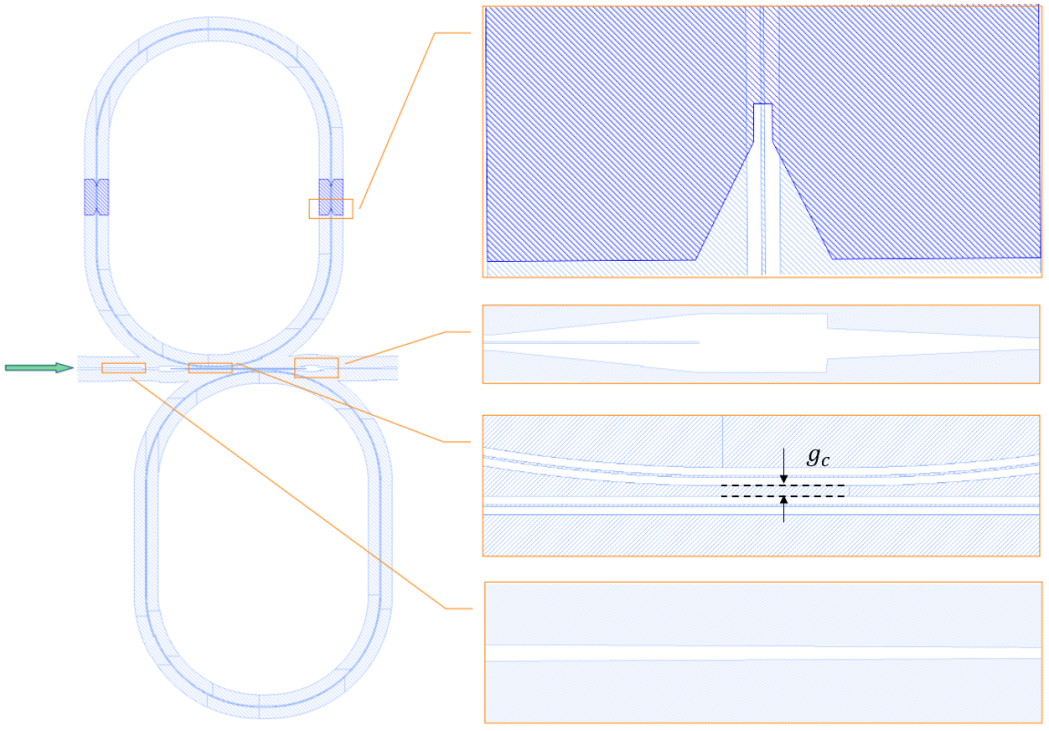

FIGURE 6.3: Test design A. Test device design for extracting coupling coefficient and propagating loss of the slot waveguide. Features of slot to suspended slot converter, rib to slot converter, slot coupler and grating taper are illustrated on the right hand side from top to bottom, respectively.

defines rib waveguide (etch depth 120 nm) and area that silicon has to be thoroughly etched (etch depth $>$120 nm), respectively. In Figure 6.3 (Test design A), ring resonators are constructed by slot waveguide and the phase shifters are constructed by suspended

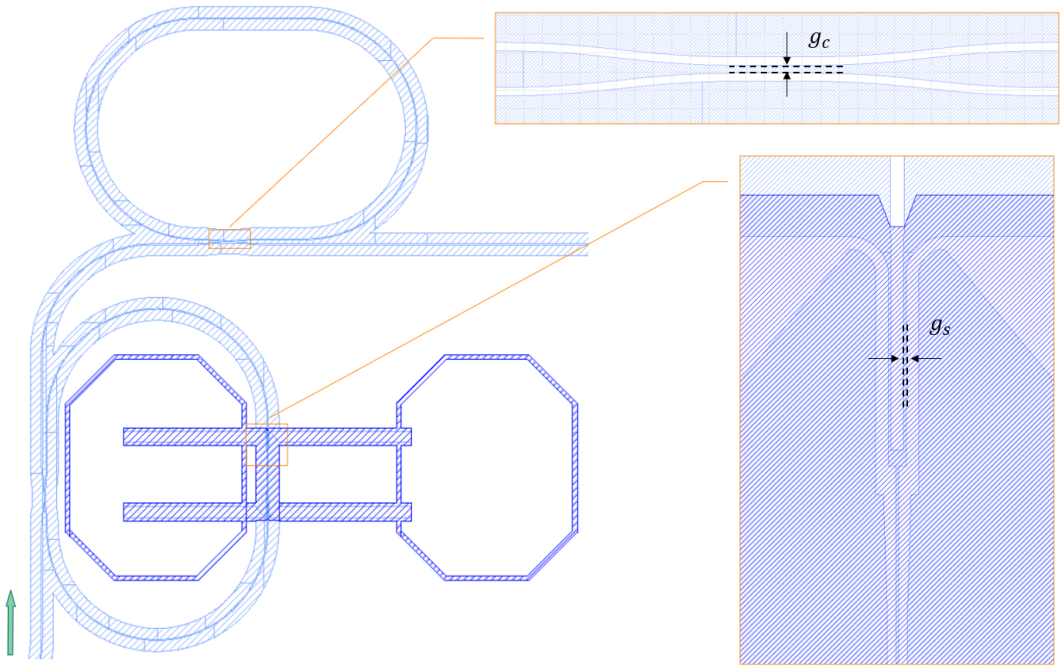

FIGURE 6.4: Test design B. Test device capable of examining the isolated mode converter. Two electroplates (cut corner rectangular) are preserved for electrostatic actuation in the future. Features of symmetrical directional coupler and rib to isolated suspended slot converter are illustrated on the right hand side from top to bottom.

slot waveguide with no electrostatic actuation. The optical force and thermo-optical effect are the possible sources of the index change. The spectrum shift caused by optical force can be recovered by rejecting the thermo-optical spectrum shift from the reference ring at a lower position in the Figure 6.3.

The feature of the mode converter for rib and slot waveguide is shown in Figure 6.3. The idea of this design is to lower the conversion loss by spreading the energy from the rib mode into multiple modes and then suppress the multiple modes into the slot mode [114]. The feature of the mode converter for slot and suspended slot waveguide is shown in Figure 6.3 as well. The optical mode is converted twice to reduce reflection and scattering. A taper is used to reduce scattering in the first stage of conversion and the second stage of conversion is designed for suppressing reflection. This design requires accurate alignment to make the taper functional, which is challenging in fabrication.

In Figure 6.4 (Test design B), ring resonators are constructed by rib waveguide and the phase shifters are constructed by suspended slot waveguide through a special mode converter that electrically isolates two slot arms for electrostatic actuation. This isolated mode converter for suspended slot waveguide is shown in Figure 6.4. The optical mode is converted three times to reduce scattering and isolate two slot arms. A taper is used to reduce scattering during the conversion between rib and strip mode in the first stage. The second stage of conversion is designed to guide the energy from the

center waveguide to adjacent waveguides. Then the energy in the separated waveguides is combined into slot mode through multi-mode region and taper to reduce the scattering.

In order to efficiently test multiple devices on a single chip, grating couplers are preferred as it is relatively fast in coupling/decoupling during the measurement. A dedicated grating design for devices with suspended structure is shown in Figure 6.5. The

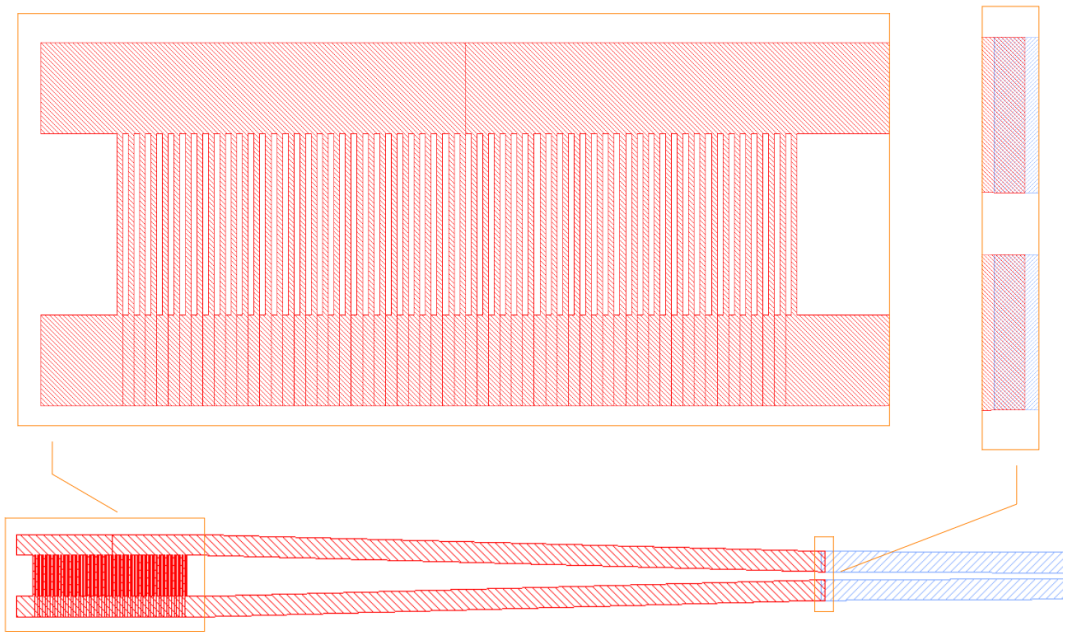

FIGURE 6.5: Grating coupler design aims to minimized coupling loss with details. The complete general structure is shown at the bottom of the picture. The details of the grating is shown on the left hand side above the general design. The details of the overlapped region between the grating and rib layers is shown on the right hand side. Grating and rib layer is overlapped for 1 μm long to ensure the connection between grating coupler and waveguide from possible misalignment.

over-etching of the silicon will happen within the overlapped region between grating (etch depth 70 nm) and waveguide layer labelled with pink and light blue, respectively. An extra loss will be induced by HF vapour etching after the over-etching of silicon as described in Section 6.3.3. By shifting the overlapped region from grating to taper, the optical loss is reduced than the one in Section 6.3.3. Test structure for extract signal feature for grating couplers used in the device is important as well. Two grating couplers connected with a short standard straight waveguide are useful in practice.

6.2 General fabrication flow for test runs

Generally, the fabrication of semiconductors involves lithography, etching, and deposition corresponding to the functionality of geometrical define, material subtracting and

adding. Every semiconductor device is stuck of various layers defined by lithography, etching and deposition. There are three masks used to define the grating coupler, waveguide and suspending structure during the fabrication. For fast prototyping, the step for making the metal contact (Aluminium sputtering) is not involved in this fabrication flow. E-beam lithography is used to transfer the designed patterns from the mask to 30mm * 40mm SOI chips (diced from wafers) to speed up the fabrication. Device fabrication flow based on commercial 220nm/3um SOI wafer is shown in Figure 6.6. Steps shown in Figure 6.6 will be discribed in following sections.

6.2.1 Hardmask

Before the pattern transferring, a layer of silicon dioxide is deposited through Plasma Enhanced Chemical Vapour Deposition (PECVD). The purpose of this hard mask is to achieve self-alignment based on E-beam lithography for defining suspension layer. The tolerance of misalignment allowed for slot waveguide ($\leq$10 nm) cannot be satisfied by fabrication equipment ($\leq$200 nm). The etching selectivity of ICP between silicon and PECVD silicon dioxide is roughly about 3:1. The hard mask should be at least 35nm thick to ensure the top surface of the silicon dioxide is not damaged, by considering the largest etch thickness is about 100 nm.

6.2.2 Rib waveguide and alignment mark

The first mask is used to define the rib waveguide and alignment mark for later processes. The processing for rib waveguide and alignment mark covers from step 2 to 4, which includes resist spin (ZEP520A used here), development, Inductively Coupled Plasma Etching (ICP) and resist strip (Plasma Asher). The etch depth of this layer is 120 nm.

6.2.3 Grating coupler

The second mask is used to define the grating coupler. The processing for grating coupler covers from the step 5 to 7. The etch depth of this layer is 70 nm.

6.2.4 Strip waveguide

The last mask is used to define the strip waveguide. The processing for grating coupler covers from the step 8 to 10. Strip waveguide produces a window to allow the etching of BOX layer so the structure can be released. Lithography for this layer does not define the geometry of the waveguide, but the area covers the strip waveguide to avoid

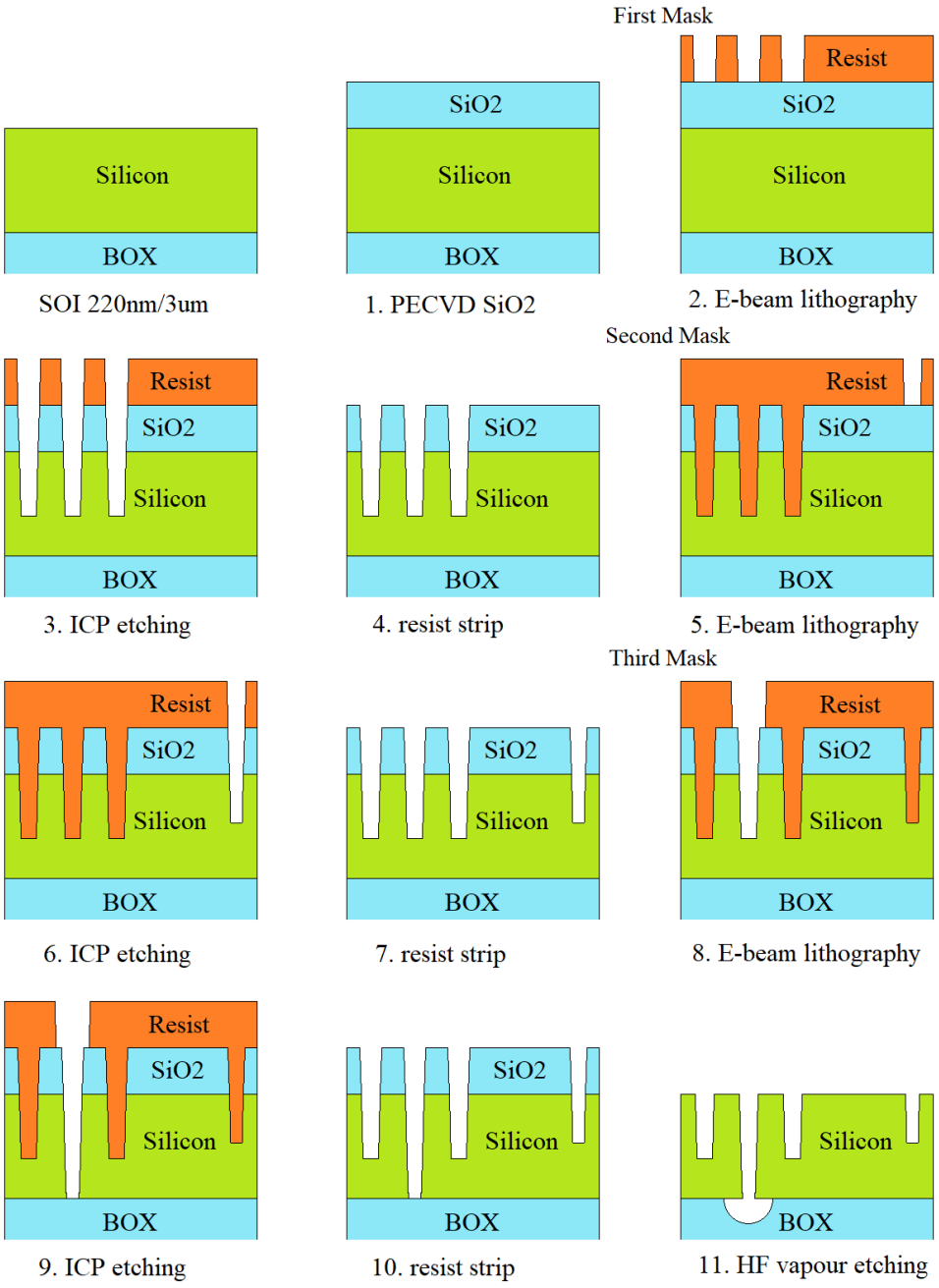

FIGURE 6.6: This is the general fabrication flow for test structures. There are totally three masks used in this fabrication flow. The steps from 2 to 4 are processed for the waveguide and alignment mark according to the first mask; The steps from 5 to 7 are processed for the grating coupler according to the second mark; The steps from 8 to 11 are processed for the suspended waveguide according to the third mask.

misalignment between different steps of lithography. Hard mask fabricated in the first step makes self-alignment available. The processing of this layer cover from the step 8 to 10. To fabricate the strip waveguide as designed, the etch depth of this layer is over 100 nm to ensure silicon between slot arms is etched through (low etch speed with a narrow gap of 70 *nm*). As an outcome, the silicon layer left on the chip will be hard mask for structural releasing.

6.2.5 Structural releasing

Structural releasing means to etch out the BOX under a specified area to produce suspended structures, which allows the mechanical movement of the structure. Hydrofluoric (HF) acid is used to etch out BOX while keep silicon structure remain on the chip. This process requires the removal of at least $1\mu m$ silicon dioxide to ensure the optical performance is not significantly affected.

6.3 Fabrication imperfection

Rather than the perfect 3D geometry considered during the design and simulation, the performance will be influenced by extra surface roughness and geometry defect produced during fabrication. Three main sources that affect the performance of the fabricated device here are excess surface roughness, structural releasing failure and misalignment between layers. Surface roughness and structural releasing failure can be improved by adjusting the fabrication recipe, while misalignment has to be overcome by designing overlarge layers to cover the possible alignment error from lithographic tools.

6.3.1 Roughness from silicon dioxide hardmask

In this particular design, PECVD silicon dioxide hard mask can induce significant surface roughness. Material Defects of the silicon dioxide layer deposited by PECVD are one of the main sources of surface roughness. For commercial 220 nm SOI, E-beam lithography can achieve a high resolution on the polished surface of the silicon layer. A SEM picture of slot waveguide ($w = 250nm$, $g = 100nm$ and $s = 100nm$) fabricated on SOI with no SiO_2 layer deposited is shown in Figure 6.7. The sidewall of the waveguide has a good quality under high magnification in Figure 6.7. The sidewall of the slot waveguide is etched directly under the photoresist mask, and it is the normal way of fabricating a silicon photonic waveguide. In Figure 6.7, the focus is adjusted on the top surface of the waveguide so the top edge of the sidewall defined by the developed photoresist can be clearly observed (two thin dark lines). White lines are the roughness produced during the etching.

Compared with the waveguide in Figure 6.7, silicon dioxide mask will increase sidewall roughness due to the imperfect quality of the deposition and increased etch depth. The rough surface of the hard mask will change the local photoresist thickness distribution after the resist spinning and post bake thus, the extra roughness is produced as a result of uneven exposure. The hard mask increases the necessary time for etching, and

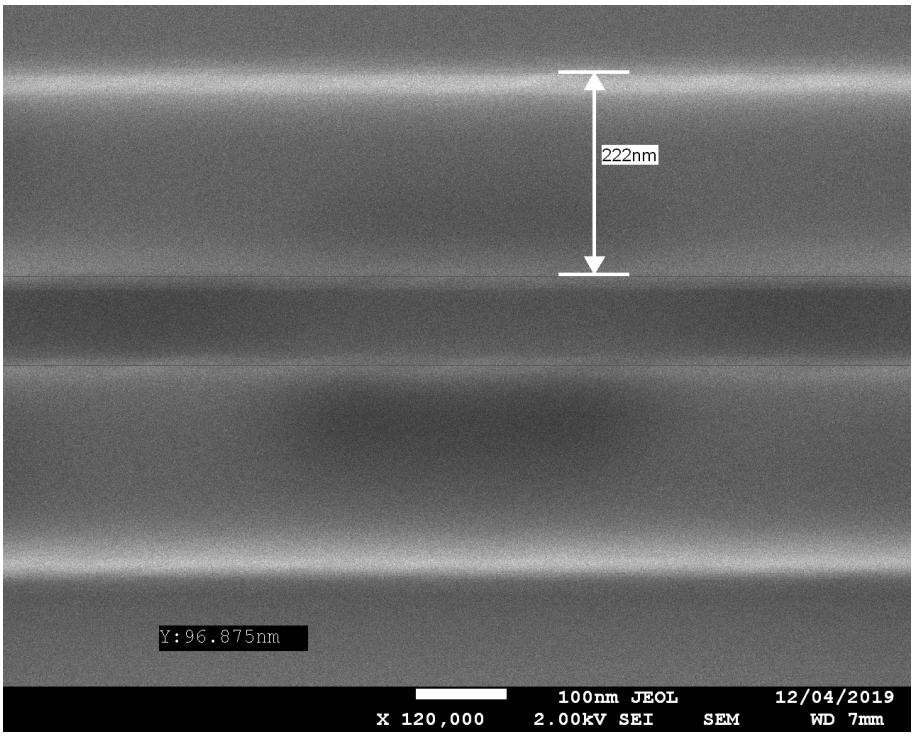

FIGURE 6.7: The top view of silicon slot waveguide ($w = 250nm$, $g = 100nm$ and $s = 100nm$) with no oxidation layer as hardmask. Please be noticed that slot arm width shown in picture is not from an accurate measurement.

it further increases the surface roughness of the waveguide, so the hard mask thickness must be controlled.

Based on the experimental results and SEM microscopy, the functional device can be achieved with SiO_2 hard mask thickness under 100 nm. The sidewall roughness from 200 nm SiO_2 hard mask on fabricated slot waveguide can be observed in Figure 6.8. The large sidewall defect makes the fabricated geometry quite different from the designed one. There are obviously many pinholes on the top of the waveguide, and they are possibly caused by the internal defects in the PECVD silicon dioxide layer and etching. The extra sidewall roughness compared with Figure 6.7 is caused by these defects as well. The fabricated geometry is worse in curved structures rather than straight waveguides. A taper grating coupler designed for consuming less chip area fabricated from 200 nm silicon dioxide hard mask is shown in Figure 6.9. Damages at the edge of the gratings cause device failures that make the coupling impossible. The surface roughness enhanced by hydrodynamical force during the resist development should be counted for the surface damages.

With a thinner silicon dioxide hard mask of $\leq 100nm$, the defect on geometry can be reduced. The fabricated grating is shown in Figure 6.10. The described sidewall roughness is still visible in high magnification mode of SEM as shown in Figure 6.11. As shown in the figure, the straight edge of the waveguide is defined by E-beam lithography and sidewall roughness introduced from silica hard mask can be more than tens

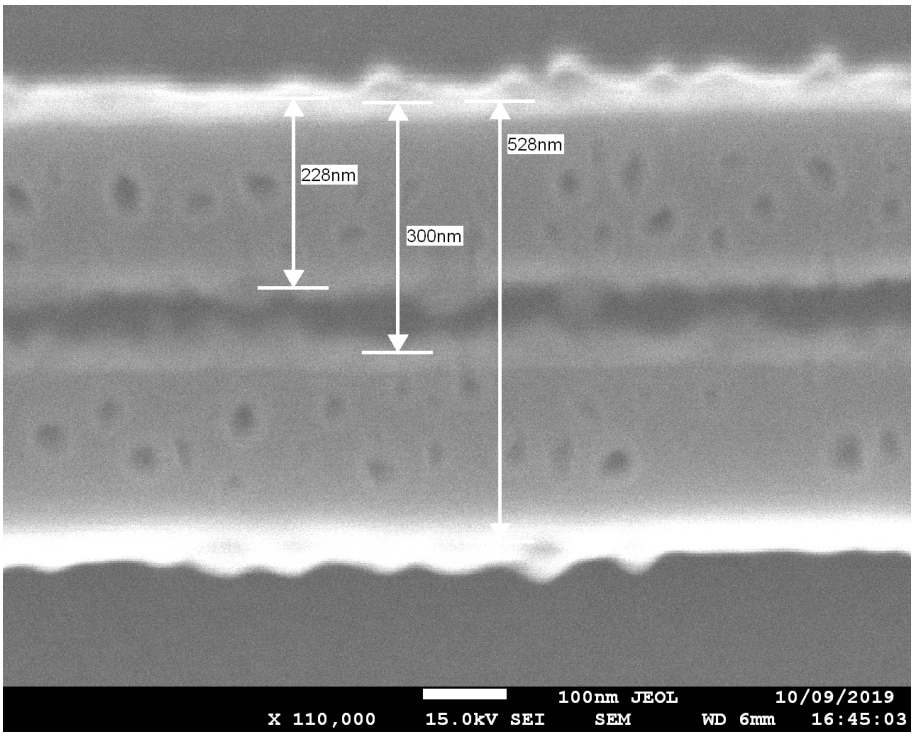

FIGURE 6.8: The top view of silicon slot waveguide ($w = 250nm$, $g = 70nm$ and $s = 100nm$) produced from 200 nm thick SiO_2 hardmask.

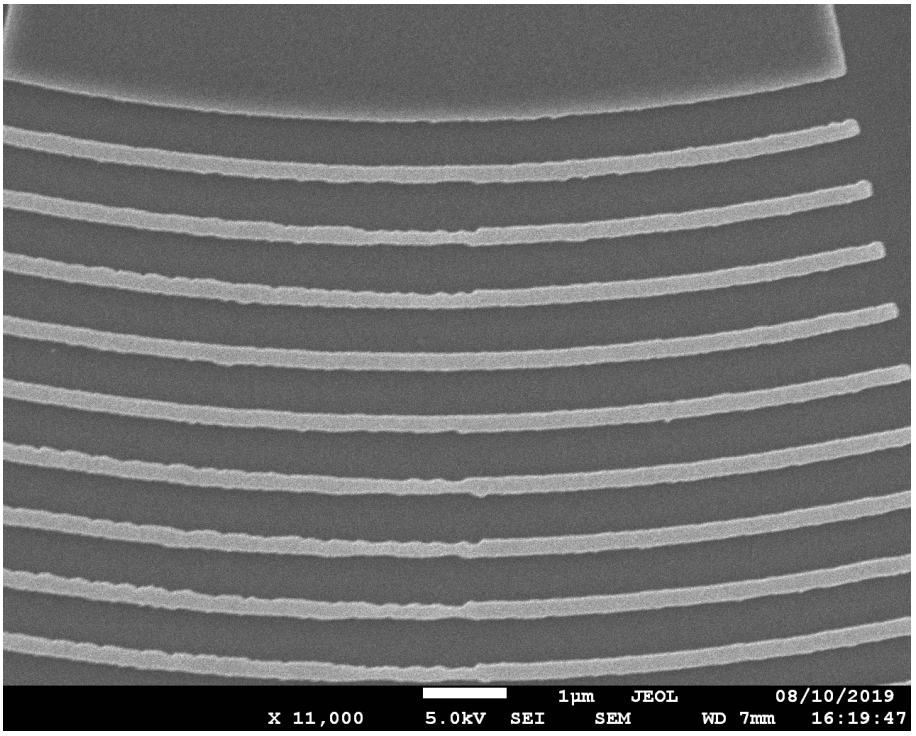

FIGURE 6.9: Grating coupler produced from 200 nm thick SiO_2 hardmask.

of nanometers. The excess roughness caused not only extra loss but also uncertainty in the power coupling ratio of the directional coupler. Fabricated slot waveguide bending is also influenced by the hydrodynamical defect in developing the exposed resist as

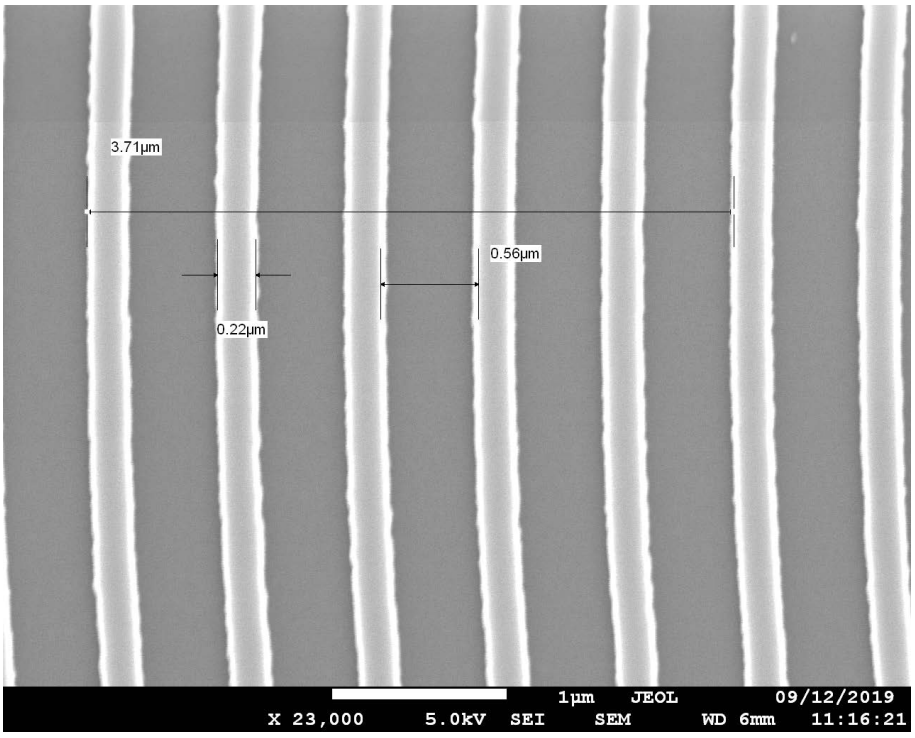

FIGURE 6.10: Grating coupler produced from 100 nm thick SiO_2 hardmask.

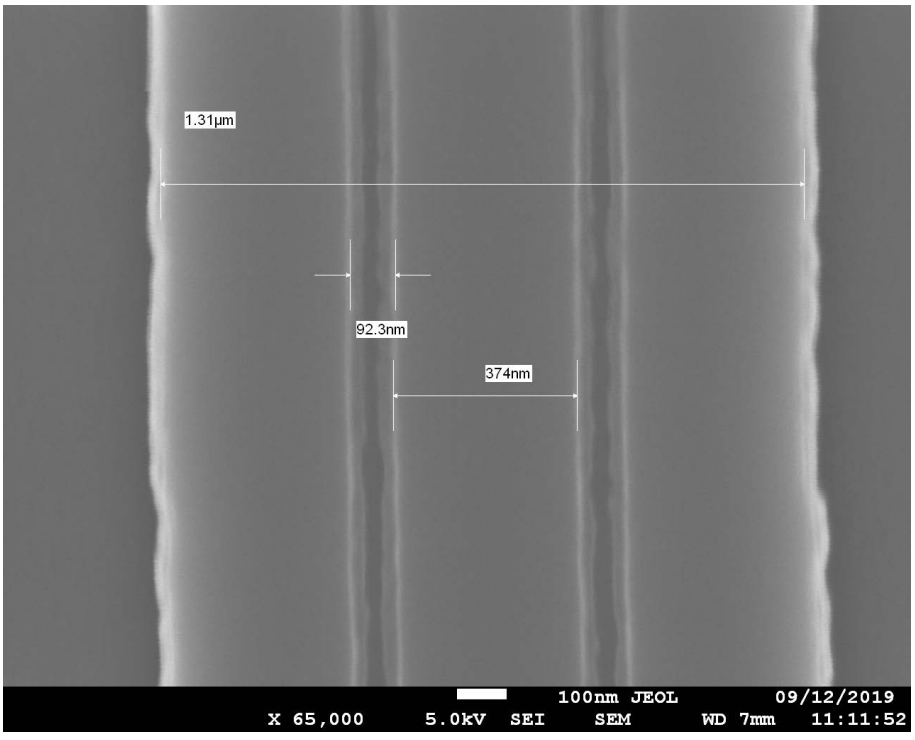

FIGURE 6.11: Direction coupler produced from 100 nm thick SiO_2 hardmask.

shown in Figure 6.12. As a result of the interaction between the developer and the narrow gap between the two arms of the slot waveguide, the inner edge of the waveguide is not as smooth as the outer edge. This defect might change the dispersion feature of the waveguide.

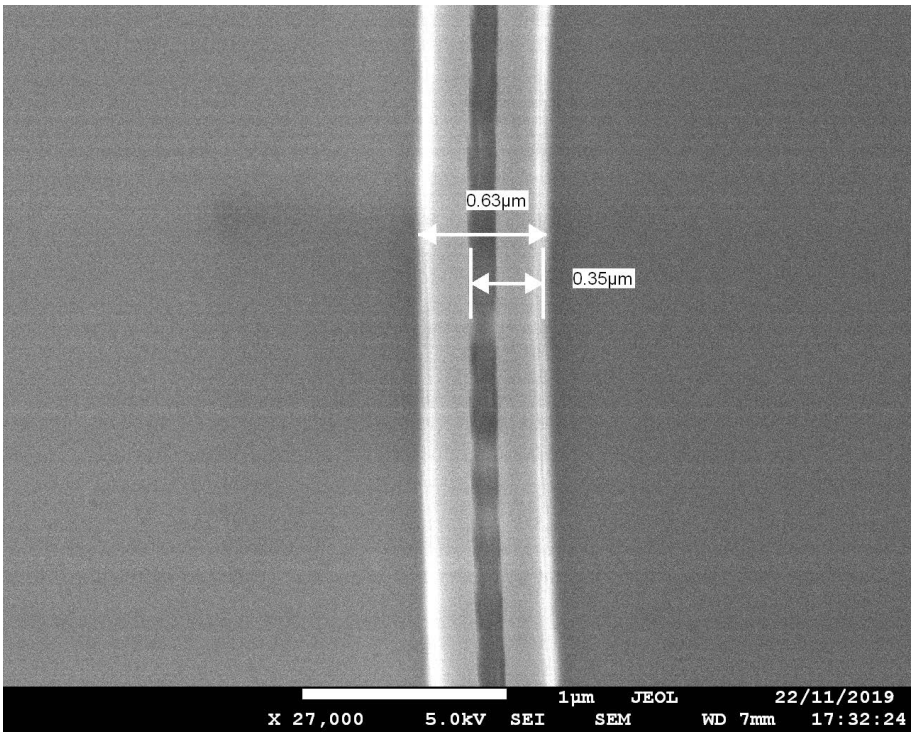

FIGURE 6.12: Bending slot waveguide produced from 50 nm thick SiO_2 hardmask.

6.3.2 Structural releasing failure

The available HF wet etching recipe is developed on the 500nm SOI platform for suspended mid-infrared (MIR) waveguide with periodic supporting around the structure as shown in Figure 6.13. More details can be found in [115]. From Figure 6.13, a MIR

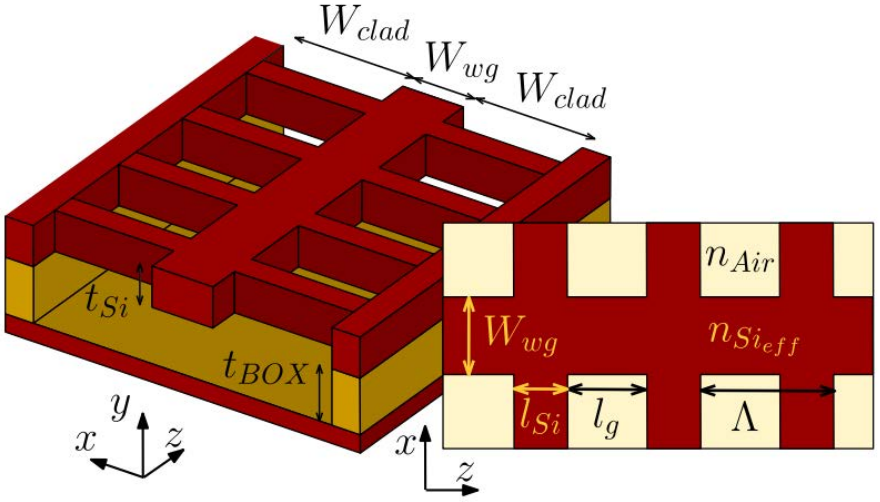

FIGURE 6.13: Suspended structure corresponding to the wet etching recipe available [115].

waveguide is supported with sub-wavelength grating (SWG) lateral cladding. By comparing the difference between [115] and the designed device, the existing 500 nm etching recipe was regarded as a good trial for devices on 220 nm SOI. However, the releasing failure is evidenced by scanning electron microscopy (SEM) inspection.

The failures include distorted structure, structures bonding with each other or substrate and metal contamination. The structural failures are possibly caused by capillary force in the fluid. The wet etching is also possible to contaminate the surface with small particles in the solution. The device can be contaminated by the metal flakes during the electrical probing during the test as well. The corresponding SEM pictures for these failures are shown in Figure 6.14 and Figure 6.15. Obviously, slots are distorted in

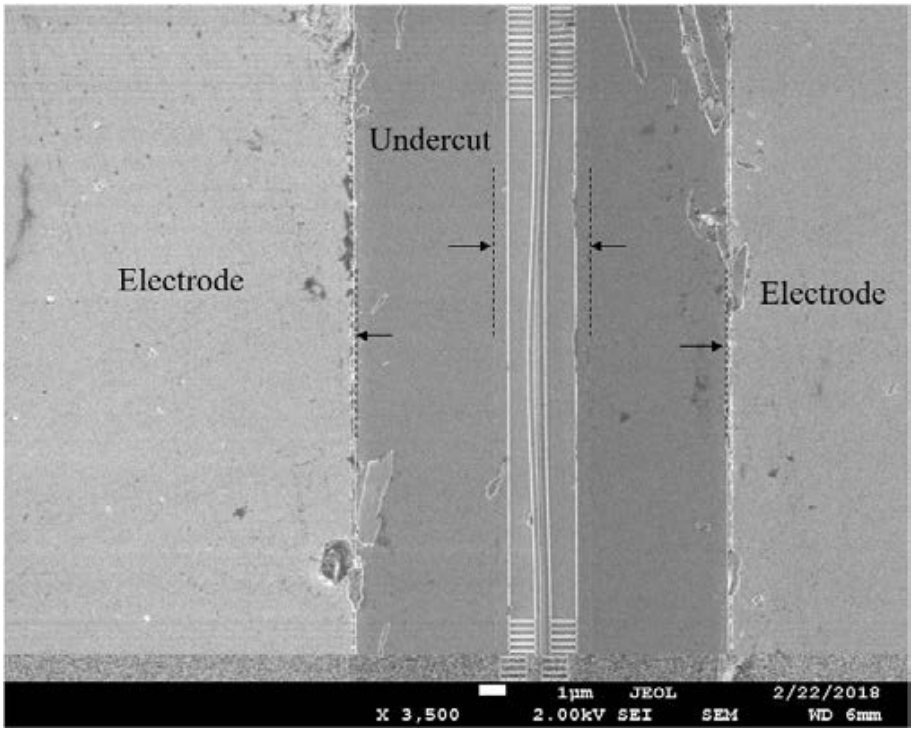

FIGURE 6.14: suspended strip waveguide with a suspending length of 20um.

Figure 6.14 by hydrodynamical force and capillary force. The under etching area is labelled out in the picture. Small pieces of metal are peeled off from the electrode. Contamination from metal flakes and surface damage on the electrode can be seen in the picture. In Figure 6.15, two slot arms are bonded together. For the fully suspended slot waveguide design for $\lambda = 1550nm$, the mechanical stiffness is not sufficient to resist capillary force.

Apart from wet etching, HF vapour etching is a good choice for a fragile structure such as the fully suspended slot waveguide. The general construction for HF vapour etching is shown in Figure 6.16. As shown in Figure 6.16, the sample is placed face down with a heater plate on the back to control the temperature of the sample. The HF vapour with water vapour will form a thin layer of HF solution on the surface of

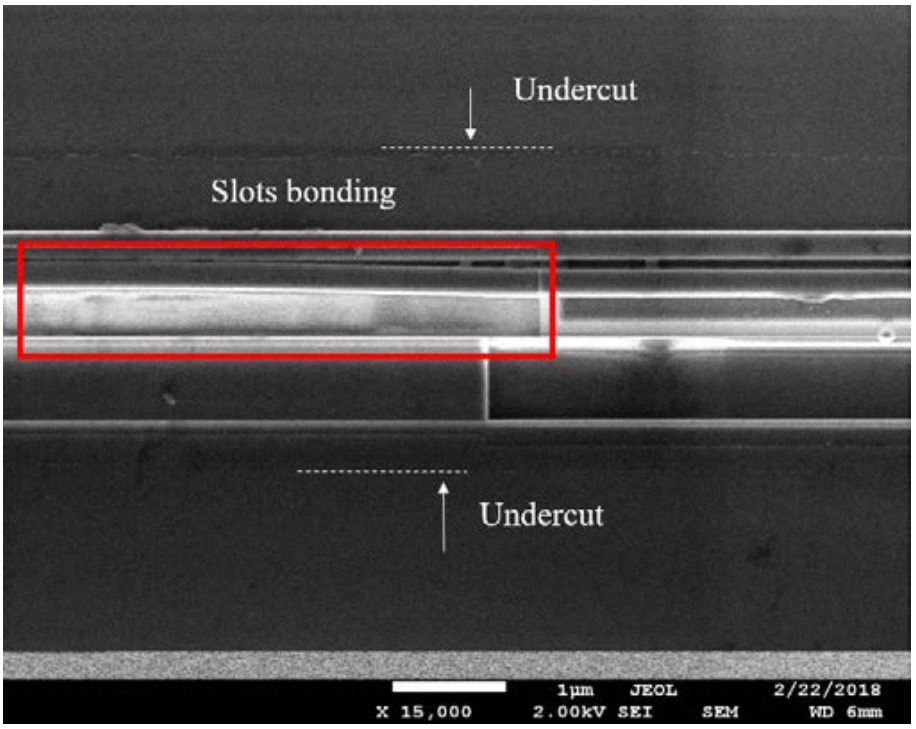

FIGURE 6.15: Single slot is designed to be released. The slot is deformed and bonded with the other slot. Contamination can be seen from the picture.

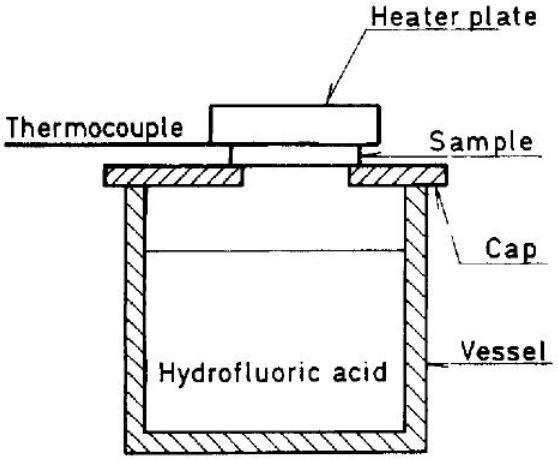

FIGURE 6.16: Experimental HF/H2O vapour etching setup [116].

the sample to react with the exposed silicon dioxide. The absorption and desorption of the water vapour are controlled by the surface temperature of the sample thus, the concentration and the thickness of the solution layer on the surface are adjustable. By further control the temperature of the acid solution in the vessel (evaporation rate of HF and water), the process is highly repeatable. With HF solution at a concentration of 25 % and ambient temperature of 20 °C, the etching rate at different heater plate temperate is shown in Figure 6.17. From Figure 6.17, at $\Delta t = 11.5°C$ the etching rate is constant, which reaches the balanced point of absorption and desorption of the water. Currently, the available HF vapour etcher in the cleanroom of the university is filled

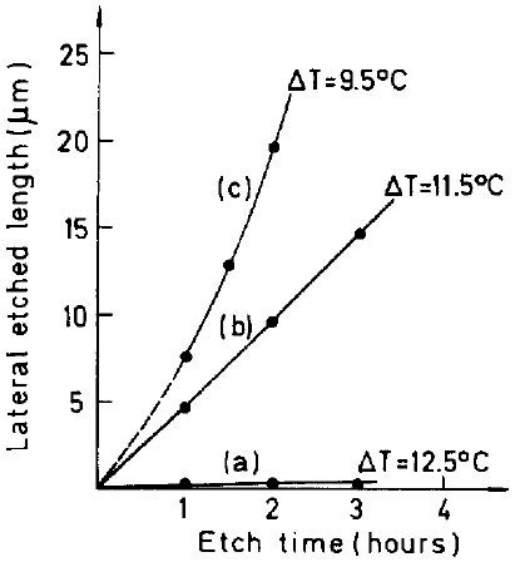

FIGURE 6.17: Silicon dioxide lateral etched length vs. etch time at different ΔT, which is the temperature difference between ambient temperature and heater plate [116].

with HF solution with a concentration of 48 %. The available recipe for etching micro-scale (thickness) device is to set the temperature of the sample holder at 40 °C, and it is proved too low for our specific design on 220 nm SOI as shown in Figure 6.18. With

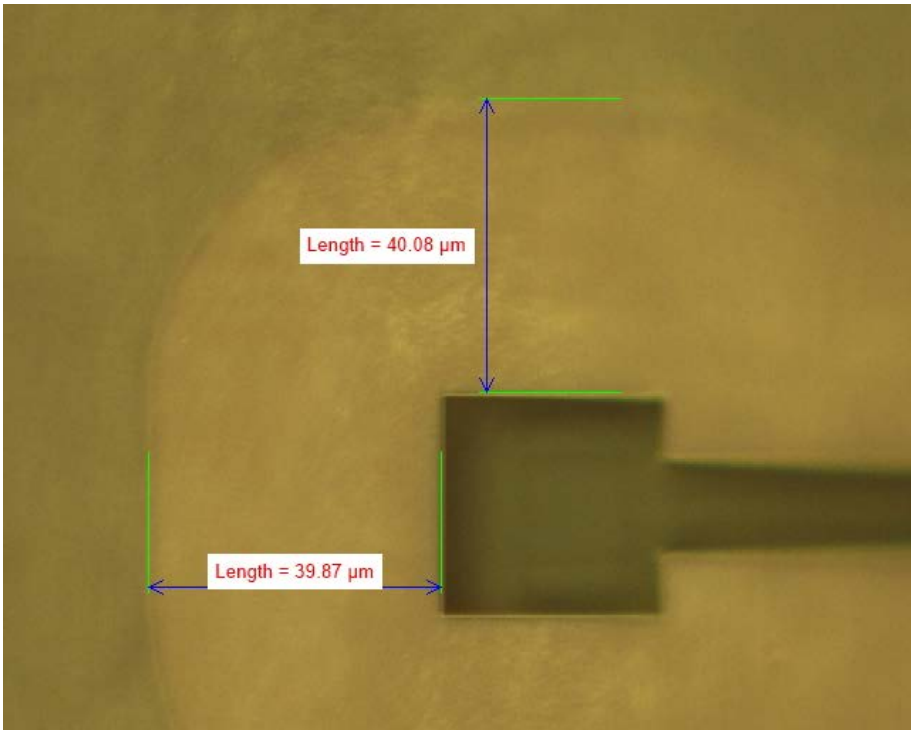

FIGURE 6.18: Sample etched at 40 °C holder for 1 hour and 15 mins. The sample is overetched according to the undercut length of 40 μm. The average etching speed is about 0.53 $\mu m/min$

reference to the etching rate shown in Figure 6.18, different samples with the same

design are etched with different reaction times to find out the suitable reaction time for the process. The results showed that the etching rate is increasing with the time of etching. This indicates that the temperature is not high enough according to [116]. The test sample etched at 45 °C is shown in Figure 6.19. The picture is slightly out of

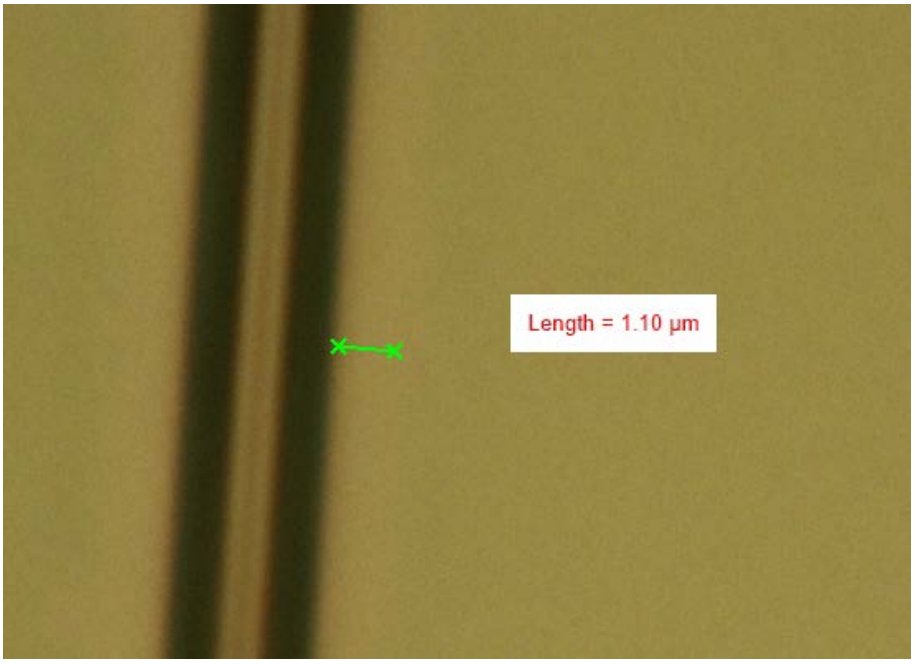

FIGURE 6.19: Sample etched at 45 °C for 2 hours. The undercut is about 1.1 μm. The average etching speed is about 0.01 $\mu m/min$

focus, but the undercut is visible in the microscope. The uniformity of the etching is affected by the thermal conduction between the holder and chips. If the contact is not firm, this nonuniform temperature distribution will be transferred to different etching speeds in different areas of the chip as shown in Figure 6.20. Different etching profile can be found in these two alignment marks (line width 10μm) in Figure 6.20. Even in the same mark, different undercuts and residual BOX profile is produced.

6.3.3 Loss from misalignment

The second mask for grating and the third mask for strip waveguide need to be designed slightly oversized to cover the possible misalignment (about 100 nm). The common grating design for silicon photonic circuit is accomplished by two masks shown in Figure 6.21. The overlapped area between the first and second masks is designed to tolerant the possible misalignment during the lithography. The silicon at the overlapped area will be etched through since it has been etched twice, and it opens additional windows for HF vapour etching, which produces unexpected BOX etching under gratings as shown in Figure 6.22. The unexpected etching causes an additional loss of about 9 dB compared with the same device without HF vapour etching. Unexpected BOX etching

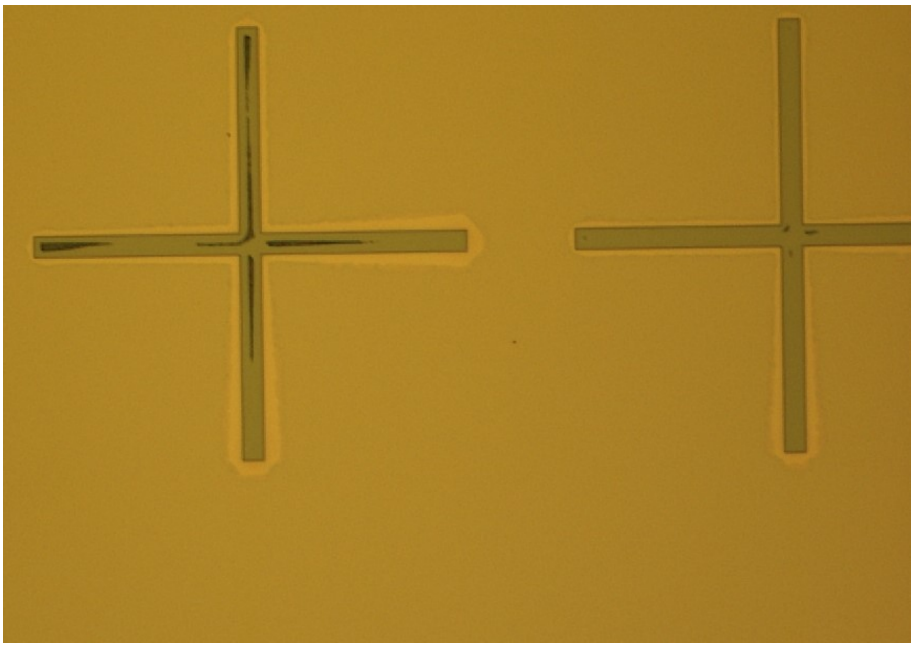

FIGURE 6.20: Nonuniform undercut of heater plate loose contacted with chip.

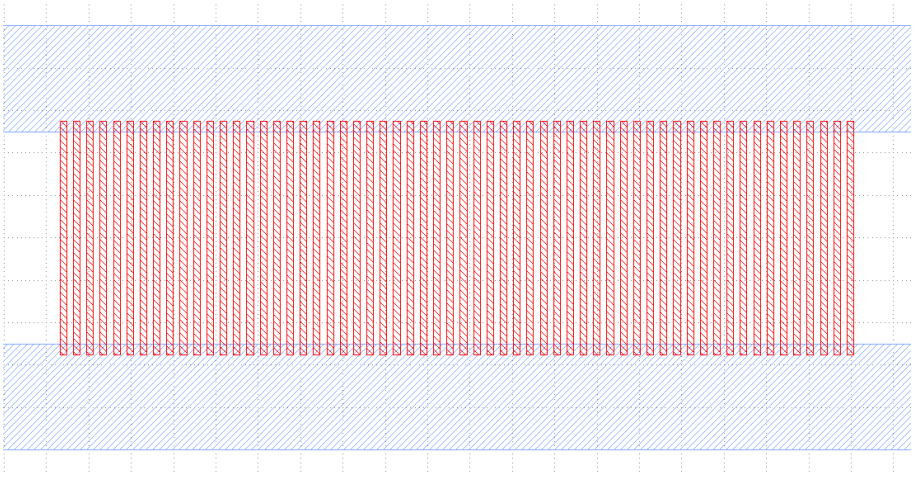

FIGURE 6.21: An example of a common grating design in silicon photonics. The first mask for the rib waveguide is labelled in blue, and the second mask for grating is labelled in red. For positive resist, the coloured area defines the area that is going to be etched, and the rest of the chip will be protected by the resist.

can hardly be avoided when multiple masks are applied on the same chip. Misalignment in the fabricated mode converters will result in significant loss as well. One way to reduce the loss is to modify the design as described in Section 6.1.

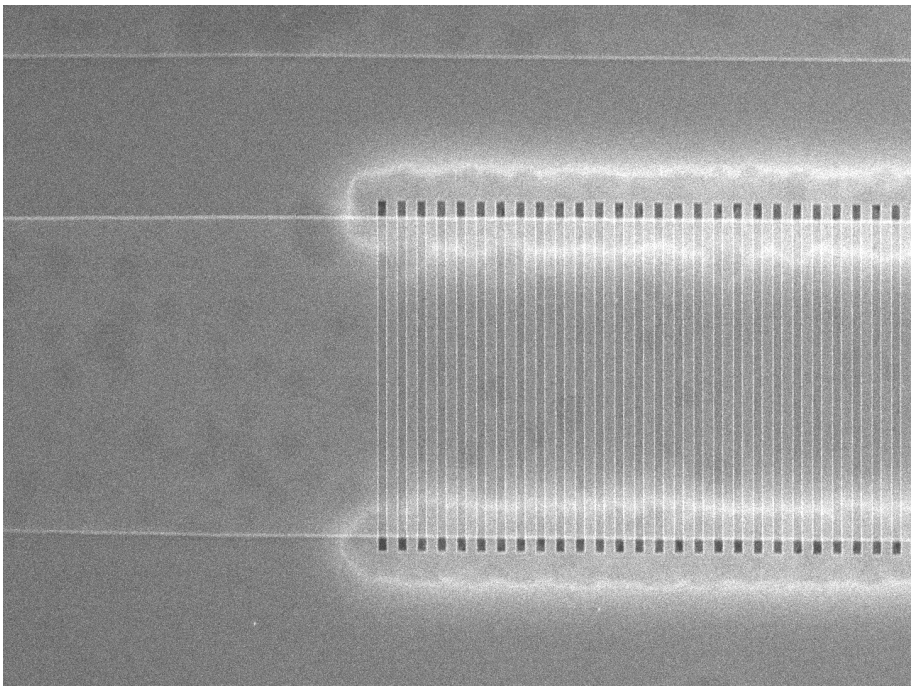

FIGURE 6.22: Unexpected BOX etching by additional etch windows. The grating is designed by a period of 630 *nm* with a duty cycle of 50 %.

6.4 Measurement and analysis

The quality of the fabrication and how the fabrication influences the performance of the test design A and B are investigated from the transmission spectrum. The experiment setup is described in Section 6.4.1. The component parameters of the devices is extracted based on the all-pass ring resonator model illustrated in Section 6.4.2. The fabrication quality is evaluated regarding the propagation loss of the waveguide and comparing the coupling coefficient with the designed value. The influence of the HF vapour etching on the devices is analysed as well.

6.4.1 Experiment setup

The basic units for spectrum scanning include variable LASER, multimeter and test bench, which allows the light coupling in and out from the test sample. By measure the transmission at different monochromatic light wavelengths and combine them together, the spectrum can be recovered. The test equipment is placed on a floating table and suspended shelf above the table. The key testing elements on the float table are shown in Figure 6.23. Controllers and equipment for signal conditioning placed on the suspended shelf are shown in Figure 6.24. As shown in Figure 6.23, light generated from Laser is guided to the test sample by fiber mounted on a special fiber holder that can adjust the incident angle of the fiber. The protection cover at the coupling end of the

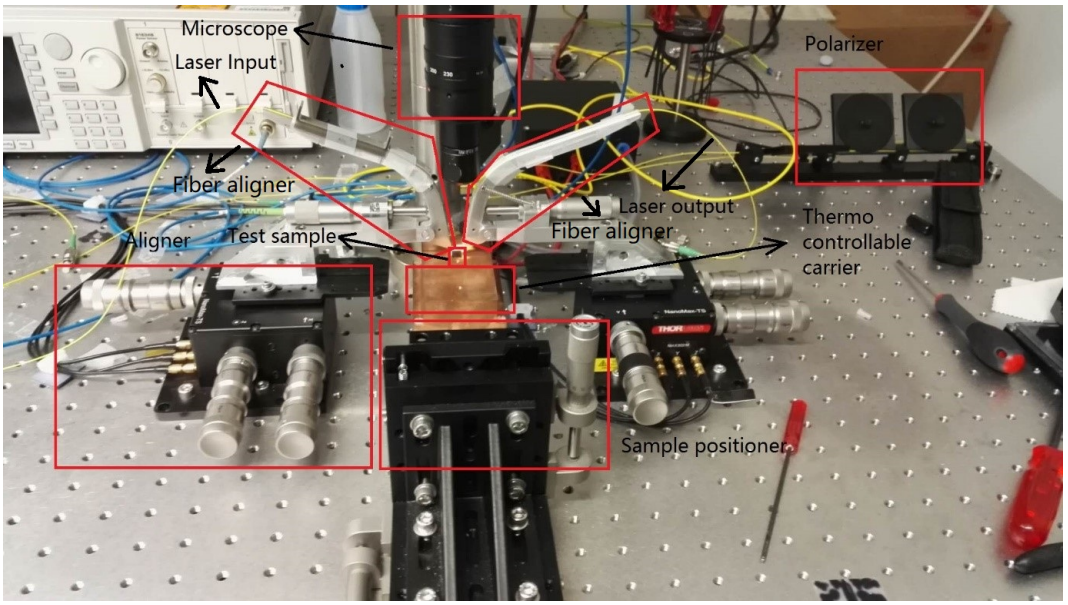

FIGURE 6.23: Test bench.

fiber is peeled off to allow the larger range of incident angle and shorter physical distance between coupler and fiber to achieve better coupling. The holders are mounted on a high-precision aligner to allow the fiber core to be moved in three-dimensional space.

The sample is placed on a thermal controllable carrier stage and fixed by a vacuum sucker (sample must be aligned upon the hole for the sucker). The Fibre holders and sample carrier can be adjusted independently by fiber aligners (or position controller shown in Figure 6.24) and sample positioner. The microscope shown in Figure 6.23 is used to help the alignment of the fibers and sample. This is an all-in-one test plat-

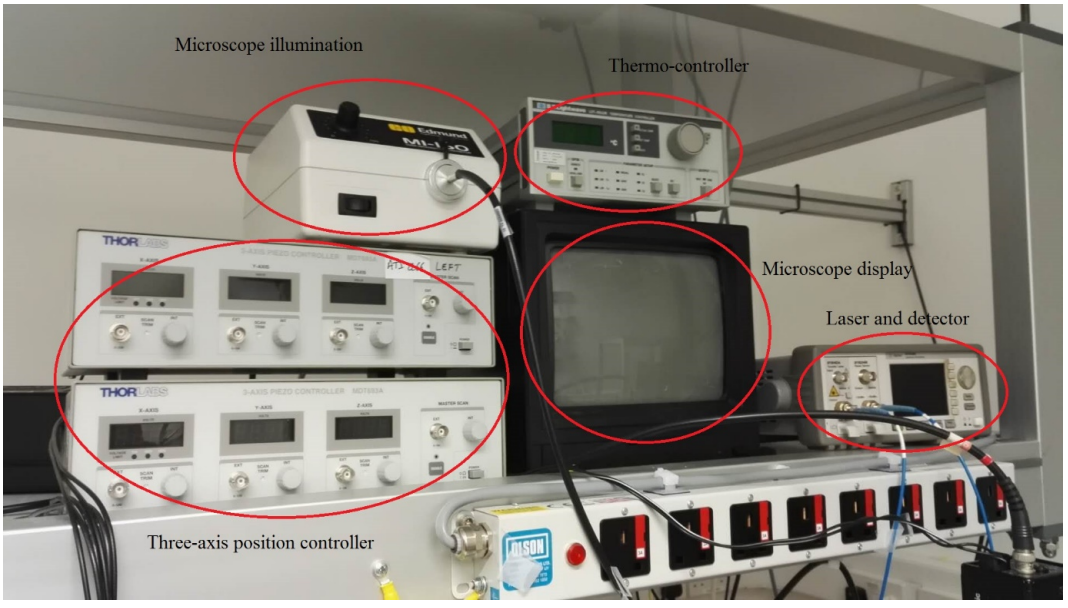

FIGURE 6.24: Controllers and equipment for signal conditioning.

form with the functionality of alignment, temperature control, and measurement. The laser is generated from Agilent 81940A tunable LASER module and polarized before it is sent into the test sample. The output signal is received by Agilent 81634B power sensor. Both modules are integrated into Agilent 8163B lightwave multimeter. The measurement can be fully controlled by dedicated software. The optical system diagram is shown in Figure 6.25.

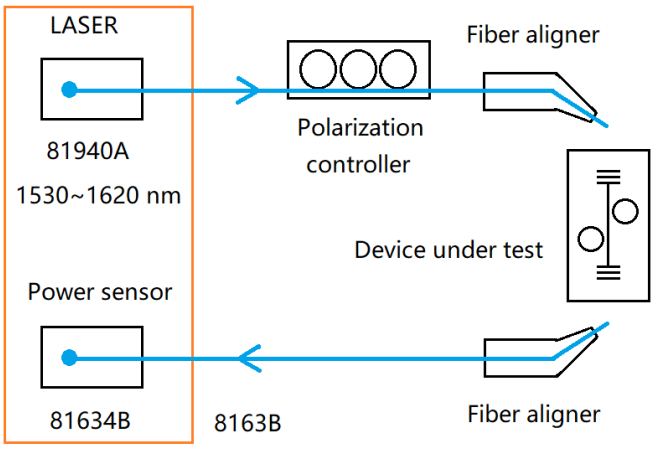

FIGURE 6.25: Optical system diagram of the test construction

The background transmission spectrum measured from grating couplers only is shown in Figure 6.26. From Figure 6.26, HF vapour etching affects not only the grating cou-

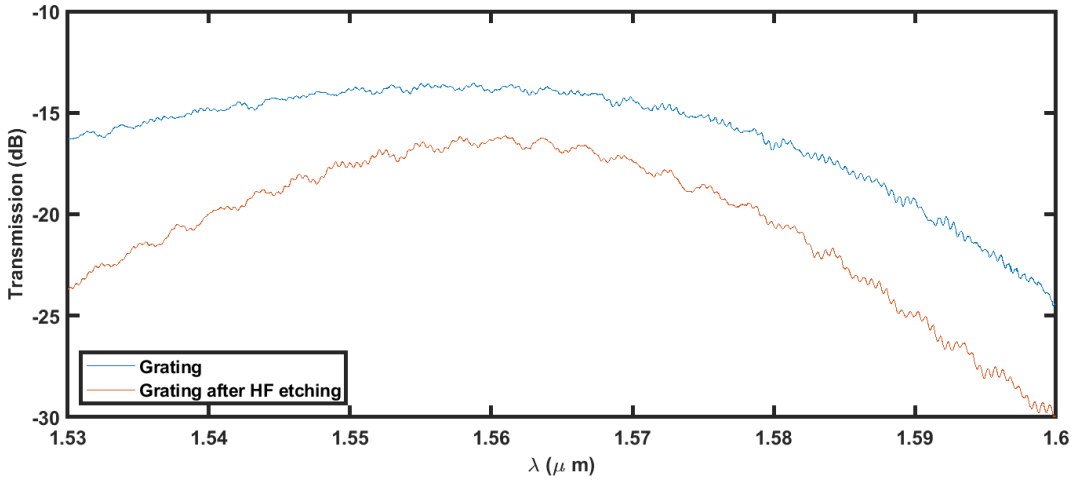

FIGURE 6.26: Background spectrum within 1530 to 1600 nm before and after HF vapour etching. The spectrum is obtained from grating couplers with tapers (300 μm). fiber injection angle is 11° and 17° before and after HF vapour etching, respectively

pling efficiency but also change the spectrum shape and injection angle of the grating coupler. This means the surface roughness and the geometry of the grating coupler are affected by highly concentrated HF vapour during the process. Extra surface roughness is possibly to be induced from the low quality silicon dioxide layer that generated by

wet oxidation of the doped silicon surface during the etching [117]. The lowest background loss before and after HF vapour etching is 13.64 dB and 16.28 dB, respectively. The periodic background intensity fluctuations are possibly the result of interferometric noise caused by reflection on the light path [118]. The first order intensity fluctuation is measured with 0.64 dB on the spectrum.

6.4.2 Parameter extraction of all-pass ring resonator

Parameters (t, κ, α) required by the model described can be extracted from FSR, λ_{res}, Q, and ER measured from transmission spectrum. Model parameters can be obtained from the following steps described below. The product of the group refractive index and light travel path length of the resonator $n_g L_0$ can be solved out by applying Equation 6.1 with measured FSR as

$$n_g L_0 = \frac{\lambda^2}{FSR} \,. \tag{6.1}$$

The product of inner loss factor and coupling coefficient (αt) is solved by applying Equation 6.2 with measured Q as

$$\alpha t = \left(\frac{\sqrt{(n_g L_0 \pi / \lambda_{res})^2 + 4Q^2)} - n_g L_0 \pi / \lambda_{res}}{2Q} \right)^2 \,. \tag{6.2}$$

If we assume $\gamma = 0$, inner loss α and coupling coefficient t can be solved by Equation 6.3 with measured extinction ratio and calculated αt value from Equation 6.2.

$$\alpha = \sqrt{\alpha t \frac{\alpha t \sqrt{ER} + \sqrt{ER} + (1 - \alpha t)}{\alpha t \sqrt{ER} + \sqrt{ER} - (1 - \alpha t)}} \tag{6.3}$$

Finally, the power enhancement factor B can be solved by applying Equation 5.41 with parameters solved from the last step. Curve fitting is a proper way to extract resonant frequency/wavelength, quality factor, and extinction ratio to reduce the interference from a noisy background. Based on the physical nature of the spectrum, a Gaussian shape is chosen to fit the data. The professional curve fitting tool Origin 2018b is used to extract the λ_{res}, Q and ER from the spectrum. The Gaussian shape is expressed as: [119]:

$$y = y_0 + A \cdot \exp\left(\frac{-4 \ln(2)(x - x_c)^2}{w^2} \right) / \left(w \sqrt{\frac{\pi}{4 \ln(2)}} \right) \tag{6.4}$$

A sample curve is illustrated in Figure 6.27

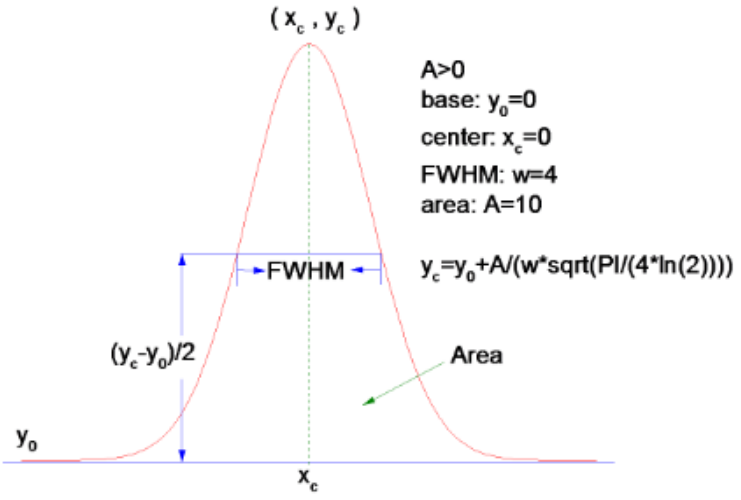

FIGURE 6.27: Illustration about the Gaussian shape defined in origin 2018b [119].

6.4.3 Test design A analysis before HF vapour etching

The test device array for test design A contains 9 devices combining different t and L from bus-ring separation of $g_c = 350, 450, 550\ nm$ (expected $t^2 = 0.5, 0.75, 0.9$) and suspended length of $L = 10, 20, 40 \mu m$ (illustrated in Figure 6.3). The target ring resonator is design with a perimeter of 422.16 μm ($100\pi + 100 + 8$). The reference ring resonator is design with a perimeter of 421.16 μm ($100\pi + 99 + 8$). There should be two resonant peaks on transmission of each device from the reference and target rings. For example, the calculated spectrum from Lumerical FDTD module and interconnection module with $g_c = 350\ nm$ and $L = 10\ \mu m$ is shown in Figure 6.28. From the figure, peaks from

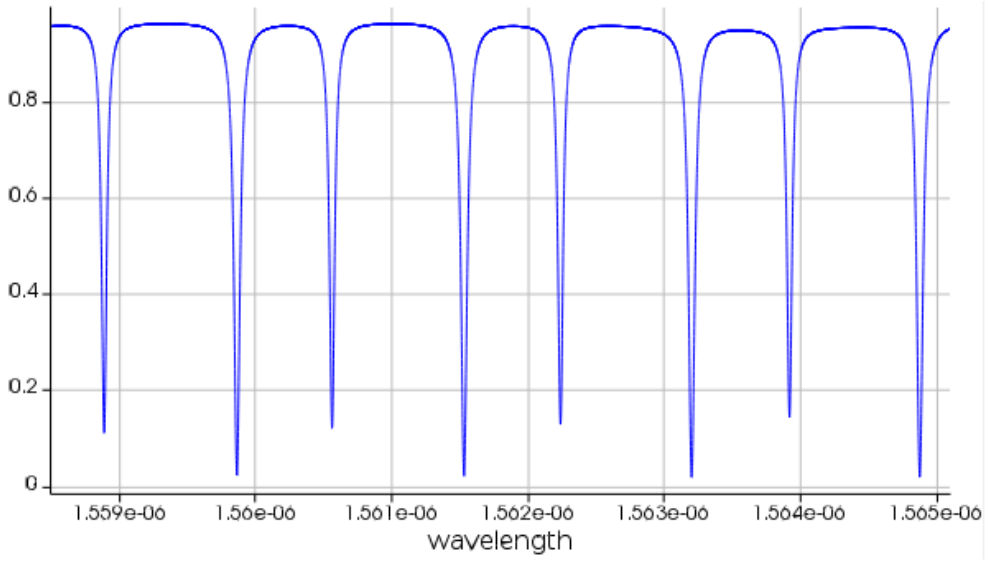

FIGURE 6.28: Resonant peaks within a range roughly from 1558 to 1565 nm from rings with $L = 10\ \mu m$ and $g_c = 350\ nm$. The vertical axis represents the normalized transmission, and the horizontal axis represents the wavelength (m).

reference and target rings can be distinguished from each other by line width and extinction ratio. The measured device transmission spectrum before HF vapour etch from 1558.42 to 1564.22 nm with an input LASER power of 6 dBm are shown in Figure 6.29, Figure 6.30 and Figure 6.31.

Different from the theoretical spectrum in Figure 6.28, unexpected resonant mode splitting can be observed from the measured spectrum. They are possibly the result from the reflection caused by excessive sidewall roughness as shown in Figure 6.12 and misalignment in the lithography at the slot to suspended mode converter from the design shown in Figure 6.3. Surface roughness leads to back-reflections into the counter-propagating mode. Because of the periodic nature of the structure, forward and backward modes become naturally phase-matched by any perturbation. Such contradirectional coupling causes the resonant peak to split as the coupling breaks the degeneracy of the forward and backward modes [120]. In the available wavelength of the tunable LASER from 1530 to 1620 nm for all 9 devices, the occurrences of the mode-splitting are not continual on the spectrum, and it is different for each devices. This might be related to the specific roughness condition of individual rings.

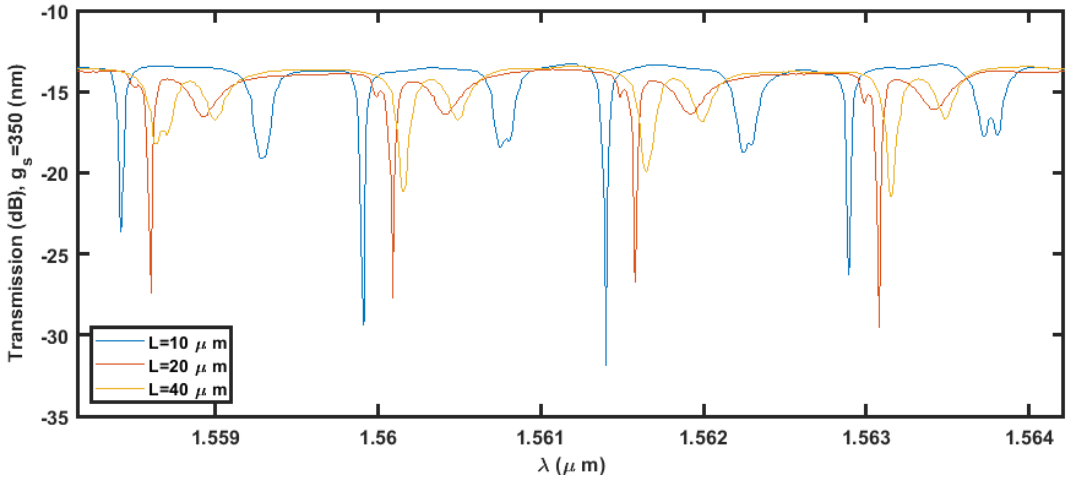

FIGURE 6.29: Resonant peaks within a range from 1558.15 to 1564.22 nm from rings with different suspended lengths L and the same coupler ($g_c = 350nm$).

In Figure 6.29, resonant peaks with a high extinction ratio are generated from the reference ring, and low extinction ratio peaks are generated from the target ring. The loss from mode converters and strip slot waveguide on the target ring makes quality factors lower. In theory, reference peaks (peaks from the reference ring) from all the devices with the same coupler should have the same resonant wavelength. However, reference peaks from different devices have different resonant wavelength shown in Figure 6.29, Figure 6.30 and Figure 6.31. Unstable coupling by excessive surface roughness between adjacent waveguides observed in Figure 6.11 should be in the count for the misaligned spectrum.

In Figure 6.30, the extinction ratio of reference peaks and target peaks are significantly

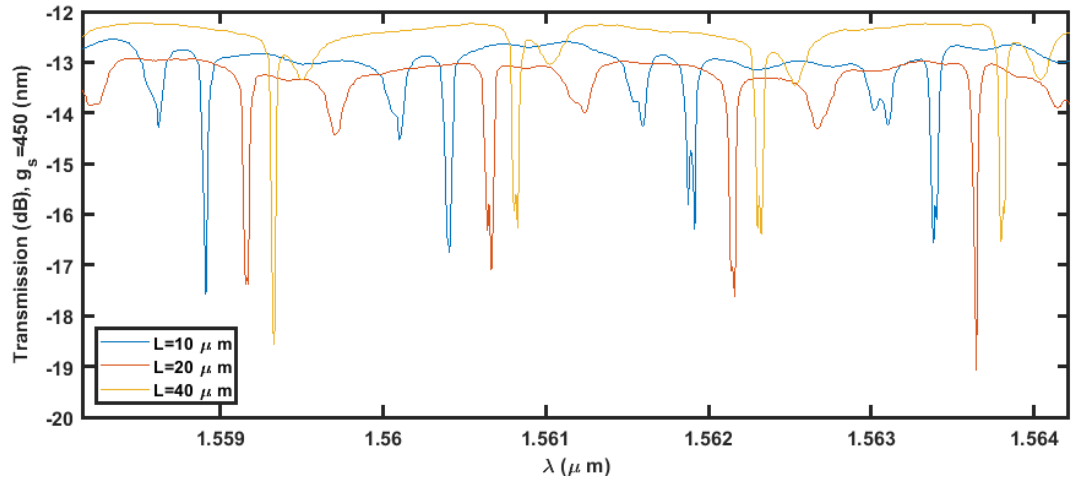

FIGURE 6.30: Resonant peaks within a range from 1558.15 to 1564.22 nm from rings with different suspended lengths L and the same coupler ($g_c = 450$ nm).

decreased compared within Figure 6.29. The distribution of the resonant peaks is different from what in Figure 6.29. The background transmission levels for different devices are different due to the defects in the grating and operating errors by hands. The same situation occurs in Figure 6.31 as well.

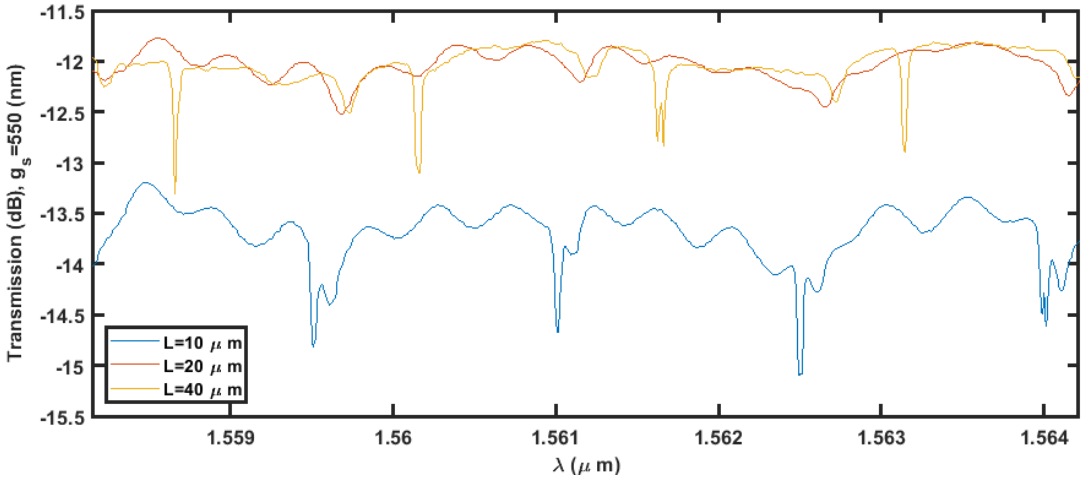

FIGURE 6.31: Resonant peaks within a range from 1558.15 to 1564.22 nm from rings with different suspended lengths L and the same coupler ($g_c = 550$ nm).

By generally observing the figures above, the most significant extinction ratio of the peaks is found in Figure 6.29 so peaks from devices with $g_c = 350$ nm are used to extract model parameters and obtain the propagation loss of the slot waveguide. For the ease of the analysis, peaks with mode splitting should be avoided as possible. Resonant peaks in four continuous periods within the range from 1538.1 to 1542.6 nm shown in Figure 6.32 are selected to be analysed.

The measurement from four reference peaks and four target peaks from $L = 10\mu m$ are shown in Table 6.1. Here we use the coupling coefficient solved from reference peaks to extract the parameters from the adjacent target peaks. From Table 6.1, coupling coef-

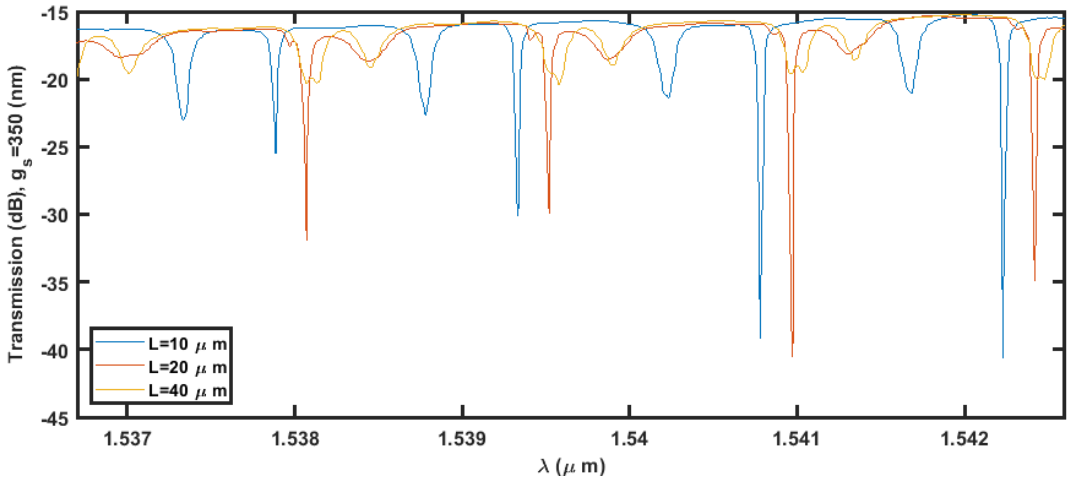

FIGURE 6.32: Resonant peaks within a range from 1536.7 to 1542.6 nm from rings with different suspended lengths L and the same coupler ($g_c = 350$ nm).

TABLE 6.1: All-pass ring resonator modal parameters obtained from four reference peaks (first four) and four target peaks from $L = 10\mu m$ and $g_c = 350nm$. The losses here are the average loss according to the perimeter of the ring. Here we use the coupling coefficient solved from reference peaks to extract the parameters from the adjacent target peaks.

Reference peaks ($g_c = 350nm$, $L = 10\mu m$)							
λ_{res} **(nm)**	**ER (dB)**	**Q**	t^2	κ^2	α^2	**loss (dB/cm)**	**B**
1537.9	9.73	27895	0.848	0.151	0.921	0.085	10.3
1539.3	13.8	29624	0.876	0.123	0.918	0.088	10.6
1540.8	23.2	26777	0.878	0.121	0.880	0.132	7.26
1542.2	24.2	25199	0.863	0.135	0.880	0.131	7.25
Target peaks ($g_c = 350nm$, $L = 10\mu m$)							
1537.3	6.39	12831	0.848	0.151	0.831	0.192	1.88
1538.8	6.13	12683	0.876	0.123	0.814	0.212	1.44
1540.2	5.46	11578	0.878	0.121	0.793	0.240	1.15
1541.7	5.54	11634	0.863	0.135	0.800	0.230	1.32

ficient t is much higher than in the simulation ($t^2 = 0.5$), which means the coupling is worse than expected due to the sidewall roughness. From Figure 6.32, it can be proved that high ER will be obtained when $t \approx \alpha$. The propagation loss of the target ring is more than twice the propagation loss of the reference ring. The extra loss is caused by mode converters and suspended slot waveguide on the target ring. For reference peaks, the average coupling coefficient (t^2) and loss are 0.866 and 0.109 dB/cm, respectively. For target peaks, the average loss is 0.219 dB/cm. Thus mode converters and suspended waveguide induces an extra loss of 0.11 dB/cm. In order to obtain the individual loss of the mode converter and suspended slot waveguide, propagation loss extracted from target peaks with different suspended lengths are necessary. However, the curve fitting is not possible for resonant peaks from $L = 20, 40\mu m$ since the reference and target peaks are too close to be identified from each other as shown in Figure 6.32.

Devices with $g_c = 450nm$ have spectrum that can be applied with curve fitting. Resonant peaks in four continuous periods within the range from 1552 to 1561.3 nm shown in Figure 6.33 are selected to be analysed.

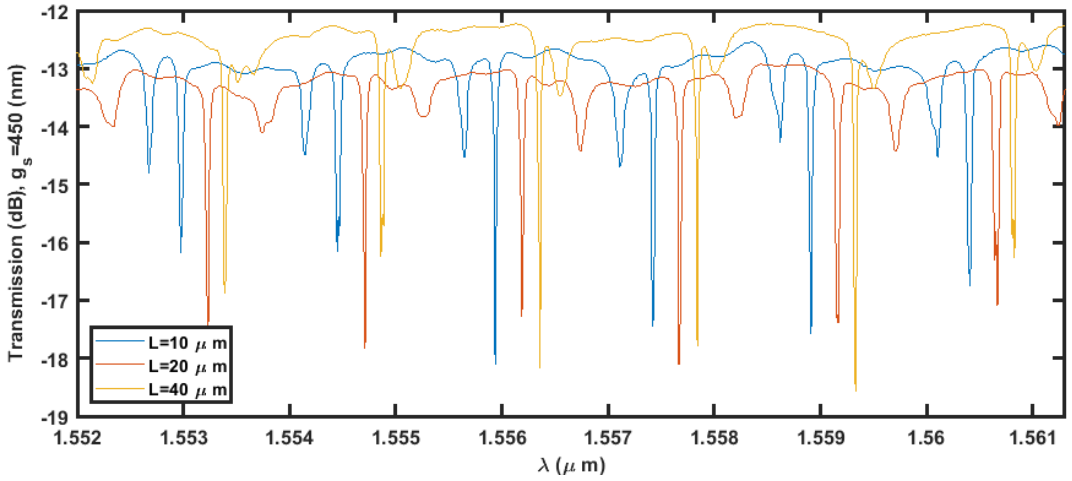

FIGURE 6.33: Resonant peaks within a range from 1552 to 1561.3 nm from rings with different suspended lengths L and the same coupler ($g_c = 450$ nm).

The measurement from four reference peaks and four target peaks from $L = 10\mu m$ are shown in Table 6.2. Here we use the coupling coefficient solved from reference peaks to extract the parameters from the adjacent target peaks.

TABLE 6.2: All-pass ring resonator modal parameters obtained from four reference peaks (first four) and four target peaks from $L = 10\mu m$ and $g_c = 450nm$. The losses here are the average loss according to the perimeter of the ring. Here we use the coupling coefficient solved from reference peaks to extract the parameters from the adjacent target peaks.

Reference peaks ($g_c = 450nm$, $L = 10\mu m$)							
λ_{res} **(nm)**	**ER (dB)**	**Q**	t^2	κ^2	α^2	**loss (dB/cm)**	**B**
1555.9	5.14	47025	0.898	0.102	0.970	0.0315	22.1
1557.4	4.66	42559	0.885	0.114	0.969	0.0324	20.4
1558.9	4.90	37374	0.872	0.128	0.963	0.0384	17.6
1560.4	3.98	29143	0.832	0.167	0.960	0.0420	14.3
Target peaks ($g_c = 450nm$, $L = 10\mu m$)							
1552.7	1.75	21041	0.898	0.102	0.895	0.115	3.51
1554.1	1.47	18378	0.885	0.114	0.890	0.120	3.45
1555.6	1.54	18819	0.872	0.128	0.901	0.108	4.12
1557.1	1.53	14819	0.832	0.167	0.880	0.132	3.33

From Table 6.2, coupling coefficient t is slightly higher than in Table 6.1, which is reasonable due to larger g_c. Resonant peak at $\lambda_{res} = 1560.4nm$ shows about 5% difference in coupling with other reference peaks rather than only 3% in Table 6.1 and 2% in rest reference peaks in Table 6.2. This may result from minor mode splitting that is not recognizable, so it is proper to be treated as an outlier. For reference peaks, the average coupling coefficient (t^2) and loss are 0.885 and 0.034 dB/cm, respectively. For

target peaks, the average loss is 0.119 dB/cm. Thus mode converters and suspended waveguide induces an extra loss of 0.085 dB/cm. The propagation losses in Table 6.2 are smaller than those in Table 6.2. The difference in propagation loss may be caused by the coupling loss that is hard to be evaluated analytically.

To evaluate the loss of the slotted strip waveguide, the propagation loss from resonant peaks from $L = 10\mu m$ and $g_c = 450nm$ are analysed. The extracted parameters are shown in Table 6.3. For reference peaks, the average coupling coefficient (t^2) and loss

TABLE 6.3: All-pass ring resonator modal parameters obtained from four reference peaks (first four) and four target peaks from $L = 20\mu m$ and $g_c = 450nm$. The losses here are the average loss according to the perimeter of the ring. Here we use the coupling coefficient solved from reference peaks to extract the parameters from the adjacent target peaks.

Reference peaks ($g_c = 450nm$, $L = 20\mu m$)							
λ_{res} **(nm)**	**ER (dB)**	**Q**	t^2	κ^2	α^2	**loss (dB/cm)**	**B**
1.5532	4.20	37730	0.870	0.130	0.967	0.0340	18.4
1.5550	4.72	45179	0.892	0.108	0.970	0.0311	21.6
1.5562	4.12	39024	0.873	0.127	0.969	0.0325	19.1
1.5577	5.01	41634	0.885	0.115	0.966	0.0354	19.6
Target peaks ($g_c = 450nm$, $L = 20\mu m$)							
1.5508	0.957	11783	0.870	0.130	0.815	0.212	1.49
1.5567	1.12	14442	0.892	0.108	0.845	0.174	1.89
1.5597	1.07	13744	0.873	0.127	0.844	0.175	2.03
1.5627	1.02	10747	0.836	0.164	0.808	0.220	1.57

are 0.855 and 0.033 dB/cm, respectively. For target peaks, the average loss is 0.195 dB/cm. Thus mode converters and suspended waveguide induces an extra loss of 0.162 dB/cm. We can combine the average propagation loss from Table 6.2 and Table 6.3 to find out the propagation loss for the mode converter and the slotted strip waveguide. The propagation loss of the slotted rib waveguide is 0.033 dB/cm. The length of the mode converter is 3 μm. The average propagation loss of the ring with the slotted strip waveguide long 20 and 40 μmu are 0.119 and 0.195 dB/cm, respectively. The propagation loss of the slotted strip waveguide and mode converter can be solved as 1.63 and 0.40 dB/cm, respectively. As a consequence, the fabrication process needs to be improved towards waveguide with less sidewall roughness to reduce the propagation loss and unexpected mode-splitting.

Usually, the measured propagation loss of the silicon slotted strip waveguide locates between 2 to 10 dB/cm reported in literature [121] [122] [123] [124]. The extracted propagation loss (0.2 dB/cm) from test design A is much smaller compared with typical value in literature (5 dB/cm). The oversized side wall roughness of the fabricated waveguide may be accounted for small propagation loss and large reflection in C band. From Figure 6.11 and Figure 6.10, the side wall roughness is more significant compared with simulation result shown in [124]. This oversized roughness may be possible to

cause more reflection than scattering in C band and it may cause different amount of reflection in different wavelength, which means the extracted parameters from fitted data are not precise. This perhaps explains why the condition of the mode-splitting is not consistent in the measured spectrum.

6.4.4 Test design B analysis before HF vapour etching

The test device array for test design B contains 8 devices combining different t and mode converters from bus-ring separation of $g_c = 300, 380\ nm$ (expected $t^2 = 0.5, 0.75$) and converter coupling distance from $g_m = 68$ to $80nm$ (illustrated in Figure 6.4). The aim of setting different converter coupling distances is to see how the design needs to be modified according to the product quality. The suspended length of all 8 devices is 15 μm. The reference and target ring resonator are designed with a perimeter of 415.74 μm ($100\pi + 100 + 1.58$). The measured device transmission spectrum before HF vapour etch from 1530 to 1600 nm with an input LASER power of 6 dBm are shown in Figure 6.34 and Figure 6.35.

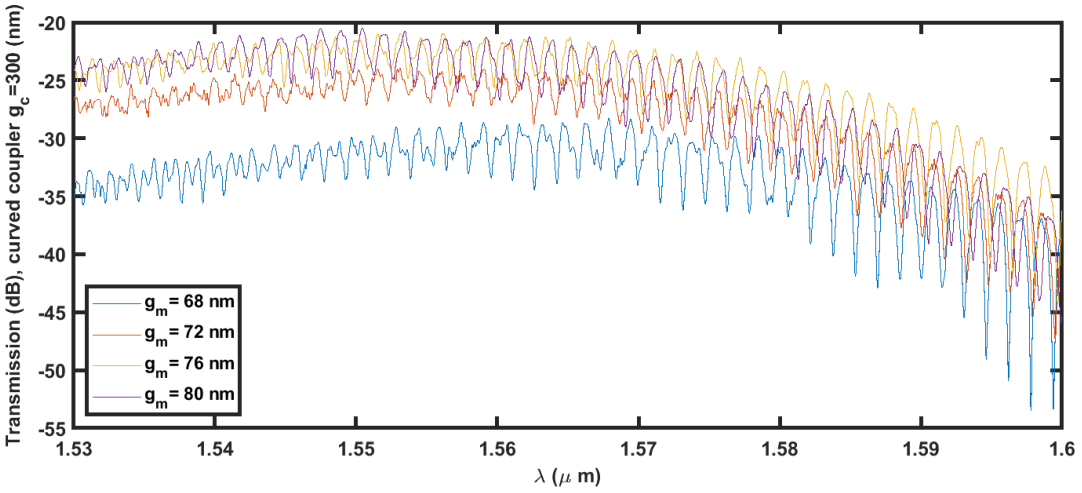

FIGURE 6.34: Resonant peaks within 1530 to 1600 nm from rings with $L = 15\mu m$ and $g_c = 300nm$.

In Figure 6.34, target peaks can hardly be recognized in the whole spectrum and especially in where $\lambda > 1.56\mu m$, which means the mode converter does not working properly (high loss) for g_m from 68 to 80 nm. The result agrees with the analysis result from test design A that the fabricated directional coupler has a different coupling coefficient compared with the simulation result due to the sidewall roughness. The extinction ratio of reference peaks is increased with the wavelength increased, which means the ratio of loss/coupling coefficient approaches to one with the wavelength increasing (according to Equation 5.32). Compared with the measurement results from the test design A, it is clear that this unique spectrum feature is the result of the curved

directional coupler. The extra loss is induced by the sidewall roughness, and it is enhanced by the bending waveguide applied in the curved directional coupler design.

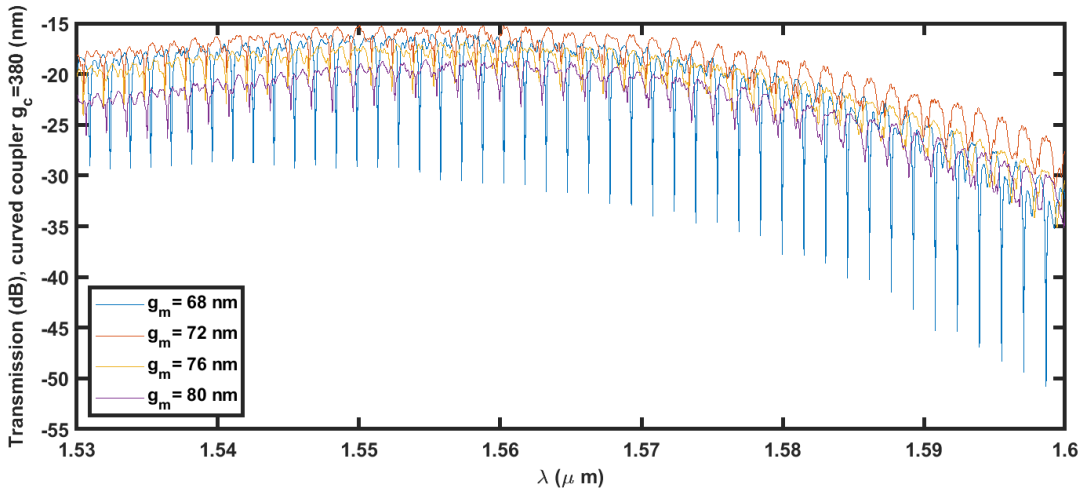

FIGURE 6.35: Resonant peaks within 1530 to 1600 nm from rings with $L = 15\mu m$ and $g_c = 380nm$.

The general feature of the spectrum shown in Figure 6.35 is similar to Figure 6.34, but the target peaks can be clearly recognized in the spectrum. Based on the fact that mode converter applied in Figure 6.35 are the same in Figure 6.34, curved coupler with larger coupling gap ($g_c = 380nm$) induces less loss than smaller one ($g_c = 300nm$), which is consistent with analysis in Section 6.4.3. Details of the resonant peaks are shown in Figure 6.36.

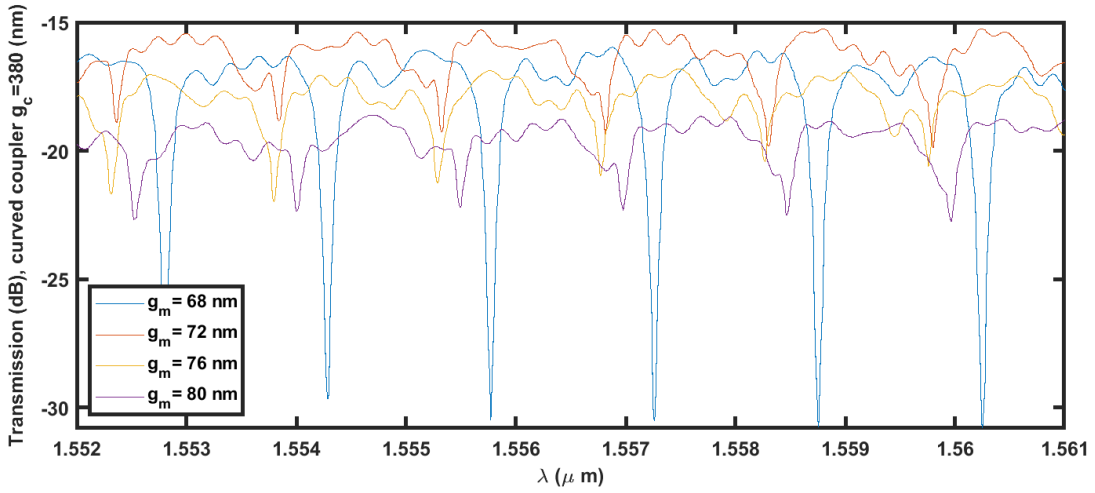

FIGURE 6.36: Resonant peaks within 1552 to 1561 nm from rings with $L = 15\mu m$ and $g_c = 380nm$.

From Figure 6.36, reference and target peaks can be clearly observed on the spectrum from the device with $g_c = 380nm$ and $g_c = 300nm$, but peaks from other devices are not at the same level regarding the extinction ratio. The quality of the fabricated curved directional coupler needs to be improved to provide better uniformity.

6.4.5 The performance degrading after HF vapour etching process

A comparison the spectrum before and after the HF vapour etching from device with $g_c = 350nm$, $L = 10\mu m$ are shown in Figure 6.37 and Figure 6.38. Generally, the coupling loss from the grating coupler is enhanced by HF vapour. This can be the result of the surface damage caused by high concentration HF solution during the etching. The highly concentrated HF will not only etch the silicon dioxide but also damaging the surface of the silicon, so the coupling efficiency is decreased due to the geometry change of the grating structure. This can be proved by the slightly different background spectrum shape in Figure 6.37 and Figure 6.38. Extra grating loss is roughly about 3 dB per coupler. There are two different results produced from HF vapour etching in different spectrum range for the same device.

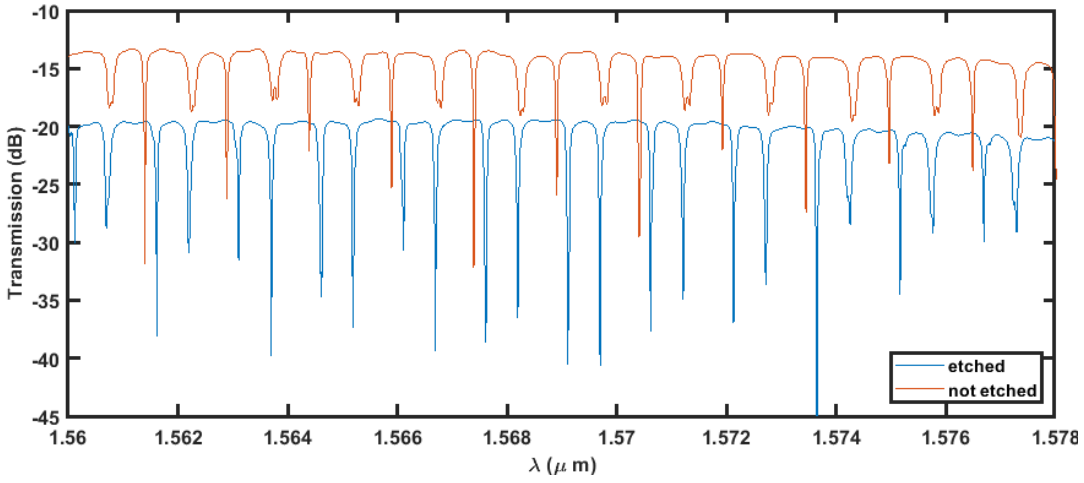

FIGURE 6.37: Resonant peaks within 1560 to 1578 nm from rings with $g_c = 350nm$, $L = 10\mu m$.

For the spectrum range from 1560 to 1578 nm shown in Figure 6.37 and longer wavelengths, the unexpected mode splitting is significantly improved, and the extinction ratio is enlarged. A spectrum shift after the etching can be clearly observed. We can recognize the reference and target peaks by evaluating the different spectrum shifts between reference and target peaks. The resonant frequency shift of reference peaks is relatively larger compared with one of the target peaks due to the thermo-optical spectrum shift from significant power enhancement factor B.
For the spectrum range from 1540 to 1558 nm shown in Figure 6.37 and shorter wavelengths, the condition of mode-splitting on target peaks is worse. If we look in detail at the shape of the reference peaks over the whole spectrum from HF etched device, minor mode-splitting can be observed on reference peaks as well, which is not the case before HF etching. Details of some HF etched reference peaks are shown in Figure 6.39 and Figure 6.40. In Figure 6.39 (a), a new and weaker resonant peak appears after HF vapour etching regarding resonant shape before HF vapour etching shown in Figure 6.39 (b). The new peak is possibly the result of extra silicon surface roughness due

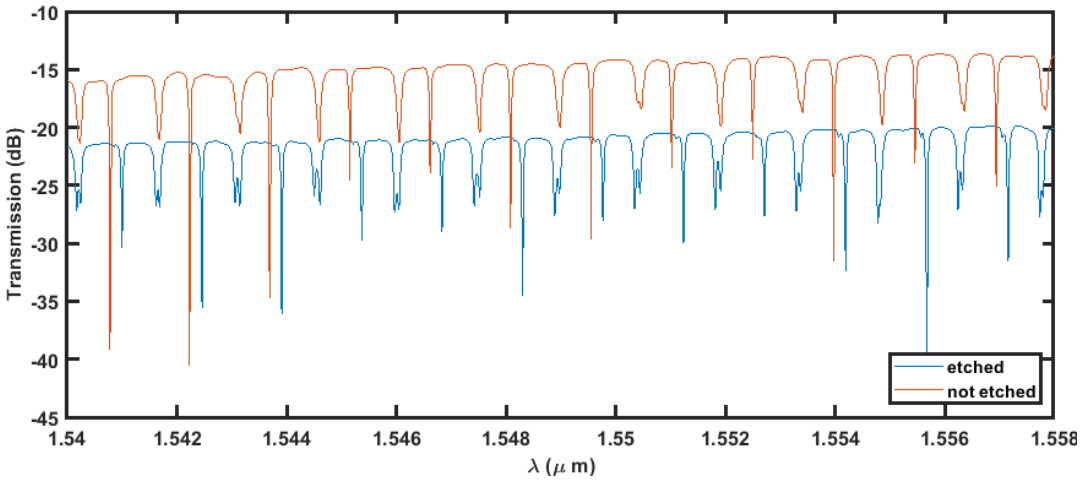

FIGURE 6.38: Resonant peaks within 1540 to 1558 nm from rings with $g_c = 350nm$, $L = 10\mu m$.

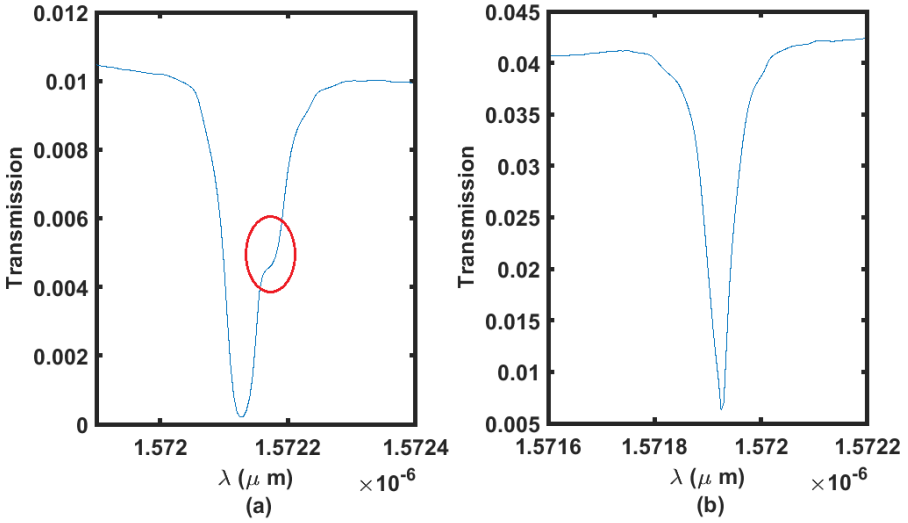

FIGURE 6.39: The same reference peak after ($\lambda_{res} = 1.5719\mu m$ in (b)) and before HF vapour etching ($\lambda_{res} = 1.5721\mu m$ in (a)). The shift of the resonant wavelength is $\Delta\lambda = 3nm$. Peaks can be found in Figure 6.37.

to the high concentration of HF vapour. In Figure 6.40 (a), a new resonant peak appears adjacent to resonant shape before HF vapour etching shown in Figure 6.40 (b).

In summary, HF vapour etching can seriously affect the performance of the device by damaging the silicon surface with vapour from high concentration HF vapour (48%). This will change the sidewall roughness of the waveguide and brings uncertainty to the fabrication quality. The mode-splitting on the reference peaks is enhanced with λ_{res} shorter than 1.558 μm. For target peaks, the mode splitting is enhanced when λ_{res} shorter than 1.54 μm while reduced at a longer wavelength. For a longer wavelength larger than 1.592 μm, no significant difference in mode-splitting is found between all peaks (reference and target) due to HF vapour etching. The uncertainty caused by HF

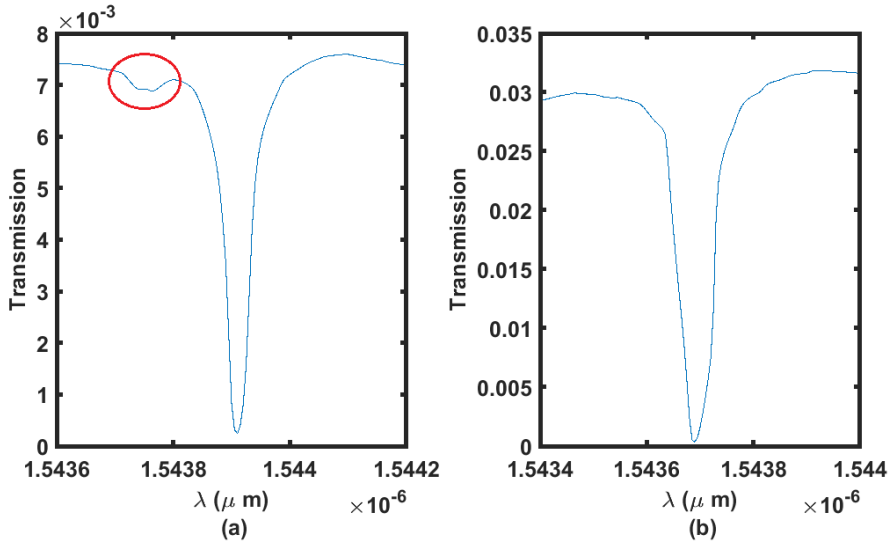

FIGURE 6.40: The same reference peak after ($\lambda_{res} = 1.5439\mu m$ in (b)) and before HF vapour etching ($\lambda_{res} = 1.5437\mu m$ in (a)). The shift of the resonant wavelength is $\Delta\lambda = 2nm$. Peaks can be found in Figure 6.38.

vapour etching can be improved by producing a smooth waveguide side before etching and applying the HF solution with a lower concentration (25%). Another method to improve the device performance is to shift the working wavelength from near-infrared range to middle infrared range, which is possible to make the current surface roughness tolerable.

6.5 Chapter conclusions

The feasibility of fabricating optical mode localized electrometer based on the specific fabrication conditions of the available equipment is investigated by several test runs of the fabrication with originally designed test devices dedicated in extracting parameters for electrometer design. The analysis shows that the fabricated suspended slot waveguide suffers from oversized sidewall roughness caused by silicon dioxide hard mask and HF vapour etching process. Further improvement of this problem is possible by alternative design and fabrication flow.

Experimental results showed that the surface roughness during the etching seriously affects the output spectrum with unexpected mode splitting from waveguide mode reflection in the ring resonator. The propagation loss of the waveguide or addition optical loss is induced by surface roughness that can hardly be considered during the design. The critical damage of the structure or additional optical loss is induced with inappropriate structural releasing by HF vapour. The HF solution with a lower concentration probably helps in producing less roughness if the wet oxidation of silicon during the HF etching can be reduced as assumed.

Chapter 7

Conclusions

7.1 Summary of findings

We established an analytical approximation of the index and phase change induced by the NOEMS slot modulator using the finite element analysis (FEA), including the Casimir force, optical force, electrostatic force and pull-in effect. The modulator performance can be adjusted by configuring the electrostatic actuator in different ways to provide more flexibility in modulator design. The fully suspended conducted slot and grounded slot are analysed in detail due to the strong tuning ability of the index and phase of the waveguide.

The modulator configured in the fully suspended conducted slot configuration has a stronger tuning ability compared with the grounded slot configuration. For the conducted slot, the Casimir force, optical force and electrostatic force are in the same direction, which makes the tuning energy efficient. The narrow actuating gap between slot arms provides a large actuating force but limits the tuning range and suspended slot length due to the strong pull-in effect. The analytical approximation agrees with the simulation result from conducted slot configuration.

In the grounded slot configuration, the electrostatic force is set in the opposite direction of the rest forces, which needs more energy in tuning but achieves a wide tuning range. The external electrodes in this configuration allow the modulator to be designed with a flexible actuating gap and a longer suspended slot. It is preferred considering the integration between the modulator and other silicon photonic devices.

The simulation results showed that the slot modulator operated at the near-infrared range has the advantages of low energy consumption and high tuning ability compared with conventional carrier-based modulators. The highest modulating frequency is limited to tens of megahertz that are relatively low for communication but suitable

for sensing applications. It can be used as a transducer that converts the charge variation into effective index variation of the waveguide.

The analytical model of the coupled ring resonators is established and examined by Lumerical simulation. The feedback theory of the signal flow graph, or Mason's rule, provides an analytical method of analysing photonic circuitry without the help of the numerical simulation, though the accuracy is limited by numerical approximation during the calculation. Based on the four-port structure originate from the add-drop filter, two output spectrum with mode-localization and symmetric mode-splitting provide a new dimension for signal analysis. Combining the two spectrum allows the high-sensitivity sensing and dual-channel calibration to be carried out simultaneously, which makes the sensor adopts sensing in harsh environments.

We proved that the optical mode-localization sensing has advantages in sensitivity, accuracy, anti-aliasing and noise immunity compared with mechanical mode-localization one. The optomechanical electrometer designed from coupled ring resonators and NOEMS slot modulator is proved to be more sensitive among other on-chip electrometers in theory.

The capability of the device fabrication is investigated through few test runs. The specific structural releasing process based on HF vapour etching is developed for suspended waveguide. The dedicated test device designed for extracting the basic components parameter from the all-pass ring configuration is proved as a useful method of examining the fabrication quality. The scanning electron microscopy (SEM) inspection and output spectrum analysis indicated that the surface roughness caused by fabrication imperfections would significantly affect the performance of the devices.

The evidence is clear that the current fabrication flow does not provide enough quality (surface roughness) for the electrometer design. The HF vapour causes significant surface damage on silicon from highly concentrated HF solutions during the HF vapour etching.

7.2 Future works

The specific mode converter is necessary to reduce the insertion loss between the supported waveguide and suspended waveguide to integrate the suspended slot modulator with the ring resonators. In the conducted slot configuration, the existed mode converter design consumes a large chip area that makes the light travel path length too long to have a reasonable free spectrum range for the ring resonators. The grounded slot configuration of the modulator can offer a compact modulator to achieve integration but with the cost of lower tuning ability. A further investigation into the compact

mode converter design for the conducted slot configuration is necessary to realize the theoretical best sensitivity.

Based on the analysis in section 5.4, the state of art sensitivity is achieved by embedding the conducted slot modulators as transducers. However, the measurement range is extremely narrow in the available suspended lengths, allowing the eletrometer to be applied as a scientific instrument only. This drawback is capable of being covered by replacing the conducted slot configuration with grounded one. The investigation about the mode localization with grounded slot modulator towards electrometer design for general purpose sensing should be considered in the future.

The energy coupling path between the ring resonator and bus waveguide is constructed by a directional coupler in the current design. The experimental analysis showed that the cross-coupling coefficient of the directional couplers is always lower than the designed values due to the unexpected surface roughness. Uncertainties in getting the expected coupling coefficient in the experiment result in a high workload in fabricating many devices and finding the suitable one for analysis. More robust coupling can be realized by utilizing 2×2 multi-mode interferometer (MMI). The performance of the MMI is less affected by the surface roughness by keeping most modal energy away from the boundary scattering. However, the limited number of available power coupling ratios (50:50,15:85,10:90) needs to be considered.

Minimizing the influences from the sidewall roughness is essential in reflection and noise reduction. It can be improved by either modifying the electrometer design to a single-layer device to eliminate the excessive roughness induced from PECVD silicon dioxide or shift the working wavelength from near-infrared range to middle-infrared range, which is less sensitive to surface roughness at the current level. The surface damage caused by HF vapour may be improved by developing a new HF vapour etching recipe with less concentrated HF solution from 48 % to 25 %.

In principle, the concept of the optical mode localized sensing can be adopted to a wide range of waveguide systems such as fiber and radio frequency waveguide. More sensing applications are possible to be investigated under the topic of optical mode localized sensing by alternative waveguide material, working frequency and transducer for different physical quantities. A broad range of research can be expected in the future. The high sensitivity nature of the optical mode localized sensing can help improving the performance of some conventional design and to push them a step further, which could be valuable from industrial side of view. Regarding the current design of the NOEMS electrometer, high performance inertial sensors could be an excellent candidate to be adopted with optical mode localized sensing.

Chapter 8

List of publications

8.1 Published papers

Yu Feng, David J. Thomson, Goran Z. Mashanovich, and Jize Yan. "Performance analysis of a silicon NOEMS device applied as optical modulator based on a slot waveguide" *Optics Express* 28.25 (2020): 38206-38222.

Lidong Du, Zhan Zhao, Zhen Fang, Yu Feng, and Jize Yan. "Thermodynamic control of MEMS meteorology pressure sensing element in low-temperature application down to $-45°C$." *IET Science, Measurement & Technology* 11.7 (2017): 907-913. (technical support)

8.2 In progress

Yu Feng, Shumeng Wang, Goran Z. Mashanovich and Jize Yan. "Theory analysis of the optical mode localized sensing based on coupled ring resonators"

Fei He, Yu Feng, Hailong Pi, Jize Yan, Kevin F. MacDonald and Xu Fang. "Coherently switching the light focus of all-dielectric metalenses"

References

[1] Yu Feng, David J Thomson, Goran Z Mashanovich, and Jize Yan. Performance analysis of a silicon noems device applied as an optical modulator based on a slot waveguide. *Optics Express*, 28(25):38206–38222, 2020.

[2] Winnie N Ye and Yule Xiong. Review of silicon photonics: history and recent advances. *Journal of Modern Optics*, 60(16):1299–1320, 2013.

[3] Alex Abramovici, William E Althouse, Ronald WP Drever, Yekta Gürsel, Seiji Kawamura, Frederick J Raab, David Shoemaker, Lisa Sievers, Robert E Spero, Kip S Thorne, et al. LIGO: The laser interferometer gravitational-wave observatory. *Science*, 256(5055):325–333, 1992.

[4] Chun Zhao, Mohammad H Montaseri, Graham S Wood, Suan Hui Pu, Ashwin A Seshia, and Michael Kraft. A review on coupled mems resonators for sensing applications utilizing mode localization. *Sensors and Actuators A: Physical*, 249: 93–111, 2016.

[5] Matthew Spletzer, Arvind Raman, Alexander Q Wu, Xianfan Xu, and Ron Reifenberger. Ultrasensitive mass sensing using mode localization in coupled microcantilevers. *Applied Physics Letters*, 88(25):254102, 2006.

[6] Pradyumna Thiruvenkatanathan, Jize Yan, and A Ashwin Seshia. Common mode rejection in electrically coupled mems resonators utilizing mode localization for sensor applications. In *2009 IEEE International Frequency Control Symposium Joint with the 22nd European Frequency and Time forum*, pages 358–363. IEEE, 2009.

[7] Robert A Minasian. Photonic signal processing of microwave signals. *IEEE Transactions on Microwave Theory and Techniques*, 54(2):832–846, 2006.

[8] Han Du, Fook Siong Chau, and Guangya Zhou. Mechanically-tunable photonic devices with on-chip integrated MEMS/NEMS actuators. *Micromachines*, 7(4):69, 2016.

[9] GC Righini, Yannick Dumeige, Patrice Féron, Maurizio Ferrari, G Nunzi Conti, Davor Ristic, and Silvia Soria. Whispering gallery mode microresonators: fundamentals and applications. *Rivista del nuovo cimento*, 34(7):435–488, 2011.

[10] TJ Kippenberg, H Rokhsari, T Carmon, A Scherer, and KJ Vahala. Analysis of radiation-pressure induced mechanical oscillation of an optical microcavity. *Physical Review Letters*, 95(3):033901, 2005.

[11] Dries Van Thourhout and Joris Roels. Optomechanical device actuation through the optical gradient force. *Nature Photonics*, 4(4):211, 2010.

[12] Tobias J Kippenberg and Kerry J Vahala. Cavity optomechanics: back-action at the mesoscale. *Science*, 321(5893):1172–1176, 2008.

[13] Alejandro W Rodriguez, Pui-Chuen Hui, David P Woolf, Steven G Johnson, Marko Lončar, and Federico Capasso. Classical and fluctuation-induced electromagnetic interactions in micron-scale systems: designer bonding, antibonding, and casimir forces. *Annalen der Physik*, 527(1-2):45–80, 2015.

[14] Evgenni Mikhailovich Lifshitz, M Hamermesh, et al. The theory of molecular attractive forces between solids. In *Perspectives in Theoretical Physics*, pages 329–349. Elsevier, 1992.

[15] GL Klimchitskaya, U Mohideen, and VM Mostepanenko. The casimir force between real materials: Experiment and theory. *Reviews of Modern Physics*, 81(4): 1827, 2009.

[16] Robert W Boyd. *Nonlinear optics*. Elsevier, 2003.

[17] PL Kelley. Self-focusing of optical beams. *Physical Review Letters*, 15(26):1005, 1965.

[18] Daniel Royer and Eugene Dieulesaint. *Elastic waves in solids II: generation, acousto-optic interaction, applications*. Springer Science & Business Media, 1999.

[19] LS Hounsome, R Jones, MJ Shaw, and PR Briddon. Photoelastic constants in diamond and silicon. *physica status solidi (a)*, 203(12):3088–3093, 2006.

[20] John David Jackson. *Classical electrodynamics*. American Association of Physics Teachers, 1999.

[21] Jacob T Robinson, Kyle Preston, Oskar Painter, and Michal Lipson. First-principle derivation of gain in high-index-contrast waveguides. *Optics Express*, 16(21): 16659–16669, 2008.

[22] Albert Birner, Ralf B Wehrspohn, Ulrich M Gösele, and Kurt Busch. Silicon-based photonic crystals. *Advanced Materials*, 13(6):377–388, 2001.

[23] Min Ren, Jianguo Huang, Hong Cai, Julius Minglin Tsai, Jinxiong Zhou, Zishun Liu, Zhigang Suo, and Ai-Qun Liu. Nano-optomechanical actuator and pull-back instability. *ACS nano*, 7(2):1676–1681, 2013.

[24] Hossein Rokhsari, Tobias J Kippenberg, Tal Carmon, and Kerry J Vahala. Radiation-pressure-driven micro-mechanical oscillator. *Optics Express*, 13(14): 5293–5301, 2005.

[25] Raphaël Van Laer, Bart Kuyken, Dries Van Thourhout, and Roel Baets. Interaction between light and highly confined hypersound in a silicon photonic nanowire. *Nature Photonics*, 9(3):199, 2015.

[26] Joris Roels, Iwijn De Vlaminck, Liesbet Lagae, Bjorn Maes, Dries Van Thourhout, and Roel Baets. Tunable optical forces between nanophotonic waveguides. *Nature nanotechnology*, 4(8):510, 2009.

[27] Franck Chollet. Devices based on co-integrated MEMS actuators and optical waveguide: A review. *Micromachines*, 7(2):18, 2016.

[28] Sangyoon Han, Tae Joon Seok, Niels Quack, Byung-Wook Yoo, and Ming C Wu. Large-scale silicon photonic switches with movable directional couplers. *Optica*, 2(4):370–375, 2015.

[29] M-CM Lee, Dooyoung Hah, Erwin K Lau, Hiroshi Toshiyoshi, and Ming Wu. MEMS-actuated photonic crystal switches. *IEEE photonics technology letters*, 18(2): 358–360, 2006.

[30] Hongbin Yu, Guangya Zhou, Xiongyue Chew, Sujeet K Sinha, and Fook Siong Chau. Nano-tribometer integrated with a nano-photonic displacement-sensing mechanism. *Journal of Micromechanics and Microengineering*, 21(6):065014, 2011.

[31] Renilkumar Mudachathi and Prita Nair. Low-voltage widely tunable photonic crystal channel drop filter in SOI wafer. *Journal of Microelectromechanical systems*, 21(1):190–197, 2011.

[32] Karel Van Acoleyen, Joris Roels, Pauline Mechet, Tom Claes, Dries Van Thourhout, and Roel Baets. Ultracompact phase modulator based on a cascade of NEMS-operated slot waveguides fabricated in silicon-on-insulator. *IEEE Photonics Journal*, 4(3):779–788, 2012.

[33] FL Degertekin, B Hadimioglu, T Sulchek, and CF Quate. Actuation and characterization of atomic force microscope cantilevers in fluids by acoustic radiation pressure. *Applied Physics Letters*, 78(11):1628–1630, 2001.

[34] King Y Fong, Wolfram HP Pernice, Mo Li, and Hong X Tang. Tunable optical coupler controlled by optical gradient forces. *Optics Express*, 19(16):15098–15108, 2011.

[35] Jun-Yu Ou, Eric Plum, Jianfa Zhang, and Nikolay I Zheludev. An electromechanically reconfigurable plasmonic metamaterial operating in the near-infrared. *Nature nanotechnology*, 8(4):252, 2013.

[36] John Heebner, Rohit Grover, Tarek Ibrahim, and Tarek A Ibrahim. *Optical microresonators: theory, fabrication, and applications*, volume 138. Springer Science & Business Media, 2008.

[37] Joris Roels, Björn Maes, Wim Bogaerts, Roel Baets, and Dries Van Thourhout. Parametric instability of an integrated micromechanical oscillator by means of active optomechanical feedback. *Optics Express*, 19(14):13081–13088, 2011.

[38] Mo Li, WHP Pernice, C Xiong, T Baehr-Jones, M Hochberg, and HX Tang. Harnessing optical forces in integrated photonic circuits. *Nature*, 456(7221):480, 2008.

[39] JN Westwood-Bachman, Z Diao, VTK Sauer, D Bachman, and WK Hiebert. Even nanomechanical modes transduced by integrated photonics. *Applied Physics Letters*, 108(6):061103, 2016.

[40] Parag B Deotare, Irfan Bulu, Ian W Frank, Qimin Quan, Yinan Zhang, Rob Ilic, and Marko Loncar. All optical reconfiguration of optomechanical filters. *Nature Communications*, 3:846, 2012.

[41] Bin Dong, H Cai, Geok Ing Ng, P Kropelnicki, JM Tsai, AB Randles, M Tang, YD Gu, ZG Suo, and Ai Qun Liu. A nanoelectromechanical systems actuator driven and controlled by Q-factor attenuation of ring resonator. *Applied Physics Letters*, 103(18):181105, 2013.

[42] VB Braginsky, SE Strigin, and S Pr Vyatchanin. Parametric oscillatory instability in fabry–perot interferometer. *Physics Letters A*, 287(5-6):331–338, 2001.

[43] Albert Schliesser, Pascal Del'Haye, Nima Nooshi, KJ Vahala, and TJ Kippenberg. Radiation pressure cooling of a micromechanical oscillator using dynamical backaction. *Physical Review Letters*, 97(24):243905, 2006.

[44] Markus Aspelmeyer, Tobias J Kippenberg, and Florian Marquardt. Cavity optomechanics. *Reviews of Modern Physics*, 86(4):1391, 2014.

[45] Allen HJ Yang, Sean D Moore, Bradley S Schmidt, Matthew Klug, Michal Lipson, and David Erickson. Optical manipulation of nanoparticles and biomolecules in sub-wavelength slot waveguides. *Nature*, 457(7225):71, 2009.

[46] Vittorio Passaro, Francesco Dell'Olio, Caterina Ciminelli, and Mario Armenise. Efficient chemical sensing by coupled slot SOI waveguides. *Sensors*, 9(2):1012–1032, 2009.

[47] Carlos A Barrios, Kristinn B Gylfason, Benito Sánchez, Amadeu Griol, Hans Sohlström, Miquel Holgado, and Raphael Casquel. Slot-waveguide biochemical sensor. *Optics Letters*, 32(21):3080–3082, 2007.

[48] Vilson R Almeida, Qianfan Xu, Carlos A Barrios, and Michal Lipson. Guiding and confining light in void nanostructure. *Optics Letters*, 29(11):1209–1211, 2004.

[49] Lukas Chrostowski, Samantha Grist, Jonas Flueckiger, Wei Shi, Xu Wang, Eric Ouellet, Han Yun, Mitch Webb, Ben Nie, Zhen Liang, et al. Silicon photonic resonator sensors and devices. In *Laser Resonators, Microresonators, and Beam Control XIV*, volume 8236, page 823620. International Society for Optics and Photonics, 2012.

[50] JE-Y Lee, Y Zhu, and AA Seshia. A micromechanical electrometer approaching single-electron charge resolution at room temperature. In *2008 IEEE 21st International Conference on Micro Electro Mechanical Systems*, pages 948–951. IEEE, 2008.

[51] Goran Stemme. Resonant silicon sensors. *Journal of Micromechanics and Microengineering*, 1(2):113, 1991.

[52] Hemin Zhang, Jie Huang, Weizheng Yuan, and Honglong Chang. A high-sensitivity micromechanical electrometer based on mode localization of two degree-of-freedom weakly coupled resonators. *Journal of Microelectromechanical Systems*, 25(5):937–946, 2016.

[53] Dong F Wang, Keisuke Chatani, Tsuyoshi Ikehara, and Ryutaro Maeda. Mode localization analysis and characterization in a 5-beam array of coupled nearly identical micromechanical resonators for ultra-sensitive mass detection and analyte identification. *Microsystem technologies*, 18(11):1923–1929, 2012.

[54] Pradyumna Thiruvenkatanathan, Jim Woodhouse, Jize Yan, and Ashwin A Seshia. Limits to mode-localized sensing using micro-and nanomechanical resonator arrays. *Journal of Applied Physics*, 109(10):104903, 2011.

[55] Ross Gunn. Principles of a new portable electrometer. *Physical Review*, 40(2):307, 1932.

[56] H Palevsky, RK Swank, and Rev Grenchik. Design of dynamic condenser electrometers. *Review of Scientific Instruments*, 18(5):298–314, 1947.

[57] Gerardo Jaramillo, Cesare Buffa, Mo Li, Fred J Brechtel, Giacomo Langfelder, and David A Horsley. MEMS electrometer with femtoampere resolution for aerosol particulate measurements. *IEEE Sensors Journal*, 13(8):2993–3000, 2013.

[58] B Starmark, Torsten Henning, T Claeson, P Delsing, and AN Korotkov. Gain dependence of the noise in the single electron transistor. *Journal of applied physics*, 86(4):2132–2136, 1999.

[59] Andrew N Cleland and Michael L Roukes. A nanometre-scale mechanical electrometer. *Nature*, 392(6672):160, 1998.

[60] H Krömmer, Artur Erbe, A Tilke, S Manus, and RH Blick. Nanomechanical resonators operating as charge detectors in the nonlinear regime. *EPL (Europhysics Letters)*, 50(1):101, 2000.

[61] Pallab Bhattacharya, Roberto Fornari, and Hiroshi Kamimura. *Comprehensive Semiconductor Science and Technology: Online Version*. Newnes, 2011.

[62] Yu A Pashkin, Y Nakamura, and Jaw-Shen Tsai. Room-temperature al single-electron transistor made by electron-beam lithography. *Applied Physics Letters*, 76 (16):2256–2258, 2000.

[63] Joshua Lee, Yong Zhu, and Ashwin Seshia. Room temperature electrometry with sub-10 electron charge resolution. *Journal of Micromechanics and Microengineering*, 18(2):025033, 2008.

[64] Andreas Menzel, Angel T-H Lin, Pedro Estrela, Peng Li, and Ashwin A Seshia. Biomolecular and electrochemical charge detection by a micromechanical electrometer. *Sensors and Actuators B: Chemical*, 160(1):301–305, 2011.

[65] Joshua E-Y Lee, Behraad Bahreyni, and Ashwin A Seshia. An axial strain modulated double-ended tuning fork electrometer. *Sensors and Actuators A: Physical*, 148(2):395–400, 2008.

[66] Jiuxuan Zhao, Hong Ding, Sheng Ni, Lifeng Fu, Wen Wang, and Jin Xie. High-resolution and large dynamic range electrometer with adjustable sensitivity based on micro resonator and electrostatic actuator. In *2016 IEEE 29th International Conference on Micro Electro Mechanical Systems (MEMS)*, pages 1074–1077. IEEE, 2016.

[67] Dongyang Chen, Jiuxuan Zhao, Yinshen Wang, and Jin Xie. An electrostatic charge sensor based on micro resonator with sensing scheme of effective stiffness perturbation. *Journal of Micromechanics and Microengineering*, 27(6):065002, 2017.

[68] Jing Yang, Hao Kang, and Honglong Chang. A micro resonant electrometer with 9-electron charge resolution in room temperature. In *2018 IEEE Micro Electro Mechanical Systems (MEMS)*, pages 67–70. IEEE, 2018.

[69] Peter T Rakich, Paul Davids, and Zheng Wang. Tailoring optical forces in waveguides through radiation pressure and electrostrictive forces. *Optics Express*, 18 (14):14439–14453, 2010.

[70] Tobias J Kippenberg and Kerry J Vahala. Cavity opto-mechanics. *Optics Express*, 15(25):17172–17205, 2007.

[71] Tamma Satya Narasimhamurty. *Photoelastic and electro-optic properties of crystals*. Springer Science & Business Media, 2012.

[72] Michelle L Povinelli, Marko Lončar, Mihai Ibanescu, Elizabeth J Smythe, Steven G Johnson, Federico Capasso, and John D Joannopoulos. Evanescent-wave bonding between optical waveguides. *Optics Letters*, 30(22):3042–3044, 2005.

[73] H Cai, KJ Xu, AQ Liu, Q Fang, MB Yu, Guo-Qing Lo, and Dim Lee Kwong. Nano-opto-mechanical actuator driven by gradient optical force. *Applied Physics Letters*, 100(1):013108, 2012.

[74] Jianping Zou, Zsolt Marcet, Alejandro W Rodriguez, Michael T Homer Reid, Alexander P Mccauley, Ivan I Kravchenko, T Lu, Y Bao, Steven G Johnson, and Ho Bun Chan. Casimir forces on a silicon micromechanical chip. *Nature communications*, 4(1):1–6, 2013.

[75] FP Beer, ER Johnston, and JT DeWolf. Mechanics of materials, 5th si edition. *Stress*, 1(10):1–12, 1999.

[76] John Milton Amiss, Franklin D Jones, and Henry H Ryffel. *Guide to the Use of Tables and Formulas in Machinery's Handbook*. Industrial Press Inc., 2004.

[77] John Baker, Lord Baker, and Jacques Heyman. *Plastic design of frames 1 fundamentals*, volume 1. CUP Archive, 1980.

[78] David EJ Armstrong and Edmund Tarleton. Bend testing of silicon microcantilevers from 21 c to 770 c. *Jom*, 67(12):2914–2920, 2015.

[79] William W Seto. Theory and problems of mechanical vibrations. *Schaum's Outline Series, New York: Schaum Publications, 1964*, 1964.

[80] Sayanu Pamidighantam, Robert Puers, Kris Baert, and Harrie AC Tilmans. Pull-in voltage analysis of electrostatically actuated beam structures with fixed–fixed and fixed–free end conditions. *Journal of Micromechanics and Microengineering*, 12 (4):458, 2002.

[81] Harvey C Nathanson, William E Newell, Robert A Wickstrom, and J Ransford Davis. The resonant gate transistor. *IEEE Transactions on Electron Devices*, 14(3): 117–133, 1967.

[82] Giuseppe Coppola, Luigi Sirleto, Ivo Rendina, and Mario Iodice. Advance in thermo-optical switches: principles, materials, design, and device structure. *Optical Engineering*, 50(7):071112, 2011.

[83] Saeed Sharif Azadeh, Florian Merget, Sebastian Romero-García, Alvaro Moscoso-Mártir, Nils von den Driesch, Juliana Müller, Siegfried Mantl, Dan Buca, and Jeremy Witzens. Low v π silicon photonics modulators with highly linear epitaxially grown phase shifters. *Optics Express*, 23(18):23526–23550, 2015.

[84] Tianran Liu, Francesco Pagliano, and Andrea Fiore. Nano-opto-electro-mechanical switch based on a four-waveguide directional coupler. *Optics Express*, 25(9):10166–10176, 2017.

[85] Christian Haffner, Andreas Joerg, Michael Doderer, Felix Mayor, Daniel Chelladurai, Yuriy Fedoryshyn, Cosmin Ioan Roman, Mikael Mazur, Maurizio Burla, Henri J Lezec, et al. Nano–opto-electro-mechanical switches operated at cmos-level voltages. *Science*, 366(6467):860–864, 2019.

[86] Francesco De Leonardis, Martino De Carlo, and Vittorio Passaro. Design rules for a nano-opto-mechanical actuator based on suspended slot waveguides. *Photonics*, 4(3):43, 2017.

[87] Yuxin Sun, Daining Fang, and Ai Kah Soh. Thermoelastic damping in micro-beam resonators. *International Journal of Solids and Structures*, 43(10):3213–3229, 2006.

[88] Chuanli Zhang, Guanshui Xu, and Qing Jiang. Analysis of the air-damping effect on a micromachined beam resonator. *Mathematics and mechanics of solids*, 8(3):315–325, 2003.

[89] Zhili Hao, Ahmet Erbil, and Farrokh Ayazi. An analytical model for support loss in micromachined beam resonators with in-plane flexural vibrations. *Sensors and Actuators A: Physical*, 109(1-2):156–164, 2003.

[90] Graham T Reed, G Mashanovich, F Yand Gardes, and DJ Thomson. Silicon optical modulators. *Nature photonics*, 4(8):518–526, 2010.

[91] David AB Miller. Energy consumption in optical modulators for interconnects. *Optics Express*, 20(102):A293–A308, 2012.

[92] Chi Xiong, Douglas M Gill, Jonathan E Proesel, Jason S Orcutt, Wilfried Haensch, and William MJ Green. Monolithic 56 gb/s silicon photonic pulse-amplitude modulation transmitter. *Optica*, 3(10):1060–1065, 2016.

[93] Jeremy Witzens. High-speed silicon photonics modulators. *Proceedings of the IEEE*, 106(12):2158–2182, 2018.

[94] Joyce KS Poon, Jacob Scheuer, Shayan Mookherjea, George T Paloczi, Yanyi Huang, and Amnon Yariv. Matrix analysis of microring coupled-resonator optical waveguides. *Optics express*, 12(1):90–103, 2004.

[95] V Yu Venediktov, Yu V Filatov, and Egor Vadimovich Shalymov. Passive ring resonator micro-optical gyroscopes. *Quantum Electronics*, 46(5):437, 2016.

[96] Zhanshi Yao, Kaiyi Wu, Bo Xue Tan, Jiawei Wang, Yu Li, Yu Zhang, and Andrew W Poon. Integrated silicon photonic microresonators: emerging technologies. *IEEE Journal of Selected Topics in Quantum Electronics*, 24(6):1–24, 2018.

[97] Shaoqi Feng, Ting Lei, Hui Chen, Hong Cai, Xianshu Luo, and Andrew W Poon. Silicon photonics: from a microresonator perspective. *Laser & photonics reviews*, 6 (2):145–177, 2012.

[98] Amnon Yariv. Universal relations for coupling of optical power between microresonators and dielectric waveguides. *Electronics letters*, 36(4):321–322, 2000.

[99] Samuel J Mason. Feedback theory-some properties of signal flow graphs. *Proceedings of the IRE*, 41(9):1144–1156, 1953.

[100] Seungwoo Jung, Ickhyun Song, and John D Cressler. Systematic methodology for applying mason's signal flow graph to analysis of feedback circuits. In *2014 IEEE International Symposium on Circuits and Systems (ISCAS)*, pages 2421–2424. IEEE, 2014.

[101] Sanjoy Mandal, Kamal Dasgupta, TK Basak, and SK Ghosh. A generalized approach for modeling and analysis of ring-resonator performance as optical filter. *Optics Communications*, 264(1):97–104, 2006.

[102] Sabitabrata Dey and Sanjoy Mandal. Modeling and analysis of quadruple optical ring resonator performance as optical filter using vernier principle. *Optics Communications*, 285(4):439–446, 2012.

[103] Chun Zhao, Graham S Wood, Jianbing Xie, Honglong Chang, Suan Hui Pu, and Michael Kraft. A force sensor based on three weakly coupled resonators with ultrahigh sensitivity. *Sensors and Actuators A: Physical*, 232:151–162, 2015.

[104] Thomas B Gabrielson. Mechanical-thermal noise in micromachined acoustic and vibration sensors. *IEEE transactions on Electron Devices*, 40(5):903–909, 1993.

[105] Dominik G Rabus. *Integrated ring resonators*. Springer, 2007.

[106] Lukas Chrostowski and Michael Hochberg. *Silicon photonics design: from devices to systems*. Cambridge University Press, 2015.

[107] Amnon Yariv and Pochi Yeh. *Photonics: optical electronics in modern communications*, volume 6. Oxford university press New York, 2007.

[108] Wim Bogaerts, Peter De Heyn, Thomas Van Vaerenbergh, Katrien De Vos, Shankar Kumar Selvaraja, Tom Claes, Pieter Dumon, Peter Bienstman, Dries Van Thourhout, and Roel Baets. Silicon microring resonators. *Laser & Photonics Reviews*, 6(1):47–73, 2012.

[109] Reja Amatya, Charles W Holzwarth, MA Popovic, F Gan, HI Smith, F Kartner, and RJ Ram. Low power thermal tuning of second-order microring resonators. In *2007 Conference on Lasers and Electro-Optics (CLEO)*, pages 1–2. IEEE, 2007.

[110] Bradley J Frey, Douglas B Leviton, and Timothy J Madison. Temperature-dependent refractive index of silicon and germanium. In *Optomechanical technologies for Astronomy*, volume 6273, page 62732J. International Society for Optics and Photonics, 2006.

[111] CZ Tan and J Arndt. Temperature dependence of refractive index of glassy sio2 in the infrared wavelength range. *Journal of Physics and Chemistry of Solids*, 61(8): 1315–1320, 2000.

[112] Brent E Little, JS Foresi, G Steinmeyer, ER Thoen, ST Chu, HA Haus, E Pb Ippen, LC Kimerling, and W Greene. Ultra-compact si-sio 2 microring resonator optical channel dropping filters. *IEEE Photonics Technology Letters*, 10(4):549–551, 1998.

[113] Samuel J Mason. Feedback theory: Further properties of signal flow graphs. 1956.

[114] Qingzhong Deng, Lu Liu, Xinbai Li, and Zhiping Zhou. Strip-slot waveguide mode converter based on symmetric multimode interference. *Optics Letters*, 39 (19):5665–5668, 2014.

[115] J Soler Penadés, C Alonso-Ramos, AZ Khokhar, Milos Nedeljkovic, LA Boodhoo, A Ortega-Moñux, I Molina-Fernández, Pavel Cheben, and GZ Mashanovich. Suspended SOI waveguide with sub-wavelength grating cladding for mid-infrared. *Optics Letters*, 39(19):5661–5664, 2014.

[116] J Anguita and F Briones. HF/H2O vapor etching of SIO2 sacrificial layer for large-area surface-micromachined membranes. *Sensors and Actuators A: Physical*, 64(3):247–251, 1998.

[117] M Wong and RA Bowling. Silicon etch using vapor phase hf/h 2 o and o 3. *Journal of the Electrochemical Society*, 140(2):567, 1993.

[118] Wei Jin. Investigation of interferometric noise in fiber-optic bragg grating sensors by use of tunable laser sources. *Applied optics*, 37(13):2517–2525, 1998.

[119] OriginLab. Originlab online help, 2021. URL https://www.originlab.com/doc/Origin-Help/Gaussian-Function-FitFunc.

[120] Brent E Little, Juha-Pekka Laine, and Sai T Chu. Surface-roughness-induced contradirectional coupling in ring and disk resonators. *Optics Letters*, 22(1):4–6, 1997.

[121] Antti Säynätjoki, Lasse Karvonen, Tapani Alasaarela, X Tu, TY Liow, Marianne Hiltunen, Ari Tervonen, GQ Lo, and Seppo Honkanen. Low-loss silicon slot waveguides and couplers fabricated with optical lithography and atomic layer deposition. *Optics Express*, 19(27):26275–26282, 2011.

[122] Ran Ding, Tom Baehr-Jones, Woo-Joong Kim, Xugang Xiong, Richard Bojko, Jean-Marc Fedeli, Maryse Fournier, and Michael Hochberg. Low-loss strip-loaded slot waveguides in silicon-on-insulator. *Optics Express*, 18(24):25061–25067, 2010.

[123] Tom Baehr-Jones, Michael Hochberg, Chris Walker, and Axel Scherer. High-q optical resonators in silicon-on-insulator-based slot waveguides. *Applied Physics Letters*, 86(8):081101, 2005.

[124] Tapani Alasaarela, D Korn, Luca Alloatti, A Säynätjoki, Ari Tervonen, R Palmer, J Leuthold, W Freude, and Seppo Honkanen. Reduced propagation loss in silicon strip and slot waveguides coated by atomic layer deposition. *Optics Express*, 19 (12):11529–11538, 2011.